Imperial College of Science, Technology and Medicine
Department of Life Sciences

Biomolecular Design of DNA Aptamers to Target α-Synuclein Oligomers in Parkinson's Disease – Metal Interactions of α-Synuclein Probed by NMR Amide-Proton Exchange

Mario Gonzalez Garcia

PhD thesis submitted for the degree of Doctor of Philosophy
Prof. Alfonso De Simone & Prof. Tony Cass
September 2023

For mi Tio Luismi y mi Yayo

ABSTRACT

α-Synuclein is a small, monomeric intrinsically disordered protein mainly expressed at the presynaptic terminal of neurons. By establishing interactions with neuronal and synaptic vesicle membranes, α-Synuclein is believed to be a critical component in neurotransmission. Under certain conditions, however, the aberrant misfolding and aggregation of α-Synuclein may be triggered, which are strongly linked to the pathology of Parkinson's disease.

Recent findings have identified the disruption of biological membranes as the main underlying pathological mechanism. Essential structural knowledge of the membrane binding ability of α-Synuclein fundamental to the mechanism of toxicity is exploited in this thesis, with the aim of selecting DNA aptamers targeted at the key N-terminal region to block the detrimental interactions of α-Synuclein oligomeric species with lipid membranes. Identified aptamers, however, failed at showing preferential binding to α-Synuclein at different biophysical assays. Instead, sequences with affinity for streptavidin, which was used to immobilise the target, were unintentionally selected for and isolated.

It is now established that α-Synuclein interacts with a variety of metal ions, which may alter its conformational properties and promote aggregation. Abnormal metal ion levels in neurons may therefore directly contribute to the development of idiopathic Parkinson's disease by shifting the conformational ensemble of α-Synuclein through the disruption of native intramolecular interactions.

To characterise the nature of these conformational changes, nuclear magnetic resonance was used to study hydrogen exchange of the backbone amide protons as a measure of solvent exposure. These experiments were complemented with chemical shift perturbation and ^{15}N relaxation measurements to obtain a comprehensive view of the interaction between α-Synuclein and the pathophysiologically relevant metal ions Ca^{2+}, Cu^{2+}, Cu^{+}, Mn^{2+} and Zn^{2+}. Overall, the data presented in this thesis indicate that binding of different metals may induce effects of different structural nature that have the potential of skewing the conformational ensemble towards aggregation-prone conformers.

DECLARATION

I declare that the work presented in this thesis is my own unless stated otherwise in the text as a reference or an acknowledgement. This thesis was written and composed by myself in its entirety and has not been submitted anywhere else for any other degree or qualification. This thesis was submitted for the degree of Doctor of Philosophy in Life Sciences at Imperial College London, April 2023.

Parts of the work presented in this document have led to the publication of a peer-reviewed research article and review:

- Gonzalez-Garcia, M., Fusco, G. and De Simone, A. Membrane interactions and toxicity by misfolded protein oligomers. *Frontiers in Cell and Developmental Biology* (2021).

- Gonzalez-Garcia, M., Fusco, G. and De Simone, A. Metal interactions of α-Synuclein probed by NMR amide-proton exchange. *Frontiers in Chemistry* (2023).

The copyright of this thesis rests with the author. Unless otherwise indicated, its contents are licensed under a Creative Commons Attribution-Non Commercial 4.0 International Licence (CC BY-NC 4.0). A copy of the license deed can be found on: https://creativecommons.org/licenses/by-nc/4.0/

Under this licence, you may copy and redistribute the material in any medium or format. You may also create and distribute modified versions of the work. This is on the condition that: you credit the author and do not use it, or any derivative works, for a commercial purpose. When reusing or sharing this work, ensure you make the licence terms clear to others by naming the licence and linking to the licence text. Where a work has been adapted, you should indicate that the work has been changed and describe those changes.

Please seek permission from the copyright holder for uses of this work that are not included in this licence or permitted under UK Copyright Law.

ACKNOWLEDGEMENTS

Firstly, I would like to thank my supervisors Alfonso and Tony for their support throughout my PhD, as well as BBSRC for funding my research.

I would also like to thank the greatly underestimated work of everyone at Imperial who made my experiments possible, from the lovely people running the autoclave and washing facility with no end, to the guys at the Chemistry stores, who were a pleasure to see every time I would go to pick up a parcel. To also Yingqi, for knowing how to decipher the spectrometers and their endless settings and helping me set up my NMR experiments. I would also like to thank Sondes Ben Aissa, for generating the 3D models of the R12S91 and TR12S91 aptamers for me. Thank you also to Steve and Ernesto for their invaluable suggestions and useful discussions in lab meetings.

I am also extremely thankful for having come across so many great people on the 6th floor of SECB during all these past years, even if living during the COVID pandemic meant avoiding each other in narrow lab spaces like two like charges: Montse, Sophie, Phivo, Sabine, Flo, Harold, Grace and Amit. Thank you also to everyone for the warm will to help and giving me a hand whenever I most needed it, particularly late in the evening. But I am especially grateful for having met Carlos, Joe and Yu, who I know will stay my very close friends for at least a very long time. Thank you for all the laughs and making the lab a fun place, it really felt like home whenever you were there. To all those moments teaching the Brits with Carlos how to eat sunflower seeds, or all those times Yu would start sassy conversations full of gossip.

To all my friends in London and Madrid, who constantly put up with my moaning about my results and my struggles bringing experiments to work and always unconditionally cheered me up.

To Zo for always being my rock and the daily sunshine that brightened up even the gloomiest of days. Thank you for being the greatest teacher anyone could wish for, for constantly inspiring me with your endless knowledge and always being willing to give a hand, even if that means having to

share the wonders of statistics with me until the wee hours of the morning. To all the brainstorming biochemistry sessions he would always propose to have in order to help me with my never-ending complaints about my negative results, even with his limited knowledge of molecular biochemistry. And to every single day of hard work, which was always rewarded with the joy of coming home to you.

Most importantly, to my family, especially my parents Ana and Angel, without whom I would not be the person I am today. I cannot but express my warmest gratitude for their eternal support and for being the pillars of my life. They will probably never understand how proud I am of them, for having worked as hard as they could all their lives to allow me and my brother have the best education and choices we could have ever wished for.

To my grandparents, who are the biggest role models of my life. To the extraordinary love they spread, their generosity and their unjustified endless admiration for their grandchildren. They are just the kindest and most warm-hearted people I have ever met, who have given me the motivation throughout my studies to keep pushing in the hardest times. To all those moments during our weekly videocalls when they would start the countdown to my coming back home for holidays like an impatient child asking to go to a theme park, which completely filled me with pure happiness and joy. To my uncle, Tio Luismi, who, unsurprisingly being my grandparent's son, had the biggest heart in this world. To all the infinitely happy moments we spent as a family together and to all those memories of you giving me the tightest hugs when my whole family expectantly waited for me at the airport every time I would fly back home. Os quiero infinito.

ACRONYMS

ABB Aptamer Binding buffer

AD Alzheimer's Disease

ALS Amyotrophic Lateral Sclerosis

AMPAR AMPA Receptor

ASO Antisense Oligonucleotides

αSyn α-Synuclein

Ac-αSyn Acetylated α-Synuclein

α3-NKA α3-Na^+/K^+-ATPase

BBB Blood-Brain Barrier

CEST Chemical Shift Saturation Transfer

CLEANEX CLEAN Chemical EXchange

CNS Central Nervous System

COMT Catechol-O-Methyl Transferase

CPP Cell-Penetrating Peptide

Cryo-EM Cryo-Electron Microscopy

CSP Chemical Shift Perturbation

DBS Deep-Brain Stimulation

dsDNA Double-Stranded DNA

ELONA Enzyme-Linked Oligonucleotide Assay

EM Electromagnetic

ER Endoplasmic Reticulum

FID Free Induction Decay

FRET Förster's Resonance Energy Transfer

H/D Exchange Hydrogen/Deuterium Exchange

HD Huntington's Disease

HSQC Heteronuclear Single Quantum Coherence

IAPP Islet Amyloid Polypeptide

IDP Intrinsically Disordered Protein

IMM Inner Mitochondrial Membrane

LB Lysogeny Broth

LBs Lewy Bodies

LRP1 Low-density lipoprotein Receptor-related Protein-1

mPTP Mitochondrial Permeability Transition Pore

mGluR Metabotropic Glutamate Receptor

MAO Monoamine Oxidase-B

MWCS Mean Weighted Chemical Shift

nAChR Nicotinic Acetylcholine Receptor

NCM Nitrocellulose Membrane

NGS Next-Generation Sequencing

NMDAR N-Methyl-D-Aspartate Receptor

NMR Nuclear Magnetic Resonance

NOE Nuclear Overhauser Effect

NTA N-Terminal Acetylation

OMM Outer Mitochondrial Membrane

PBS Phosphate Buffered Saline

PCR Polymerase Chain Reaction

PD Parkinson's Disease

PMD Protein Misfolding Disease

PRE Paramagnetic Relaxation Enhancement

PrP^c Cellular Prion Protein

PTM Post-Translational Modification

ROE Rotating-frame Overhauser Effect

ROS Reactive Oxygen Species

RT Room Temperature

RVG Rabies Virus Glycoprotein

SA-Mag beads Streptavidin-Magnetic Beads

SELEX Systematic Evolution of Ligands by EXponential Enrichment

SERCA Sarcoplasmic Reticulum Ca^{2+}-ATPase

SOD1 Superoxide Dismutase 1

ssDNA Single-Stranded DNA

ssNMR Solid-State Nuclear Magnetic Resonance

SUV Small Unilamellar Vesicle

VDAC Voltage-Dependent Anion Channel

Contents

Abstract **III**

Declaration **IV**

Acknowledgements **V**

Acronyms **VII**

1 Introduction **1**

1.1 Structure of this thesis 1

1.2 Parkinson's disease 1

1.3 α-Synuclein in physiology and pathology 4

1.4 Membrane binding ability of α-Synuclein 8

1.5 Oligomeric α-Synuclein, the cytotoxic species 10

1.6 The disruption of the membrane as a neurotoxic event 14

1.6.1 Disruption of biological membranes by toxic protein oligomers 14

1.6.2 Mitochondrial membrane disruption 17

1.6.3 Receptor-mediated toxicity by protein oligomers 18

1.7 Nucleic acid aptamers: the new class of molecular recognition tools 23

1.8 Aptamers as therapeutics for PD 26

1.9 Metal ion interactions 31

1.9.1 Calcium 34

1.9.2 Copper 36

1.9.3 Zinc 39

1.9.4 Manganese 40

1.10 Research aims 42

2 Materials and Methods **45**

2.1 Design of DNA Library 45

2.2 Aptamer selection 46

2.2.1 Selection of initial library 47

2.2.2 Amplification of DNA library 47

2.2.3 Generation of a ssDNA library 48

2.2.4 Selection against the target αSyn_{1-25} peptide (SA-Mag beads-SELEX) . . . 48

2.2.5 Selection against the target full-length αSyn (NCM-SELEX) 49

2.3 Purification of ssDNA 49

2.4 Purification of dsDNA 51

2.5 Library cloning and sequencing 51

2.6 Structural modelling of aptamer sequences 52

2.7 Enzyme-Linked Oligonucleotide Assay (ELONA) 52

2.8 NHS-Rhodamine labelling 54

2.9 Förster's Resonance Energy Transfer (FRET) 54

2.9.1 Assay design and preparation 55

2.9.2 Data collection 55

2.10 αSyn expression and purification 56

2.10.1 Bacterial Transformation 56

2.10.2 Expression in M9 minimal media 57

2.10.3 Purification 58

2.11 Generation of Cu^{+} 61

2.12 Heteronuclear single quantum coherence (HSQC) experiments - Aptamer interactions 61

2.13 Heteronuclear single quantum coherence (HSQC) experiments - Metal interactions . 63

2.14 Phase-modulated CLEAN chemical exchange (CLEANEX) NMR experiments . . . 64

2.15 Transverse and longitudinal relaxation NMR experiments 66

2.16 Error analysis 67

2.17 Theoretical background of NMR 67

2.17.1 ^{1}H-^{15}N experiment 72

2.17.2 NMR for IDPs 73

2.17.3 Residue resonance assignment 74

2.17.4 Protein-ligand interactions by NMR 75

2.17.5 Hydrogen exchange in proteins 79

2.17.6 NMR relaxation 83

3 Aptamer Selection **89**

3.1 Introduction 89

3.2 Results 91

3.2.1 Optimisation of initial selection conditions 92

3.2.2 Aptamer selection with SELEX 99

3.2.3 Purification of the ssDNA library temporarily removes large PCR by-products 103

3.2.4 Progression of selection gave rise to a short ∼70 nt-long band 106

3.2.5 Sequencing of different selection libraries revealed a high abundance of primer-derived sequence and the presence of sequences with random core regions . . 112

3.3 Discussion 116

4 Aptamer Characterisation **128**

4.1 Introduction 128

4.2 Results 130

4.2.1 8^{th} Round 130

4.2.2 12^{th} Round 135

4.2.3 15^{th} Round 143

4.2.4 17^{th} Round 143

4.2.5 20^{th} Round 145

4.2.6 18^{th} Round 146

4.3 Discussion 151

5 Interactions with Metal Ions **159**

5.1 Introduction 159

5.2 Results 163

5.2.1 Calcium 163

5.2.2 Copper 171

5.2.3 Zinc 177

5.2.4 Manganese 181

5.3 Discussion 183

6 Discussion **197**

6.1 Aptamer selection 197

6.2 Interactions with metal ions 202

6.2.1 Calcium 203

6.2.2 Copper 203

6.2.3 Zinc 204

6.2.4 Manganese 205

6.3 Future Work 207

6.3.1 Aptamer selection 207

6.3.2 Interactions with metal ions 209

Bibliography **210**

List of Figures

1.1 Deposits of aggregated αSyn in the form of Lewy bodies in the brains of synucleinopathy patients . . . 3

1.2 Schematic representation of the different regions of αSyn. . . . 5

1.3 Structural ensembles adopted by αSyn in solution and upon association with the membrane. . . . 9

1.4 Aberrant interactions between misfolded protein oligomers and biological membranes. 11

1.5 Representation of the fibrillisation process of αSyn. . . . 13

1.6 Schematic representation of the binding of toxic αSyn oligomers to the membrane. . 14

1.7 Mechanisms of membrane disruption by misfolded protein oligomers. . . . 15

1.8 Aberrant interactions of misfolded protein oligomers with membrane receptors. . . . 20

1.9 Illustration of the process of DNA aptamer selection through SELEX. . . . 25

2.1 Set-up of FRET. . . . 55

2.2 FRET experimental set-up with ratios of fluorescein-labelled DNA aptamers to rhodamine-labelled αSyn. . . . 56

2.3 Purification of αSyn and Ac-αSyn . . . 59

2.4 Anion Exchange Purification of Ac-αSyn 60

2.5 Manufacturer's chromatographic separation and calibration curves of standard proteins on a HiLoad 16/60 Superdex 75 pg column. 61

2.6 SEC Purification of αSyn and Ac-αSyn 62

2.7 Bulk magnetisation of nuclei containing spin ½ at equilibrium in an external magnetic field, B_0 68

2.8 Zeeman Splitting 69

2.9 Shielding effects and their influence in chemical shift 71

2.10 3D spectra from ^{1}H-^{15}N HSQC 75

2.11 3D Backbone assignment 76

2.12 Representative spectra for two different molecules (M1 and M2) as a function of different exchange regimes 78

2.13 Hydrogen exchange EX1 (pH-independent) and EX2 (pH-dependent) regimes 79

2.14 Relationship between correlation time for rotational diffusion, τ_c, and the relaxation times, T_1 and T_2 87

3.1 Electrophoresis analysis of the 111-bp PCR products from the recovered first round library after symmetric amplification for 16 cycles, showing intervals of 2 cycles per lane. 93

3.2 Agarose gel analysis of the effect of different incubation temperatures of selection on library amplification, showing the PCR products of the first 16 cycles of amplification, in intervals of 2 cycles. 95

3.3 Agarose gel analysis of the effect of different selection incubation ratios between αSyn_{1-25} target and the ssDNA library, showing the PCR products of the first 16 cycles of amplification, in intervals of 2 cycles. 96

3.4 Electrophoresis analysis of the effect of magnetic bead concentration on library amplification, showing the PCR products of the first 16 cycles of amplification, in intervals of 2 cycles. 97

3.5 Electrophoresis analysis of the PCR products from the fourth round library after symmetric amplification for 16 cycles, showing intervals of 2 cycles per lane. 98

3.6 NCM-SELEX 102

3.7 Electrophoresis analysis of the PCR products of the 4^{th} and 7^{th} libraries showing the formation of larger by-products, and their removal. 105

3.8 Electrophoresis analysis of the PCR products of the 3^{rd}, 5^{th} and 8^{th} libraries showing the presence of the $\sim$70 nt band. 107

3.9 Electrophoresis analysis of the PCR products after purification of the $\sim$70 nt band. . 108

3.10 Electrophoresis analysis of the PCR products after amplification of the 14^{th}, 15^{th} and 16^{th} round NCM libraries upon modification of the selection conditions to prevent the formation of primer-derived sequences 110

3.11 Comparison of primer-derived and N42 library aptamer sequences. 113

3.12 SELEX library sequencing statistics. 116

4.1 Characterisation of the binding of the primer-derived FSeq1 and 65ntSeq identified upon sequencing of the 8^{th} round library. 131

4.2 Characterisation of the binding of 65ntSeq. 133

4.3 Characterisation of the binding of 65ntSeq and R12S91 in the absence of streptavidin using different antibody dilutions 134

4.4 Characterisation of the binding of the six aptamer sequences identified upon sequencing of the 12^{th} round library. 136

4.5 Characterisation of the binding of R12S91. 138

4.6 Structural prediction of the R12S91 and TR12S91 sequences 141

4.7 Comparison of the binding of R12S91 and TR12S91 to αSyn_{1-25} 142

4.8 Characterisation of the binding of the aptamer sequences identified upon sequencing of the 15^{th}, 17^{th} and 20^{th} round libraries. 144

4.9 Phylogenetic tree of the different aptamer sequences identified from the 18th round NCM library illustrating different groups of aptamers with sequence similarity. . . . 147

4.10 Characterisation of the binding of six sequences identified from the 18^{th} round library of NCM-SELEX 148

5.1 NMR analysis of Ca^{2+} binding to αSyn. 164

5.2 Collection of Ac-αSyn CLEANEX NMR spectra recorded at different mixing times. 166

5.3 Overlay of ^{1}H-^{15}N HSQC spectra of Ac-αSyn in the presence of the various metal ions tested before and after CLEANEX 167

5.4 Protection factor profile of αSyn as measured by CLEANEX. 168

5.5 Representative example of peak intensity changes recorded with CLEANEX at different mixing times. 169

5.6 ^{15}N relaxation of Ac-αSyn complexed with Ca^{2+}, Cu^{+} and Cu^{2+}. 170

5.7 Effect of addition of Na-ascorbate and EDTA on αSyn and Ac-αSyn, respectively . . 172

5.8 NMR analysis of copper binding to Ac-αSyn. 174

5.9 NMR analysis of Zn^{2+} binding to Ac-αSyn. 178

5.10 ^{15}N relaxation of Ac-αSyn complexed with Zn^{2+} and Mn^{2+}. 180

5.11 NMR analysis of Mn^{2+} binding to Ac-αSyn. 182

List of Tables

1.1 Development stages of aptamers in clinical trials as of 2018. 28

2.1 Sequences of the primers and aptamers identified from sequencing of the different round libraries throughout SELEX. 46

2.2 Selection conditions per round of SA-Mag beads-SELEX and NCM-SELEX 50

4.1 Affinities of the aptamer sequences identified and tested in this work for αSyn_{1-25} . . 150

Introduction

1.1 Structure of this thesis

The work contained in this document is comprised of two main parts corresponding to two separate research projects involving α-Synuclein. The first part of this thesis reports on the selection of DNA aptamers against an N-terminal peptide from α-Synuclein and the characterisation of the identified sequence candidates. The second part of this thesis presents the findings of the study investigating metal ion interactions of α-Synuclein by NMR.

An introductory Chapter is included at the start of this thesis to provide a detailed background to the work presented here. Each results Chapter is then divided into an Introduction, Results and Discussion sections specific to each topic. A general discussion Chapter towards the end of this thesis is divided into two parts corresponding to the two different research studies presented in this document, and discusses the implications of the findings together with possible future directions.

1.2 Parkinson's disease

Parkinson's disease (PD) is a progressive neurodegenerative disease affecting people in late stages of life. It accounts for the second most common neurodegenerative disorder after Alzheimer's disease (AD). In industrialised countries, cases of PD are estimated to account for 0.3% of the whole

population and approximately 1% of the people aged 60 and above, with its incidence and prevalence expected to increase as the global average age rises [1]. In Europe, its prevalence has been reported to be 3.5% of the population aged 85-89 [2]. Globally, PD was estimated to affect 8.5 million individuals in 2019 and is projected to grow to over 12 million by 2040 [3, 4]. PD is also the most prevalent synucleinopathy [5], a collective term for a group of debilitating neurodegenerative diseases that mainly includes dementia with Lewy bodies, multiple system atrophy and PD [6, 7]. Common to these disorders is the pathological accumulation of large neuronal deposits known as Lewy bodies (LBs), found in the cytoplasm of neurons of multiple brain regions (Figure 1.1) [8, 9, 10]. These intracellular large inclusions are composed of a mixture of proteins [11], lipids [12, 13] and cellular organelles including mitochondria and lysosomal structures [14, 15, 16, 17, 18]. With the main constituent of LBs being the fibrillar aggregates of the protein α-Synuclein (αSyn) [10, 9, 19, 20], it is believed that this protein is a key effector in the aetiology of PD. Neurodegeneration in PD is characterised by the presence of LBs and the progressive loss of dopaminergic neurons in the substantia nigra of the brain, which together constitute the pathological hallmark of the disease [21]. Clinically, this generally translates into tremor, rigidity, bradykinesia (slowness of movement) and postural instability, whilst non-motor symptoms are also common in PD patients. These include sleep disorders, neuropsychiatric syndromes, impairment of the olfactory sense and increased constipation, among others [22]. Additionally, cognitive deterioration and dementia are also common features whose risk may be exacerbated in advanced stages of severity of the disease [23, 22].

Currently, treatments available for PD are limited and only offer an ameliorating effect of its debilitating symptoms. Most of the therapeutic approaches focus on restoring dopamine levels in the brain striatum, as a way of replacing the loss of dopamine signalling as dopaminergic neuronal death unravels in PD. Levodopa, a dopamine precursor, is the most commonly prescribed treatment for PD, and has remained the most effective therapeutic drug since its development in the 1960s. Other drugs have been discovered and are used as adjuvant therapy together with levodopa or on their own, including dopamine agonists, dopamine metabolism inhibitors or nondopaminergic therapy, although these are generally less effective [25]. Examples of these include carbidopa, a dopamine carboxylase inhibitor, or catechol-o-methyl transferase (COMT) inhibitors, which interfere with dopamine metabolism to

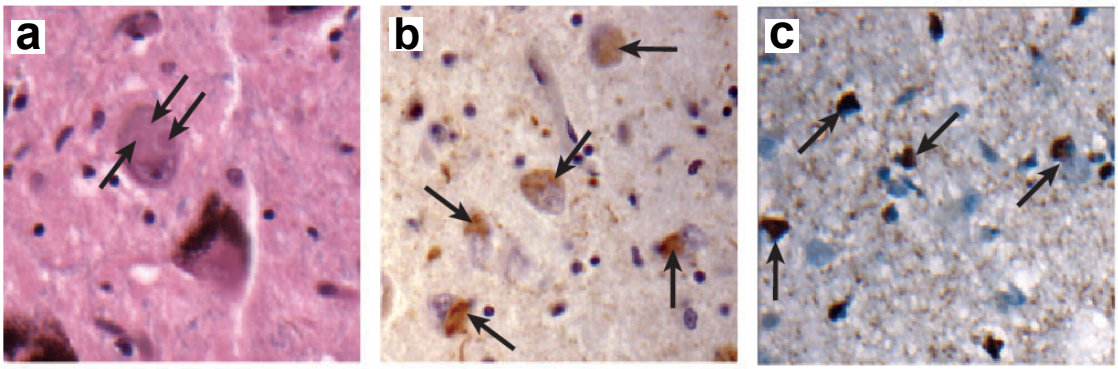


Figure 1.1: Deposits of aggregated αSyn in the form of Lewy bodies in the brains of synucleinopathy patients. a) Luxol fast blue-, haematoxylin and eosin-stained brain section of the substantia nigra of a patient with PD. b) Immunohistochemistry for αSyn on a section of the amygdala from a patient with dementia with Lewy bodies. c) Immunohistochemistry for αSyn on a section of the putamen from a patient with multiple system atrophy. Arrows indicate cytoplasmic LB inclusions, of which αSyn is the major component. Figure adapted from [24].

make it more available in the brain [26]. Whilst current treatments have proven dramatically effective at managing parkinsonian symptoms and improving the quality of life of the patient, especially at early stages of the disease, long-term use can lead to the development of significant adverse effects, as a result of the uptake of dopamine by other brain regions different to the striatum, effects of non-physiological continuous dopamine release on dopamine receptors and variability in absorption and transport across the blood-brain-barrier [25]. In fact, it has been estimated that around half of all patients develop cognitive deficits and levodopa-induced bradykinesia, whilst all of them are expected to experience periods of on-off drug efficacy fluctuations, at 10 years from diagnosis [25]. These side-effects become a significant burden that add to the clinical symptoms in advanced disease states and can drastically reduce quality of life of the patient. This is therefore why dopamine agonists are generally prescribed at early stages after diagnosis, to delay the introduction of levodopa and hence the onset of levodopa-induced complications [26].

Another common complication associated with levodopa is the "wearing off" effect, a term that refers to the decrease in the drug's effectiveness. Given the loss of dopaminergic terminals in the striatum, an impaired ability to store and distribute the absorbed levodopa might result in a gradual shortening of the half-life of levodopa and therefore a dampened therapeutic effect [26]. Administration of several drugs like a COMT or a monoamine oxidase-B (MAO-B) inhibitor my help alleviate the mo-

tor shortcomings associated with levodopa therapy by blocking the breakdown of dopamine, thereby prolonging the drug's effect. In fact, the use of amantadine, an NMDA receptor antagonist belonging to the class of nondopaminergic therapeutic drugs for PD, has been shown to improve motor complications that arise from levodopa therapy [26]. Similarly, anticholinergics may also be prescribed to ease muscle stiffness and tremors, as they act by restoring homeostatic levels of acetylcholine signalling. A more detailed explanation of the molecular rationale supporting NMDA receptor inhibitors as relevant therapeutic drugs for PD is given later on in section 1.6.3.

Besides pharmacological treatment, a promising strategy for the treatment of tremors and other motor impairments, which becomes especially relevant after the exacerbation of levodopa-induced side-effects, is deep-brain stimulation (DBS). This involves the surgical implantation of electrodes in subcortical structures – such as the subthalamic nucleus and globus pallidus internus – to stimulate the reorganisation of electrical signals in the brain, thereby interfering with tremor and other motor complications [25, 26]. While DBS results in noticeable motor improvements in advanced PD patients, it offers no benefit on the treatment of non-motor features of the disease which do not respond to dopamine therapy (including cognitive deficits, freezing of gait and postural instability) [25].

Although the available treatments have proven to be effective at alleviating motor symptoms in the short term, prolonged treatment durations result in motor fluctuation problems that complicate disease management. Additionally, their effect fails at improving the particularly debilitating non-motor features of the disease, which are often the ones having the most detrimental impact on the patient's life. Most importantly, none of the current drugs have the ability to slow down the progression of PD and interfere with neuronal loss. There is therefore an urgent need to develop new, disease-modifying treatments that can target the pathological agents causing disease, and not only the disabling clinical symptoms associated with pathology.

1.3 α-Synuclein in physiology and pathology

αSyn is a 14 kDa intrinsically disordered protein (IDP) that is mostly found at the presynaptic terminals of neurons in the brain [27]. αSyn comprises 140 amino acid residues which can be broken

down into three different regions with distinct structural and dynamic properties: the N-terminal region (1-60) contains a series of seven imperfect KTKEGV repeats, which code for amphipathic class A2 lipid-binding segments throughout the sequence of the protein up to residue 90 [28, 29, 30]; the non-β-amyloid component (NAC) (61-95), which consists of a highly hydrophobic region associated with a modulatory lipid binding capacity and a self-aggregation propensity that can initiate amyloid formation [31]; and the highly negatively charged C-terminal region (96-140), which is rich in Pro and the acidic residues Asp and Glu, and plays a critical role in the physiological function of αSyn and in preventing self-assembly and aggregation (Figure 1.2) [32, 33, 34, 35, 36, 8, 37].

In its cytosolic form under physiological conditions, αSyn exists as an ensemble of dynamically interconverting structurally heterogeneous conformations in monomeric state [38]. Indeed, solution state nuclear magnetic resonance (NMR) [39] and circular dichroism [35] studies failed to show significant levels of persistent secondary or tertiary structure along the protein sequence in solution. A large body of evidence points at the existence of long-range intramolecular interactions between the slightly positively charged N-terminal and the acidic C-terminal regions via electrostatic contacts, and the C-terminal and the NAC regions through hydrophobic interactions. These long-range interactions stabilise αSyn in a conformational state that inhibits self-aggregation through the partial burial of the NAC [40, 41, 42, 43, 44, 45].

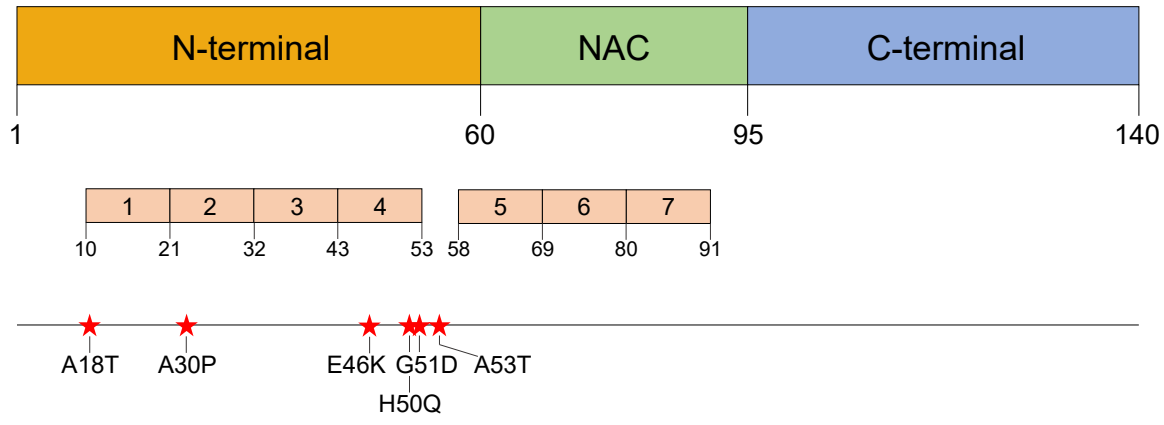


Figure 1.2: Schematic representation of the different regions of αSyn. The location of the seven imperfect repeats responsible for amphipathic helix stabilisation is represented by pink boxes, together with their amino acid positions. The position of the known missense mutations associated to Parkinsonism is marked with red stars.

In this context, the relationship between the structure of αSyn as an IDP and its function becomes particularly interesting. A common belief in biology was the existence of certain protein secondary structures that are shared by all proteins and combined in different ways to make up a folded, globular and functional tertiary protein structure. It was not until relatively recently, however, that the existence of proteins with a disordered nature was recognised. In fact, it is now believed that around 30% of the eukaryotic proteins are either partially or fully disordered [46]. Compared to globular proteins, whose fold is dictated by a strong hydrophobic effect that buries hydrophobic residues in a highly lipophobic core, the sequences of disordered proteins possess a different amino acid distribution, with low hydrophobic content and rich in charged amino acids. These characteristics confer disordered proteins or regions the capacity to become protein-protein interaction hubs, where interactions with different binding partners are strongly influenced by the environment. This interaction promiscuity is therefore a direct result of their plasticity and ability to adopt different conformational changes that accommodate for partner binding. Disordered proteins therefore have a distinct functional diversity by which their biological roles are executed in the form of interactions [47].

Although the full picture of the functional repertoire of αSyn still remains controversial in terms of the specific roles the protein performs, its specific localisation within the presynaptic terminal of neurons [27, 6], as well as its ability to bind to the membrane of vesicles [35] and promote their clustering *in vitro* [48, 49, 50], hints at a putative key role in the homeostasis of synaptic vesicles [24, 51]. αSyn might possibly regulate the trafficking of synaptic vesicles from the distal reserve pool to control synapse docking during neurotransmitter release [24, 52, 51]. Consistently, a significant preference to bind to the inner leaflet of the presynaptic membrane by which αSyn seems to stabilise the docking of synaptic-like small unilamellar vesicles (SUVs) [53] further supports the view of a regulatory role in vesicle trafficking and therefore in synaptic plasticity and learning. Additionally, αSyn may also play a part in the formation of the SNARE complex required for rapid fusion of the synaptic and presynaptic terminal membranes, by interacting with the key complex-forming component synaptobrevin-2 [54]. In fact, αSyn has been shown to rescue an impairment in SNARE formation and a consequent degeneration of the nerve terminals in mice, upon deletion of the CSPα chaperone required for normal synaptic transmission [55, 56].

A large effort by the scientific community over the last two decades has established an association between αSyn and the pathology of several motor neuron diseases, following the finding that αSyn aggregates constitute the main component of LBs [9, 10, 19, 20]. Similarly, many studies have also shown a direct involvement of αSyn in the pathology of PD in the form of six missense hereditary autosomal dominant mutations found in the αSyn *SNCA* gene (A30P, E46K, H50Q, G51D, A53T, A53E) (Figure 1.2), which are associated with familial forms of early-onset but also late-onset (H50Q) PD and higher rates of neurodegeneration compared to sporadic cases of the disease [9, 57, 58, 59, 60, 61, 62, 63, 64, 65, 66, 57, 60, 61, 62, 59]. Similarly, members of the same family harbouring duplications and triplication of the *SNCA* gene have been shown to suffer PD at an earlier age and an accelerated disease progression, most likely due to a gene dosage effect and the inability to clear excess αSyn [36, 67, 68, 69, 70, 71]. Genetic defects, however, only account for 5-10% of PD cases, with the rest being idiopathic and age related [72]. Consistently, several studies reported the abnormal accumulation of αSyn inclusions and an associated neuronal impairment upon expression of human wild-type and mutated αSyn in animal models of PD such as mice, Drosophila flies and *Caenorhabditis elegans* [73, 74, 36]. Interestingly, similar deposits were also observed in animal models where Parkinsonism was induced through the administration of neurotoxicants [75].

Existing evidence points at a prion-like spreading mechanism of toxic αSyn aggregates, by which misfolded conformations may be imposed upon αSyn monomers and therefore contribute to the propagation of pathology. In this way, αSyn aggregates that are secreted by neurons into the extracellular space can recruit further αSyn monomers after being taken up by new cells. These cells will then in turn secrete more aggregated αSyn species, which can further act like seeds to propagate disease [76, 77]. The "prion-like" spread hypothesis was first proposed as αSyn deposits were observed in grafted embryonic dopaminergic neurons in the post-mortem brain of a PD patient 14 years after they had been implanted [78, 79]. Similarly, pre-formed αSyn fibres incubated with primary cortex neurons *in vitro* had the capacity to enter the cells and recruit endogenous αSyn species that later resulted in the formation of insoluble toxic aggregates [80]. Current research on the spread of PD pathology focuses on clarifying many aspects of the proposed mechanism which still renders the hypothesis controversial, as is the fact that αSyn aggregates have been observed to spread to cells which may not

always correspond to the nearest neighbouring neuron [81].

1.4 Membrane binding ability of α-Synuclein

It is believed that αSyn may exert its function through the direct interaction between lipid membranes and the N-terminal region, which adopts a transient α-helical state upon membrane sensing that allows the adherence of αSyn to biological membranes [35, 82, 83, 30, 84]. The conformational transition into an amphipathic helix is driven and stabilised by the presence of a series of seven repeats of eleven residues long, which bear KTKEGV as a consensus sequence and are repeated imperfectly through residues 1-90 (Figure 1.2) [35, 85, 86, 87]. Research studying the interaction of αSyn with SUVs as synaptic vesicle mimics using solid-state NMR (ssNMR) revealed the importance of the interactions between the rigid ordered helical conformation adopted by the first 25 residues of the N-terminal region and the hydrophobic lipid group chains, which were shown to act as an anchor for the protein to the membrane. This anchoring interaction was also observed to be further enhanced through the partial insertion of the N-terminal initial 12 residues into the membrane, forming a tilt angle of 12º relative to the plane of the membrane [82]. Consistent with these findings is a study by Vamvaca and colleagues, which demonstrated a dramatic fall in the propensity of αSyn to bind vesicle membranes in yeast upon deletion of residues 2-11 [88]. These strong but also transient interactions allow αSyn to exist in a dynamic equilibrium between a partially ordered membrane-bound state and a disordered unbound state in solution (Figure 1.3), which seem to be fundamental for its physiological function [27, 38, 37]. At the same time, the transient nature of the association between the N-terminal region of αSyn and biological membranes prevents the long exposure of the NAC to the solvent, which could otherwise initiate aggregation with other αSyn monomers whilst long-range interactions between the N- and C-termini are interrupted.

However, the tight binding arising from the partial insertion of the α-helical N-terminus into the membrane may ultimately contribute to the initiation of amyloid formation and the onset of pathology. As mentioned above, the membrane-bound conformation of αSyn may inadvertently favour the transient detachment and exposure of the central region, which is associated with the initial steps of amyloid formation [50, 24, 89, 90]. The transient interruption of the long-range intramolecular in-

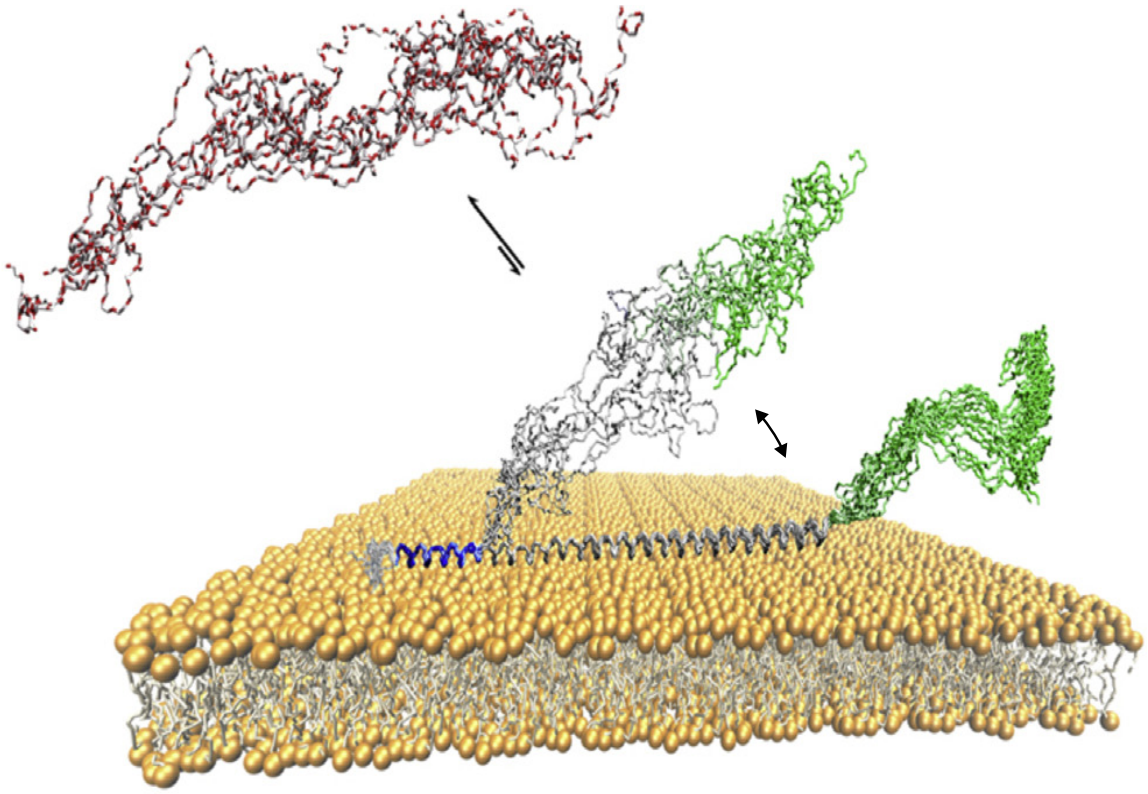


Figure 1.3: Structural ensembles adopted by αSyn in solution and upon association with the membrane. Figure adapted from [38].

teractions may therefore lead to the increased exposure and availability of the NAC to self-aggregate with other αSyn monomers and assemble into larger aggregates on the surface of membranes [50]. In fact, calcium, which is believed to be essential for the function of αSyn, has been shown to trigger its aggregation through the collapse of the C-terminal region upon charge neutralisation, leading to altered long-range contacts and enhanced hydrophobic interactions between the C-terminal and NAC regions [91]. As it will be explained later in 1.9.1 of the Introduction Chapter in more detail, abnormally high levels of intracellular Ca^{2+} may lead to the misfolding of αSyn, the skewness of the conformational equilibrium towards aggregation-prone states and the perpetuation of a feed-forward loop where αSyn oligomers disrupt cellular membranes and further increase levels of calcium [92].

αSyn is believed to undergo a variety of post-translational modifications *in vivo* that alter its structural and dynamic properties, adding an extra layer of complexity to its conformational promiscuity, including phosphorylation and N-terminal acetylation (NTA) [93, 67, 94, 95]. The latter is considered especially important and relevant as a result of its role in modulating the membrane binding ability

of αSyn. NTA increases the helical propensity of the N-terminal region, enhances membrane binding affinity [88, 94, 96, 97], and alters αSyn aggregation kinetics and morphology of the resulting fibrils [98]. Indeed, given that no deacetylases are currently known, αSyn is thought to be fully acetylated at the N-terminus *in vivo* [99].

1.5 Oligomeric α-Synuclein, the cytotoxic species

Since αSyn was identified as being a central piece in the pathological puzzle of PD and the other synucleinopathies, a wealth of knowledge has been generated from biophysical as well as biochemical studies that points at prefibrillar αSyn oligomeric, and not monomeric or fibrillar species, as being the primary pathological agents [100, 38, 36, 64, 101, 102]. An extensive body of evidence has established the variety of distinct mechanisms through which oligomeric αSyn species disrupt normal cellular function, including mitochondrial dysfunction, elevated levels of reactive oxygen species (ROS), aberrantly high intracellular levels of Ca^{2+} and proteasomal impairment (Figure 1.4) [67, 92, 102, 103, 104, 105, 106, 107, 108, 109, 110].

The focus of research on the putative pathological agents responsible for cytotoxicity in PD has been controversial and has shifted several times between the more obvious and insoluble αSyn fibrils found in PD patients' brains, and the more oblivious and soluble αSyn oligomeric species. Indeed, a series of experiments has lately highlighted the paramount importance of misfolding aggregate intermediates in neurotoxicity and disease progression. Indeed, it is their dynamic nature consisting of an ensemble of heterogeneous conformations that makes their individual isolation and study so difficult [111].

A series of recent studies have provided compelling evidence that supports small soluble oligomeric aggregates as being the most damaging and toxic species to cells (Figure 1.5) [101, 112, 111, 113]. This idea initially stemmed from the fact that the extent of fibrillar aggregates does not generally correlate with neurodegenerative disease progression and severity of cognitive impairment in patients, which proposes the existence of soluble intermediate misfolding events, rather than the end-point fibrillar amyloids observed in post-mortem analyses of brains of PD patients, as putative toxic factors

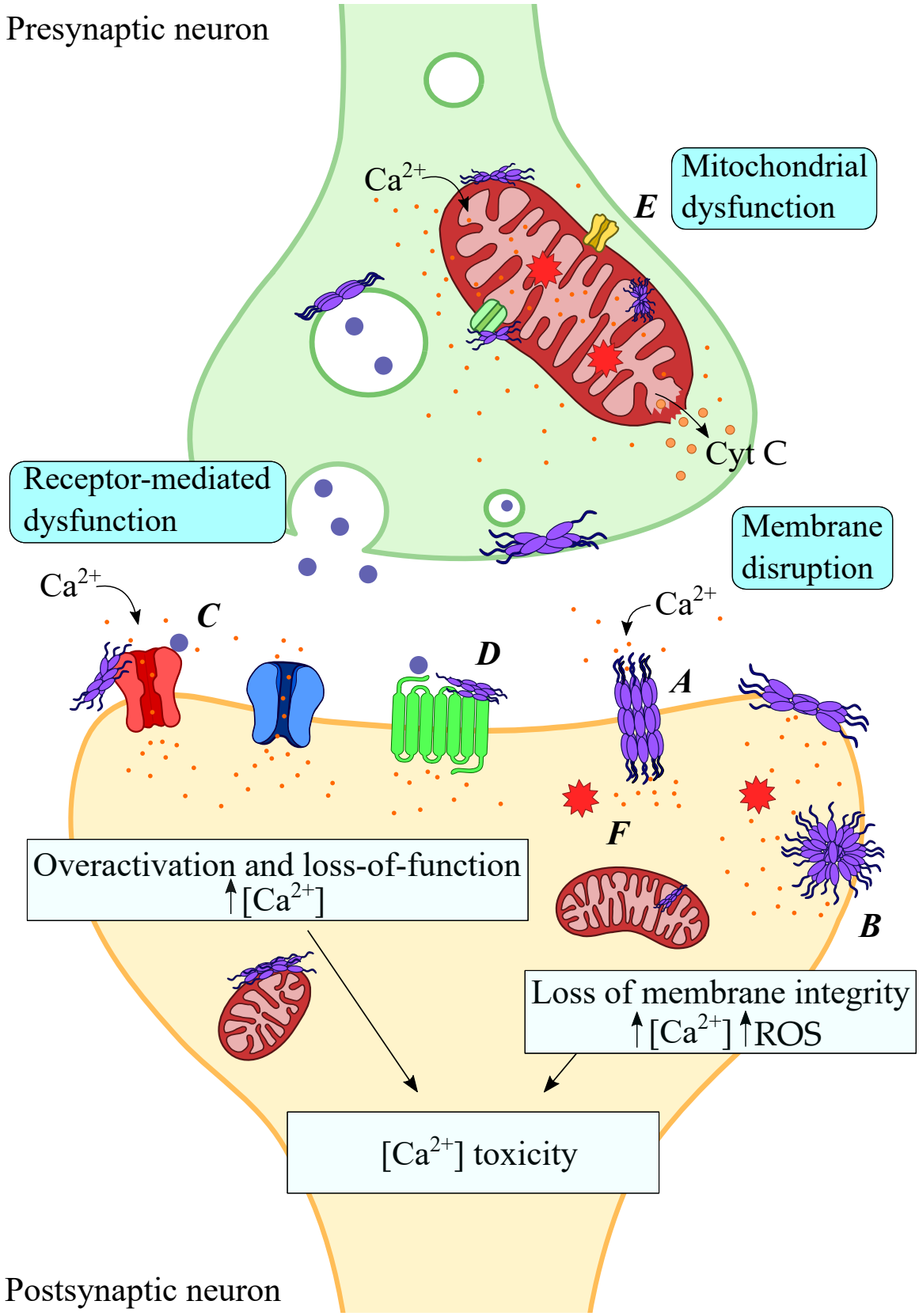


Figure 1.4: Aberrant interactions between misfolded protein oligomers and biological membranes. Toxic protein oligomers can strongly bind biological membranes, including the plasma and mitochondrial membranes, as well as proteins (e.g. receptors and ion channels) located at the membrane. Perturbation and pore formation (A) of the lipid bilayer by misfolded protein aggregates may disrupt

Figure 1.4: membrane integrity, ultimately leading to its permeabilisation (B) and associated downstream aberrant processes such as mitochondrial dysfunction, elevated intracellular ROS generation and the release of cytochrome c. In addition, interactions of misfolded protein aggregates with membrane receptors (C,D) and mitochondrial receptors (E) may result in loss of function (e.g. VDACs, α3-NKA) or overactivation (e.g. mGluRs, NMDARs), with consequent alteration of the cellular viability, associated with an underlying imbalance in Ca^{2+} gradients as well as cellular and organelle dysfunction. In fact, most of the interactions of misfolded protein aggregates with cellular membranes and membrane proteins promote a common downstream Ca^{2+}-dependent cellular toxicity. In this scheme, deleterious interactions and processes driven by protein oligomers at the surface of biological membranes are shown: (A) Pore formation. (B) Membrane permeabilisation. (C) Interaction with ionotropic/metabotropic glutamate receptors. (D) Interaction with plasma membrane receptors (e.g. α7 nAChR, α3-NKA, etc.). (E) Interaction with mitochondrial membrane receptors (VDACs, mPTP, etc.). (F) Elevated intracellular ROS production. Protein aggregates are schematically shown in purple, Ca^{2+} ions in orange and neurotransmitter molecules in blue. Figure from [92].

responsible for the underlying pathology [114, 64, 115]. In fact, this has been observed in other protein misfolding diseases involving Aβ [116] and tau [117] in AD and human islet amyloid polypeptide (IAPP) in type II diabetes [118, 119].

These soluble intermediate species represent an elusive population characterised by high structural heterogeneity. Indeed, biophysical and size-exclusion chromatography (SEC) studies revealed a continuous distribution in the size of prefibrillar oligomeric αSyn isolated from post-mortem human and transgenic animal brains, ranging from small oligomers (-2-5 monomers), through medium (-5-15) to large (-15-150) particles [67]. Indeed, toxic oligomeric species have distinct biophysical properties that enhance their ability to establish aberrant interactions and cause toxicity compared to amyloid fibrils, including small size [120], exposure of hydrophobic surfaces [121] and unsaturated edge-strands [122].

Under special conditions where the likelihood of closer inter-protein contacts increases, either as a result of altered levels of metal ions, post-translational modifications, molecular overcrowding or the abnormal interaction with other proteins and lipids [64, 115], exploration of the conformational landscape by disordered αSyn monomers may encounter a new energy minimum which might lead to misfolding and aggregation. A transient conformational change may quickly favour the aberrant self-assembly with other αSyn monomers, resulting in an initial fuzzy nucleus which might at first appear

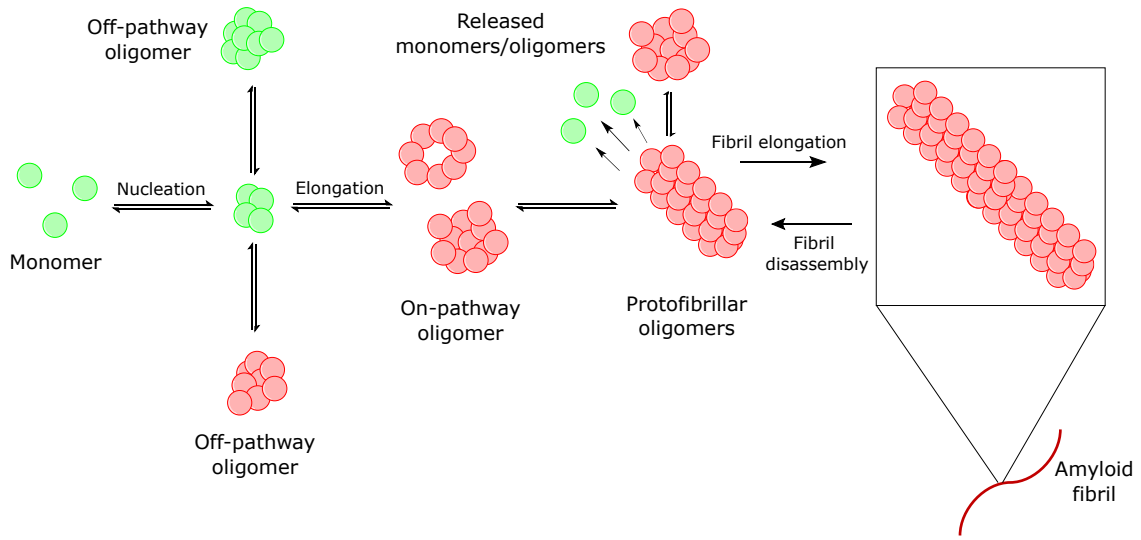


Figure 1.5: Representation of the fibrillisation process of αSyn. The intermediate pathological oligomeric species have been indeed reported to represent a highly structurally heterogeneous population which may have distinct neurotoxic abilities. Following an initial nucleation step, off-pathway oligomers may form, which do not contribute to fibril formation. On-pathway oligomers, however, elongate by monomer addition, forming prefibrillar oligomers and eventually well-structured amyloid fibrils. Dissociation and association of oligomers and monomers may happen throughout as a result of the dynamic nature of the process. In green and red, the non-toxic and toxic species, respectively.

disordered, but which may later reorganise into a highly ordered β-sheet-rich assembly, resembling the architecture of an amyloid core [64, 67, 114]. Given the wide structural heterogeneity of prefibrillar oligomers and the variety of conditions under which they may form, it is highly likely that a spectrum of oligomeric species, and not just one particular conformation, is responsible for inducing neurotoxicity in PD.

Increasing evidence points at the ability of oligomeric αSyn species to bind lipid membranes and disrupt them to be a key molecular mechanism governing neurotoxicity [50, 64, 67, 123, 124]. Either through a partial insertion into the membrane, pore formation, or a thinning of the lipid leaflets via a detergent-like mechanism [125, 92], the disruption of the integrity of biological membranes leads to their permeabilisation and consequent loss of compartmentalisation. The disruption of the cellular homeostasis may come as a result of the misfolded nature of prefibrillar oligomers, which aberrantly display on their surface hydrophobic residues that would otherwise be unexposed and inaccessible for interaction with cellular targets [114].

Indeed, a recent NMR study using structurally characterised homogeneous toxic oligomers generated *in vitro* by Fusco et al. identified that the structural basis for the enhanced membrane binding ability of oligomers is a key highly lipophilic element, which corresponds to the N-terminal region of monomeric αSyn (Figure 1.6) [124]. This allows the establishment of a tight binding interaction as αSyn oligomers anchor to the membrane through the insertion of a highly structured β-sheet-rich oligomeric core, leading to the disruption of the integrity of the membrane [124]. The capacity of the N-terminal segment to anchor the oligomeric aggregates to the membrane can therefore be regarded as a key step in the induction of cytotoxicity through membrane permeabilisation. Indeed, consistent with the pathology observed in PD brains, inoculation of the *in vitro*-generated human toxic αSyn oligomers mentioned above [124] into the brain of a rat model of PD induced the aggregation of endogenous αSyn and prompted the deposition of p129-αSyn in the striatum and substantia nigra [126].

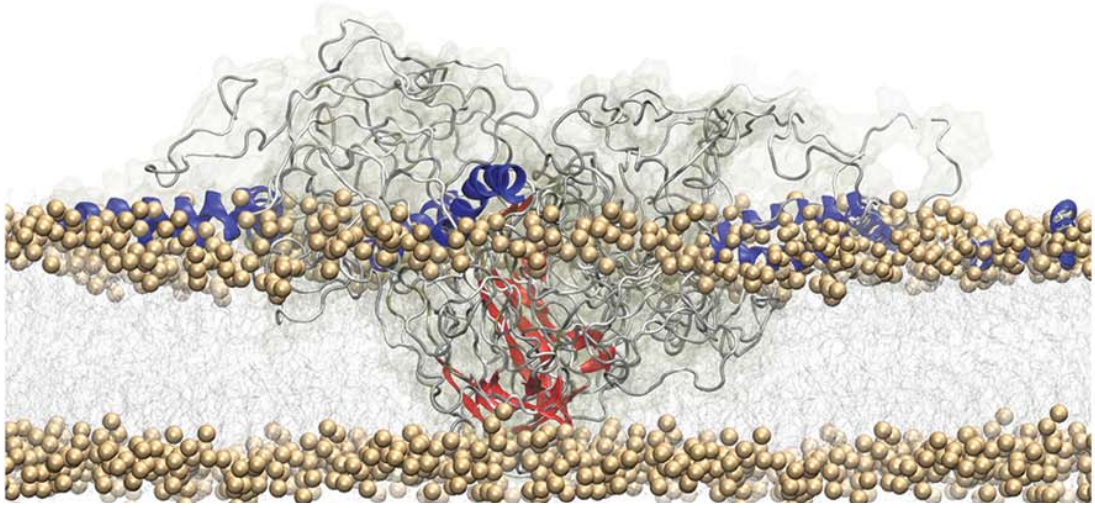


Figure 1.6: Schematic representation of the binding of toxic αSyn oligomers to the membrane. α-helical elements responsible for the anchoring step of the oligomers to the membrane surface are coloured blue. The β-sheet-rich core involved in membrane disruption and permeabilisation is coloured red. Figure adapted from [124].

1.6 The disruption of the membrane as a neurotoxic event

1.6.1 Disruption of biological membranes by toxic protein oligomers

Recent studies on the molecular mechanisms underlying the neurotoxicity characteristic of protein misfolding diseases (PMDs) point at a common aetiology involving the aberrant interaction between

misfolded protein oligomers and biological membranes (Figure 1.4) [127, 128] and the consequent alteration of calcium signalling [129, 111, 92]. Two major mechanisms can be identified by which the function of membranes is disturbed in PMDs, namely through membrane disruption (Figure 1.7) and receptor-mediated dysfunction (Figure 1.8).

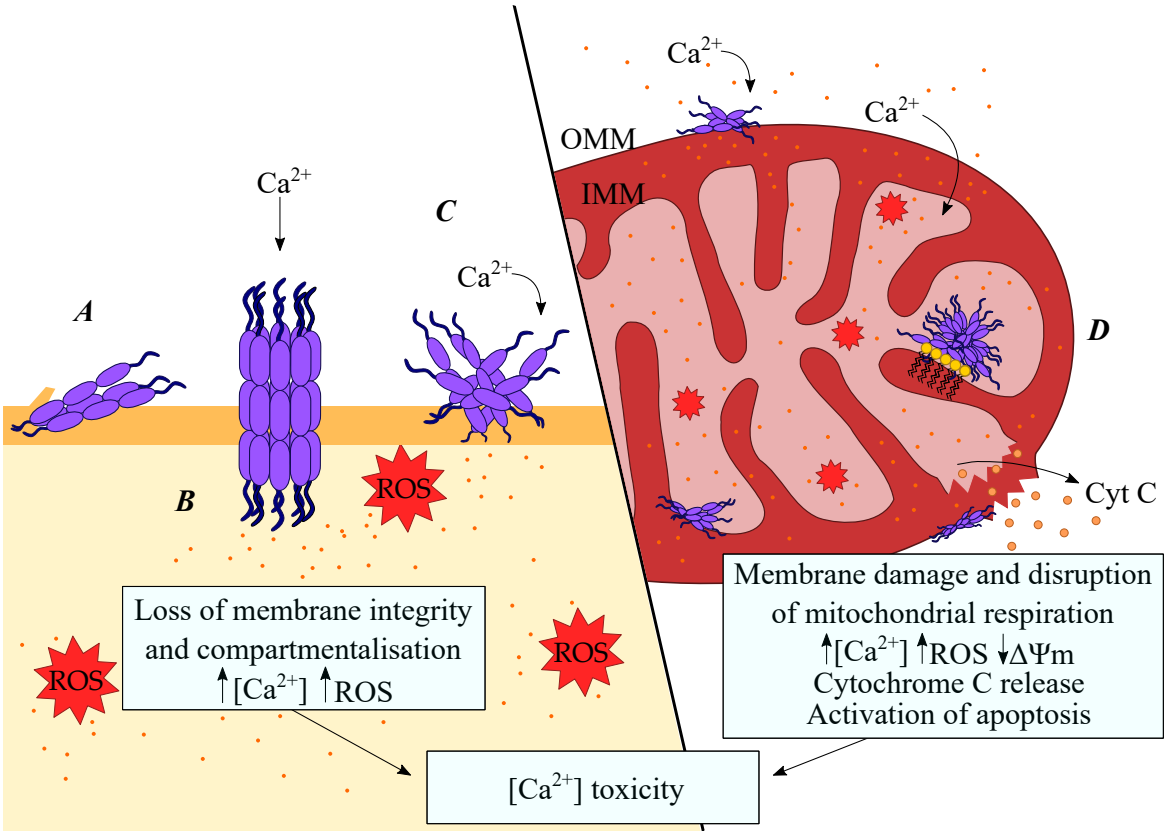


Figure 1.7: Mechanisms of membrane disruption by misfolded protein oligomers. Biological membranes can be disrupted by misfolded protein oligomers in a variety of ways, including (A) partial insertion of the oligomers into the hydrophobic region of the membrane, (B) pore formation, (C) membrane thinning and redistribution of lipids through a detergent-like mechanism [125]. The consequent loss of membrane integrity results in an aberrant influx of Ca^{2+} ions, the generation of ROS and the alteration of signaling pathways, ultimately inducing cell death in a Ca^{2+}-dependent manner. (D) In the mitochondria, preferential binding to cardiolipin (depicted as yellow lipids) by protein oligomers promotes aberrant protein-membrane interactions. Defects in the mitochondrial membranes lead to altered ionic gradients, which in turn interrupt the electron transport chain and compromise the process of mitochondrial respiration. An impaired mitochondrial electron transport chain, in association with an elevated influx of Ca^{2+} ions result in an increase in intracellular ROS. The loss of the mitochondrial membrane potential ultimately induces the release of cytochrome c and the activation of apoptosis. Figure from [92].

As described above, αSyn oligomers seem to induce neurotoxicity by directly disrupting the integrity of biological membranes through the binding of the N-terminal portion and the insertion of a highly hydrophobic core into the lipidic interior [124]. This ultimately leads to membrane thinning and

permeabilisation, leading to fluxes of small ions and larger molecules like the calcein dye through the neuronal membrane [103]. By interfering with the initial anchoring step of these toxic αSyn oligomers that allows their insertion into the membrane through the use of N-terminal-specific antibodies, cytotoxicity was abolished *in vitro* and in *C. elegans* [103]. Studies on conductance across biological membranes have also demonstrated the permeabilisation of the plasma membrane upon interacting with protein oligomers [130]. This is consistent with findings from atomic force microscopy studies which have shown the formation of membrane pores of a range of dimensions after incubation with protein oligomers [131, 108, 132, 133].

Another line of research supports the formation of protein oligomeric pores spanning both sides of the plasma membrane as an underlying alternative mechanism responsible for the alteration of ion gradients and homeostasis. In terms of αSyn, annular oligomers have been reported to have ion channel-like activity [111, 112], similar to that observed of Aβ by atomic force microscopy [127, 129, 134].

Membrane lipid peroxidation as a result of elevated levels of oxidative stress has also been described as a defining feature of neurodegenerative diseases. Oxidised lipids favour protein aggregation at the surface of membranes and weaken cellular membranes by introducing defects in the packing of phospholipids which makes membranous structures more vulnerable to permeabilisation [135, 136, 137]. This leads to a feed-forward loop where oxidised lipids induce an increase in αSyn misfolding and aggregation into oligomers [138], which in turn enhances oxidative stress and lipid peroxidation, thereby perpetuating a self-inflicting cytotoxic mechanism. Consistently, oxidised lipids have been found in post-mortem studies of the brains of patients with PD [139], as well as in brains of AD patients [140]. Recently, free lipids in solution have been proposed to pre-bind to misfolded proteins and induce their further aggregation by driving their insertion into membranes in a chaperon-like mechanism (lipid-chaperone hypothesis) [141, 142, 143].

1.6.2 Mitochondrial membrane disruption

PMDs have been extensively associated with mitochondrial damage and dysfunction [144], for which a role of toxic protein oligomers has been established in the impairment of mitochondrial function (Figure 1.7 and 1.8). Indeed, protein aggregate deposits of αSyn, Aβ and tau have been found to co-localise with mitochondrial membranes [145] and mitochondrial-associated membranes [146] in brains of PD and AD patients. Studies using transmission electron microscopy have also revealed abnormalities in the morphology of mitochondria, including fragmentation and malformations of the cristae, upon overexpression of wild-type αSyn in dopaminergic neurons [147]. Consistent with these findings, neuronal death has been reported in *in vitro* studies as well as in animal models after prefibrillar oligomer-induced mitochondrial membrane damage and impairment [148, 149, 144, 150]. At a genetic level, mutations in several genes that play a key role in the maintenance of mitochondrial homeostasis and the generation of reactive oxygen species (*PINK1*, *PINK2* (Parkin), *LRRK2* and *DJ-1*) have been directly linked to the neurotoxicity of PD, further strengthening a putative role between the mitochondrion and the aetiology of the disease [151, 152, 153, 154].

The high binding affinity of protein oligomers for mitochondrial membranes may be explained by their lipid composition, which is rich in cardiolipin. This type of lipid is exclusively found in mitochondria and is fundamental to the function of the organelle [155, 156, 157, 158]. By being formed by two phosphatidyl residues and four acyl chains linked by a glycerol bridge, cardiolipin has a characteristic structure that determines the curvature, packing and hence fluidity of the mitochondrial membrane lipids [159], making them attractive binding partners for protein oligomers [160]. Indeed, membrane lipid composition has been observed to influence the accumulation of αSyn in mitochondria, where a higher cardiolipin content in the internal mitochondrial membrane (20% of lipid content) coincides with a higher binding preference of αSyn, compared to the outer mitochondrial membrane (5% of total lipids) [161, 162, 159, 163]. Similarly, the formation of mitochondrial membrane pores *in vitro* has been described to be dependent on cardiolipin content in incubation assays of αSyn with isolated mitochondria [158].

Mitochondrial dysfunction following defects in membrane integrity has also been reported in other

neuropathic as well as and non-neuropathic amyloidoses. Aggregates of superoxide dismutase 1 (SOD1), associated with the pathology of amyotrophic lateral sclerosis (ALS), have been shown to perturb mitochondrial membranes in cultured neurons [164, 165], in transgenic rodent models expressing mutant SOD1 [166, 167] and in patients of ALS [168, 169]. In type-2 diabetes, mitochondrial membrane depolarisation following membrane perturbation and accumulation of human IAPP aggregates at mitochondrial cristae [157, 170] leads to an alteration of normal cellular function and apoptosis [171].

Unregulated influx of Ca^{2+} as a result of membrane permeabilisation by αSyn oligomers can also have detrimental effects in mitochondrial function, as has been observed through an overload of the internal calcium stores in isolated mitochondria as well as in dopaminergic neuronal models [172, 128]. Disruption of calcium homeostasis results in a cascade of events, which begins with the opening of the mitochondrial permeability transition pore (mPTP) [172]. The alteration of concentration gradients across mitochondrial membranes induces the depolarisation of the mitochondria as a result [173, 174, 175], the release of cytochrome c [145, 161, 172] and ultimately the activation of caspases, thereby triggering a downstream apoptotic signalling response [147]. A similar effect has been observed with Aβ42 oligomers, which have been shown to induce apoptosis [176, 177, 178] by disrupting mitochondrial membrane integrity [149, 179, 155, 180], altering calcium homeostasis and interfering with the activity of the respiratory chain complexes I and IV [181, 182, 183].

1.6.3 Receptor-mediated toxicity by protein oligomers

In addition to disturbing membrane integrity, extensive evidence suggests that protein oligomers can also induce toxicity by directly interacting with membrane proteins. In this "receptor-mediated" model of toxicity, misfolded protein aggregates are believed to modulate the function of a variety of membrane proteins and receptors, which results in the transduction of deleterious signalling events and ultimately cytotoxicity (Figure 1.8).

Especially important seems the glutamate receptor family, as metabotropic glutamate receptors (mGluR), N-methyl-D-aspartate receptors (NMDAR) and AMPA receptors (AMPAR) have been identified as

targets for the toxic interactions of protein aggregates. In particular, metabotropic glutamate mGluR5 receptors constitute a major class of binding partners for Aβ aggregates, whose co-localisation has repeatedly been observed [184, 185, 186]. By sequestering mGluR5 receptors, Aβ aggregates increase the local density of these receptors at excitatory synapses and dendritic spines, giving rise to constitutively active signalling complexes that result in unregulated intracellular fluxes of Ca^{2+}, both from the extracellular space and internal endoplasmic reticulum cellular stores [187, 188]. An observed upregulation of the expression of mGluR5s in the brains of PD patients suggests a similar mechanism to that of Aβ oligomers in AD [189, 190, 191], in which an increased association with αSyn aggregates might trigger an abnormal influx of Ca^{2+} into the cell that may destabilise the intracellular signalling homeostasis.

Neurotoxicity might also be induced in AD through the overactivation of the ionotropic glutamate receptor NMDA, which plays a fundamental role in memory, learning and in the establishment of neuronal connections [192]. Aβ oligomers cause the overstimulation of the NMDA receptor and induce a state of excitotoxicity in the neuron that is accompanied by an aberrant flux of elevated levels of Ca^{2+} into the neuron [193, 194]. Recently, the cellular prion protein, PrP^c, has emerged as a putative high affinity partner for Aβ oligomers and other misfolded proteins by acting as a toxicity modulator [195, 196, 197, 198, 199], which can result in impaired synaptic plasticity and long-term potentiation in AD [200]. Given its transmembrane nature, PrP^c has therefore been proposed to act as an extracellular platform with the ability to coordinate multiprotein interactions and mediate downstream intracellular signalling from the cell surface upon Aβ binding (e.g., through mGluR5, α7 AChR) [188, 201, 202, 199, 203].

Interestingly, Aβ can promote its own internalisation into the cell by recruiting the low-density lipoprotein receptor-related protein-1 (LRP1) upon binging to the extracellular domain of PrP^c [204]. Given that LRP1 has also been involved in the cellular uptake of tau and its pathological spread [205], its function may constitute an essential component in establishing a common pathway for the internalisation of the two toxic proteins involved in AD. Additionally, by triggering a cascade of downstream signalling pathways, PrP^c acts as an inducer of synaptic impairment through the interaction with Aβ

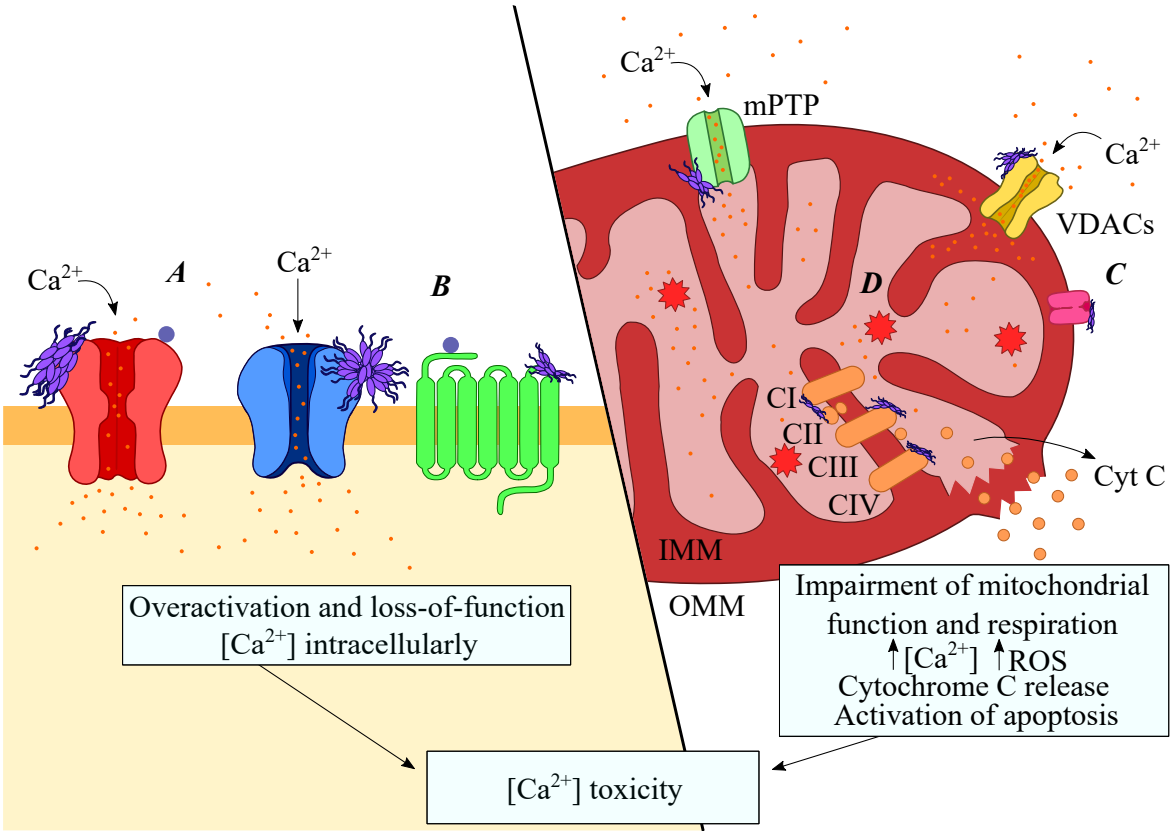


Figure 1.8: Aberrant interactions of misfolded protein oligomers with membrane receptors. Protein aggregates are able to establish binding interactions with many other proteins on the plasma and mitochondrial membranes, resulting in the alteration of their physiological functions. These interactions may result in overactivation and hence in a gain-of-function effect (e.g. mGluR5s or NMDARs) whereas internalisation (e.g. AMPARs, α7 AChR) and clustering of transporters (e.g. α3-NKA) may lead to loss-of-function. The binding to membrane receptors has been shown to alter the ionic gradients and generate an excess of intracellular and mitochondrial Ca^{2+}. The resulting opening of the mPTP causes the depolarisation of the mitochondria, which triggers the release of cytochrome c and the consequent signalling for apoptosis. Disruption of the electron transport chain by direct binding of oligomers to the respiratory complexes exacerbates the Ca^{2+}-mediated toxicity through the unregulated generation of ROS. In this schematic figure, interactions with (A) ionotropic/metabotropic glutamate receptors, (B) nicotinic receptors (e.g. NKA transporter) and (C) mitochondrial receptors (e.g. TOM20), are shown in association with (D) the resulting elevated generation of ROS. Figure from [92].

and αSyn by evoking the activation of Fyn kinase, which activates the NMDA receptor by phosphorylating its NR2B subunit, leading to dendritic spine loss and an associated altered calcium homeostasis in *in vivo* mouse models [206, 197, 207]. The activation of the downstream tyrosine kinase Pyk has been shown to, in turn, trigger the phosphorylation of tau [208], which is a defining feature of the pathology of AD [209].

A receptor-mediated mechanism of synaptic dysfunction and neurotoxicity may not only rely on

overstimulation and gain of function signalling responses, but may also result in loss of function interactions which are deleterious to cellular function. Both Aβ and αSyn aggregates are known to interact with the α3-Na^+/K^+-ATPase (α3-NKA) sodium pump, an essential ion transporter responsible for maintaining membrane potentials in neurons [210, 211]. In particular, αSyn aggregates impair the pump's ability to export sodium ions out of the cell by crowding the pre-synaptic space, whilst Aβ acts by compromising the catalytic activity of the NKAα subunit [210, 211]. Even though the function of the NKA sodium pump may be impaired by different misfolded protein aggregates through differing mechanisms, the common resulting pathway is a pre-synaptic overload of calcium which disrupts the cellular homeostatic levels and induces the activation of deleterious downstream signalling events [210].

The cholinergic pathway is currently being heavily studied for its proposed role in the characteristic toxicity observed in AD, as reflected by the several therapeutic avenues being investigated to interfere with its downstream signalling [212]. This excitatory pathway involves two main receptor families, namely muscarinic (mAChR) and nicotinic acetylcholine (nAChR) receptors [213, 214]. In fact, α7 nAChR antagonists have been observed to have neuroprotective effects in rats, rescuing learning deficits associated with the overstimulation of cholinergic receptors [215]. Evidence suggests that Aβ aggregates might accumulate and result in an impairment of the activity of α7 AChR as well as induce receptor internalisation, leading to synaptic dysfunction and memory loss. Additionally, studies on the binding of these two interacting partners suggests an increase in tau hyperphosphorylation [216] and the induction of plaque formation [217, 218] upon complex formation, with both features representing pathological hallmarks of AD.

As a compensation mechanism for the internalisation of the Aβ-receptor complex and loss of functional α7 nAChR at the synapses, the expression of α7 nAChR is upregulated [219]. This inadvertently results in a positive feedback loop with an increased availability of α7 nAChR, consequently leading to the intracellular accumulation of Aβ, the overwhelming of the lysosomes and neuronal death [220]. An upregulation of the cholinergic α7 nAChR might simultaneously result in elevated calcium fluxes into the neuron [221], further contributing to the cocktail of dysregulated signalling

pathways and toxicity inside the cell.

Similar to the aberrant interactions with neuronal membrane receptors, misfolded protein aggregates have also been shown to induce detrimental effects in mitochondria through the interaction with mitochondrial membrane receptors. In fact, voltage-dependent anion channels (VDACs) have recently become a large subject of study as a result of their apparent direct implication in these toxic events. VDACs have previously been shown to facilitate the transport of αSyn into the mitochondria [222], suggesting a critical role in modulating the initial step in the unfolding of mitochondrial toxicity by which toxic aggregates are trafficked inside. At the same time, αSyn have been shown to cause VDAC dysfunction *in vitro*, resulting in the reduction of ATP and ADP levels and the concomitant impairment of mitochondrial respiration [223]. Aggregates of mutant SOD1 similarly accumulate on the OMM by directly interacting with VDAC1 [224] and Bcl-2 [225], inducing loss of channel function and a consequent perturbation of mitochondrial membrane potential and morphology, as well as protein transport. Interactions of mutant SOD1 with Bcl-2 on the OMM have been proposed to underlie the molecular mechanism responsible for the onset of motor neuron loss in ALS [226], through a conformational change in Bcl-2 which enhances the affinity for VDACs and leads to channel closure [227].

Aggregates of mutant huntingtin (Htt) involved in Huntington's disease (HD) have also been shown to promote cell death through a combination of mechanisms, in which interactions with the InsP3 receptor on the ER membrane, together with hyperstimulation of NMDAR [228], result in both the release of calcium from ER stores and the influx of calcium from the extracellular space. Combined with the fact that mutant Htt is involved in the opening of the mPTP in the IMM, cytochrome c is released in response, and apoptosis induced as a result [229]. Consistent with the pathology of HD, the degeneration of GABAergic neurons was observed in the striatum of rat brains upon injection of NMDA agonists [230], most likely as a result of a hyperstimulation of the excitatory receptors that leads to excitotoxicity.

Extensive experimental evidence therefore highlights the relevance of biological membranes in the

toxic molecular mechanisms that underlie the pathology of PMDs. Two major mechanisms, namely through membrane disruption and receptor-mediated dysfunction, have been identified. Whilst one describes the perturbation of membrane integrity as the initiation of a series of downstream toxic events, the other model points at aberrant interactions of protein aggregates with receptors that can result in their hyperactivation or their loss of function. However, regardless of the multiple concurrent factors, both proposed mechanisms have the membrane as centrepiece for their toxicity and share the same molecular outcomes which are common to most PMDs, namely an imbalance in calcium homeostasis and signalling resulting in cell death.

1.7 Nucleic acid aptamers: the new class of molecular recognition tools

Currently, no disease-modifying treatment exists that interferes with the toxicity associated with αSyn aggregates and halts the progression of PD. Instead, drugs and therapies that alleviate the associated symptoms are routinely prescribed, in an attempt to increase the quality of life of the patient, whilst not targeting the pathomolecular aetiology of the disease. A traditional structure-based drug design approach to target the toxicity of oligomeric αSyn species seems intractable, however, as a result of the intrinsically disordered nature of αSyn monomers, and the exquisite heterogeneity of the ensemble of structures oligomeric aggregates can adopt. Notably, significant advances have been made in the last few years in the field of therapeutic research for neurodegenerative diseases, including the generation of antibodies targeting αSyn aggregates [231].

In 1990, the work from two independent research groups reported the first *in vitro* generation of single-stranded RNA molecules that were selected to specifically bind certain targets [232, 233]. After selecting several small RNA oligonucleotides that could bind a small dye with high affinity, Ellington and Szostak called this new class of recognition molecules “aptamers” [233]. At the same time, Tuerk and Gold generated some other RNA molecules that showed affinity and bound to the bacteriophage T4 DNA polymerase in a similar manner to how its natural ligand binds, through a process they named as Selective Evolution of Ligands by Exponential Enrichment (SELEX) [232]. The findings

of these two studies led to the introduction of a versatile new class of molecules, with potential as therapeutic and diagnostic agents: Aptamers are short single-stranded DNA or RNA oligonucleotides (20-100 nucleotide bases), which can recognise and bind to a huge variety of molecules, ranging from small molecules and even ions to cells, with striking specificity and affinity, in the nM to pM range [232, 233, 234, 235, 236]. Aside from the most well-known function of nucleic acids in the storage of genetic information as part of the central dogma, single-stranded nucleic acids also have the ability to fold into specific three-dimensional structures that can recognise specific target motifs. As a result of their innate ability to complementary base pair, aptamer sequences can fold back on themselves and form networks of electrostatic salt-bridges, hydrogen bond, Van der Waals and pi-stacking interactions that give them their characteristic secondary and tertiary conformations (stem loops, hairpin, pseudoknot and G-quadruplex) [236]. The combination of sequence composition and base distribution, as well as environmental conditions such as temperature and ionic strength determines the structural basis of the recognition surfaces of aptamers, which dictate the affinity and specificity of their binding.

As opposed to protein antibodies, which are typically discovered and produced in animal and cell models, aptamer sequences are usually generated *in vitro* through SELEX. This technique relies on the *in vitro* evolution of sequences from combinatorial libraries that can bind to a target of interest [237, 232, 233]. The procedure consists of iterative cycles of incubation between the target and a library of nucleic acid sequences in what is known as rounds of selection, to allow binding sequences to remain in solution and "evolve" throughout the iterative incubation rounds (Figure 1.9). The continuous evolutionary pressure to which aptamer sequences are exposed may gradually lead to the selection of a subset of sequences showing sufficient specificity and affinity to the target of interest. Amplification by PCR at every round of selection expands the population of the binding sequences, leading to those with highest affinity and/or specificity eventually dominating the library. The principle of SELEX therefore relies on the view that single copies of sequences with affinity for a particular target will be present in an initially randomised library of nucleic acids, which is predicted to contain approximately 10^{16} distinct sequences. Following multiple rounds of selection (typically up to around 20), the individual sequences from the aptamer pool are cloned and sequenced to identify high affinity binders

[236]. The waning cost of sequencing has recently made Next-Generation Sequencing (NGS) the preferred sequencing method when the technology is available, as a high-throughput alternative to provide a deeper understanding of the composition of different libraries throughout the evolution process [238]. Interestingly, this may lead to the discovery of sequences which may show a higher affinity or specificity for a particular target, and which were not necessarily carried over and selected up to the last round of selection simply as a result of, for instance, being more difficult to amplify than other sequences during PCR or having a lower affinity but higher specificity for the target.

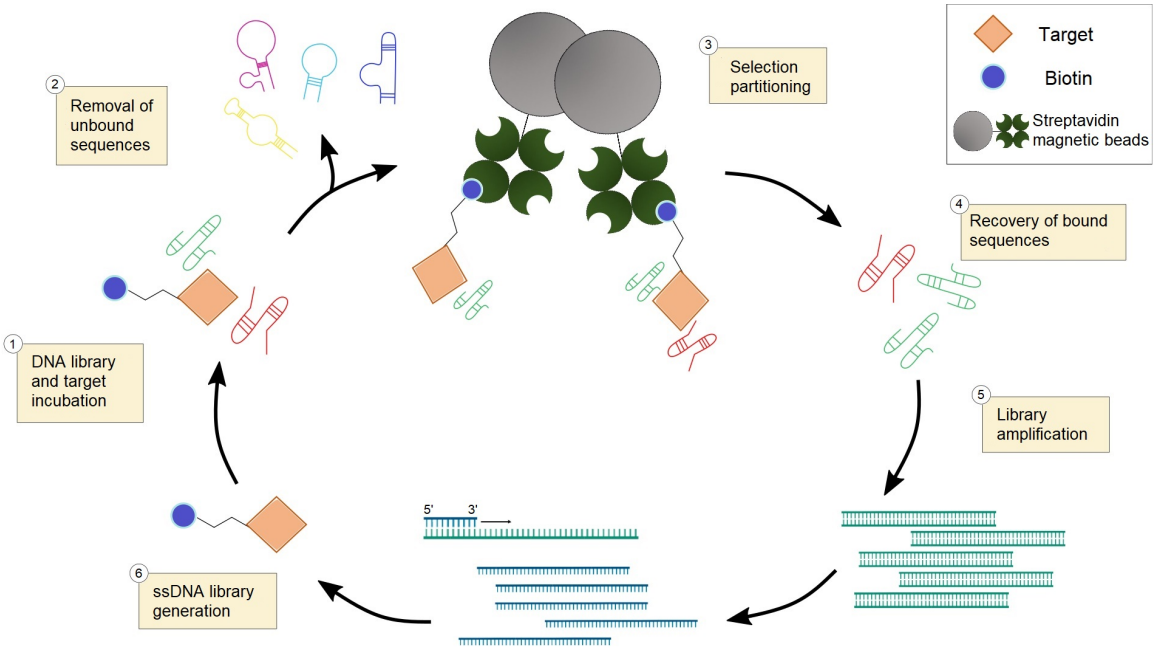


Figure 1.9: Illustration of the process of DNA aptamer selection through SELEX. Briefly, selection of aptamers can be broken down into three essential steps that are iteratively repeated: incubation of the combinatorial DNA library with the target followed by the partitioning of the bound sequences from the unbound sequences, through immobilisation of the biotinylated target using streptavidin-coated magnetic beads, amplification of this new pool of sequences, and the generation of a single-stranded library in preparation for the next selection round.

Since the development of the first aptamers and the establishment of an *in vitro* protocol for their generation, the large number of studies and successful entries into clinical trials manifests the growing interest for these molecular recognition tools and their potential as therapeutic molecules [239]. Indeed, it is no surprise that aptamers have been proposed to be promising alternatives to protein antibodies, which constitute the largest group of available therapeutic biomolecules. With aptamers being sometimes referred to as “chemical antibodies”, they mimic the merits of their protein counterparts whilst overcoming their limitations, making them more suitable as high affinity recognition

therapeutics: higher flexibility and thermostability, lack of immunogenicity given that nucleic acids do not usually elicit immune responses, and comparably smaller size (6-30 kDa and 2 nm in diameter, compared to 150-180 kDa and 15 nm in diameter) [236]. Such features present aptamers with the ability to overcome the limitations of antibodies in certain therapeutic avenues, including membrane crossing events, especially in the case of the blood-brain-barrier (BBB), and the accessibility to hidden epitopes difficult to reach because of their large size (e.g. in solid tumours). Similarly, the production of large-scale quantities of aptamers can be achieved at a relatively low cost whilst also boasting wide chemical reproducibility, as opposed to the possibility of bath-to-batch variation in efficacy of antibodies produced using animal cells, and an inherent risk of contamination [236]. Additionally, the ease of chemical modification or labelling and their remarkable binding properties have made of aptamers emerging excellent molecular choices for analytical, diagnostic and therapeutic tools [240, 239, 241].

1.8 Aptamers as therapeutics for PD

Following the introduction of SELEX in the 1990's, aptamer technology started being exploited for the generation of therapeutic molecules and diagnostic tools. By 2008, studies on aptamer research had reported the selection of over 2000 aptamers with binding affinity for more than 140 targets [242]. Since original intellectual property restrictions eventually expired and hurdles were lifted, interest on aptamer-based technology has been steadily increasing, represented by the more than 800 registered aptamer-related patents [243]. In 2004, the FDA approved the commercialisation of the first therapeutic RNA aptamer, pegaptanib sodium (Macugen®), for the treatment of age-related macular degeneration in humans [244]. The approval of this first-in-class therapeutic, used to treat a common ocular condition which can result in severe loss of central vision, represented an unprecedented breakthrough in the drug development field.

However, the vast number of preclinical aptamer studies reporting promising *in vitro* data does not reflect the current rate of approval. The restrictions associated with the original patents and the scepticism of the biopharmaceutical industry to invest in an entirely novel class of therapeutic molecules and to partly divert from the well-established antibody industry, has caused the development of ap-

tamers to lag behind [243, 245]. Despite the slow start, the therapeutic effect and safety of several aptamers was recently being evaluated in clinical trials (Table 1.1) [239], with some of them expected to successfully become available in the market in the next 5-10 years. Interestingly, AS1411 has become the first aptamer for the treatment of various cancer indications in humans in entering clinical trials [239, 246], after demonstrating potent anticancer activity with little side effects [247]. Certainly, the presence of aptamers is increasingly becoming stronger both in the therapeutic industry and in the world of diagnostics, where aptamers are making noticeable contributions [239, 248, 249].

As life expectancy improves worldwide, and the average age increases, the cases of neurodegenerative diseases are projected to dramatically rise in the next few decades. As a result of their unique properties, including their small size compared to protein antibodies, aptamers seem promising to open new ways of treating neurodegenerative disorders like PD [250, 251]. Substantial efforts have been made in the generation of aptamers for neurodegenerative diseases, as evidenced by the extensive literature available on the identification of aptamers for these disorders [250, 251, 252]. For instance, aptamer-based biosensors or probes have been developed for the detection of amyloid plaques in AD [253, 254] and different prion isoforms in prion diseases [251, 255], to aid in the early diagnosis of these disorders. Similarly, the selection of aptamers against amyloid-β [256], tau [257] and the prion protein [255, 258] has also been reported, with some showing encouraging neuroprotective effects [257, 258].

To date, only two research groups have reported the selection of aptamers against αSyn species with the aim of establishing initial drug candidates for PD [259, 260, 261]. The first DNA aptamer, named M5-15, that was reported to have affinity for αSyn oligomers and monomers was generated by Tsukakoshi et al [261]. Later, by using a competitive screening method to discard binders to αSyn monomers and fibrils, the same group identified eight aptamers that showed affinity for β-sheet-rich architectures present in both αSyn and Aβ oligomers [260]. Similarly, Zheng et al. were recently successful at isolating two high affinity DNA aptamer sequences, called F5R1 and F5R2, against monomeric αSyn, which were shown to reverse aggregation and trigger the degradation of αSyn aggregates *in vitro* [259]. Previous unpublished work investigating the interaction between F5R1 and

Aptamer	Company	Target	Dissociation constant (k_d)	Therapeutic indication	Clinical stage
Pegaptanib sodium/ Macugen	OSI Pharmaceuticals/ Pfizer	$VEGF_{165}$	200 pM	- AMD (Approved for this indication) - Proliferative diabetic retinopathy - Diabetic macular oedema	FDA approved (2004)
E10030	Ophtotech	PDGF	0.1 nM	- AMD - Von Hippel-Lindau	Completed Phase III
ARC1905	Ophtotech	Human complement C5	2-5 nM	- AMD - Wet AMD - Stargardt disease 1 - Idiopathic polypoidal choroidal vasculopathy - Geographic atrophic conditions	Phase III
AS1411	Antisoma	Nucleolin	54.8 ± 7.3 nM	- Acute myeloid leukaemia (AML) - Metastatic renal cell carcinoma - Advanced solid tumours	Phase III
NOX-A12	NOXXON PHARMA	CXCL12 (C-X-C Chemokine ligand 12)	200 pM	- Multiple myeloma - Hematopoietic stem cell transplantation - Autologous stem cell transplantation - Metastatic colorectal cancer - Metastatic pancreatic cancer - Chronic lymphocytic leukaemia	Phase III
NOX-E36	NOXXON PHARMA	CCL2 (C-C Chemokine ligand 2)/MCP-1 (Monocyte chemoattractant protein 1)	1.32 nM	- Type 2 diabetes mellitus - Systematic lupus erythematosus - Albuminuria - Renal dysfunction	Phase III
NOX-H94	NOXXON PHARMA	Hepcidin	0.65 ± 0.06 nM	- Anaemia - End-stage renal disease - Inflammation	Phase III
ARC1779	Archemix	A1 domain of von Willebrand Factor	2 nM	- Von Willebrand disease - Thrombotic thrombocytopaenic purpura - Von Willebrand disease type 2b - Percutaneous coronary intervention - Thrombosis	Phase III
NU172	ARCA Biopharma	Thrombin	Not published	- Heart disease	Phase III
REG1 system	Regado Biosciences	Coagulation factor IX1	2.83 ± 0.4 nM	- Acute coronary syndrome - Coronary artery disease	Completed Phase III
BX499 (formerly ARC19499)	Baxter	Tissue Factor Pathway Inhibitor	2.8 ± 0.3 nM	- Haemophilia	Phase II

Table 1.1: Development stages of aptamers in clinical trials as of 2018. The large number of nucleic acid aptamer entries being evaluated for their safety and efficacy highlights the growing relevance and importance of these recognition molecules as therapeutics. Table modified from [239].

αSyn by NMR revealed intensity changes in the residue peaks of the NAC region, suggesting that F5R1 interacts with this region of the protein [262].

Although aptamer research has received increasing attention in the last few years by groups working on developing disrupting therapies for neurodegenerative diseases, none of them have been yet tested in the clinic. This is largely as a result of the obstacle that therapeutics targeted to the Central Nervous System (CNS) face, which is the challenge of crossing the BBB. This highly specialised and selective protective membrane forms the interface between the brain and blood supply and controls the brain homeostasis by regulating the transport of substances across it [263]. By consisting of a uniform continuous membrane with low pinocytosis activity, it shields the brain from the non-specific uptake of potentially damaging molecules and microorganisms, whilst also representing a hurdle for the delivery of therapeutic molecules. Generally, molecules with a high brain accessibility rate are highly lipophilic and have a molecular weight of no more than 400 Da [264, 265]. As a result of their larger size and high negative charge, aptamers are predicted to be uncapable of passively diffusing across the BBB [266].

Despite this structural hindrance and data on aptamer delivery into the brain being scarce, several promising strategies have been suggested that open encouraging therapeutic perspectives for the brain by surpassing the BBB. These include hijacking receptor-mediated transport [263, 267, 268], the use of nanoparticle vectors [269], delivery with the help of cell-penetrating peptides (CPPs) [270] and the *in vivo* selection of aptamers [265]. In particular, the transferrin receptor has become an especially attractive target as a result of its high expression in the brain capillary compared to other body tissues [271]. Therefore, conjugation of a therapeutic aptamer to the transferrin ligand or to an antibody raised against the receptor may represent an innovative way of crossing the BBB, as it has been proven to be effective at permitting membrane trafficking [263].

Recent efforts in the gene therapy field involve the delivery of antisense oligonucleotides (ASOs) into the brain for the treatment of neurological diseases [267]. These single-stranded nucleic acids, which are intended to interfere with protein expression levels, closely resemble aptamers in their size and charge, and therefore share comparable challenges in entering the CNS. As a result of their similar characteristics, the merits of an extensive literature reporting the development of promising strategies allowing the entry of ASOs into the brain may be extrapolatable to that of aptamers [271, 268, 269,

270, 272]. Additionally, the transient opening of the BBB through the disruption of the function of structural proteins responsible for maintaining membrane integrity has also been proposed as a strategy for therapy delivery [273, 274]. Such an increase in BBB permeability has been shown to enhance the biodistribution of an ASO targeting malat-1 RNA levels [273] and chemotherapy *in vivo* [274], although questions remain about the safety of such techniques, in which the non-specific uptake of substances by the brain also increases.

Interestingly, efforts to develop novel CNS-targeting delivery methods have lately focussed on the engineering of exosomes as potential nanocarriers of therapeutic molecules. Exosomes are nanovesicles that are secreted by all cell types whose major role is the transport of effectors and signalling molecules between cells, as well as the removal of cellular toxins [275, 276, 277]. As a result of their ability to carry high amounts of an exogenous molecule in an enclosed environment whilst ensuring its stability inside the body, they may be isolated and used as carriers by expressing the cargo of interest in cultured cells. Indeed, a follow-up study from Zheng et al. on the high affinity DNA aptamer F5R1 mentioned earlier [259] involved the encapsulation of the aptamer in exosomes isolated from HEK293 cells to assess its therapeutic potential [278]. By expressing the rabies virus glycoprotein (RVG), these cells secreted exosomes that were decorated on the outer membrane by RVG. Intraperitoneal injection of these exosomes containing F5R1 into wild-type mice that had previously received an intrastriatal injection of preformed αSyn fibrils allowed retrograde transport into the brain through the neurons of the peripheral system, thereby surpassing the BBB. This resulted in a reduction of the aggregated αSyn in the substantia nigra and the amelioration of motor symptoms in the treated mice. Whilst such experiments provide useful proof-of-concept results for the development of delivery systems of therapeutic molecules targeting the CNS, the viability of exosomes as carriers is still being discussed owing to their natural origin, which makes controlling their composition and cargo difficult, thereby raising concerns about their clinical safety.

Remarkably, such aptamer selection strategies against αSyn did not bear structural considerations in their design. Since the N-terminal region of αSyn has been shown to be critical in the establishment of aberrant interactions with membranes that lead to their disruption and prove detrimental to neurons,

it is reasonable to think that an aptamer selection strategy targeting this portion of the sequence may result in a highly protective effect. In this PhD project, I therefore exploited the structural knowledge of the mechanism of toxicity by oligomeric αSyn aggregates, to guide the selection of aptamers through SELEX against the key first 25 residues of αSyn, αSyn_{1-25}.

1.9 Metal ion interactions

The misfolding of proteins into toxic aggregates has been suggested to be the underlying molecular pathological event responsible for the cellular death observed in disorders such as PD and AD [279]. As mentioned earlier in this Chapter, neurodegeneration in PD is characterised by the progressive loss of dopaminergic neurons in the substantia nigra and the deposition of amyloid fibrillar aggregates in the form of LBs in multiple brain regions [280, 21, 281]. Although a detailed understanding of how αSyn promotes cellular toxicity is still missing, there is growing compelling evidence supporting a causative role for αSyn in the development and progression of PD [67, 101, 282].

The modular organisation of the different regions of the protein promotes long-range interactions between the highly-negatively charged C-terminal and the partially positively charged N-terminal regions through electrostatic interactions, and between the C-terminal and the NAC regions through hydrophobic contacts. This leads to the stabilisation of aggregation-resistant conformations that protect the NAC from exposure to the solvent and self-assembling with other αSyn monomers, and ultimately from aggregation and amyloid formation [94, 39, 283, 284, 285, 286, 40, 41, 42, 43]. These weak intramolecular interactions are responsible for αSyn's observed smaller radius of gyration than what would be expected from a 140 residue-long fully disordered polypeptide [287]. The surrounding environment strongly modulates the dynamics of αSyn, which means that environmental perturbations can lead to a skewing of the conformational ensemble that may have implications in its ability to aggregate [288]. For instance, mutations in the protein sequence lead to changes in the local charge and hydrophobicity of αSyn that translate into alterations in the long-range intramolecular contacts, as is the case with familial genetic mutants, which have been shown to result in differences in the protein's aggregation propensity [289, 290, 291, 292].

Although the aetiology of PD is recognised as being multifactorial, in which genetic and environmental factors modulate the development of the disease, the aggregation of αSyn is considered a key factor in the generation of the associated pathology [293, 19, 32, 57, 9, 58, 294, 68, 73, 295, 296, 297]. Whilst the misfolding of αSyn can be triggered by several mechanisms, including post-translation modifications and oxidative stress, interactions with metal ions, which had until recently been overseen as an important factor in the development of PD, are now being considered as one of the mechanisms leading to αSyn aggregation. Indeed, the properties of IDPs are exquisitely sensitive to changes in the environment, where binding to different metals could cause local or global changes in the conformation and behaviour of the protein and potentially aggregation propensity. Metals are essential for the normal physiological function of the body and the development of the brain in particular [298]. Apart from providing positive counterions that help keep charge neutrality, metal ions also act as important electron carriers and catalytic centres for proteins as a result of their ability to undergo reduction and oxidation. For instance, Cu^{2+} provides the catalytic centre for the detoxifying protein SOD1, by which it is reduced to Cu^{+} by superoxide ions in the process of oxygen radical removal [299].

A large body of evidence has been built during the last two decades that supports the importance of interactions of metal ions with αSyn [300, 301, 302, 303, 304, 305]. Ca^{2+} has been proposed as an essential modulator of the physiological function of αSyn at the presynaptic terminal, where calcium fluctuations are coupled to neurotransmission. Binding of Ca^{2+} to the anionic C-terminal tail of αSyn drastically alters the charge distribution of the C-terminal region, masking the highly negatively charged density and allowing the association of αSyn with cellular membranes [37]. However, interactions with metal ions have also been shown to alter the aggregation kinetics of αSyn [305, 306], which might therefore play a central role in the pathological aetiology of disease. In fact, it is now clear that different metal ions can act synergistically to induce neurotoxicity in PD [302]. In a complex multifactorial landscape that attempts at understanding the aetiology of PD, increasing age becomes the main risk factor. Amounting evidence has demonstrated a link between aging and increased levels of metal ions in the brain [307, 308]. Metal ions are ubiquitously present in the brain, given their essential roles in neurotransmission and normal neuronal functioning [301, 309]. It

has therefore been hypothesised that a perturbation in the homeostasis of brain metal ion levels and the aberrant interaction with key proteins involved might be a putative factor in the development of multiple age-related neurodegenerative disorders.

In the case of PD, several studies have pointed at iron and zinc as important toxic modulators of αSyn, as abnormally high levels of zinc and iron have been found in the parkinsonian substantia nigra and striatum of patients [310, 311, 312, 36, 313] and LBs [314], respectively. The co-localisation of elevated concentrations of zinc and αSyn has been observed in post-mortem examinations of the olfactory bulb [315], as well as high levels of copper in the cerebrospinal fluid of PD patients [316]. In fact, epidemiological studies have shown a link between a prolonged exposure to certain environments rich in copper, manganese, zinc or iron and a higher predisposition to develop PD later in life [317]. To confirm the *ex vivo* findings, much research has been done to elucidate the precise role metal ions might play in the aggregation of αSyn and the subsequent cellular toxicity.

Interestingly, the variety of co- and post-translational modifications that decorate αSyn as well as the different pathological genetic variants add an extra layer of complexity to the interactions with metal ions [93, 318]. For instance, Cu^{2+} has been shown to be the most efficient at promoting fibrillation of non-acetylated αSyn *in vitro* at physiologically relevant micromolar concentrations [319, 320], but not of the acetylated form. Whilst metal ion binding may alter the amyloid assembly pathways, the sole binding event might not be sufficient to induce aggregation, but it may require the induction of a structural transition. This is the case with Cu^{2+}, which was observed to bind the familial A53T variant, but not to noticeably alter its aggregation rate [321]. Cryo-EM analysis of αSyn aggregates in the presence of Cu^{2+} revealed a variety of different morphologies including annular, fibrillar and protofibrillar species after 60 hours of incubation, which after a week had all formed amyloid fibrils [322]. A similar effect in which the aggregation kinetics are accelerated *in vitro* is observed with Zn^{2+} [36, 313, 323, 324, 325, 326], which specifically interacts with His50 and the C-terminal region of αSyn [309]. Again, Fe^{3+} accelerates fibrillation of non-acetylated αSyn, but slows down the aggregation kinetics of the acetylated form. In contrast, the binding of Mn^{2+} and Fe^{2+} was characterised by non-specificity and low-affinity at the acidic C-terminal tail, which most likely serves as a sink for

cations. Indeed, several studies have suggested that the precise binding properties of different metal ions define the aggregation propensity and kinetics of αSyn [327, 328, 329, 330, 331, 332, 333].

Another way in which redox metals can result in pathology is through their ability to catalyse the generation of ROS through the Fenton and Haber-Weiss reactions [334]:

(1)

$$M^{n+1} + O_2^{-\cdot} \rightarrow M^n + O_2$$

(2) Fenton reaction

$$M^n + H_2O_2 \rightarrow M^{n+1} + OH^- + OH^\cdot$$

(3) Net Haber-Weiss reaction (1) + (2)

$$O_2^{-\cdot} + H_2O_2 \rightarrow O_2 + OH^- + OH^\cdot$$

Highly reactive hydroxyl radicals can result in cytotoxicity by promoting the oxidation of DNA, protein and lipids, which is considered a major contributing factor in the pathological mechanism responsible for dopaminergic neuronal death in PD. Indeed, redox cycling of copper ions between its (I) and (II) oxidation states results in the formation of hydroxyl radicals which have the capacity to cause intra- and intermolecular dityrosine cross-linking [335, 336, 337]. Consistently, chaperones (such as Hsp70) and antioxidants which are known to quench the damaging action of ROS have been observed to have their function impaired in neurodegenerative diseases [338, 339, 340].

1.9.1 Calcium

Calcium is vital for most of the processes in the brain involving signalling, such as neurotransmission and synaptic plasticity, as well as cell survival [341]. Under resting conditions, homeostatic Ca^{2+} levels are tightly regulated between the intracellular Ca^{2+} stores such as the endoplasmic reticulum, and the extracellular environment, to keep its cytoplasmic concentration at around 200 nM [342]. Upon neuronal stimulation and arrival of an action potential, free cytosolic Ca^{2+} levels rapidly rise

to low micromolar concentrations (1-100 μM), either by an influx of calcium ions into the cells from the extracellular space (extracellular calcium concentration is around 1.4 mM) and/or the release of internal stores of Ca^{2+} [342, 343]. Homeostasis is rapidly re-established after stimulation and the intraneuronal concentration of Ca^{2+} is rapidly lowered to resting levels. In fact, this might constitute one of the factors that accounts for the selective vulnerability of dopaminergic neurons, which present intrinsically low Ca^{2+} buffering capacity together with a low firing threshold for Ca^{2+} entry in rodents [344, 345]. A decreased ability to return to resting intracellular calcium levels has also been observed as a result of an impaired export of Ca^{2+} into the outer extracellular space through membrane Ca^{2+} ATPases [346, 347, 348].

Indeed, dysregulation of the homeostasis of Ca^{2+} has been demonstrated in a mouse model of α-synucleinopathies [349], which replicated the observation of deposits of calcium in LBs of PD patients [350]. *In vitro* fibrillation assays have shown the induction of αSyn aggregation in the presence of calcium [37], in line with previous findings of thapsigargin, ionophores or depolarising stimuli-induced calcium influxes that triggered αSyn oligomerisation in different cell lines [351, 352, 353]. It has therefore been hypothesised that the prolonged deregulation of calcium levels in the presynaptic terminal caused by a delay in the re-establishment of resting concentrations might lead to αSyn misfolding, nucleation and aggregation [352, 351, 354]. αSyn might also contribute to cytotoxicity by triggering a pathological increase in intracellular levels of Ca^{2+}, which might in turn result in a positive-feedback loop that amplifies the aggregation process [355, 356, 357, 110, 358]. This could be the result of an αSyn oligomer-dependent permeabilisation of the neuronal membranes and/or a direct interaction with Ca^{2+} protein transporters, such as the sarcoplasmic reticulum Ca^{2+} ATPase (SERCA) [128, 359, 360, 361]. Importantly, αSyn oligomer-induced cell death was abolished upon removal of extracellular Ca^{2+} in cultures of primary neurons and astrocytes [128], suggesting that Ca^{2+} dysregulation is required for the induction of cellular toxicity. Of note, ROS seem to aggravate the aggregation and formation of stable oligomeric αSyn in the presence of Ca^{2+}, further establishing a feed-forward loop relevant to understand the pathological unfolding of events upon elevated Ca^{2+} levels [362].

Calcium has been shown to bind along the sequence of the C-terminal region of αSyn, which is rich in Asp and Glu residues, with a dissociation constant of approximately 20 μM [37]. The interaction with calcium is believed to be a key factor for the physiological role of αSyn, by which its membrane-binding ability is enhanced through the involvement of the acidic tail in the binding interaction [37]. This ultimately means that αSyn is also able to interact with synaptic vesicles through its C-terminal region, whose binding to biological membranes seems to be modulated by Ca^{2+}. For this reason, it has been recently proposed that αSyn is a calcium-dependent regulator of synaptic vesicle homeostasis through the modulation of the binding of its C-terminal tail [37]. Interestingly, this change in conformation from a free C-terminal tail to one having an active role in lipid binding has been shown to result in the aggregation of αSyn into short fibrils [363]. Additionally, abnormal levels of αSyn or Ca^{2+} can also result in the clustering of synaptic vesicles, as seen *in vitro* and *ex vivo* [37]. The chances of such an event might be minimised in healthy neurons, where high levels of Ca^{2+} are required to saturate the calcium binding sites in the acidic C-terminal region, but which might be fully occupied upon an abnormal excess of Ca^{2+} during pathology.

The intricate relation between αSyn and calcium therefore suggests a fine balance between physiology and pathology which needs tight regulation. Interestingly, abnormal levels of calcium seem to be intricately linked to an αSyn-dependent dopamine toxicity [37]. Dopamine is known to induce αSyn oligomerisation, which promotes an increase in cytotoxicity and cell demise [364, 365, 366, 367]. Lowering the levels of Ca^{2+} or αSyn dramatically reduces dopamine-induced toxicity [37], suggesting a close interplay between the three molecules which might constitute a window for therapeutic intervention. In this way, isradipine, which is a calcium channel inhibitor prescribed for high blood pressure, may prove to be a potential drug candidate to treat PD by reducing the detrimental levels of intracellular calcium [368, 369] to rescue dopaminergic neural activity, as observed in an mPTP murine model of PD [370].

1.9.2 Copper

Copper is an essential trace element in the brain that sustains fundamental biochemical processes, by serving as a cofactor for critical proteins involved in the generation of energy such as cytochrome

c oxidase, as well as in the detoxification of oxygen radicals through the catalytic action of Cu-Zn superoxide dismutase [371]. Within the cell, copper primarily exists as Cu(I) given the reducing environment of the cytosol, whereas its oxidised form, Cu(II), is mostly found extracellularly [372].

Structural studies using NMR intended to elucidate the binding sites of copper in αSyn revealed that Cu^{+} binds both acetylated (Ac-αSyn) and non-acetylated αSyn at three independent, non-interacting sites with differing NMR-derived apparent affinities, which are coordinated by the side chain sulfur atoms of Met1 and Met5 (dissociation constant, k_d= 12 ± 4 μM in Ac-αSyn) (site 1), the imidazole ring of His50 (50 ± 6 μM) (site 2) and the sulfur side chains of Met116 and Met127 (≥ 200 μM) (site 3) [95]. Acetylation of the N-terminus of αSyn is believed to happen ubiquitously *in vivo* [99]. This co-translational modification has profound changes in the behaviour of the protein, as it induces the adoption of a partial α-helical conformation in the N-terminus which possesses an enhanced binding affinity for membrane lipids [94, 39, 373]. Interestingly, Cu^{+} binding to Met1 and Met5 of Ac-αSyn seems to substantially stabilise and induce the elongation of this transient and short α-helical conformation [95]. At the same time, acetylation of the N-terminus abolishes Cu^{2+} binding at the high-affinity binding site Met1 [283] that is observed in the non-acetylated protein. Both N-terminal methionine residues organised in the motif MDVFM (site 1) are essential structural determinants for constituting the high affinity binding site of Cu^{+} for the N-terminal region [284, 374, 375]. In fact, removal of both Met residues completely abolishes binding of Cu^{+} to that site [285]. In contrast, binding to the acidic C-terminal tail seems to harbour an interaction characterised by low affinity and specificity.

Given that Ac-αSyn is abundantly expressed in brain synaptosomes (50 μM) [376] and that concentrations of copper can reach up to 300 μM in synaptic vesicles [377, 330], it is highly likely to find copper complexed with αSyn whilst forming a stabilised α-helically folded N-terminus *in vivo*. Complexation of Ac-αSyn with Cu^{+} may foreseeably have physiologically relevant implications in membrane binding and synaptic transmission, given the increase in the ability of αSyn to tightly bind biological membranes upon acetylation. These reported concentrations for copper might be even higher in pathological circumstances where the normal copper homeostasis is perturbed, as is the

case for several neurodegenerative diseases, possibly turning the equilibrium towards an enhancement of the copper-complexed αSyn population [307]. Consistently, altered copper levels have been observed to exacerbate αSyn toxicity in an *in vitro* dopaminergic neuroblastoma cellular model [378].

Whilst copper binding is likely to enhance the physiological function of αSyn, interaction with copper ions may prove to be deleterious, by inducing the generation of oxidative stress that can influence the amyloid aggregation kinetics of αSyn and ultimately cause cell demise [379, 380]. Indeed, the aggregation of αSyn has been found to be enhanced through a direct interaction with Cu^{2+} [319] and Cu^{+} [381, 382]. As with the other metals discussed here, metal dyshomeostasis has a strong link with neurodegeneration, as is the case with impaired copper metabolism resulting in Menke's disease or Wilson's disease [383]. In fact, copper homeostasis in the cell is tightly regulated to prevent an imbalance which may be associated with increased levels of oxidative stress. For instance, complex formation between Cu^{+} and αSyn has been shown to undergo cycles of oxidation and reduction, leading to the release of H_2O_2 and other ROS that result in dopaminergic neuronal death [381]. As a result of the susceptibility of Met and other residues to oxidation, ROS generated upon the redox cycling of copper ions can lead to site-specific copper-catalysed oxidation of amino acids in the vicinity of the coordination complex [285]. Indeed, copper-catalysed oxidation of interacting residues in αSyn correlates with the binding affinity of copper, with the Met residues at the N-terminus being more readily oxidised than Met116 and Met127 [285].

Additionally, oxidation of αSyn might directly influence its ability to self-aggregate, as has been suggested by the oxidation of the methionine residues, which was proposed to result in the simultaneous inhibition of fibrillation and the aggregation into stable prefibrillar oligomers instead [384, 385, 386, 387, 323]. Of note, several studies focusing on the cellular effects of the oxidation of αSyn have shown that oxidised αSyn hinders the degradation of oligomers through autophagy [379, 388] as well presenting an impaired membrane-binding ability [389]. Copper-mediated oxidation at Met residues might therefore lead to an impairment of the normal physiological membrane-associating function of αSyn, and the accumulation of damaged and misfolded protein in the cytosol, which might show an increased propensity to aggregate. In an *in vitro* assay using SH-SY5Y cells

overexpressing αSyn in the presence of an excess of Cu^{2+}, the antioxidants glutathione and ascorbic acid demonstrated an enhancement of cell survival [381], proposing the use of metal chelators as a valuable potential therapeutic to avoid metal-mediated ROS generation in PD. Like with calcium, dopamine seems to exacerbate the copper-induced oligomerisation of αSyn by affecting its folding [390] and associated toxicity through an increased production of ROS [391], which suggests that there might exist a mechanism common to all redox metals by which they contribute to an enhanced vulnerability of dopaminergic neurons in PD.

1.9.3 Zinc

By being an essential metal ion for the cellular biochemistry, zinc acts as a key cofactor for several enzymes involved in protein biosynthesis, the inflammatory response and oxidative stress, including phospholipase C, alcohol dehydrogenase and carbonic anhydrase [392, 393, 394, 395], as well as in neurotransmitter release [396, 397]. The interaction between αSyn and Zn^{2+} is characterised by a low affinity binding mode with two main independent, non-interacting sites, which seem to be centred around the Asp121 (1.1 ± 0.2 mM) in the C-terminus and residue His50 in the N-terminal region (1.3 ± 0.3 mM) [309]. As revealed by NMR studies, multiple interacting sites exist along the C-terminal region comprising residues 110-140 which might harbour additional several Zn^{2+} ions or might help in the coordination with the main anchoring Asp121 residue [309]. Whilst levels of Zn^{2+} in neurons are in the 10-20 nM range [398], increases of up to 50% have been reported in the substantia nigra of patients with PD [310, 311, 312], which might enhance αSyn-Zn^{2+} complex formation and sustain any potentially induced changes in the protein conformation that may have otherwise been transient under low levels of zinc.

Increasing evidence hints at the fact that a perturbation in the balance of Zn^{2+} levels in the brain might lead to metal accumulation and the cytotoxicity observed in PD [399]. For instance, elevated levels of Zn^{2+} *in vitro* have been demonstrated to be cytotoxic and trigger autophagy and apoptosis in PD models [400]. Even though the concentration of zinc used was artificially high and therefore may not precisely reflect the real *in vivo* cellular conditions, the results of this study served to establish a link between excess Zn^{2+} and cellular toxicity. Another interesting finding of the same study identified a

Zn^{2+}-dependent increase of phosphorylated αSyn [400], which could help explain the co-localisation of zinc deposits in LBs and the elevated proportion of up to 90% of αSyn aggregates present in LBs being Ser129-phosphorylated [401]. In fact, mutations in the *PARK9* gene, which is believed to encode for a lysosomal cation pump, result in zinc dyshomeostasis, mitochondrial and lysosomal dysfunction and αSyn aggregation, accounting for early onset PD [402, 403, 404]. Similarly, through a combination of *in vitro* and *in vivo* models of Parkinsonism, accumulation of Zn^{2+} was identified as a risk factor for αSyn aggregation, the impairment of the ubiquitin-proteasome degradation system and dopaminergic neuronal degeneration and death [405, 406, 407, 408, 409].

However, several clinical analyses have surprisingly identified a significantly low level of Zn^{2+} in the plasma and the cerebrospinal fluid of patients with PD, compared to healthy individuals [410, 411, 412, 413, 414]. In line with this finding, some studies have also highlighted a putative role for a deficiency in Zn^{2+} in an accelerated progression of PD [415, 416, 417], although this might be through the disturbance of neuronal processes rather than a direct interaction with αSyn that might affect its folding.

1.9.4 Manganese

Although present in smaller amounts in the brain than the other mentioned metals, manganese is an essential trace element that acts as a cofactor for several enzymes such as pyruvate carboxylase, serine/threonine glutamine synthase, mitochondrial superoxide dismutase and arginase [418]. Previous NMR studies identified the C-terminal region of αSyn as being the binding region for Mn^{2+}, which directly interacts with the negatively charged carboxylates of the acidic tail with low affinity ($\sim$1 mM dissociation constant, k_d) [419, 328]. In a similar way as with the other metals, an imbalance in the homeostatic concentrations of Mn^{2+} constitutes a risk for neurodegeneration [420, 421]. Interestingly, studies have established a link between αSyn expression and the levels of manganese, by which intracellular manganese concentration increased upon αSyn overexpression in primary midbrain neurons [422]. Conversely, an increased expression of αSyn has also been reported after treatment of cells with Mn^{2+} [423, 424], suggesting an active interplay between the levels of the two molecules. Consistently, examination of organotypic rat brain slices revealed the Mn^{2+}-induced up-regulation

and subsequent oligomerisation of αSyn [425]. Indeed, it has been proposed that a sustained increase in αSyn levels as a result of exposure to Mn^{2+} may in turn lead to αSyn accumulation, aggregation and cytotoxicity [426, 427, 428, 423, 429].

Whilst further structural studies are imperative to elucidate the structural basis of the direct interaction between αSyn and manganese, it has recently become clear that Mn^{2+} induces αSyn aggregation and promotes its cell-to-cell transmission in a prion-like manner, contributing to the spread of pathology and induction of neuroinflammatory and neurodegenerative responses in cell and animal models [429]. Furthermore, Mn^{2+} was observed to increase the fibrillation rate of αSyn *in vitro* [430], as well as to induce αSyn aggregation in brains of non-human primates [428]. Recently, Xu and colleagues identified a possible mechanism by which Mn^{2+} leads to αSyn aggregation, in an attempt to shine light on the structural aspects of the interaction [431]. In this study, the authors demonstrated a Mn^{2+}-dependent induction of a liquid-to-solid phase transition of αSyn to form solid-like condensates, which then act as nuclei for the further recruitment of soluble αSyn monomers and an accelerated amyloid formation [431]. Phase transition was also observed in the presence of membranes where lipids were recruited by αSyn condensates, which is consistent with the co-localisation of lipids and αSyn fibrillar aggregates in LBs [432]. Indeed, increasing evidence exists on the ability of αSyn to undergo liquid-to-liquid phase transition, highlighting a mechanism for amyloid formation with a potential early intermediate step common to other toxic aggregates [433, 434, 435].

It is not surprising that chronic exposure to certain environmental triggers, such as elevated metal ion levels, might cause a predisposition to develop PD at a later stage in life. In fact, several epidemiological studies identified a link between prolonged occupational exposure to environments rich in manganese such as welding, mining and smelting fumes and an increased risk of early onset PD [436, 437, 438, 439, 440, 441, 442, 443, 444, 445, 446]. Similarly, excessive exposure to Mn^{2+} results in Manganism, a debilitating neurological disorder similar but not clinically identical to PD [447] that is characterised by psychiatric and movement impairment, including bradykinesia and rigidity [448, 449]. This Mn^{2+}-induced cytotoxicity has been confirmed experimentally by several studies, which showed a decrease in striatal dopamine and therefore neurotransmission in mice fed with

manganese-rich food [450, 451]. Given that Mn^{2+} has been shown to interfere in the PINK1/Parkin-mediated mitophagy [427], it is likely that Mn^{2+} concertedly exerts cytotoxicity in a combination of ways: By preventing the clearance of damaged mitochondria and inducing the up-regulation of levels of αSyn, increased interactions between damaged mitochondria and αSyn oligomers might result in ROS generation and neuronal injury in a feed-forward loop.

1.10 Research aims

Given the structural plasticity of αSyn, traditional structural-based drug design approaches to guide the development of a therapeutic molecule to target the toxicity of αSyn oligomers seem impractical. In addition, the intrinsic heterogeneity defining αSyn oligomeric species hinders the development of recognition molecules towards these cytotoxic agents. Furthermore, the location of these soluble aggregates within the brain makes the delivery of highly specific but also large therapeutic biomolecules like antibodies across the BBB into the brain extremely challenging. For these reasons, aptamers have emerged as promising alternatives with high binding affinity and specificity for the treatment of neurodegenerative diseases involving hard-to-reach targets in the brain.

In contrast to the highly dynamic N-terminus, which is believed to transiently sample helical conformations which are stabilised upon a membrane binding event, the central NAC region of αSyn has a stronger tendency to self-associate and initiate the aggregation process through β-sheet formation [452]. For this reason, the αSyn aptamer F5R1 may have more easily been specifically selected for its high binding affinity to the central NAC region of monomeric αSyn [259, 262], which may constitute a less volatile structural aptatope than the N-terminus. However, the key region of αSyn oligomers involved in establishing detrimental contacts with the membrane is the N-terminus and not the NAC [124]. Therefore, aptamers that specifically target this critical N-terminal region are imperatively needed, as they will most predictably show the highest neuroprotective capacity by blocking the association of toxic oligomeric species with neuronal membranes.

By using key structural information of the disruption mechanism of lipid membranes in PD, I aim to specifically select aptamer sequences against the essential lipophilic element corresponding to the

N-terminal region of monomeric αSyn [124]. This portion of the protein is believed to enable the anchoring and initial association of αSyn oligomeric species with membranes and is hence considered fundamental in the establishment of deleterious interactions with lipid membranes. The generation of an aptamer against this region is therefore hypothesised to physically block the aberrant interaction of αSyn oligomers with biological membranes, thereby preventing their detrimental association and the disruption of the lipid packing.

IDPs like αSyn challenge the canonical structure-function paradigm given their characteristic conformational plasticity that is heavily influenced by the environment [453, 454, 455, 456, 457, 458]. It is partly for this reason that a full understanding of their function and roles in pathology is still lacking. Given the large conformational space that is dynamically sampled by αSyn, identifying disease-relevant conformers is particularly difficult. By understanding the interplay between genetic and environmental factors and the structure and dynamics of αSyn, we may only then start to grasp the different mechanisms that may lead to self-association and disease onset.

A better understanding of the consequences on the conformational space of αSyn upon interaction with metal ions is required to elucidate the mechanisms by which metals might alter its aggregation pathways and kinetics. Indeed, structural transitions induced by metal binding might cause misfolding events that may lead to protein oligomerisation. Given the dependency on charge to maintain a stable aggregation auto-inhibited conformation [41, 40], interactions with metal ions might lead to the local neutralisation of charge clusters, triggering the collapse of the long-range weak intramolecular protective contacts and the full exposure of the aggregation-prone NAC. Since the hydration sphere is essential in defining the conformational landscape of any given protein, we hypothesised that metal ion binding might alter the exposure of different regions of αSyn to the aqueous solvent, thereby indicating protein conformational transitions. To investigate these changes in solvent exposure, I used the phase-modulated CLEAN chemical exchange (CLEANEX) NMR pulse sequence [459, 460] to sample long-timescale local or global conformational effects of αSyn upon binding of a series of metals important for neuronal function: Ca^{2+}, Cu^{2+} Cu^{+}, Mn^{2+} and Zn^{2+}. This experiment therefore provides a sensitive residue-specific tool to measure the exchange of labile backbone amide protons

with water protons. In this way, residual protein structural changes in the ms timescale can be distinguished from the folded native conformation of αSyn without the need for a deuterated buffer, overcoming the limitations of hydrogen/deuterium (H/D) exchange where exchange rates are in the seconds-to-days timescale. In addition, amide backbone relaxation was measured to provide further structural cues, to aid in our understanding of the series of structural transitions that promote the formation of aggregation-prone αSyn conformers upon metal ion binding.

Materials and Methods

2.1 Design of DNA Library

The initial N42 combinatorial library consisted of single-stranded DNA (ssDNA) sequences containing a randomised core region of 42 nucleotides, surrounded by 45- and 24-nucleotide long specific primer binding sites at the 5' and 3' ends, respectively (5'-GATAATACGACTCACTATAGGGAATG GATCCACATCTACGAATTC-N42-TTCACTGCAGACTTGACGAAGCTT-3'; 111-nt long in total). The randomisation of the central region was carried out through incorporation of equal molar amounts of each A:T:G:C base during chemical synthesis (Integrated DNA Technologies). The sequences of the primers complementary to the respective constant primer-binding sites are given in Table 2.1 [461, 462].

Aptamer	Length	Sequence
Forward Primer	41	5'-GATAATACGACTCACTATAGGGAATGGATCCACATCTACGA-3'
Reverse Primer	24	5'-AAGCTTCGTCAAGTCTGCAGTGAA-3'
Truncated Reverse Primer	20	5'-GCTTCGTCAAGTCTGCAGTG-3'
N42 Library	111	5'-GATAATACGACTCACTATAGGGAATGGATCCACATCTACGAATTC(N42)TTCACTGCAGACTTGACGAAGCTT-3'
FSeq1	50	5'-GATAATACGACTCACTATAGGGAATGGATCCACATCTACGGATAATACGA-3'
65ntSeq	65	5'-GATAATACGACTCACTATAGGGAATGGATCCACATCTACGATTCACTGCAGACTTGACGAAGCTT-3'
R12S15	42	5'-CACCCATGCTGATCCTGATTCATTGCCCCCAGGAGTGACGCT-3'
R12S16	42	5'-CTTACTATATATTTTGATCTTCTCCGCTCTTAGACCGACTCG-3'
R12S24	41	5'-TAAACCCTATTACCTAGTAGCAATTCAGTCATGTGCTCTTT-3'
R12S29	42	5'-AGCCATTCTTTATAGTAACCCAGCTACTCCCTTCATGAATTA-3'
R12S55	41	5'-TACAAGTTCATTCGAACCTGATACCATGTTGCACAGTTTCA-3'
R12S91	42	5'-GGGTCGGCAAGATAGAGAAGTGCAAAACCCATACAGCCCTCA-3'
TR12S91	30	5'-GGGTCGGCAAGATAGAGAAGTGCAAAACCC-3'
R12S93	42	5'-TTAATCAACAGATCCCCAACCCACTCTTAACTCGGACATTCC-3'
R15S2	38	5'-GCCAACCCTAACTCGCGGTAGGACCGAGATCATTTCGA-3'
R15S15	43	5'-CGTTTGCGCCCGGCAAGGAAATCCTTAAAAAGTCCTCCCCCCT-3'
R17S17	42	5'-CGAAACGCACGGTTATAATCCTGGCGCCAATACCAATGAATA-3'
R18S10N	42	5'-CTCTTACAGTTAATATAATACACGTTTATTTTTTTATTTACA-3'
R18S16N	41	5'-CTTTCATAACTTTTCCAAATATCTAAGCGTACACATGTATC-3'
R18S17N	42	5'-CTTATTTAGTGCCTTAATCATAGCACCATTTCTCTGTAACTA-3'
R18S25N	42	5'-TTGTTTTTTCCGCCTTATTCTTAACGGTCCGCCCGAGCACTA-3'
R18S30N	42	5'-AAGAGCGCATTCACATCTTCCTCGCTTTAACCACATCCAGAC-3'
R18S51N	42	5'-AAGGGTTTGTCTCTGTAGTCTCCTCTTGTTTTTATAAGACCA-3'
R20S35	42	5'-AGAAGTAGAAGCGTCGACTCTGTCTTGTCTGGGTTTATTATC-3'
R20S38	42	5'-TAGATCATACAAAAAAAGTAACAACATACGATCGCGGCCCTA-3'

Table 2.1: Sequences of the primers and aptamers identified from sequencing of the different round libraries throughout SELEX.

2.2 Aptamer selection

SELEX was used for the isolation of aptamers against the target αSyn_{1-25} peptide (Biotin-MDVFMK GLSKAKEGVVAAAEKTKQG-CH_2-CH_2-NH_2) (Thermo Fisher Scientific). Optimisation tests and counter-selection incubation steps were carried out using the γSyn_{1-25} peptide (Biotin-MDVFKKGFS IAKEGVVGAVEKTKQG-NH_2). Amplification of the pools of bound sequences at each round of selection was performed by PCR. Selection conditions were optimised in each round to ensure enrichment of binding sequences (Table 2.2).

2.2.1 Selection of initial library

The initial N42 DNA library was first reconstituted in Aptamer Binding Buffer (ABB) (20 mM Tris-HCl, 150 mM NaCl, 5 mM $MgCl_2$, pH 7.4), and heated at 95 ºC for 4 min for conformational equilibration. The ssDNA library was then allowed to cool down at room temperature (RT) for 20 min. Incubation of 10 nmol of the library with the target αSyn_{1-25} peptide followed, in a 100-fold ratio of ssDNA:peptide at RT for 1h whilst rotating gently. The mixture was subsequently incubated with Streptavidin MagneSphere® Paramagnetic Particles (Promega) (SA-Mag beads) at 1x the binding capacity relative to the molar amount of biotinylated peptide (0.75 nmol biotinylated molecule/mg of SA-Mag beads) at RT for 45 min whilst rotating, to immobilise the biotinylated peptide together with any target-bound sequences. Using a magnetic support, the paramagnetic beads were captured, and the supernatant containing the unbound library ssDNA sequences was discarded. The SA-Mag beads were then washed once with ABB, captured, and the supernatant removed. Later, the SA-Mag beads onto which the biotinylated target and any target-bound sequences were immobilised was resuspended in ultrapure DNase-free H_2O. This was then incubated at 95 ºC for 4 min to allow the recovery of the bound sequences, and the SA-Mag beads immediately captured and discarded. The obtained pool of bound sequences was amplified by PCR and carried over to the next round of selection. The following steps were iteratively repeated as part of SELEX:

2.2.2 Amplification of DNA library

The recovered subpool of bound sequences was symmetrically amplified by PCR, i.e. using both forward and reverse primers. To determine the number of cycles required for the optimal amplification of this subset of DNA sequences, a small-scale amplification was performed in which sample aliquots were taken every two PCR cycles, for a total of 16 cycles. Amplification conditions were 3 min at 95 ºC initially, and cycles of 1 min at 95 ºC, 1 min at 45 ºC, and 1 min at 72 ºC. Electrophoresis of the test PCR samples was carried out on a 3% (w/v) agarose gel in 1x TAE buffer at 150 V for 1h. DNA bands were then visualised under UV light after incubating the agarose gel with SYBR® Gold Nucleic Acid Gel Stain (Thermo Fisher) for 30 min. Following visual inspection of the results, the DNA subpool was amplified for an optimum number of X cycles to obtain high copy numbers of double-stranded

sequences. The number of cycles of amplification was chosen based on the intensity of the band corresponding to the PCR product of the library sequences, whilst minimising the amplification of PCR artefacts.

2.2.3 Generation of a ssDNA library

A test PCR amplification of the amplified double-stranded DNA sublibrary was performed using the forward primer only (i.e. asymmetric PCR) in the same way as described above. This was done to generate a pool of forward strands of the target-bound sequences, following their previous exponential amplification by symmetric PCR. Sample aliquots were taken every 2 PCR cycles, for a total of 10 cycles.

The library was subsequently amplified asymmetrically for an optimum number of X cycles to obtain single-stranded sequences from the double-stranded sublibrary. Concentration and desalting of the generated ssDNA library were carried out by ethanol precipitation: firstly, the DNA pool was mixed with 3M CH_3COONa to a final concentration of 100 mM, and 2.4x volumes of absolute ethanol were later added in order to precipitate DNA. After overnight incubation at -20 ºC, the mixture was centrifuged at 30 000 x g at 4 ºC for 1h to pellet the precipitated DNA. The pellet was washed with 80% ethanol, and centrifuged again at 30 000 x g at 4 ºC for 10 min. This was lastly vacuum-dried and resuspended in ABB ready to be carried over to the target incubation step of the next selection round. The concentration of the amplified ssDNA was measured using a NanoDrop™ spectrophotometer.

2.2.4 Selection against the target αSyn$_{1-25}$ peptide (SA-Mag beads-SELEX)

The ssDNA sublibrary was first heated at 95 ºC for 4 min and allowed to cool down at RT for 20 min. 4 nmol of the library were incubated with αSyn_{1-25} at RT for 1h whilst rotating, at a 1:100 molar ratio of target to DNA. This mixture was incubated with Streptavidin MagneSphere® Paramagnetic particles (Promega) at a 1x binding capacity of the beads relative to the molar amount of biotinylated peptide used at RT for 30 min to immobilise the αSyn_{1-25}-DNA complexes. The beads were then collected using a magnetic support, its supernatant removed, and washed with ABB. These were then resuspended in ultrapure DNase-free water and heated at 95 ºC for 4 min. The paramagnetic SA-Mag

beads were captured, and the supernatant containing the target-bound DNA subpool immediately recovered. This was directly amplified by PCR following the usual procedure.

2.2.5 Selection against the target full-length αSyn (NCM-SELEX)

The initial ssDNA library (which in NCM-SELEX corresponds to the 12^{th} round library from SA-Mag beads-SELEX) was first heated at 95 ºC for 4 min and allowed to cool down at RT for 20 min. In the meanwhile, two pieces of nitrocellulose membrane (NCM) (HAWP01300, MF-Millipore® HAWP Nitrocellulose membrane filter, 0.45 μm) were soaked in ABB for 30 min before being used. NCMs were placed inside syringe filter holders (515-2360, VWR Pop-Top™ 13 mm) and the solution to be filtered passed through them using a 1 ml syringe. Prior to every selection round, the ssDNA library was filtered through a piece of NCM that had previously been soaked in ABB. This was done as a negative selection step to remove sequences that would be non-specifically binding to the membrane. The membrane was then discarded.

The filtered library was then incubated with the target full-length αSyn at RT whilst rotating. The molar amounts of each molecule, ratios of incubation and time of incubation were varied to increase the stringency of selection at each round (Table 2.2). Later, the incubation mixture was filtered through a fresh pre-soaked NCM. This was repeated with the filtered fraction using the same piece of pre-soaked NCM to allow any target αSyn together with bound DNA sequences that may have passed through the pores of the membrane to have a second chance of adhering to the NCM. The filtered solution was then discarded. The NCM was washed with 1 ml ABB to remove low affinity binders. The bound ssDNA sequences were eluted by soaking the NCM filter in H_2O and incubating at 95 ºC for 4 min. The solution containing the target-bound library sequences was immediately recovered and directly amplified following the usual PCR protocol.

2.3 Purification of ssDNA

A 10 ml volume of large-scale asymmetrically amplified DNA library was ethanol precipitated following the usual protocol. The DNA pellets were then dissolved in dH_2O and mixed with the same

	Amount of DNA Library (nmol)	Amount of 9.07 µM αSyn1-25 target (pmol)	Ratio of incubation	Amount of SA-Mag beads (0.75 nmol/mg) (µl)	Amount of 10 µM γSyn1-25 (pmol)	No. of buffer washes	2 ml Symmetric PCR cycles	4 ml Symmetric PCR cycles	10 ml Asymmetric PCR cycles
Round 1	4	40	100	60	-	1	6	2	-
Round 2	4	40	100	60	-	2	16	2	-
Round 3	4	40	100	60	-	2	14	2	4
Round 4	1	10	100	16	-	2	14	2	-
Round 5	5	50	100	75	-	2	16	2	2
Round 6	0.8	8	100	12	-	2	6	2	2
Round 7	0.888	8.88	100	13.2	-	2	14	2	2
Round 8	0.42	4.2	100	6.3	-	3	18	2	2
Round 9	0.486	4.86	100	6.48	0.5	3	14	2	2
Round 10	0.453	4.53	100	6.2	-	3	16	2	2
Round 11	0.5808	5.808	100	7.74	-	3	14	2	2
Round 12	0.4668	4.668	100	6.4	0.48	4	16	2	2
Round 13	0.7	7	100	9.34	-	4	12	2	4
Round 14	0.963	9.63	100	12.86	-	4	14	4	3
Round 15	1.32	13.2	100	17.6	1.519	5	14	3	4
Round 16	0.945	9.45	100	12.6	-	5	14	3	4
Round 17	1.3	13	100	17.34	1.365	5	13	3	2
Round 18	0.876	4.38	200	5.84	-	5	16	2	2
Round 19	0.869	4.35	200	5.8	0.869	6	18	2	2
Round 20	1.042	5.21	200	6.94	1.07	6	16	-	-
Round 13-NCM	17.4	2499	7	-	-	0	4	4	4
Round 14-NCM	19.5	777	25	-	-	1	4	3	2
Round 15-NCM	22.4	448	50	-	-	2	4	4	2
Round 16-NCM	19.6	261	75	-	-	2	5	3	3
Round 17-NCM	31	310	100	-	-	2	3	4	4
Round 18-NCM	31	310	100	-	-	2	4	-	-

Table 2.2: Selection conditions per round of SA-Mag beads-SELEX and NCM-SELEX.

volume of Novex™ TBE-Urea Sample Buffer (Thermo Fisher) before loading on a Novex™ 10% Polyacrylamide TBE-Urea gel (Thermo Fisher). This was run at 220V for 75 min.

With the help of a thin-layer chromatography plate, the migrated DNA bands were visualised under a 240 nm UV lamp. The bands of interest were excised using a scalpel and mechanically crushed before being mixed with ABB and left rotating overnight. This was done to allow the diffusion of the purified excised bands from the crushed pieces of gel to the solution. The solution was then filtered using a 0.45 μm cellulose acetate filter to remove gel parts, the concentration of DNA measured using a NanoDrop™ spectrophotometer and the purified pool subjected to the next round of selection.

2.4 Purification of dsDNA

Symmetrically PCR amplified products were run on a 3% agarose gel and the band of interest to be purified was excised with a scalpel. Purification of the excised PCR products was done following the manufacturer's instructions from the GeneJET Gel Extraction Kit (K0691, Thermo Fisher).

2.5 Library cloning and sequencing

Cloning of the various selection round libraries was done following the manufacturer's instructions enclosed within the TOPO® TA cloning® kit (K450002, Thermo Fisher), by which the Taq polymerase-amplified double-stranded sequences (bearing 3'-A overhangs) were directly inserted into the pCR™2.1-TOPO® vector. Given the heterogeneous nature of the pool of sequences, the cloning reaction was incubated longer than indicated (20 min) to ensure insertion of a variety of different PCR product sequences present in the pool. The product was then transformed into One Shot® TOP10 *E. coli* cells. Selective lysogeny broth (LB) plates containing 50 μg/ml of kanamycin were prepared by spreading 80 μl of X-Gal at 20 mg/ml in dimethylformamide on the surface. The transformation mix was plated on the LB plates and incubated overnight at 37 ºC.

Blue/white screening was performed with the help of X-Gal, which made those colonies containing a copy of the plasmid with the PCR product correctly inserted appear white. Those having no copies

of the plasmid, empty vector or copies of the plasmid with the PCR product inserted at a wrong site were observed as being blue. Individual colonies were picked and grown in LB medium with kanamycin (50 μg/ml) overnight, and their plasmid DNA isolated following the standard manufacturer's indications from the PureLink® Quick Plasmid Miniprep kit (K450002, Thermo Fisher) and the QIAprep® Spin Miniprep kit (27104, QIAGEN). Extracted plasmid DNA was then sequenced at Eurofins Genomics through Sanger sequencing.

Sequences of the aptamers identified through Sanger sequencing that were synthesised and tested for their binding affinities to the target αSyn_{1-25} are specified in Table 2.1.

2.6 Structural modelling of aptamer sequences

The 2D structures of R12S91 and TR12S91 were modelled using the web server for nucleic acid folding Mfold [463], where the parameters were set to mimic the selection conditions: a temperature of 25 ºC and an ionic strength of 150 mM Na^+ and 5 mM Mg^{2+}. Three-dimensional structural modelling of these aptamer sequences was done using the Mfold-modelled 2D structures as starting points. These were subjected to a series of servers (RNAComposer, Web 3DNA and VMD software (AutoPSF plugin)) through which the structure of each DNA aptamer sequence was transiently modelled as an RNA molecule, to finally generate a stable DNA structure by energy minimisation with the NAMD/VMD software (AutoIMD plugin) [464, 465].

2.7 Enzyme-Linked Oligonucleotide Assay (ELONA)

Pierce™ Streptavidin Coated 96-Well Clear Plates (15125, Thermo Fisher) were used for immobilisation of the biotinylated αSyn_{1-25} peptide and other absorbance-based binding assays. Triplicates of each condition were done to allow the calculation of the dissociation constant, k_d (technical replicates). Each well (pre-blocked) was first washed three times with 200 μl of wash buffer (20 mM Tris-HCl, 150 mM NaCl, 5 mM $MgCl_2$, 0.1% w/v BSA, 0.05% Tween-20, pH 7.4). 100 μl of 9.07 μM biotinylated αSyn_{1-25} peptide (0.12 μM final concentration) was incubated in each well to saturate the binding capacity of 10 pmol of biotin/well. This step was followed by gentle shaking for 2h

at RT on a microplate shaker. Each well was then washed again three times with 200 µl wash buffer. In the meanwhile, the ssDNA sequences dissolved in ABB were heated at 95 ºC for 4 minutes and allowed to cool down at RT for 20 min to allow for conformational equilibration.

A serial dilution of each 5'-fluorescein-coupled sequence was made (5 µM, 2 µM, 1 µM, 0.5 µM, 0.2 µM, 0.1 µM, 0.05 µM, 0 µM), of which 100 µl of each was added to each well and incubated for 1½ h with shaking at RT. The plate was then washed again as described above. 100 µl of anti-fluorescein HRP antibody (ab19492, Abcam) was incubated in each well at a 1:500 dilution for 30 min at RT with shaking. The plate was further washed, and 100 µl of TMB substrate (N301, Thermo Fisher) was added to each well to develop the absorbance signal. After incubating for 30 minutes, the reaction was stopped by adding 100 µl of 0.18 M sulfuric acid to each well. Absorbance was then immediately measured at 450 nm on a CLARIOstar Plus (BMG Labtech) microplate reader.

ELONA was also carried out using MaxiSorp™ Clear Flat-Bottom 96-Well Plates (439454, Thermo Scientific™) to immobilise αSyn_{1-25} on a streptavidin-free plate and assess the binding of aptamer sequences in a streptavidin-free environment. The wells of the plate were first blocked using diluted Blocker BSA Blocking Buffer in TBS (10X) (37520, Thermo Scientific™) following the manufacturer's instructions, to prevent nonspecific binding. Aptamer incubation and signal measurement was carried out following the standard ELONA protocol outlined above.

Analysis and calculation of the dissociation constant was done by fitting the binding data to the hyperbolic model $y = B_{max}X/(k_d + X)$ using Origin 2020 (OriginLab Corporation), where y refers to absorbance recorded at 450 nm; B_{max} is the maximum number of binding sites; X is the concentration of aptamer; and k_d denotes the dissociation constant of the interaction.

This equation describes a one-site specific binding mode within a saturation binding experiment. Here, the k_d (the aptamer ligand concentration that binds to half of the protein αSyn_{1-25} sites at equilibrium) is to be determined to provide a measure of the binding affinity of the interaction. To account for nonspecific binding sites, background binding absorbance in buffer in the absence of

aptamer was subtracted from each titration reading.

2.8 NHS-Rhodamine labelling

To study the interaction between the identified aptamer sequences and αSyn, αSyn was labelled with NHS-rhodamine to allow Förster's Resonance Energy Transfer (FRET) measurements to be made between the fluorescein-labelled DNA sequences and rhodamine 6G-labelled αSyn. This was done following the manufacturer's instructions from the Pierce NHS-Rhodamine Antibody Labelling Kit (53031, Thermo Scientific™). Briefly, the protein was first prepared by dialysing αSyn in ABB at a concentration of 2 mg/ml in 5L of Phosphate Buffered Saline (PBS) (137 mM NaCl, 2.7 mM KCl, 10 mM Na_2HPO_4, 1.8 mM KH_2PO_4, pH 7.4) three times. 40 µl of the provided borate buffer (0.67 M) was added to 0.5 ml of dialysed αSyn in PBS. Later, the prepared protein was labelled by being added to the vial of NHS-Rhodamine reagent enclosed within the kit and incubated for 60 min at RT protected from light. The labelling reaction was then mixed with the Purification Resin included in the kit and centrifuged for 45s at 1000 x g to collect the purified rhodamine-labelled protein.

2.9 Förster's Resonance Energy Transfer (FRET)

FRET is a physical phenomenon that relies on the transfer of excitation energy from a donor fluorophore to a neighbouring acceptor fluorophore through non-radiative long-range dipole-dipole interactions (Figure 2.1) [466]. FRET happens when the acceptor fluorophore gets excited by the emission light coming from the donor fluorophore and only if the distance between an appropriate donor-acceptor pair is 8-10 nm or less. For energy to be transferred and for FRET to take place, the donor emission spectrum and the acceptor excitation spectrum need to overlap. Its efficiency is dependent on the inverse of the sixth power of the intermolecular distance, which makes it an accurate and sensitive measure of molecular proximity. This is therefore particularly useful for investigating molecular binding events in biochemistry, which commonly involve the physical interaction of at least two cellular components.

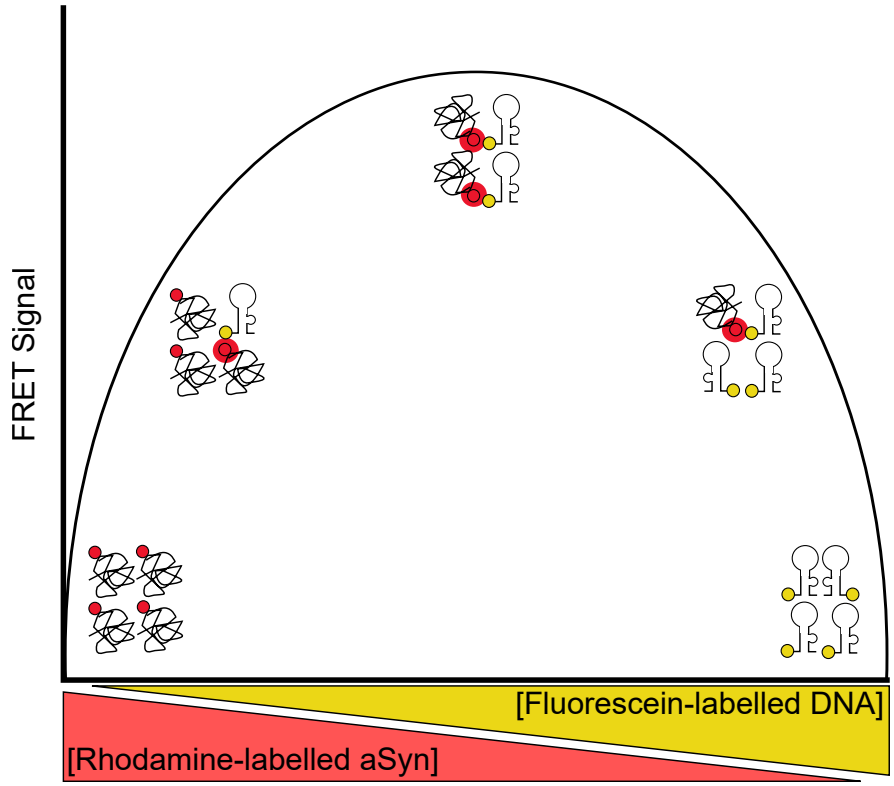


Figure 2.1: Set-up of FRET. Schematic illustrating the principle of the FRET Job plot assay.

2.9.1 Assay design and preparation

Here, FRET was measured to study the interaction between fluorescein-coupled ssDNA aptamer sequences and rhodamine-labelled αSyn. The experimental set-up was adapted from [467] and was carried out in a black opaque 384-well plate (Corning™ 384-Well Solid Black Polystyrene Microplate with Flat Bottom). Briefly, 100 µM stocks of rhodamine-labelled αSyn (acceptor fluorophore) and fluorescein-labelled DNA aptamers (donor fluorophore), as well as unlabelled, were prepared. Solutions were prepared at twice the concentration required for the reactions in the plate wells. Each well reaction was set up in duplicates and was prepared by mixing in situ 20 µl of αSyn with 20 µl of DNA aptamer (Figure 2.2).

2.9.2 Data collection

Fluorescence intensity was measured using a CLARIOstar Plus (BMG Labtech) microplate reader under the following settings: For each type of measurement 50 flashes were applied, together with a settling time of 0.1s. Dichroic was set to automatic.

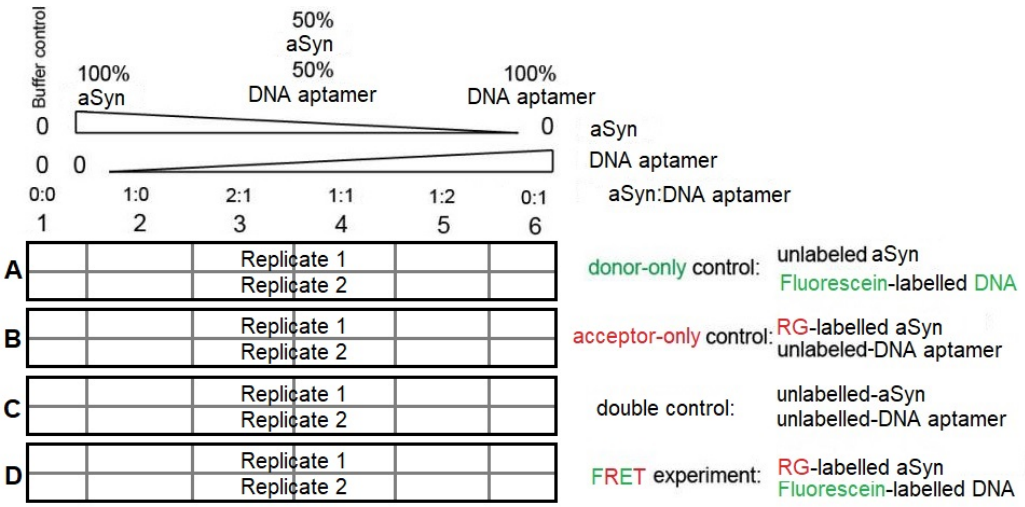


Figure 2.2: FRET experimental set-up with ratios of fluorescein-labelled DNA aptamers to rhodamine-labelled αSyn.

- Donor fluorescence measurement: Excitation wavelength-bandwidth: 475-435 nm. Emission wavelength-bandwidth: 543-530 nm. Gain settings were adjusted automatically by using the reaction in well A6, which contains the highest donor dye concentration with no acceptor dye present.

- Acceptor fluorescence measurement: Excitation wavelength-bandwidth: 510-465 nm. Emission wavelength-bandwidth: 575-555 nm. Gain settings were adjusted automatically by using the reaction in well C2, which contains the highest acceptor dye concentration with no donor dye present.

- FRET measurement: Excitation wavelength-bandwidth: 475-435 nm. Emission wavelength-bandwidth: 575-555 nm.

2.10 αSyn expression and purification

2.10.1 Bacterial Transformation

αSyn was expressed in BL21 *E. coli* cells using the pT7-7 αSyn WT plasmid, or both pT7-7 αSyn WT and pNatB plasmid to achieve NTA by co-expressing the components of the NatB complex [97].

Firstly, BL21 cells were incubated with the respective plasmid/s on ice for 30 min. The samples were then heat-shocked for 20s and quickly placed on ice for a further 2 min. 200 µl of sterile LB medium were added into each sample, and these were then incubated with shaking for 1h at 37 ºC. 60 µl of each sample were transferred and spread on selective LB plates (containing 100 µg/ml ampicillin for pT7-7 αSyn WT-transformed bacteria, and 100 µg/ml ampicillin and 100 µg/ml chloramphenicol for the double plasmid sample). These were then incubated at 37 ºC overnight.

To verify the correct amino acid sequence of each plasmid product under the T7 promoter, both plasmids were also transformed into the higher copy number *E. coli* strain DH5α. Sanger sequencing was carried out by Eurofins Genomics.

2.10.2 Expression in M9 minimal media

Starter cultures were set up with 10 ml LB medium, ampicillin (100 µg/ml) and a single colony that had been transformed with pT7-7 αSyn WT or co-transformed with pT7-7 αSyn WT/pNatB. These were left incubating at 37 ºC overnight.

To allow the incorporation of the NMR-active stable radioisotopes ^{13}C and ^{15}N, protein expression was carried out in M9 minimal media. Per litre of sterile M9 media (6.4 g Na_2HPO_4, 1.5g KH_2PO_4, 0.25g NaCl), the following components were sterile filtered and added: Thiamine (3.8 nM final concentration), Biotin (2.7 nM), $CaCl_2$ (200 µM), $MgSO_4$ (1 mM), 1g ^{15}N-labelled NH_4Cl, 3g ^{13}C-labelled glucose. 1g of the supplement ISOGRO®-^{15}N Powder (606871, Merck) was added per 1L of bacterial culture co-expressing WT αSyn and NatB to enhance recombinant protein expression and therefore ensure complete acetylation of all expressed αSyn protein.

To scale up the bacterial culture, the 10 ml starter culture was centrifuged at 4000 x g for 15 min and added to 1L of M9 minimal media, together with ampicillin (100 µg/ml) for expression of αSyn alone, and ampicillin and chloramphenicol (100 µg/ml each) for expression of αSyn and NatB. This was incubated at 37 ºC whilst shaking at 180 rpm until the OD600 reached 0.6-1.0. The expression of the recombinant proteins was then induced by addition of IPTG (1 mM final concentration) and

overnight incubation at 28 ºC with shaking.

2.10.3 Purification

The cells were harvested by centrifugation at 6 200 x g for 20 min at 4 ºC, using a JLA-8.1000 rotor in a Beckman Coulter centrifuge (Beckman Coulter Brea, USA). The pellets were resuspended in 1x PBS (137 mM NaCl, 2.7 mM KCl, 10 mM Na_2HPO_4, 1.8 mM KH_2PO_4, pH 7.4) and recentrifuged at 24 500 x g for 1h at 4 ºC.

Each pellet obtained from a 1L culture was resuspended in 20 ml lysis buffer (200 µl of 1M Tris pH 7.7, 40 µl of 0.5M EDTA and 1/2 of cOmplete™ protease inhibitor cocktail tablet (11697498001, Merck)). This was then sonicated on ice (2s on, 4s off, total time 8 min). The sonicated samples were then centrifuged at 24 500 x g for 30 min at 4 ºC on a benchtop centrifuge and the resulting cell debris pellets discarded. The supernatant was heated for 20 min at 94 ºC to precipitate heat-sensitive proteins. A further centrifugation step at 24 500 x g for 30 min at 4 ºC on a benchtop centrifuge pelleted the precipitated protein fraction. The supernatant was then treated with 10 mg of Streptomycin sulfate (11860038, Gibco™) per ml of supernatant to precipitate DNA, and incubated for 15 min at 4 ºC whilst rolling. The samples were again centrifuged at 24 500 x g for 30 min at 4 ºC. The supernatants were recovered and 361 mg of ammonium sulfate ($(NH_4)_2SO_4$) was slowly added per ml of volume to precipitate αSyn. This was incubated for 30 min at 4 ºC whilst rolling. A further centrifugation step at 24 500 x g for 30 min at 4 ºC recovered the precipitated αSyn, which was then resuspended in 6 ml of 25 mM Tris, pH 7.7 per 1L of original bacterial culture. Samples were dialysed in 4L of dialysis buffer (25 mM Tris-HCl, pH 7.7) overnight at 4 ºC using a molecular weight cut-off filter of 3.5 kDa (Figure 2.3).

Dialysed αSyn was then loaded onto an anion exchange column (Figure 2.4). The ion exchange column (Q Sepharose HP HiScale 26/20, 6-7 cm, Cytiva) was equilibrated with buffer line A (filtered 25 mM Tris, pH 7.7) for 2 column volumes. Buffer line B (filtered 25 mM Tris, 1.5 M NaCl, pH 7.7) was used to elute the protein from the column through a concentration gradient. The eluted protein fractions were concentrated to a volume of 20 ml per 6L culture media using 3 kDa Vivaspin

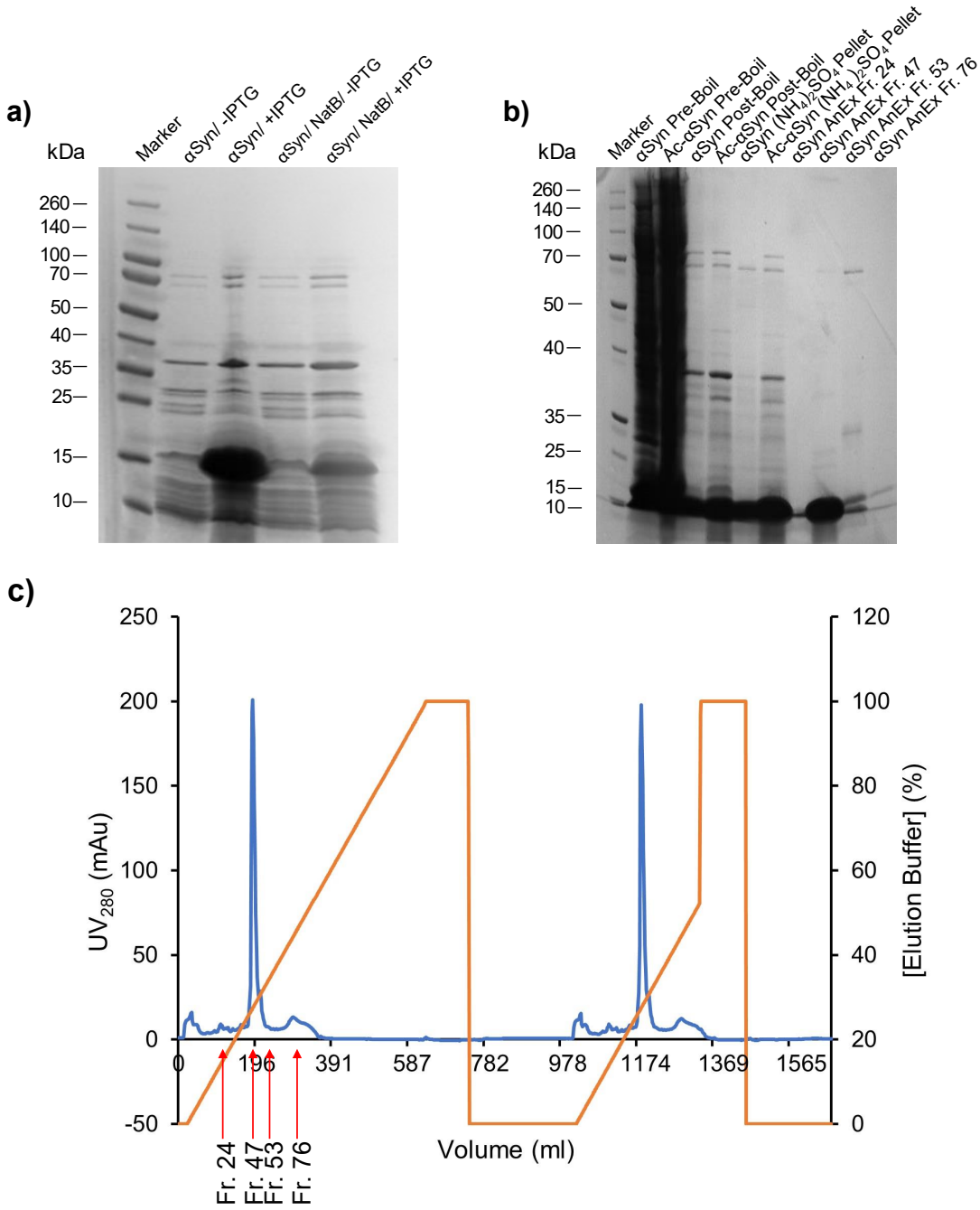


Figure 2.3: Purification of αSyn and Ac-αSyn. a) Test expression of αSyn and Ac-αSyn. Expression of the proteins under the T7 promoter was induced by incubation with IPTG at a final concentration of 1 mM. Control samples in which no IPTG was added are also shown. The overexpression of both species of αSyn (14 kDa) can clearly be seen on a Tris-Glycine 4-20% gradient polyacrylamide gel. b) First steps in the purification of αSyn and Ac-αSyn, in which the samples were boiled to denature all heat-sensitive proteins and separate them from the intrinsically disordered αSyn; ammonium sulfate was then used to precipitate αSyn and Ac-αSyn. Last four lanes correspond to four fractions of the eluted αSyn protein chromatogram from anion exchange purification in Figure 2.3c). Both αSyn species (14 kDa) are observed at the expected size on a 12% polyacrylamide gel. The 10 and 15 kDa marker bands have not correctly separated and appear as almost a unique band. c) Anion exchange chromatogram for αSyn, showing in blue the UV absorption at 280 nm, and in orange the percentage of elution buffer, which was added in a gradient manner to elute the protein off the column. The protein sample was purified in two batches, corresponding each of them to the two groups of peaks.

molecular cut-off filters (Sartorius Stedim Biotech, Göttingen, Germany).

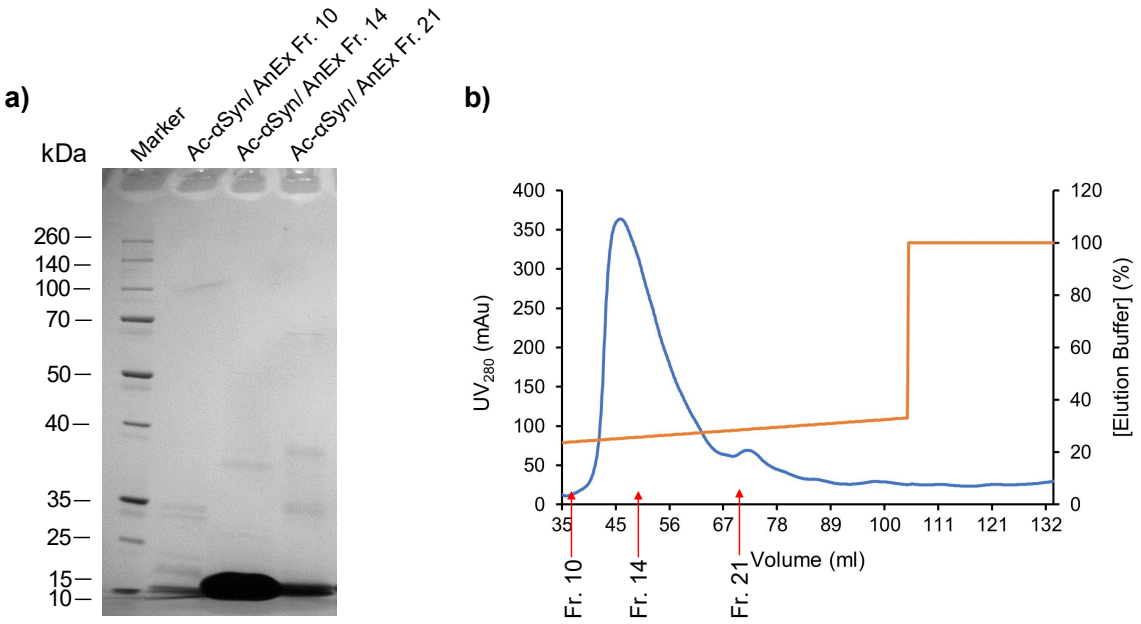


Figure 2.4: Anion Exchange Purification of Ac-αSyn. a) Samples from fractions 10, 14 and 21 from the anion exchange purification of Ac-αSyn, as run on a 12% polyacrylamide gel. The protein of interest (14 kDa) is observed at the expected migration size. The 10 and 15 kDa marker bands have not correctly separated and appear as almost a unique band. b) Anion exchange chromatogram for Ac-αSyn, showing in blue the UV absorption at 280 nm, and in orange the percentage of elution buffer, which was added in a gradient manner to elute the protein off the column. The protein sample was purified in one batch.

Samples were then filtered with a 0.22 µm filter membrane and loaded onto the gel filtration column (HiLoad 16/60 Superdex 75 pg) for SEC (Figure 2.5 and 2.6). Eluted samples were then pooled and concentrated as outlined above to 350 µM and stored at -20 ºC. Prior to NMR experiments involving aptamers, samples were dialysed in 5L of ABB at 4 ºC overnight. Prior to experiments to study the interactions of the metal ions investigated in this thesis (Ca^{2+}, Cu^{+}, Cu^{2+}, Zn^{2+}, Mn^{2+}), stored αSyn samples that had previously been dissolved in buffers containing metal ions were dialysed in 5L of 25 mM Tris-HCl, pH 7.0 buffer three times to remove any traces of metals. The purity of the fractions was monitored after every major purification step by SDS-PAGE and the concentration of monomeric αSyn determined by the absorbance at 280 nm using a molar extinction coefficient of 5960 $M^{-1}cm^{-1}$ with a NanoDrop. The same purification procedure was repeated for Ac-αSyn.

Acetylation of αSyn was achieved using an established plasmid and protocol [97]. However, the

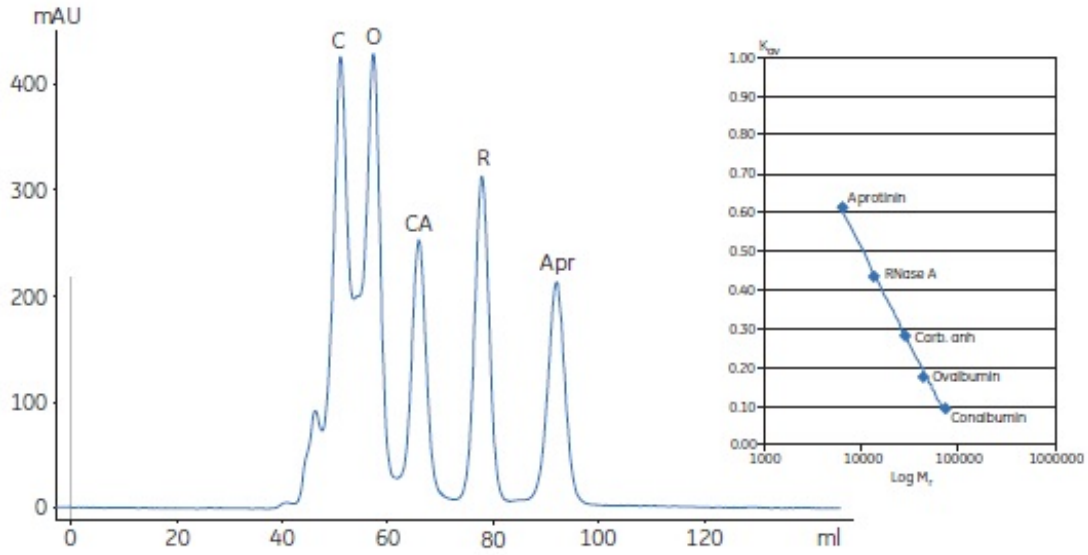


Figure 2.5: Manufacturer's chromatographic separation and calibration curves of standard proteins on a HiLoad 16/60 Superdex 75 pg column.

complete acetylation of the sample was confirmed by visual inspection of an overlay of TROSY-HSQC spectra of non-acetylated and acetylated αSyn at pH 6.0 recorded at 15 ºC [39].

2.11 Generation of Cu^+

Ascorbic acid is known to be present in neurons at high concentration [468, 469]. Cu^{2+} ions (85 μM $CuCl_2$) were reduced to Cu^+ through the addition of 10 mM Na-Ascorbate to 25 mM Tris-HCl, pH 7.0 (ascorbate ions were present in excess relative to Cu^{2+} ions at a ratio of 120:1) [374, 470]. A thin layer of mineral oil was added on top of the sample to ensure changes in the resonances of methionine residues were attributed to interactions with Cu^+ and not to air oxidation effects.

2.12 Heteronuclear single quantum coherence (HSQC) experiments - Aptamer interactions

A series of ^1H-^{15}N heteronuclear single quantum coherence (HSQC) spectra were recorded of αSyn alone and in the presence of the DNA sequences 65ntSeq and R12S91, at various molar ratios: αSyn:65ntSeq at ratios 1:0 (50 μM αSyn, 96 scans), 1:1 (100 μM αSyn to 100 μM 65ntSeq, 64

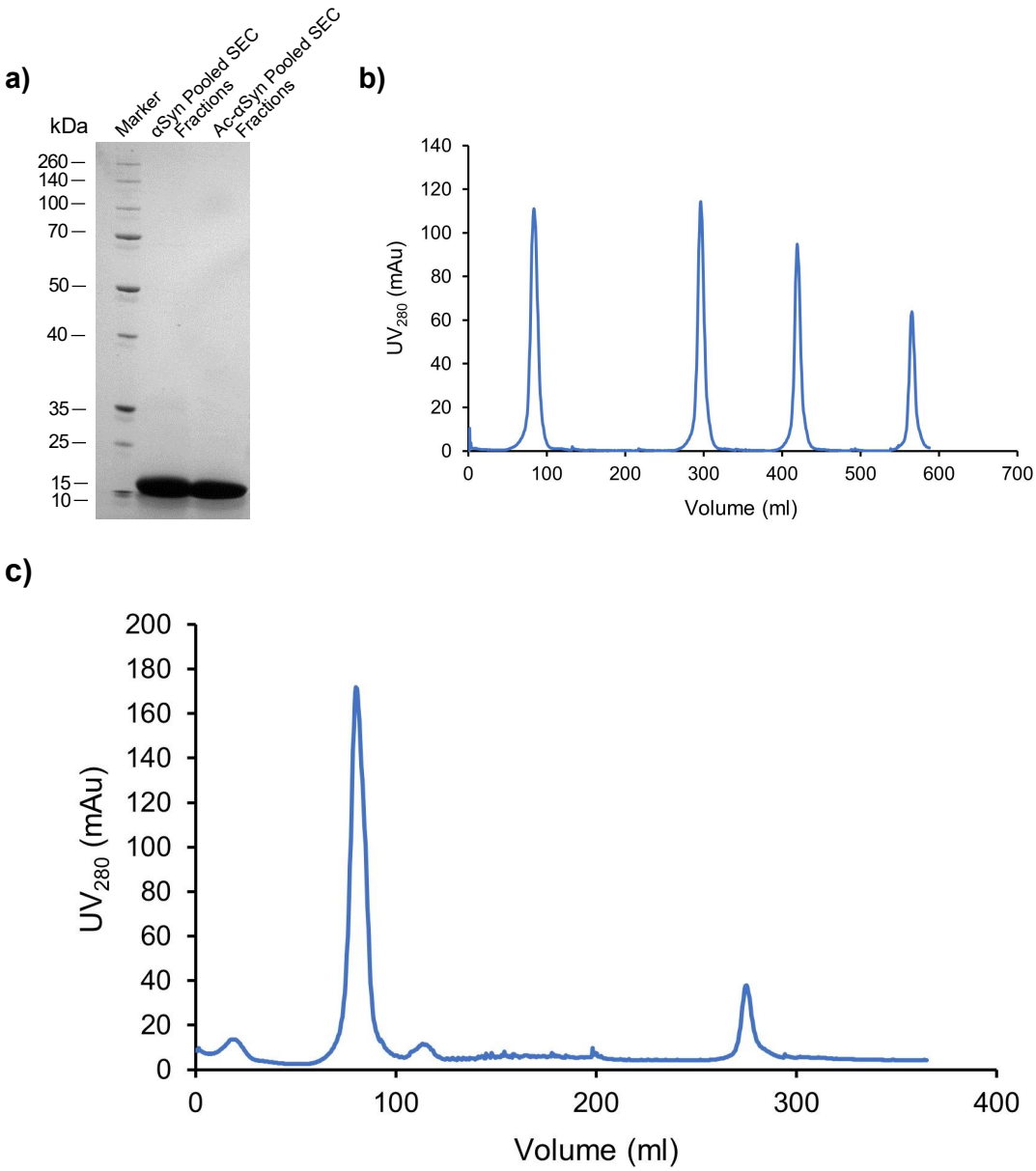


Figure 2.6: SEC Purification of αSyn and Ac-αSyn. a) Pooled fractions from the SEC purification of αSyn and Ac-αSyn prior to concentration showing very pure bands of the proteins of interest (14 kDa), as run on a 12% polyacrylamide gel. The 10 and 15 kDa marker bands have not correctly separated and appear as almost a unique band. b) SEC chromatogram for αSyn, showing in blue the UV absorption at 280 nm. Protein was purified in four batches, corresponding each of them to one of the single absorption peaks. Sample came out of the column at the expected volume, as advised from the manufacturer's column calibration curve and the molecular weight of the protein. c) SEC chromatogram for Ac-αSyn, showing in blue the UV absorption at 280 nm. Protein was purified in two batches, corresponding each of them to the two largest absorption peaks. Sample came out of the column at the expected volume, as advised from the manufacturer's column calibration curve and the molecular weight of the protein.

scans) and 1:3 (50 μM αSyn to 150 μM 65ntSeq, 96 scans); αSyn:R12S91 at ratios 1:0 (125 μM αSyn, 16 scans), 1:2 (125 μM αSyn to 250 μM R12S91, 16 scans), 1:4 (62.5 μM αSyn to 250 μM R12S91, 32 scans), 1:6 (41.5 μM αSyn to 250 μM R12S91, 48 scans), 1:8 (31.25 μM αSyn to 250 μM R12S91, 64 scans) and 1:10 (25 μM αSyn to 250 μM R12S91, 80 scans). Samples were dissolved in ABB, 10% D_2O. The experiments were performed at 298K using a 800 MHz Bruker spectrometer with a triple resonance HCN cryo-probe (Bruker, Coventry, UK). Internal chemical shift referencing was done using D_2O. Mean weighted chemical shift (MWCS) profiles were calculated as $\sqrt{[(\Delta\delta^1\text{H})^2+(\Delta\delta^{15}\text{N}/10)^2]}$. For the intensity ($I/I_0$) and MWCS analyses, only well-resolved and unambiguously assigned cross-peaks were used. Residue resonances of the ^{1}H-^{15}N spectra were assigned using cross-speaks generated from three-dimensional HNCACB and HN(CO)CACB experiments. Resonance assignment was done with the help of previously available literature resonance lists [115].

Experiments were measured as data matrices composed of 2048 (t_2, ^{1}H), x 220 (t_1, ^{15}N) complex points. Spectral widths: 2270.948 Hz (28.0 ppm) ^{15}N, 12820.513 Hz (16.0 ppm) ^{1}H; time domain size: 168 for ^{15}N, 2048 for ^{1}H; window function used for processing in both ^{15}N and ^{1}H dimensions was qsine; HSQC pulse sequence: BRUKER hsqcetf3gpsi2; recycle delay, d1: 1s. Data were acquired and processed with TopSpin 3.2.0 (Bruker, AXS GmbH, DE), and analysed using the CCPNmr v2.0 Analysis software [471].

2.13 Heteronuclear single quantum coherence (HSQC) experiments - Metal interactions

2D ^{1}H-^{15}N HSQC experiments were recorded at 283K using αSyn and Ac-αSyn at a concentration of 415 μM dissolved in 25 mM Tris-HCl pH 7.0, 10% D_2O, alone and in combination with 10 mM $CaCl_2$, 2.1 mM $ZnCl_2$, 85 μM $CuCl_2$ and 55 μM $MnCl_2$. Mean weighted chemical shift (MWCS) profiles were calculated as $\sqrt{[(\Delta\delta^1\text{H})^2+(\Delta\delta^{15}\text{N}/10)^2]}$. For the intensity ($I/I_0$) and MWCS analyses, only well-resolved and unambiguously assigned cross-peaks were used. Residue resonances of the ^{1}H-^{15}N spectra were assigned using cross-speaks generated from three-dimensional HNCACB and

HN(CO)CACB experiments. Resonance assignment was done with the help of previously available literature resonance lists [115].

Experiments were recorded as data matrices consisting of 2048 (t_2, ^{1}H) × 220 (t_1, ^{15}N) complex points and 8 scans, using a Bruker 800 MHz spectrometer equipped with a triple resonance HCN cryo-probe (Bruker, Coventry, UK). Internal chemical shift referencing was done using D_2O. Spectral widths: 2270.948 Hz (28.0 ppm) ^{15}N, 12820.513 Hz (16.0 ppm) ^{1}H; time domain size: 168 for ^{15}N, 2048 for ^{1}H; window function used for processing in both ^{15}N and ^{1}H dimensions was qsine; HSQC pulse sequence: BRUKER hsqcetf3gpsi2; recycle delay, d1: 1s. Data were acquired and processed with TopSpin 3.2.0 (Bruker, AXS GmbH, DE), and analysed using the CCPNmr v2.0 Analysis software [471].

2.14 Phase-modulated CLEAN chemical exchange (CLEANEX) NMR experiments

CLEANEX measurements probe the chemical exchange between the solvent water molecules and the protein labile amide protons, thereby reporting on the extent of exposure of the protein to the solvent [459, 460]. Measurements were recorded at 283K, a condition that allows the observation of ^{1}H-^{15}N resonances with excellent signal-to-noise in HSQC spectra of αSyn. Experiments were recorded of αSyn and Ac-αSyn (415 μM) upon incubation with 10 mM $CaCl_2$, 2.1 mM $ZnCl_2$, 85 μM $CuCl_2$ and 55 μM $MnCl_2$, in 25 mM Tris-HCl pH 7.0, 10% D_2O. Residue resonance assignments were done in the same way as for HSQC experiments. CLEANEX provides an estimation of the hydrogen-hydrogen exchange rates for each residue from the slope of the linear interpolation of the intensities of amide peaks obtained from spectra recorded at different mixing times, τ_m (5, 10, 15, 20, 25 ms).

The volumes, V_i, of the peaks were normalised by dividing the residue peak volumes obtained at each recorded mixing time by the ^{1}H-^{15}N HSQC residue peaks of the same sample, V_0, to obtain V_i/V_0. By plotting V_i/V_0 as a function of τ_m, the rate constant of chemical exchange, k_{ex}, can be defined from the slopes of the linear interpolation, which are of the form $y = m\tau_m$, where y represents

V_i/V_0, m the slope (k_{ex}) for that particular residue, and τ_m the mixing time. The function is forced through the origin and so the y-intercept is null. k_{ex} values were normalised with theoretical values for the intrinsic chemical exchange rates for each residue (k_{int}) determined from the protein sequence [472] by calculating the ratio of k_{int}/k_{ex}, assuming that the polypeptide chain is in a random coil conformation.

The logarithm of k_{int}/k_{ex} returned the protection factor, log$P$, for each residue as a measure of solvent exposure. Error bars represent the fitting error in the calculation of the k_{ex} for each residue based on the deviation of the recorded data from the calculated line of best fit $y = m\tau_m$, whose slope corresponds to k_{ex}. By adding these error values to and subtracting from each calculated k_{ex} rate, upper and lower boundaries for the k_{ex} of each residue amide hydrogen were established, which were then converted into protection factors as mentioned above. To calculate the effect of metal ion binding on the extent of solvent exposure of αSyn, the protection factor of the residues of αSyn in the absence of metals were subtracted from that in the presence of the different metals investigated. The combined protection factor errors for each residue were then calculated as the sum of the difference between the upper and lower protection factor limits of both conditions, and were presented in the form of error bars. Analysis of the data and calculation of the protection factor profiles were carried out in Microsoft® Excel.

NMR measurements were carried out using a Bruker 800 MHz spectrometer equipped with a triple resonance HCN cryo-probe (Bruker, Coventry, UK). Internal chemical shift referencing was done using D_2O. CLEANEX experiments were performed using a data matrix consisting of 2048 (t_2, ^{1}H) × 220 (t_1, ^{15}N) complex points and 64 scans. Spectral widths: 2270.948 Hz (28.0 ppm) ^{15}N, 12820.513 Hz (16.0 ppm) ^{1}H; time domain size: 168 for ^{15}N, 2048 for ^{1}H; window function used for processing in both ^{15}N and ^{1}H dimensions was qsine; CLEANEX pulse sequence: BRUKER fhsqccxf3gpph; recycle delay, d1: 1s. NMR spectra were acquired and processed using TopSpin 3.2.0 (Bruker, AXS GmbH, DE), and analysed with CCPNmr v2.0 [471].

2.15 Transverse and longitudinal relaxation NMR experiments

^{15}N R_1 and R_2 relaxation experiments were acquired using standard pulse sequences [473], including the watergate sequence [474] to enhance water suppression. T_1 and T_2 values were obtained by fitting the data to an exponential decay function with single relaxation delays (T_1 τ delays: 4, 30, 70, 120, 200, 300, 400, 500, 700, 1000 ms; T_2 τ delays: 0, 20, 40, 50, 60, 80, 100, 120, 140, 160, 170, 200 ms). Relaxation was measured at 283K on samples of Ac-αSyn (415 μM) in 25 mM Tris-HCl pH 7.0, 10% D_2O, incubated with the five different types of metals considered in this research (10 mM $CaCl_2$, 2.1 mM $ZnCl_2$, 85 μM $CuCl_2$ and 55 μM $MnCl_2$). Relaxation measurements of free protein were performed in the presence of 1 mM EDTA in the buffer. Resonance assignments were done in the same way as with CLEANEX measurements.

Relaxation data were analysed in a similar way to CLEANEX data. Briefly, the intensities, I_i, of the residue peaks were normalised by diving I_i obtained for each residue at the different time delays investigated, by the intensity, I_0, of each corresponding residue peak recorded at the shortest time delay (i.e., 4 ms for T_1 and 0 ms for T_2) to calculate the intensity change ratio, I_i/I_0. This was plotted vs. τ to obtain an exponential decay function in the form of $y= A\exp^{-\tau/T}$ or $y= A\exp^{-R/\tau}$, where y corresponds to I_i/I_0, A corresponds to the y-intercept, τ is the applied time delays, T is the time relaxation constants, and R is the relaxation rates.

The recorded data were fitted to the exponential decay function and a curve of best fit was calculated. Deviation of the data from the calculated curve of best fit was reported as standard error. Relaxation rates at each condition were shown by plotting R_1 and R_2 rates against residue number along the protein sequence. Error bars were computed with the standard error of the fitting to the exponential decay function from the calculation of R_1 and R_2 for each residue. Analysis of the data was carried out in Microsoft® Excel.

Experiments were recorded using a Bruker spectrometer operating at a ^{1}H frequency of 800 MHz equipped with a triple resonance HCN cryo-probe (Bruker, Coventry, UK). Internal chemical shift

referencing was done using D_2O. Experiments were recorded as data matrices consisting of 2048 (t_2, ^{1}H) × 220 (t_1, ^{15}N) complex points in 8 scans. Spectral widths: 2270.948 Hz (28.0 ppm) ^{15}N, 12820.513 Hz (16.0 ppm) ^{1}H; time domain size: 256 for ^{15}N, 2048 for ^{1}H; window function used for processing in both ^{15}N and ^{1}H dimensions was qsine; pulse sequence for T_1 and T_2 HSQC series, respectively: BRUKER hsqct1etf3gpsi and hsqct2etf3gpsi; recycle delay, d1: 1s. NMR data were acquired and processed using TopSpin 3.2.0 (Bruker, AXS GmbH, DE), and analysed with CCPNmr v2.0 [471].

2.16 Error analysis

Variation in the data from ELONAs is given as standard error, which is a statistical measure of the uncertainty of the mean. The values given for the standard error in the reported dissociation constants describe how accurate the mean of a particular k_d compares to the true k_d value. A low standard error shows that the calculated k_d is a more accurate representation of the recorded data. Given that sample size is inversely proportional to standard error, ELONA data were recorded as a set of three technical replicates to minimise standard error and provide a more accurate k_d value. Data analysis and error calculation were done using Origin 2020 (OriginLab Corporation).

Error in the CLEANEX and relaxation data is provided in the form of error bars, which was computed with the standard error obtained from the fitting of the data to the calculated lines of best fit, as described in more detail in sections 2.14 and 2.15. The analysis and error calculation of NMR data were carried out in Microsoft® Excel.

2.17 Theoretical background of NMR

In this thesis, a brief overview of the principles behind biomolecular NMR and its advantages for the study of proteins is given. Please refer to [475] and [476], as well as reviews [477], [478] and textbook [479] for a detailed explanation of the fundamental concepts of NMR.

NMR is a physical phenomenon that relies on the resonance transition between different magnetic

energy states when atomic nuclei are placed in an external magnetic field and a pulse of electromagnetic radiation frequency is applied. Atomic nuclei are associated with the intrinsic quantum property of spin, which means that they rotate around a given axis with a spin angular momentum vector. The most common atomic nuclei dealt with in protein NMR (i.e. ^{1}H, ^{15}N and ^{13}C) have spin= ½ [476]. Isotopic labelling of proteins with carbon-13 and nitrogen-15 is required to enhance the intrinsically low sensitivity of the NMR measurement that would otherwise be recorded using the naturally abundant carbon-12 and nitrogen-14. As with all charged particles, moving nuclei will produce a magnetic field. This makes nuclei behave like magnetic dipoles associated with a magnetic moment that is related to the intrinsic angular momentum of that nucleus. These magnetic moments, which can be thought of as vectors with both magnitude and direction, will be randomly aligned in the ground state in the absence of an external magnetic field, meaning that the bulk magnetisation arising from that nucleus will be zero (Figure 2.7). However, when these nuclei are placed in an external magnetic field (typically denoted as B_0), they may align either with (low energy) or against (high energy) the field and result in a non-zero bulk magnetisation [475, 476].

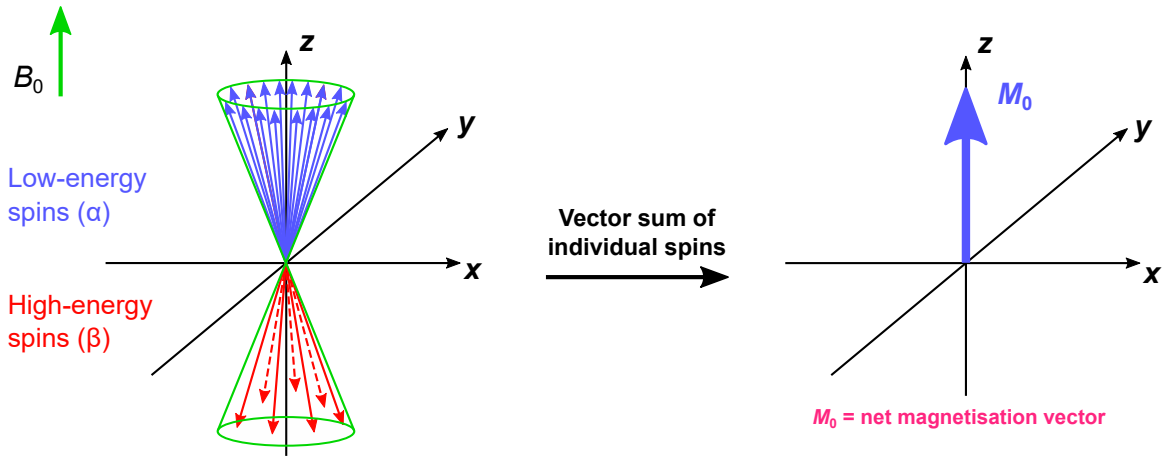


Figure 2.7: Bulk magnetisation of nuclei containing spin ½ at equilibrium in an external magnetic field, B_0. A slightly higher proportion of low-energy (α) states precess randomly in the direction of an externally applied magnetic field, and a smaller proportion of spins at high-energy states (β) precess in the opposite direction to the applied magnetic field. The sum of the spin vector contributions yields a bulk magnetisation, M_0, along the z axis.

The rotating nuclei will precess around the axis of the applied external magnetic field vector in any direction, in what is described as Larmor precession. This is an intrinsic property of a given nucleus and is proportional to the size of the magnetic field. The application of a magnetic field splits the energy levels and forces the nuclei into energy states that are either aligned parallel or anti-parallel with

the external magnetic field. This phenomenon is known as Zeeman splitting. Nuclei are described as having $2I+1$ nuclear energy levels when placed in an external magnetic field, where I stands for the spin of a given nucleus (Figure 2.8). Those spins which align with the magnetic field will be associated with a lower energy, and those aligned against the magnetic field will have a higher energy. The magnitude of the splitting between the different spin states is dependent on the strength of the magnetic field. Therefore, the application of an external magnetic field gives rise to distinct energy levels populated by spins with the same angular momentum. For nuclei with spin ½, which is the case for the most relevant nuclei concerning protein NMR, two spin states exist: spin -½, aligned with the external magnetic field (lower energy state), and spin +½, aligned against the external magnetic field (higher energy state) [475]. In fact, the energy difference between these two states is very small and thermal energy arising from atomic collisions is enough for spins to transition from a lower energy to a higher energy state. The distribution of the nuclei in the different energy levels is described by the Boltzmann distribution, which denotes the relationship between energy and temperature. At room temperature, the population of nuclei in the lower energy state outnumbers that in the higher energy state. Therefore, in a sample with many nuclei, each having a different magnetic moment aligned with or against the external magnetic field, the resulting component of the magnetic moment of the precessing nuclei is a vector in the direction of the axis of the applied field.

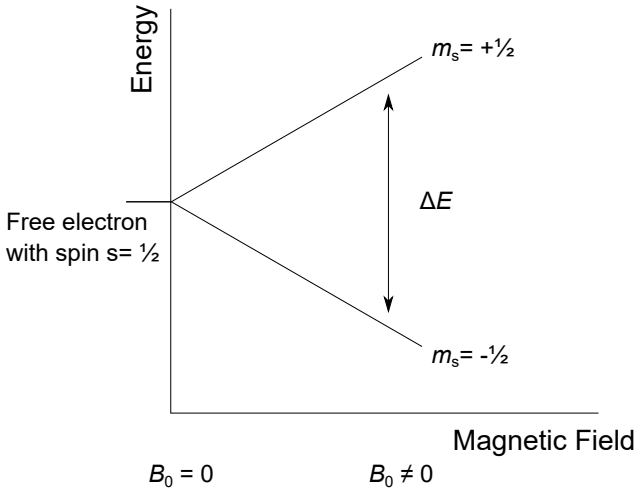


Figure 2.8: Zeeman Splitting. The energy gap, ΔE, between spin states, m (in this case +½ and -½), is directly proportional to the strength of the magnetic field, B_0.

The bulk magnetisation in the z plane cannot be observed and needs to be transferred perpendicularly to the xy plane. By applying a 90° pulse of electromagnetic (EM) radiation with a specific frequency

equalling the Larmor frequency of the precessing nuclei, the bulk magnetisation will be directed to the y plane. If the frequency of the EM pulse (Larmor frequency) matches the energy between the two different spin energy levels, this will induce a transition of the nuclei to the higher energy state in a resonance effect [475, 479]. The rotation of the bulk magnetisation will induce an electric current which will be recorded as a signal of the spectral absorption of the sample nuclei.

After the application of a pulse of radio frequency, the bulk nuclear magnetisation perpendicular to the magnetic field will decrease and return to the z axis to the direction of the external magnetic field. This will be detected as a fluctuating declining amplitude with time from which a frequency and decay rate can be calculated, which is referred to as the free induction decay (FID). A Fourier transform is then applied, which converts the FID as a function of time to frequency data, which is how it is then displayed in NMR spectra [479].

When an external magnetic field is applied to a nucleus, the surrounding electrons will induce local electric currents which will produce an alternative magnetic field (according to Lenz's law) that will oppose the applied external field. The extent of the external magnetic field that acts on any given nuclear magnetic moment will therefore depend on the strength of the locally opposing induced field, in a phenomenon known as shielding effect. The strength of this effects depends on the size of the external field, as well as the chemical and geometrical structures of the molecule. This shielding will therefore reduce the effective external magnetic field experienced by the nuclei to different extents, causing their magnetic moment to precess at different angular velocities, which explains the different resonance values associated with different nuclei. The chemical shift of a given nuclear spin is described as its resonant frequency in an external magnetic field. It is therefore the result of the shielding and deshielding effects (although the shielding effects will always be greater in magnitude than the deshielding).

Given that this shielding effect reduces the effective applied magnetic field experienced by the spins, the difference in their energy levels is also reduced and the resonant frequency decreases. This results in a decrease in the recorded chemical shift for a given nucleus. The recorded FID will therefore

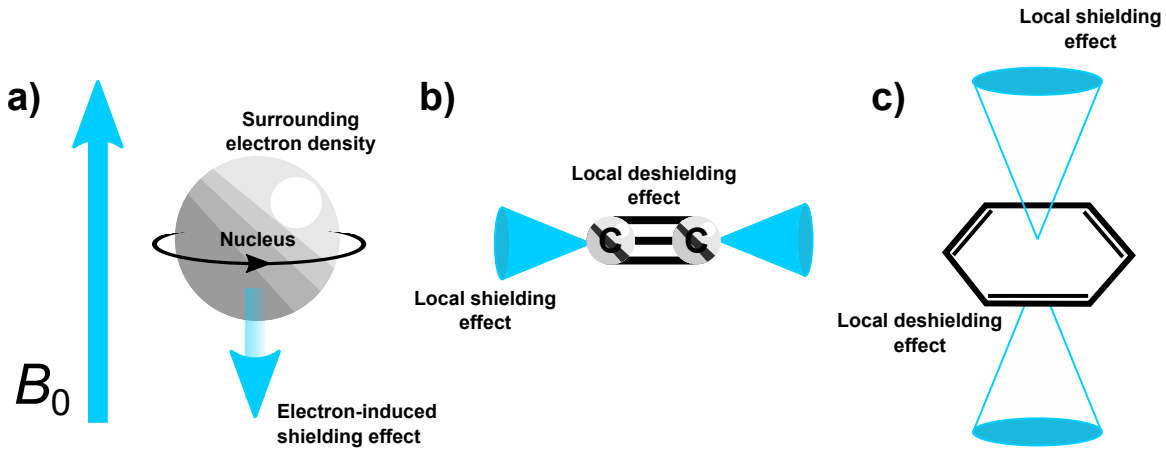


Figure 2.9: Shielding effects and their influence in chemical shift. a) Shielding of the nucleus by the outer electron shell. The electronic environment around the nucleus generates an opposing magnetic field to the magnetic field applied, B_0, thereby lowering the chemical shift of the nuclear species. b, c) Chemical anisotropic effects in different chemical groups. The geometry of chemical bonds restricts the movement of electrons, thereby creating opposing shielding magnetic fields that are non-uniform (illustrated as blue cones). If a nearby proton is in close proximity to the generated shielding field, the effect of the external magnetic field on it will be reduced and it will therefore experience a lower chemical shift (b). On the other hand, if it is found outside the neighbouring generated opposing magnetic field, it will experience a deshielding effect and will therefore have a higher chemical shift (c). In this way, the spatial organisation of different electron-induced magnetic fields will determine the chemical shift landscape of a system.

have several resonant frequency components and the Fourier transform will produce signals for the individual nuclei with different resonance properties. In order to allow the comparison of NMR spectra recorded at different external magnetic fields, resonance frequencies are readjusted using the spectrometer frequency and reported in parts per million, ppm [475]. In this way, the dependency on chemical shift is removed, and can instead be quoted as a relative quantity in comparison to a standard reference (e.g. tetramethylsilane in ^{13}C and ^{1}H NMR experiments performed in organic solvents, or liquid NH_3 in ^{15}N protein NMR). NMR signals coming from ^{1}H (protons) can be displayed against their respective recorded frequencies in the simplest form of NMR spectrum, a 1D spectrum. In fact, this provides a very quick way to follow the folding process of a protein or even look for global changes in the conformation of a protein upon ligand binding [475, 476].

Another factor affecting the observed chemical shifts is magnetic anisotropy. Electrons in chemical groups affect the shielding of nuclei in the proximity following the same principle as the shielding effect seen with atomic shell electrons. However, bonded electrons are not free to move and so the

shielding effect they produce is described as not being uniform, or anisotropic (Figure 2.9). The fields generated by this anisotropic phenomenon are typically depicted by cones. If a nucleus is present within the cone, it will see a reduction in its chemical shift in the same way as it happens with atomic electron shielding. If a nucleus is located outside of the cone, however, deshielding of that nucleus occurs and its associated chemical shift increases. For instance, a nucleus located in the vicinity of an electron-dense aromatic ring will experience a strong shielding effect, causing a drastic decrease in chemical shift. This is frequently observed with methyl protons in the core of folded globular proteins, whose chemical shift might fall below zero ppm when they are in close proximity to an aromatic ring side chain. This effect is commonly searched for on a 1D spectrum when assessing the folding of a protein. Similarly, molecular interactions might also have an effect on the strength of the chemical shift of a given nucleus. Hydrogen bonding causes protons involved to be associated with higher chemical shift values. Strong electronegative groups may drag electrons away, effectively deshielding the nearby nuclei and causing their shifting to higher frequencies. Solution parameters like temperature, pH and ionic strength, which determine the strength of molecular interactions, therefore also influence the resonant frequencies of nuclei.

Since the recorded chemical shifts are an average of the chemical states experienced by the nuclei in a protein during signal measurement, protein dynamics in the millisecond timescale will have an effect on the observed frequencies, either as a result of fluctuations in the electronic environments or conformational changes in the structure of the protein. As a result of the many factors affecting their magnitude, chemical shifts are considered exquisite probes of protein structure and dynamics.

2.17.1 ^{1}H-^{15}N experiment

The duration of the excited state before the signal relaxes and the equilibrium of a nuclear moment is re-established can extend up to the millisecond and second timescales [476]. This effect is exploited by complex heteronuclear NMR experiments, which have been developed to record the resonance frequency of multiple correlated nuclei by allowing the transfer of magnetisation through bond and space [475, 476]. By employing these kinds of experiments which involve different nucleus types, we can obtain information about the local environment of particular amino acid residues or atoms

within a protein [476, 480]. Signal intensities measured in such experiments involving more than one nucleus type are commonly displayed using a 2D ^{1}H-^{15}N HSQC spectrum [476]. This experiment, which is generated through the transfer of magnetisation between the H and N atoms of amide groups, is described as the "protein fingerprint" as a result of its versatility in informing about the properties of the constituting amino acids in a given protein. In this spectrum, each peak represents the backbone amide of each amino acid residue (except proline, which lacks an amide -H), as well as the side chain amides of asparagine, glutamine, lysine and arginine when working at low pH, and the tryptophan indole [476]. Each peak is associated with an intensity and chemical shift value, which provide very precise probes that enable the quantitative analysis of many protein parameters. Particularly important in the study of IDPs, the degree of disorder can be estimated through the peak dispersion in the ^{1}H dimension, with IDPs showing a narrower and restricted dispersion in this dimension compared to folded globular proteins. This is due to nuclei in disordered proteins experiencing an almost identical chemical environment given their intrinsic structural flexibility [481, 476, 480].

2.17.2 NMR for IDPs

For the study of IDPs like αSyn, NMR is an incredibly valuable tool that provides exquisitely sensitive detail on residue-specific information at an atomic resolution. Indeed, it is a powerful technique to probe the structure, interactions and dynamics of proteins in their native state, without the need for chemical modification [482].

Compared to natively folded globular proteins, which are characterised by defined structural features with little dynamic range, disordered proteins lack instead rigid atom positions and dihedral angles, with no major energy minima in their conformational landscape. Indeed, the dynamic conformational nature of IDPs and the small size of many of them renders X-ray crystallography and cryo-EM studies impractical at studying these proteins. Curiously, the intrinsic properties of IDPs resolve some of the constraints of NMR as a tool for structural biological studies. The fast dynamics that characterise IDPs overcome the size limitation observed in the study of globular proteins, whose slow molecular tumbling leads to extensive peak broadening and low-resolution spectra after sample size exceeds approximately 40 kDa. For this reason, the only real limitation to the study of disordered proteins

with NMR becomes the crowding of peaks in spectra, which can be addressed through selective labelling and multidimensional experiments. Likewise, information coming from traditional methods for the study of folded globular proteins by NMR including dihedral angles, distances from Nuclear Overhauser Effects (NOEs) or ^{3}J couplings [483] are unsuitable for probing disordered proteins.

Instead, information from chemical shift, intensities [484] and residual dipolar couplings [485, 486] have proved important observables to study disordered systems. These are particularly useful in probing long-range intramolecular interactions [47] and residual local secondary structure [487]. Other NMR techniques that are routinely used to discern the interactome of IDPs include paramagnetic relaxation enhancement (PRE) [488] and chemical shift saturation transfer (CEST) experiments [489], which can provide information on the conformation of key residues involved in the interaction with other molecules.

2.17.3 Residue resonance assignment

The assignment of protein backbone resonances can be addressed by using a combination of 2D and 3D NMR experiments. In this way, the preferred approach involves using a 2D ^{1}H-^{15}N HSQC spectrum that serves as the fingerprint of the protein, whilst having a set of complementary 3D spectra reporting resonances connecting the backbone amide proton, nitrogen and carbon atoms [490]. The 3D experiments can be visualised as "strips" through the third dimensional space, containing the carbon resonance corresponding to a given peak in the 2D HSQC spectrum (Figure 2.10). Essentially, the combination of adjacent strips in the third dimension of sequential residues "i" and "i-1", where i refers to a given peak in the HSQC spectrum, allows the sequential assignment of the protein residues. In the case of the work presented in this thesis, HNCACB and HN(CO)CACB 3D experiments were recorded for the assignment of the αSyn protein, which provide complementary peaks for C_α and C_β atoms of both "i" and "i-1" (Figure 2.11). Alternatively, the combination of HNCA/HN(CO)CA experiments is also often used, which in this case provide peaks for only C_α atoms of residues "i" and "i-1".

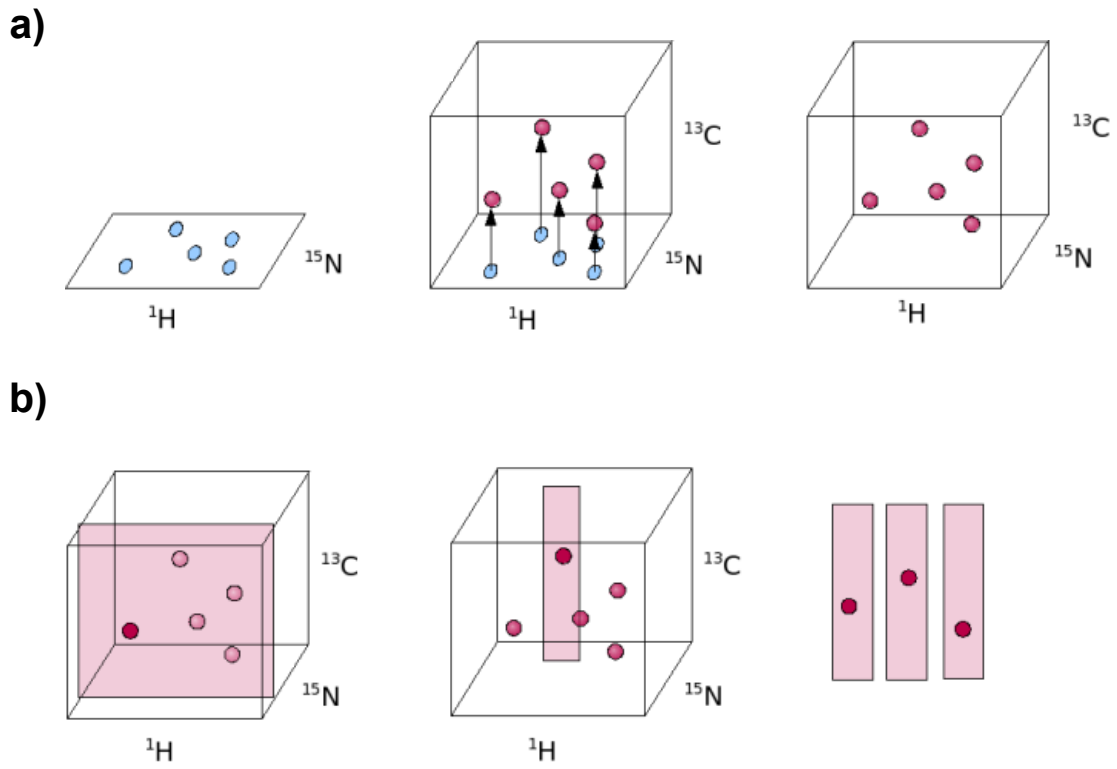


Figure 2.10: 3D spectra from ^{1}H-^{15}N HSQC. a) A new evolution time can be added to the pulse sequence of the ^{1}H-^{15}N HSQC to allow the magnetisation to be transferred from the ^{15}N to a given ^{13}C atom from the backbone or from the side chain of residue "i-1" or simultaneously of residues "i" and "i-1". b) Strips of the ^{13}C dimension from a 3D experiment can be extracted from single cross-peaks from a ^{1}H-^{15}N HSQC spectrum, thereby connecting the resonances of ^{1}H, ^{15}N and ^{13}C atoms associated with a given peak in a ^{1}H-^{15}N HSQC spectrum. Figure adapted from [490].

2.17.4 Protein-ligand interactions by NMR

Given that chemical shifts are very precise probes of changes to the local chemical environment of a nucleus, NMR can report on very subtle alterations that occur in the conformation of proteins and chemical exchange. This might happen if the protein undergoes exchange between two specific conformations, or if there is protein-ligand binding occurring [491, 476].

If an interacting ligand is in slow exchange with the protein, NMR signals will observe two different species, i.e. a bound and a free form. This kind of slow-exchange processes take place when the exchange rate (k_{ex}) between the two species or conformations is smaller than the chemical shift difference ($k_{ex} \ll \Delta\omega$) [491, 476]. If the rate constant increases, magnetisation is quickly transferred

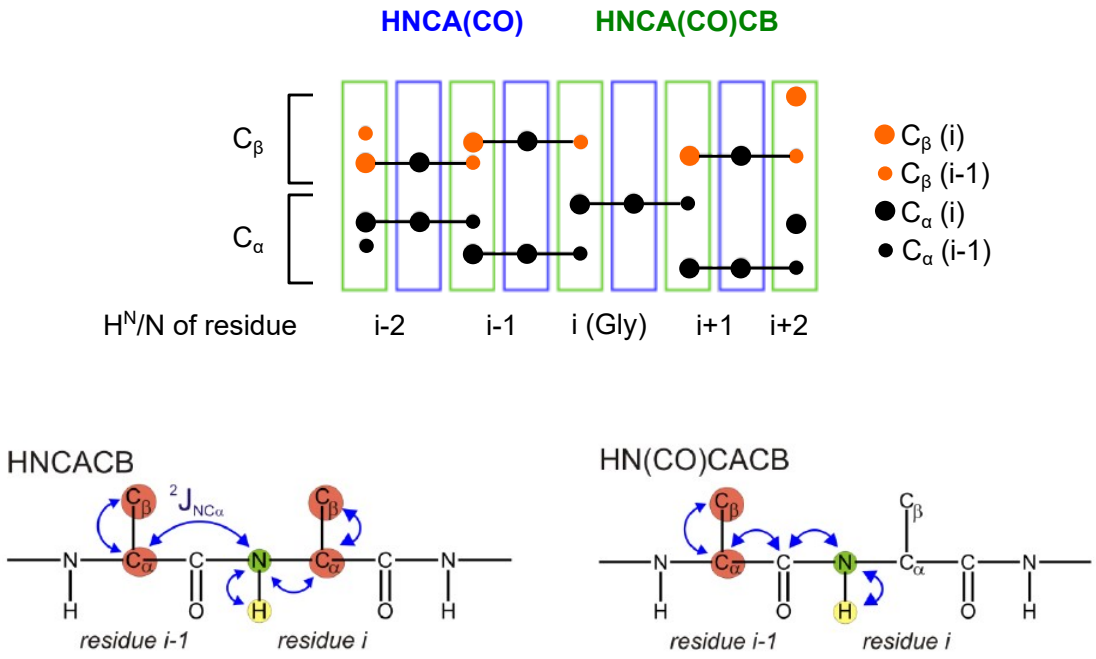


Figure 2.11: 3D Backbone assignment. HNCA(CO) and HNCA(CO)CB are considered here as an experiment pair. HNCA(CO) (blue strips) links the resonances of the amide ^{1}H and ^{15}N spectrum of residue "i" with the resonances of C_α and C_β atoms of residue "i-1". HNCA(CO)CB (green strips) links the resonances of the amide ^{1}H and ^{15}N spectrum of the residue "i" with the resonances of residue C_α and C_β atoms of residues "i" and "i-1". C_α and C_β atoms are recorded as having opposite phases. An example of a backbone resonance assignment is given, with black lines connecting corresponding C_α and C_β resonances of consecutive residues along the polypeptide sequence. Figure adapted from [490].

from one conformational state to the other and will become invisible to detection. This leads to a signal broadening effect which can lead to the signal disappearing.

At higher exchange rates larger than the difference in the chemical shift frequencies of both conformational species ($k_{ex} \gg \Delta\omega$), a single peak will appear as an average of both conformations, whose position will proportionately represent the time the magnetisation spends on each state (Figure 2.12). In this fast-exchange regime, NMR peaks will shift with increasing concentration of ligand added and will display intense peaks and sharp linewidths. This allows the fitting of NMR titration curves to theoretical binding expressions, to calculate on- and off- rate constants of ligand binding. In contrast to a slow-exchange mode, fast exchange will be observed as a shifting peak through a spectrum, and not as two peaks corresponding to two interconverting states. A single new peak will represent the formation of the protein-ligand complex state, whose intensity will increase with increasing ligand

concentration until all binding sites are occupied, and the disappearing of the peak representing the free protein state [491, 476].

Intermediate exchange between two conformations ($k_{ex} \approx \Delta\omega$) will be observed on an NMR spectrum as broadening peak linewidths.

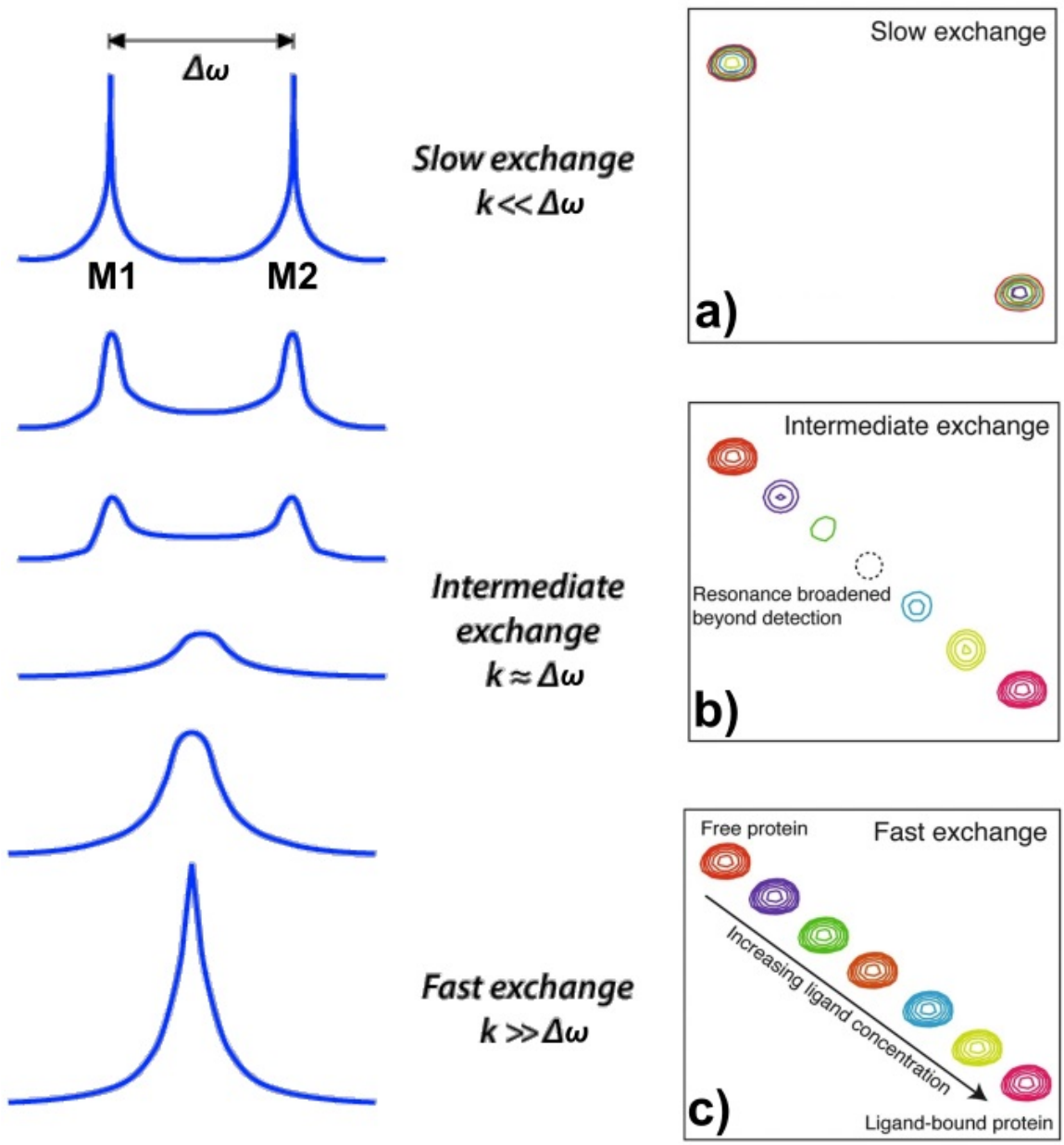


Figure 2.12: Representative spectra for two different molecules (M1 and M2) as a function of different exchange regimes. Slow (a), intermediate (b) and fast (c) exchange rates can often be encountered when studying protein-ligand interactions by NMR chemical shift titration experiments. For simplicity of this schematic, these ^{1}H-^{15}N HSQC NMR experiments are assumed to only show resonance cross-peaks of the protein, which is ^{15}N-labelled, and not of the ligand, which is unlabelled. Similarly, the concentration of the protein is assumed to remain constant and that of the ligand to increase until saturation of the protein is achieved. (a) In slow exchange ($k_{ex} \ll \Delta\omega$), changes in the intensities but not the chemical shifts of the cross-peaks corresponding to both the free and ligand-bound states can be detected, which are both simultaneously observed. (b) In intermediate exchange ($k_{ex} \approx \Delta\omega$), linewidth broadening of the signal occurs upon titration of the ligand as a result of transverse relaxation effects from conformational exchange between the free and bound states in equilibrium. (c) In fast exchange ($k_{ex} \gg \Delta\omega$), chemical shift perturbations of the protein resonances lead to a population-weighted average between the free and ligand-bound state chemical shifts. $\Delta\omega$ refers to the change in chemical shift of the protein peaks. Figure adapted from [492, 493].

2.17.5 Hydrogen exchange in proteins

In solution, the hydrogen atoms bound to protein backbone amides and side chains are labile and will exchange with hydrogen in the surrounding water molecules. For this to happen, any hydrogen bonds formed by these hydrogen atoms must be broken, which means that the exchange rate of hydrogen atoms with the solvent will depend on the rate in which they are perturbed.

Amide hydrogen exchange with the water solvent generally follows one of two kinetic mechanisms, EX1 (monomolecular exchange) or EX2 (bimolecular exchange) (Figure 2.13) [494, 495]. Some regions of a protein may follow EX1 and others EX2 exchange regimes, although one may dominate over the other based on the reaction conditions.

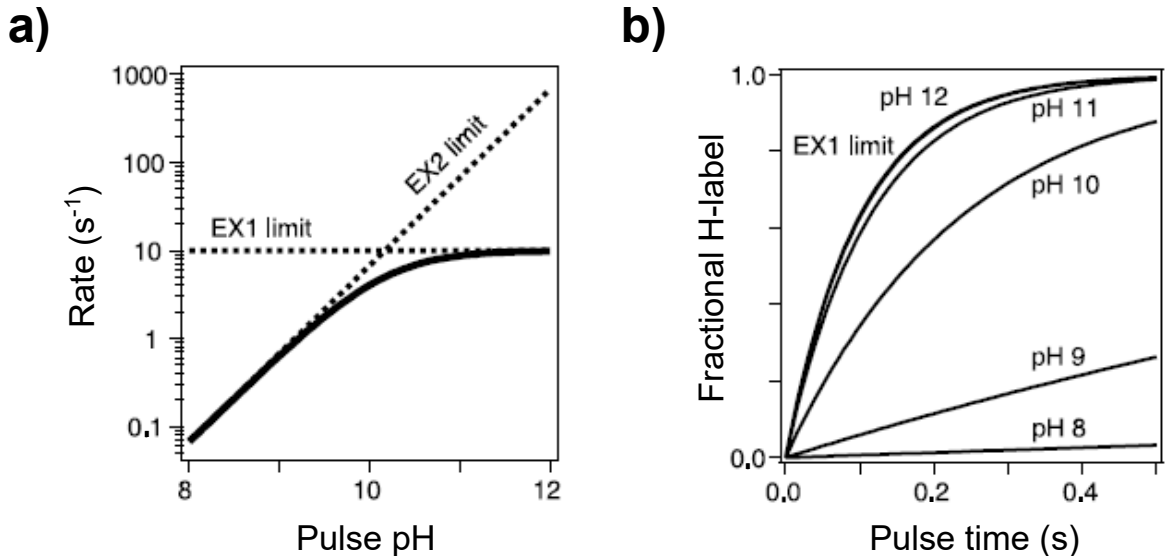


Figure 2.13: Hydrogen exchange EX1 (pH-independent) and EX2 (pH-dependent) regimes. The rate of hydrogen exchange increases 10-fold for each unit increase in pH under EX2 conditions, although it is ultimately limited by the rate of the opening reaction that exposes the hydrogens to the solvent for exchange. The limiting rate is reached under EX1 when $k_{ch} > k_{cl}$, meaning that every opening motion results in exchange and $k_{ex} = k_{op}$. Figure adapted from [495].

Linderstrøm-Lang proposed a 2-state model to explain hydrogen chemical exchange [496, 497, 495], with hydrogens either non-exchangeable in the protected state (NH (closed)) or susceptible to exchange in a transiently open conformation (NH (open)), where k_{op} and k_{cl} are the opening (unfolding) and closing (folding) rate constants, respectively:

$$\mathrm{NH\,(closed)} \underset{k_{cl}}{\overset{k_{op}}{\rightleftharpoons}} \mathrm{NH\,(open)} \xrightarrow{k_{ch}} \mathrm{H\,exchanged}$$

Essentially, this kinetic model can be broken down into two components [494, 498]: (1) a structural factor limiting the rate at which the protein undergoes conformational motions to overcome any barriers to permit exchange, and (2) a chemical factor responsible for the exchange rate of protons that are fully exposed to the solvent.

The rate of chemical exchange of unprotected amide hydrogens, k_{ch}, depends on a range of conditions, including pH, temperature, isotope effects and neighbouring amino acid side chains. Under steady-state conditions, the hydrogen exchange rate, k_{ex}, is determined by the following equation:

$$k_{ex} = \frac{k_{op} k_{ch}}{k_{op} + k_{cl} + k_{ch}}$$

where k_{ch} can be calculated separately for the unprotected amide. Assuming a stable structure ($k_{op} \gg k_{cl}$), the overall chemical exchange rate constant under steady-state conditions is given by equation:

$$k_{ex} = \frac{k_{op} k_{ch}}{k_{cl} + k_{ch}}$$

This equation can be applied in two particular cases: Under EX2 conditions, where $k_{cl} \gg k_{ch}$ (low temperature and pH), the exchange-competent and incompetent structures reach equilibrium quickly before the slower exchange step. The exchange rate in this case is given by:

$$k_{ex}{}^{EX2} = \frac{k_{op}k_{ch}}{k_{cl}} = K_{op}k_{ch}, \qquad K_{op} = \frac{k_{op}}{k_{cl}}$$

Where K_{op} is the equilibrium constant of the opening reaction.

EX2 regime describes the exchange in the native state or under mild denaturing conditions in a pH-dependent mode. Here, a pre-equilibrium state exists between open (exchange-susceptible) and closed (protected) conformations, and the observed exchange rate, k_{ex}, describes the rate constant for the base-catalysed chemical exchange, k_{ch}. Such a pre-equilibrium step is attributed to rapid changes between exchange-incompetent and exchange-competent conformations prior to chemical exchange, which are associated with protein local conformational fluctuations and global unfolding [499].

The stabilisation free energy of the protein structure can therefore be determined by:

$$\Delta G_{HX} = -RT\ln K_{op} = -RT\ln(k_{ex}/k_{ch})$$

Under EX1 conditions where $k_{cl} \ll k_{ch}$ (high temperature, high pH and low stability), the rate of exchange is limited by the opening rate of the protected protein structure, k_{op}, as it is pH independent.

$$k_{ex}{}^{EX1} = k_{op}$$

EX1, on the other hand, occurs at high temperature, high pH (pH $\geq$ 7) or high denaturant concentra-

tions. In these conditions, exchange is fast compared to the conformational motions that expose amide protons to the surrounding solvent, thereby making the slow processes of conformational opening or global unfolding dictate the observed exchange rate.

The ratio of the exchange rates k_{ch}/k_{ex}, also referred to as the protection factor for a particular residue, is a useful and common way of reporting hydrogen exchange results. Protection factors are a measure of the rate of exchange of a given backbone amide when it is in a fully solvent-exposed conformation (commonly obtained from model peptides or by modelling statistical coils) to the rate of exchange in a folded state. Protection factors therefore provide a measure of the resistance of amide protons to freely exchange with the solvent in folded structures relative to residue-specific intrinsic rates in a random polypeptide.

Typically, protection factor values range from less than 5 for backbone amide protons in fully denatured proteins to more than 10^5 for amides in folded protein cores. Protection factors obtained for αSyn (see Chapter 5) ranged from 6 to 8, which is indicative of the generally unfolded native state of the protein. The kinetic theory developed to describe the hydrogen exchange behaviour of proteins in solution was specifically based on folded globular proteins, which means that its application to disordered proteins may have its limitations. However, the fact that αSyn transiently samples partially structured conformations, the application of the simple kinetic model developed to describe hydrogen exchange becomes relevant to study changes to the global intramolecular long-range contacts of the protein [41].

Hydrogen chemical exchange can be closely monitored using NMR. Traditionally, this has been done by dissolving a protein sample in deuterium oxide, which will readily exchange with labile hydrogen atoms in the protein and will incorporate deuterium, ^{2}H, which is not detected by NMR at this frequency. Accordingly, spectrum peaks of hydrogen atoms undergoing hydrogen-deuterium exchange will reduce in intensity, thereby providing information on the stability of hydrogen bonds, local exposure to the solvent and hence protein dynamics.

NOESY and ROESY are NMR experiments which can provide information on the chemical exchange between the labile protons and the solvent. However, contributions from different magnetisation pathways can result in artefacts which can mask the detection of strict water-protein interactions, including NOE/ROE (Rotating-frame Overhauser Effect) peaks from $C_\alpha H$ protons with chemical shifts coincident with water, TOCSY-type interactions and NOE/ROE from rapidly exchanging side chain groups. To circumvent these challenges, phase-modulated CLEAN chemical exchange spectroscopy (CLEANEX-PM) has been developed to specifically detect water-macromolecule interactions [459, 460]. Magnetisation pathways suppress intramolecular NOE and ROE contributions as a result of the opposite signs of longitudinal and transverse cross-relaxation rates.

Here, water is selectively excited, while other spins outside the excitation profile are dephased by gradients during the mixing period. Chemical exchange between the excited water and labile NH protons then causes the magnetisation to be transferred to the protein, where detection happens (fast exchange rates in the 5–500 ms range). The application of CLEANEX therefore overcomes the limitations of hydrogen/deuterium (H/D) chemical exchange, which relies on the slow exchange in the s-min timescale regime of labile amide protons with deuterium atoms in a fully deuterated buffer.

2.17.6 NMR relaxation

Relaxation is a fundamental NMR phenomenon describing the loss of coherence of magnetisation along the xy plane, and the recovery of relaxation along the z axis. Essentially, coherent magnetisation in the xy plane after a pulse of radiofrequency will recover along the spin equilibrium position, as the external magnetic field forces the spins to align with it. This is known as T_1 relaxation. At the same time, coherence of the excited nuclei is lost, as the bulk magnetisation returns to equilibrium. This is referred to as T_2.

Spin-lattice (longitudinal) relaxation, or T_1, represents the time constant required for around 63% of the bulk magnetisation to return to its initial equilibrium position along the z axis. Field fluctuations (both magnetic and electric) can affect the magnitude of T_1. Therefore, phenomena that may result in alternating fields, such as chemical shift anisotropy, dipolar coupling and J-coupling, can provide

detailed information on the inter- and intra-molecular dynamics of a sample. Shorter relaxation time values will represent a more efficient relaxation process. Smaller biomolecules will have a faster tumbling rate in solution and will therefore experience shorter T_1 values than larger proteins and macromolecules, which will show long T_1 values as a result of restricted tumbling motions. At the same time, spin-spin (transverse) relaxation, or T_2, accounts for the loss in coherence between the excited nuclei as the bulk magnetisation returns to equilibrium. This effect results from the transfer of energy between neighbouring spins via dipole and exchange interactions. T_2 may be shorter or equal to T_1 [500, 501, 479].

Spin-lattice or longitudinal relaxation

T_1 represents the rate of transfer of energy from the nuclear spin system to the neighbouring molecules (the lattice). This relaxation happens in the z direction and leads to a restoration of the Boltzmann equilibrium.

As a result of the interactions with other nuclear spins as they tumble in solution, the individual magnetic moments constituting the magnetisation will experience slightly different local magnetic fields. These fields fluctuate in time (as a result of molecular tumbling), inducing random transitions between the NMR spin states which, in turn, cause the magnetisation to decay back to equilibrium along the xy plane through various mechanisms [479]:

- Dipolar mechanism: The magnetic moment associated with each spin gives rise to a magnetic field, which can interact with neighbouring spins. In any given pair of magnetically interacting nuclei, the field generated by one spin will be experienced by the second spin. In turn, the second nuclei will also generate a field which will be felt by the first spin, making this phenomenon a reciprocal interaction.

- Chemical shift anisotropy mechanism: As molecules tumble in solution, their orientation with respect to the external magnetic field B_0 will change. This will alter the magnetisation that is experienced by the molecules, which will appear as a randomly varying external magnetic field.

- Paramagnetic mechanism: The large magnetic moment associated with unpaired electrons in paramagnetic species (e.g., O_2) as a result of the large gyromagnetic ratios is particularly effective at promoting relaxation, which is experimentally observed as extensive linewidth broadening.

The most common source of induced local fluctuating fields for spin ½ nuclei is direct dipolar couplings. The rapid reorientation of the dipolar interactions as a result of molecular motions leads to fluctuating fields. Therefore, since this relaxation mechanism depends on the rate of molecular motion, T_1 is temperature dependent. For this reason, NMR experiments involving IDPs should be conducted at low temperatures. This interferes with the rate of relaxation by reducing molecular motion and tumbling, hence slowing down the decay of magnetisation back to equilibrium, resulting in longer T_1 times and sharp spectrum peaks. High experimental temperatures, on the other hand, enhance chemical exchange with the solvent of already highly dynamic IDPs, leading to short T_1 times and broader spectrum peaks.

Dipole-dipole relaxation mechanisms strongly depend on the inverse cube of the distance between the interacting nuclei, as well as on the direction of the combined vector of the two nuclei relative to that of the applied magnetic field. As molecules tumble in solution, the direction of this vector changes, making the magnetic field change too. Changes in the distance between neighbouring interacting nuclei will result in changes in the experienced magnetic field. In this way, changes in molecular orientation promote signal relaxation. Interacting pairs of nuclei can arise from within the same or different molecules, leading to intra- and intermolecular relaxation phenomena, although the closer physical proximity of nuclei within a given molecule makes intramolecular relaxation dominant.

The magnitude of a dipolar interaction is dictated by the product of the gyromagnetic ratios of the two interacting nuclei, making the resulting relaxation rate depend on the square of this [479]. Therefore, pairs of interacting nuclei with high gyromagnetic ratios are highly efficient at inducing relaxation. Relaxation induced by dipolar coupling is thus proportional to the square of the coupling:

$$\gamma^2{}_1\gamma^2{}_2\,\frac{1}{r_{12}^6}$$

Molecular motion and collisions continuously change the orientation of the spins in what is described as rotational diffusion. Correlation time, τ_c, which is the time taken for a molecule to rotate by 1 radian, describes the timescale of random molecular motion and is proportional to molecule size and solution viscosity. Large biomolecules have restricted motion and are associated with large τ_c. Smaller proteins present faster motions and therefore have shorter τ_c.

The relationship between the fluctuating magnetic fields and τ_c is represented by the spectral density [479], which describes how much the random fields are fluctuating at each frequency, ω:

$$j\omega = \frac{2\,\tau_c}{1 + \omega^2\tau^2}$$

The key frequency to consider in relaxation is the Larmor frequency, ω_0:

$$j\omega_0 = \frac{2\,\tau_c}{1 + \omega_0^2\tau^2}$$

By differentiating this equation with respect to τ_c, it becomes apparent that this is at a maximum when $\tau_c = 1/\omega_0$. As the rate of spin-lattice (longitudinal) relaxation is proportional to $j(\omega_0)$, it will be fastest when $\tau_c = 1/\omega_0$. When τ_c decreases below or increases above this, spin-lattice relaxation will be slowed down and T_1 will increase. T_1 decay is therefore fastest and most effective when

the Larmor frequency of the molecular motion is of the same frequency as the transition frequency (Figure 2.14).

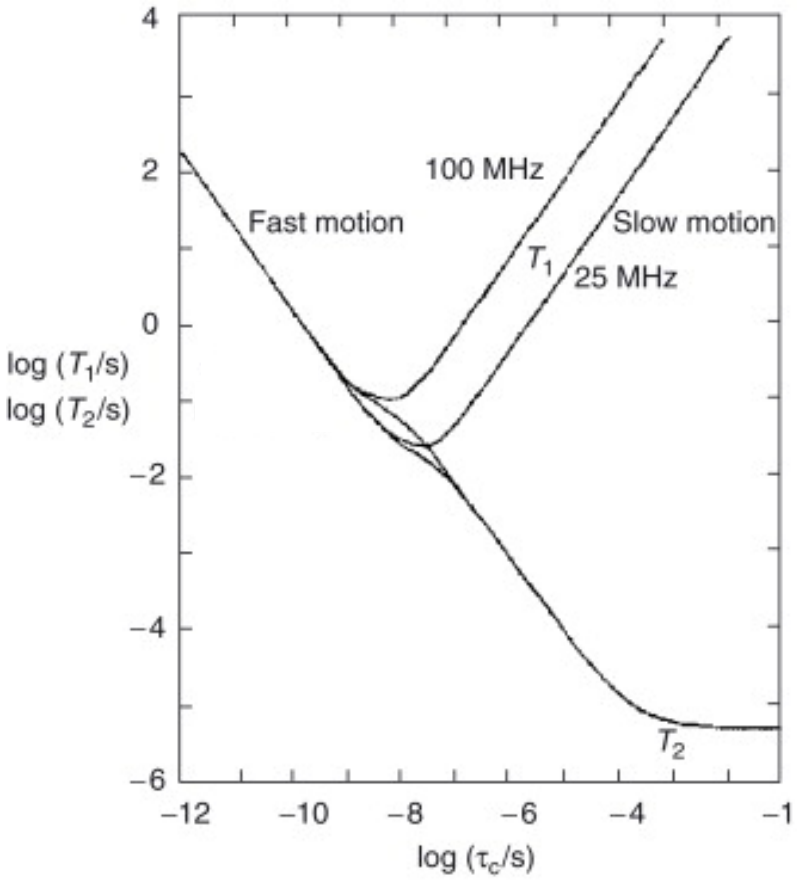


Figure 2.14: Relationship between correlation time for rotational diffusion, τ_c, and the relaxation times, T_1 and T_2. Relaxation is less efficient at higher external magnetic field B_0 strengths (curves for 25 MHz and 100 MHz carbon resonance frequencies shown as examples). Figure adapted from [502].

Spin-spin or transverse relaxation

Following the 90º pulse, field inhomogeneities and direct spin-spin interactions result in a gradual loss of coherence between the spins without energy transfer to the lattice. T_2 relaxation therefore affects the degree of synchronisation of the magnetisation components in the xy plane. Essentially, transverse relaxation determines the rate of decay of the FID and hence the linewidth. In this way, T_2 is related to the linewidth at half-height ($\Delta\nu_{1/2}$) of the NMR signal, and so $T_2 \sim 1/\Delta\nu_{1/2}$.

Both relaxation time constants, T_1 and T_2, are intrinsically related, as an increase in the magnetisation along the z plane is not possible without a decrease in the magnetisation in the xy plane. Therefore,

T_2 can only be equal or larger than T_1. In solution, however, static dipolar fields average out due to random molecular motion, resulting in $T_2 \approx T_1$.

In contrast to the effect of correlation time on T_1, spin-spin (transverse) relaxation depends on the sum of $j(\omega_0) + j_0$. As j_0 equals $2\tau_c$, the sum of $j(\omega_0) + j_0$ will increase. Therefore, T_2 decreases when τ_c increases (Figure 2.14).

Relaxation time constants can be expressed as relaxation rates, which are given by $R_1 = 1/T_1$ and $R_2 = 1/T_2$.

Aptamer Selection

3.1 Introduction

Misfolded αSyn oligomers are known to disturb the cellular homeostasis in PD in several ways, bringing along neurotoxicity and eventual cell death [131, 124]. Disruption of biological membranes, in particular, is believed to be an especially important mechanism underlying the pathology of the disease [92]. Perturbation of the cellular membranes has been proposed to occur through a variety of different mechanisms, including partial insertion of the oligomers into the hydrophobic region of the membrane, formation of a pore complex spanning both sides of the membrane, membrane thinning and membrane lipid redistribution through a detergent-like mechanism [125]. The resulting loss of membrane integrity leads to an aberrant influx of Ca^{2+} ions, the generation of ROS and the alteration of the cellular signalling pathways, ultimately leading to a Ca^{2+}-dependent neuronal death. Extensive mitochondrial damage has been reported in cellular models and patients of PD and is believed to be at least partly caused by the toxicity associated with the ability of oligomeric αSyn to bind membranes. Detrimental protein-membrane interactions induce defects in the mitochondrial membranes, leading to alterations in mitochondrial homeostasis in the form of ionic gradient imbalances, which disturb the electron transport chain that is vital to mitochondrial respiration. A compromised mitochondrial electron transport chain and a consequent loss of mitochondrial membrane potential, coupled with an elevated influx of Ca^{2+} into the mitochondria result in an increased generation of intracellular ROS,

and ultimately the release of cytochrome c and the activation of apoptosis signalling [161, 229, 172].

Monomeric αSyn exists as an intrinsically disordered conformational ensemble with no residual structure, although its N-terminus has been shown to adopt an α-helical conformation that is induced upon membrane association [27, 38, 35, 83, 30, 84, 82]. Recent evidence supports the essential role of this lipophilic N-terminal segment in the membrane binding ability of oligomeric αSyn, which is recognised as the first mechanist step in the partial insertion of the highly hydrophobic core of oligomeric aggregates into biological membranes [124]. Efforts to inhibit this interaction are hampered by the structurally dynamic nature of αSyn, which constitutes a challenge for traditional structure-based drug design approaches. The lack of well-defined structural moieties as a result of the plethora of dynamic conformations that are being constantly probed by αSyn hinders drug discovery approaches aimed towards the inhibition of toxic protein interactions. For this reason, alternative strategies have been proposed that aim at reducing and blocking the toxic network of interactions of αSyn, either through the reduction of the αSyn protein load in neurons, immunotherapy [503] and the use of aptamers as recognition molecules [259].

Aptamers are an emerging class of therapeutic biomolecules that consist of short single-stranded oligonucleotides that can be selected to have high affinity and specificity against almost any target molecule. Although many of their binding merits are shared with antibodies, nucleic acid aptamers boast of advantageous properties that overcome some of the hurdles that are encountered with the use of antibody-based therapies. The small size of aptamers (6-30 kDa and 2 nm in diameter) compared to antibodies (150-180 kDa and 15 nm in diameter), outstanding thermostability and lack of immunogenicity all make nucleic acid aptamers fantastic competitors as therapeutic molecules [236]. In particular, aptamers have recently been proposed as promising therapeutic agents for targeting amyloidogenic proteins involved in neurodegenerative diseases, as a result of their small size compared to antibodies. This characteristic becomes exceptionally important when designing drugs targeting the brain, as the highly selective and protective BBB tightly controls the flow of molecules in and out of the brain [264, 263].

Most commonly, aptamers are generated through SELEX, of which many variations have been reported that address the properties of the target molecule used [504]. These may differ in the strategies adopted in the partitioning step to separate binder sequences from non-binders, which include magnetic bead-SELEX, where the protein-aptamer complex is captured by magnetic beads, NCM-SELEX, where the protein-aptamer complex adheres to a nitrocellulose membrane whilst unbound nucleic acid sequences are washed through, *in vivo* SELEX or Capture-SELEX, where complementary sequences immobilise the library sequences through partial hybridisation. Here, a conformational change on the immobilised library sequences induced upon target molecule binding will displace them from their hybridising partner, whilst sequences with no affinity for the target will remain hybridised [504]. Those sequences with affinity for the target will therefore fall into solution and be available for amplification by PCR. Different methods for single-strand generation are also available, each with their pros and cons, as are magnetic bead strand separation, lambda exonuclease or asymmetric PCR. All these variations achieve, in effect, the *in vitro* evolution of sequences with affinity for a particular target, although the right choice of a SELEX methodology will depend on many factors, including the physicochemical properties of the target, the conditions of selection, or even the future environment under which an aptamer will be used as a therapeutic or diagnostic agent. Optimisation of each method is required to achieve the best selection results, and often a combination of more than one strategy is used to select binders with the desired affinity and specificity [504, 505, 506].

With the aim of generating high-affinity and highly specific nucleic acid aptamers to target the key membrane binding region of oligomeric αSyn involved in toxic membrane disruptive interactions, the work presented here reports on the selection of DNA aptamers against the first 25 amino acid residues of αSyn, αSyn_{1-25}.

3.2 Results

This Chapter reports on the selection process of DNA aptamers against αSyn_{1-25}, including the optimisation of the initial conditions of selection and the changes introduced in the selection strategy throughout the process to overcome the challenges encountered. A combination of magnetic bead-based SELEX (SA-Mag beads-SELEX) and NCM-SELEX is used to tailor the selection of DNA

aptamers against αSyn_{1-25}.

3.2.1 Optimisation of initial selection conditions

SELEX rounds can be divided into three main steps, namely target binding incubation (1), partitioning (2) and PCR amplification (3) of the recovered library sequences. The binding incubation ratio between DNA library and target during step (1) was first investigated to determine the optimal sequence recovery i.e., ensuring binders to the target are selected for and non-binders removed, whilst trying not to compromise the diversity of the library by using a ratio of incubation in which too many DNA sequences would be incubated with an insufficient number of target molecules. SELEX relies on the principle of single copies of sequences with affinity for a particular target being present in the initial random combinatorial library. Selection and enrichment occur by which binder sequences "evolve" by slowly and gradually increasing their population, thereby leading to a decrease in diversity as selection progresses. To prevent the loss of high affinity binders at the start of the selection process, when theoretically only one copy per sequence is present, the aptamer library and the target must first be incubated at a low ratio. A starting molar ratio of incubation of 1:1 between the initial random library of DNA sequences and the αSyn_{1-25} target was first probed, to give every sequence that may have affinity for the target the chance to bind. During the optimisation efforts of the first rounds of selection, a peptide composed of the first 25 residues of γSyn, γSyn_{1-25}, was used as a selection target instead of αSyn_{1-25}, given that it was widely available in the laboratory when the aptamer selection was started. As a result of the high sequence similarity shared with αSyn_{1-25} (almost 63%) and the similar structural properties, γSyn_{1-25} was considered a good representative analogue of the αSyn_{1-25} peptide target against which selection will be carried out after optimisation of the initial conditions.

Given that this selection is aimed at generating aptamer sequences to be used as therapeutic candidates, a selection incubation temperature of 37 ºC was chosen with the aim of selecting for sequences with secondary structures and three-dimensional folds that are thermostable at human body temperature. The γSyn_{1-25} peptide, together with the bound sequences, were partitioned and separated from the unbound library through incubation with a 1-fold amount of SA-Mag beads required to immo-

bilise the biotinylated γSyn_{1-25} relative to the molar amount used of the target peptide. A small amount of the recovered library was amplified by PCR in small-scale to determine the optimal number of PCR amplification cycles required to amplify the library, whilst minimising the formation of PCR by-product artefacts [507].

Analysis of the recovered sequences by electrophoresis after incubation of the initial DNA library with the γSyn_{1-25} peptide at a 1:1 molar ratio revealed that a high number of PCR amplification cycles were required to produce observable bands in a 3% agarose gel (2^{14} or 2^{16}), suggesting a low recovery of binding sequences (Figure 3.1). The fact that such a large number of exponential amplification cycles were required suggested a relatively small number of recovered sequences compared to the initial random library. Given the high sequence diversity associated with the initial library, the first few cycles of SELEX are key to ensuring selection success, as a low recovery after the first selection round is most likely indicative of a huge loss of diversity, which may compromise the selection process.

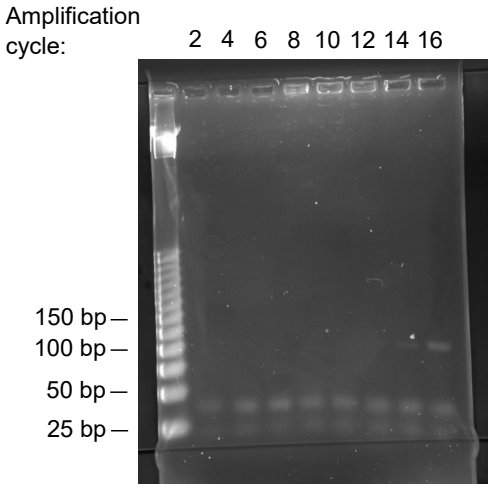


Figure 3.1: Electrophoresis analysis of the 111-bp PCR products from the recovered first round library after symmetric amplification for 16 cycles, showing intervals of 2 cycles per lane. This first selection step was carried out at 37 ºC, in a 1:1 ratio of peptide:library, using a 1x amount of streptavidin-magnetic beads. Visualisation by SYBR Gold staining; 3% agarose gel. Bands of Forward and Reverse primers can be seen at the bottom of the gel.

The low sequence recovery observed under these conditions prompted the optimisation of the different parameters important to selection. Selection conditions of the initial SELEX rounds are to be carefully chosen and optimised to avoid the loss of library sequence diversity and to ensure the selection of

high affinity and specificity binders. Several key parameters that are believed to influence selection efficiency were altered to probe their effect on aptamer-target binding and library recovery. These included the concentration of the DNA library, target and streptavidin-coated magnetic beads, the number PCR amplification cycles, and the temperature of the incubation step. To test for the effect of variations in the different conditions, test selection rounds were carried out in which a small amount of the initial library (2 nmol) was incubated with the selection target. The effect of each parameter on binding sequence recovery was assessed by determining the number of PCR amplification cycles that were required for the band corresponding to the library to be observed on a 3% agarose gel, after test-amplifying the recovered sequences.

The effect of the temperature of incubation, at which the library and target were allowed to interact during the incubation step of SELEX, was first investigated. This was done by carrying out a test selection at 37 ºC and RT, with γSyn_{1-25} and the library being incubated at a 1:100 molar ratio. A 1:100 incubation ratio was studied as an alternative to a 1:1 selection ratio, given that successful aptamer selections using such a molar ratio of incubation between target and library had previously been reported in my group. After a small-scale test amplification of the bound fraction following library-target incubation, a significantly lower number of PCR amplification cycles required to amplify the library was observed after incubation at RT, compared to that required to amplify the library to similar levels at 37 ºC (Figure 3.2). Half the number of PCR cycles were required to amplify the recovered library following library-target incubation at RT compared to incubation at 37 ºC, which indicates a higher binding sequence retention and recovery at the lower temperature studied.

To further optimise sequence recovery, the effect of three different molar ratios of incubation of γSyn_{1-25} to library was assessed: 1:1, 1:50 and 1:100 (Figure 3.3). Gel electrophoretic data revealed an equal number of PCR cycles required to amplify the recovered library after incubation with the target at a 1:50 and 1:100 ratio (eight cycles, or 2^8 duplications). This was half the number of cycles that was required to amplify the library after a 1:1 test incubation ratio, suggesting a higher rate of sequence binding after the 1:50 and 1:100 target:library ratios of incubation, compared to the lower incubation ratio investigated.

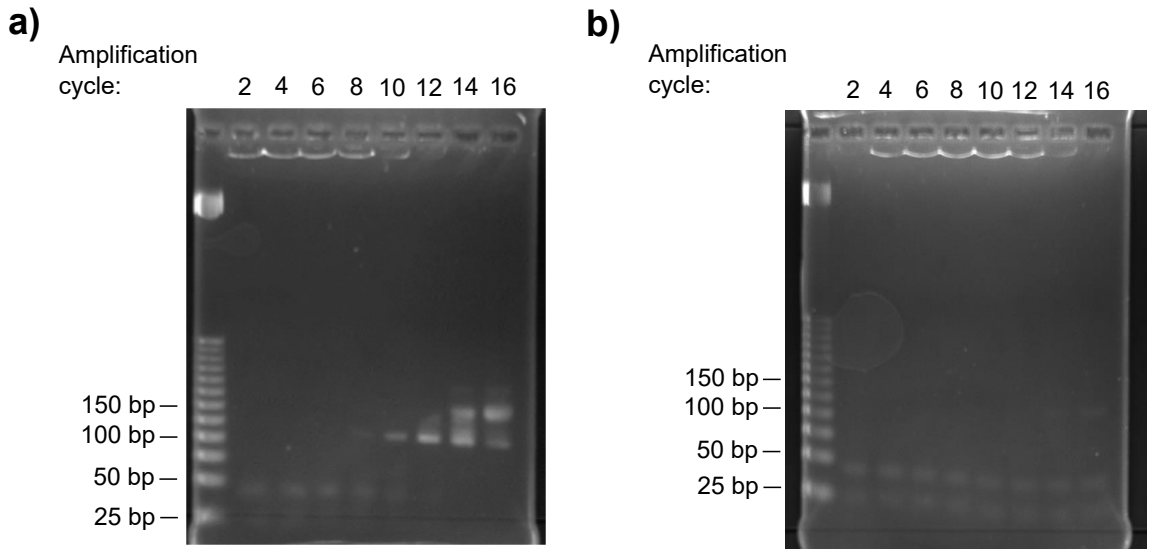


Figure 3.2: Agarose gel analysis of the effect of different incubation temperatures of selection on library amplification, showing the PCR products of the first 16 cycles of amplification, in intervals of 2 cycles. The earlier appearance of correctly sized 111-bp PCR products in the amplification series at RT (a) suggests a higher recovery after the selection step, compared to selection at 37 ºC (b). Incubation between the target peptide and the library was carried out at a 1:100 molar ratio, and using a 10x excess of magnetic beads. Visualisation by SYBR Gold staining; 3% agarose gel. Bands of Forward and Reverse primers can be seen at the bottom of the gels.

A 10-fold excess of SA-Mag beads relative to the manufacturer's recommended amount was used during the test selections to ensure that every target-aptamer complex was captured and that all target-bound sequences were recovered. To discern any possible effect that different amounts of SA-Mag beads may have on sequence binding and recovery, aside from the expected decrease in sequence recovery upon a lower amount of magnetic beads used, the target-aptamer complexes were partitioned using different relative amounts of magnetic beads. After incubating the target and library mixture at a 1:50 ratio at RT, the effect on sequence recovery of a 1-, 5- and 10-fold amount of SA-Mag beads was studied (Figure 3.4). The different amounts were calculated relative to the molar amount of biotinylated peptide used and based on the manufacturer's indications on the binding capacity of the magnetic beads. Surprisingly, partitioning of the target-aptamer complexes using the lowest ratio of magnetic beads investigated (1-fold) resulted in the smallest number of PCR cycles required to amplify the recovered library (eight cycles). Larger ratios of magnetic beads to target, i.e. 5- and 10-fold, however, revealed that larger numbers of amplification cycles were required for library amplification (16 cycles vs. 10 cycles in the absence of an excess of magnetic beads), suggesting a poorer sequence binding rate and hence lower library retention. This is consistent with the PCR

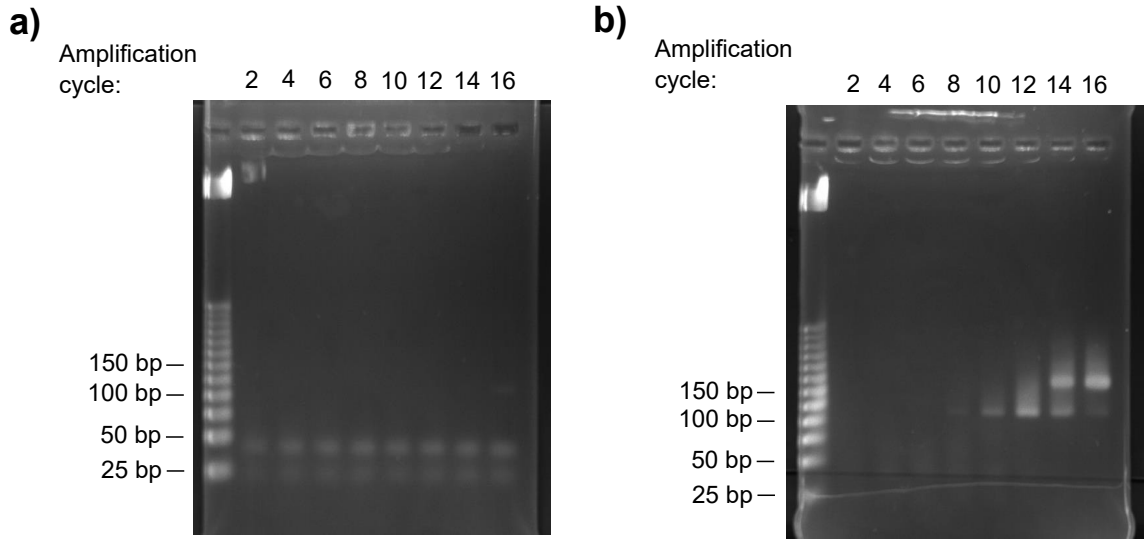


Figure 3.3: Agarose gel analysis of the effect of different selection incubation ratios between αSyn_{1-25} target and the ssDNA library, showing the PCR products of the first 16 cycles of amplification, in intervals of 2 cycles. 111-bp PCR products were observed to appear after a smaller number of amplification cycles at ratios of 1:50 (b) and 1:100 (Figure 3.2a) of target:library, compared to at a ratio of 1:1 (a). Incubation between the target peptide and library was carried out at RT, and using a 1x amount of magnetic beads. Visualisation by SYBR Gold staining; 3% agarose gel. Bands of Forward and Reverse primers can be seen at the bottom of the gels.

amplification results from the preliminary initial selection that was carried out at an incubation ratio between target and library of 1:1, which required larger amounts of magnetic beads to capture the biotinylated peptide in its entirety compared to that needed at an incubation ratio of 1:50. Under such conditions, the large number of PCR amplification cycles required suggests a link between a large relative amount of SA-Mag beads and a deficient DNA recovery, which may indicate a rapid and substantial loss of sequence diversity.

A test aptamer selection was carried out against the αSyn_{1-25} target using the optimised selection conditions, in which the target and DNA library were incubated at both 1:50 and 1:100 molar ratio at RT, and target-aptamer complexes were partitioned using a 1-fold amount of SA-Mag beads relative to that used of biotinylated peptide target. Target and library were incubated at these two ratios because optimisation tests had revealed very similar amplification results for both incubation ratios. Their suitability was determined by parallelly carrying out selection at both incubation ratios and assessing the progress of selection in terms of library recovery.

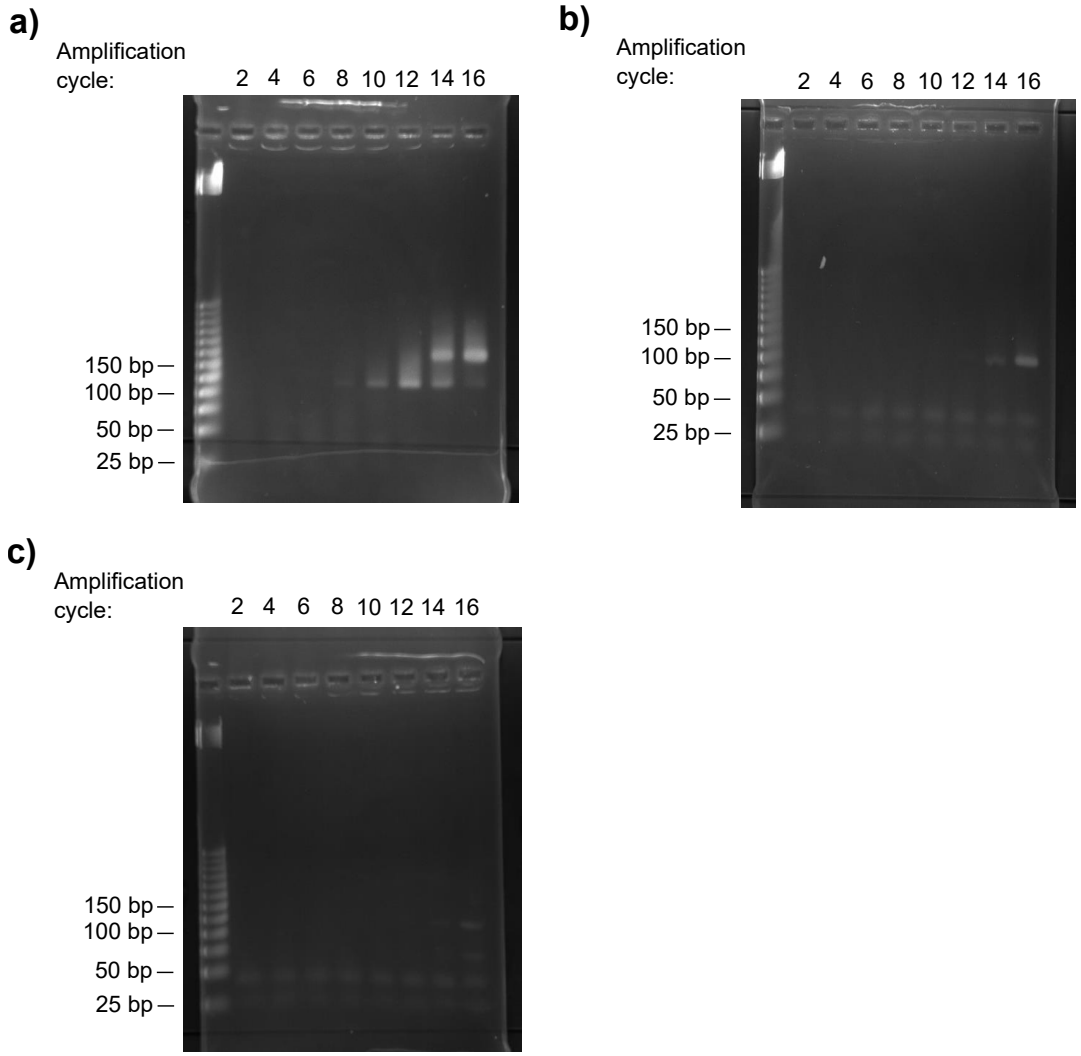


Figure 3.4: Electrophoresis analysis of the effect of magnetic bead concentration on library amplification, showing the PCR products of the first 16 cycles of amplification, in intervals of 2 cycles. a) 1x magnetic beads; b) 5x magnetic beads; c) 10x magnetic beads. The appearance of correctly sized 111-bp PCR products at early amplification cycles after performing selection in the absence of an excess of magnetic beads suggested a higher recovery of the library. Selection incubation was carried out at a 1:50 molar ratio between target and library, and at RT. Visualisation by SYBR Gold staining; 3% agarose gel. Bands of Forward and Reverse primers can be seen at the bottom of the gels.

After three rounds of selection, PCR by-product artefacts that had been accumulating during the first selection rounds were starting to constitute a large proportion of the library (Figure 3.5). The removal of these by-products was therefore imperative to avoid them from compromising the aptamer selection process. Visual comparison of the electrophoresis results from the test PCR amplification of the libraries that had been selected at a 1:50 and at a 1:100 incubation ratio revealed a slightly smaller proportion of these longer PCR artefacts after incubation at a 1:100 ratio compared to after incubation at a 1:50 ratio. Given that removal of these PCR by-products is not trivial and that it is important to restrict their gradual growth in population throughout selection, a "cleaner" library with a lower abundance of sequence by-products will be advantageous for the successful selection of aptamers. Therefore, the 1:50 incubation molar ratio was discarded and a 1:100 ratio of target to library was implemented as the incubation ratio of the aptamer selection against αSyn_{1-25}.

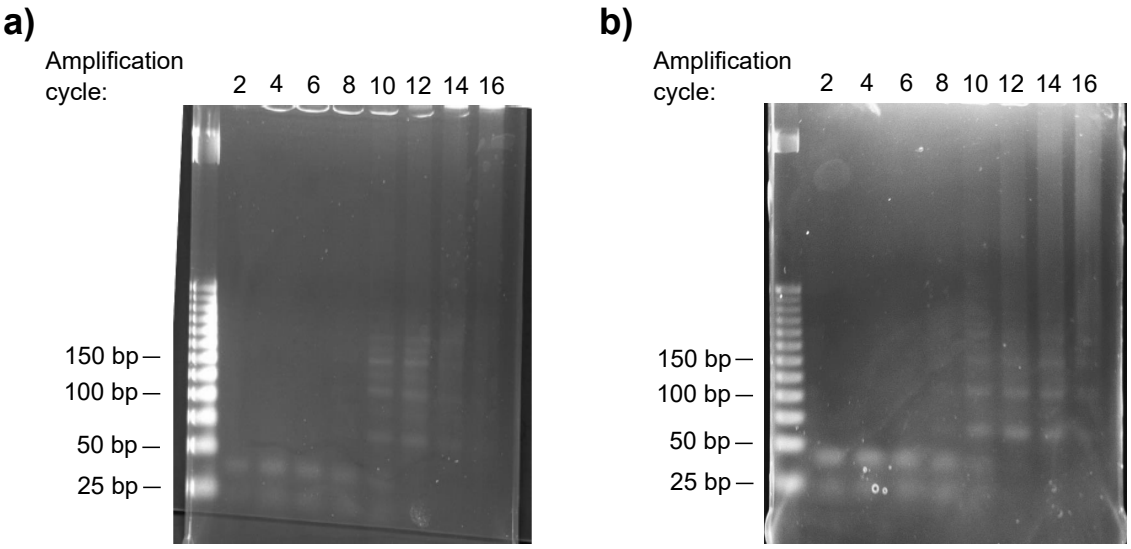


Figure 3.5: Electrophoresis analysis of the PCR products from the fourth round library after symmetric amplification, showing intervals of 2 cycles per lane. Non-specific by-product bands can be seen as additional DNA bands to that of 111 bp and primer bands. Selection incubation was carried out at a (a) 1:50 and (b) 1:100 molar ratio between target and library, at RT and using 1x the recommended amount of streptavidin-magnetic beads. Visualisation by SYBR Gold staining; 3% agarose gel. Bands of Forward and Reverse primers can be seen at the bottom of the gels.

A further alteration to the aptamer selection protocol involved the removal of the DNA precipitation and washing steps after library recovery. Recovered DNA is commonly precipitated through incubation with CH_3COONa and absolute EtOH, and the resulting pellet washed through a two-step process involving a first wash with 80% EtOH followed by water. These washing steps after library recov-

ery were removed from the protocol, as aspiration of the washes was often observed to accidentally include small amounts of precipitated library, resulting in the loss of some target-binding sequences after each selection round. Sample loss was believed to be at least partly responsible for the large number of PCR cycles required for library amplification after each selection round, which was expected to be reduced after restricting the number of pellet-handling steps in the aptamer selection protocol. In this way, removal of the precipitation and washing steps does not only avoid sample loss through aspiration, but is also expected to reduce the formation of PCR by-product artefacts, given that the larger number of iterative amplification cycles required to amplify a smaller recovered library is associated with a faster generation of by-products.

3.2.2 Aptamer selection with SELEX

Selection strategy

With the aim of selecting for only those aptamers with the highest affinity for the αSyn_{1-25} target, selection conditions were gradually altered to increase the stringency of selection (Table 2.2).

One way in which low affinity aptamers can be discarded, and high affinity ones selected for, is by increasing the volume of buffer used to wash target-aptamer complexes. Mechanical stress through complex washing will get rid of those binders that do not form tight interactions with the target and will not perturb those binding interactions that are high in affinity. On the 2^{nd} round, washes of the binding complex were increased from one to two. On the 5^{th} round, the first negative selection against SA-Mag beads was introduced. This step was repeated before target-library incubation at every other selection round. After 8 rounds, an additional washing step of the target-aptamer complex was introduced to increase the total number of washes to three. On round 9 of selection, a counter selection step against the γSyn_{1-25} peptide was introduced to increase the specificity of the enriched sequences. This was then repeatedly performed on every other round of selection coinciding with the negative selection steps against SA-Mag beads (except for the 11^{th} and 13^{th} rounds, which were shifted to the 12^{th} round of selection). A further wash of the binding complex was introduced into the selection protocol at the 12^{th} round, thereby increasing the number of buffer washes to four.

On the 15^{th} round of selection, the selected aptamer library was negative- and counter-selected for the 5^{th} and 3^{rd} times against SA-Mag beads and the γSyn_{1-25} peptide, respectively. On the same round of selection, the number of washes of the bound complex was increased to 5. Following selection under these new and more stringent conditions, the aptamer library was sequenced to inform on the extent of sequence enrichment, the results of which are discussed in section 4.2.3. Two rounds later, upon carrying out the 17^{th} round of selection, the aptamer library was further negative-selected against SA-Mag beads (6^{th} time) and counter-selected against γSyn_{1-25} (4^{th} time). The library was then again sequenced to inform on the progress of aptamer selection against αSyn_{1-25}.

To further select for those aptamer sequences that only bind to the peptide target with high affinity, the ratio of αSyn_{1-25} to aptamer library was doubled, from 1:100 to 1:200, on the 18^{th} round. On the 19^{th} round, a further negative selection step against SA-Mag beads (7^{th} time) and a counter selection step against γSyn_{1-25} at a 1:100 ratio (5^{th} time) were incorporated. To ensure correct removal of low-affinity binders, the library was consecutively incubated twice with SA-Mag beads and the unbound fractions were discarded before incubation with the target αSyn_{1-25}. Additionally, the number of washes of the target-bound complex was increased to 6. A final negative selection step against SA-Mag beads (8^{th} time) and a counter selection against γSyn_{1-25} (6^{th} time) were carried out on the 20^{th} round of selection, after which the current selection protocol was terminated and the library was sequenced. Like on the 19^{th} round, the aptamer library was negative-selected against SA-Mag beads twice prior to incubation with the target.

Sequencing results of the various round libraries throughout selection did not reveal the enrichment of a subpopulation of sequences that could hint at the selection of high-affinity binders, as is discussed in section 3.2.5 below. Additionally, binding assays performed on selected aptamer sequences that had been identified up to now showed a generalised lack of affinity for αSyn_{1-25}, but pointed at a possible inadvertent selection that may have occurred for the SA-Mag beads. For this reason, the selection strategy was modified to address this issue. Therefore, to remove streptavidin from the incubation mixture, and with it any potential streptavidin-binding sequences that may have been selected for instead of against αSyn_{1-25}, the target-bound aptamers were partitioned from the unbound sequences

by using a NCM, as opposed to capturing the biotinylated peptide target with SA-Mag beads. This method of separation relies on the fact that hydrophobic molecules like proteins will interact with the chemical groups of nitrocellulose, thereby adhering to the membrane and being retained within the porous membrane matrix, whilst highly hydrophilic and charged molecules like DNA sequences will pass through the membrane pores. Target size is, however, a matter of concern when using a NCM for the partitioning step, since small hydrophobic targets may be unable to adhere to the membrane and may be washed away as a result, together with any bound sequences. To address this issue, full-length αSyn (14.5 kDa) was used as a target for the selection rounds involving NCM partitioning, as it is larger than αSyn_{1-25} (2.85 kDa) and may have a better chance of being retained on the membrane upon partitioning.

In this modified SELEX protocol, selection was carried out against αSyn by using the 12^{th} round library as a starting library. This was chosen as the starting library given that sequencing had revealed the presence of single copies of several different aptamer sequences, which suggests that the library still bears a high sequence diversity. At the same time, this provides a pre-selected library from which sequences have been selected for 12 rounds against αSyn_{1-25}. This library is therefore predicted to be populated by enriched sequences with affinity for the target, compared to a newly randomised library on which no previous rounds have been performed.

This change in the partitioning method requires optimisation to ensure conditions are adequate for the success of aptamer selection. Several groups working on aptamer selection have previously reported the need to treat NCMs prior to use by immersing them in 0.4 M KOH [508]. This is supposed to enhance the adhering capacity of the membrane for hydrophobic molecules. Additionally, NCM-SELEX is also known to be very sensitive to inappropriate target concentration, which may lead to poor retention and the loss of target-bound sequences. Therefore, a test experiment was carried out to assess the binding capacity of NCMs for different concentrations of target protein after treatment with KOH compared to ABB buffer.

Six pieces of NCM were each incubated with either 0.4 M KOH or ABB for 40 mins, and then washed

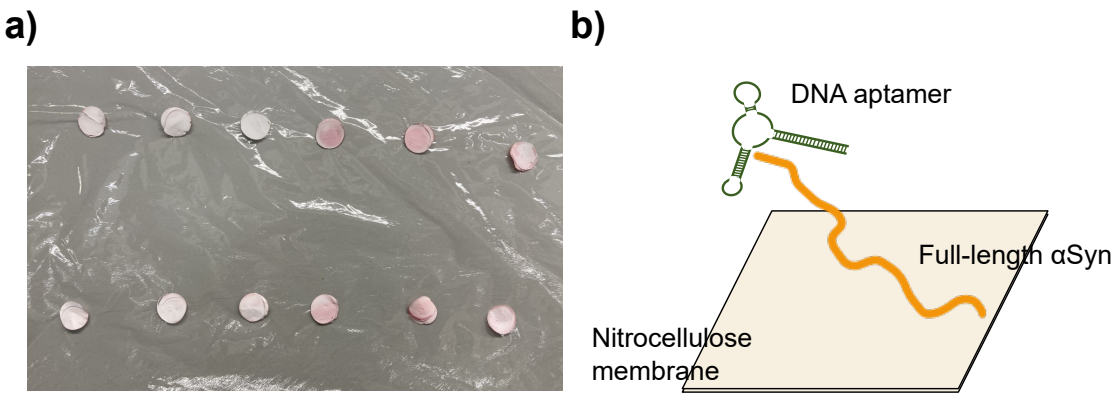


Figure 3.6: NCM-SELEX. a) NCMs stained with Ponceau solution after having had monomeric full-length αSyn passed through them to test for the retention capacity of the membranes at different protein concentrations. The pieces of NCM were treated with either ABB (upper row) or KOH (lower row) prior to incubation with αSyn. From left to right: 200 nM, 500 nM, 1 μM, 5 μM, 10 μM and 20 μM of αSyn. b) Schematic illustrating the principle of NCM-SELEX, by which full-length αSyn is immobilised on the NCM, and with it any DNA aptamer sequences with affinity for the protein.

with H_2O for 20 mins and ABB for 20 mins. Next, the target αSyn was slowly passed through a NCM at different concentrations (200 nM, 500 nM, 1 μM, 5 μM, 10 μM and 20 μM), after which the membranes were washed with ABB. Ponceau solution was then used to assess protein immobilisation and retention at every condition tested, after which the membrane was again washed with ABB to remove excess dye (Figure 3.6). The results from this test showed that KOH did not significantly increase the membrane's retention capacity compared to treatment with ABB prior to use. In addition, 5 μM and 10 μM seemed to be the concentrations of target protein that yielded the strongest red Ponceau colour, suggesting that the highest retention happened at these two concentrations of all amounts tested. Interestingly, the 20 μM protein concentration did not show a higher colour intensity compared to 5 μM and 10 μM concentrations. Based on these test results, it was decided to only pre-wash the membrane with ABB prior to use in the partitioning steps of selection. Additionally, 5 μM was set to be the concentration of αSyn target used during the incubation steps with the aptamer library.

The 13^{th} round of selection (and 1^{st} round of NCM-SELEX) was carried out by incubating the target αSyn and DNA library at a 1:7 ratio for 1h. To allow enrichment of any single copies of sequences that may be binding to the target, the bound complex was not washed with ABB during this round.

On the next round, prior to target incubation, the library was filtered through a fresh NCM to remove non-specifically membrane-binding sequences (negative selection). The eluent was then used for the next incubation step with the target, and the membrane used in this negative selection step was discarded. This was repeated prior to incubation with the target at every round. On this 14^{th} round, the ratio of incubation of target to library was increased to 1:25 to gradually increase the stringency of selection. Additionally, the target-bound complex was washed once with ABB following membrane filtration of the incubation mixture, to remove low-affinity binders. On the 15^{th} round, the incubation ratio between target and library was further increased to 1:50, and the number of buffer washes of the bound complex raised to 2. On the following selection rounds, target and library were incubated at ratios 1:75, 1:100 and 1:100 on rounds 16, 17 and 18, respectively. Selection stringency was further increased on the 17^{th} round by decreasing the incubation time between target and library from 1h to 40 min. On the 18^{th} round, the aptamer library was filtered twice through a fresh membrane prior to incubation with the target. Additionally, the time of incubation between target and library was reduced from 40 to 20 min. This was the last round of NCM-SELEX that was carried out, after which the library was sequenced in the search of enrichment of sequences which may have affinity for αSyn and, specifically, αSyn_{1-25}.

3.2.3 Purification of the ssDNA library temporarily removes large PCR by-products

Considering the results from the selection optimisation tests, DNA aptamers were selected against the αSyn_{1-25} target. The initial round of selection was carried out by incubating the target and DNA library at a 1:100 molar ratio at RT, and target-aptamer complexes were partitioned using a 1-fold amount of SA-Mag beads relative to that used of biotinylated peptide target. Surprisingly, after the 3^{rd} round of selection, the formation of PCR by-product artefacts was observed upon test amplification (Figure 3.5). These sequences, which are longer than the library sequences as they are thought to form as a result of the nonspecific annealing of primer sequences to PCR products and the nonspecific amplification of the primer sequences [507], may gradually increase in abundance and constitute the bulk of the sequences in the library through PCR bias. As a result, these PCR products are often described as being “parasitic” as they compete with the sequences from the library for

resources such as dNTPs and primers, thereby compromising the process of aptamer selection. Most likely, these sequences may have started forming early on during the first rounds of selection and were only detected upon the test amplification of the library after the 3^{rd} selection round once their concentration was high enough. To prevent their build-up and avoid the process of aptamer selection from being affected, these artefacts must therefore be systematically removed from the sequence pool.

To achieve this, a library purification step was introduced after ssDNA generation in the 3^{rd} round, just before continuing further to the 4^{th} round of selection. As a result of the fact that these undesired PCR by-products differ from the aptamer library in length, a simple electrophoresis experiment will result in their separation. Therefore, the ssDNA aptamer library from the 3^{rd} round of selection was run through a denaturing urea-TBE polyacrylamide gel. With the help of a thin-layer chromatography plate under UV light, the sequence bands in the gel were visualised without the need to be stained, and the band corresponding to the size of the aptamer library was excised. This purified library was then directly incubated with the αSyn_{1-25} peptide target as part of the 4^{th} round of selection. Amplification of the recovered library after incubation and partitioning showed the correct removal of the large PCR by-products, together with an increase in the intensity of the band corresponding to the N42 aptamer library (Figure 3.7), indicating a preferential amplification of the library sequences in the absence of larger "parasitic" sequence artefacts that would have otherwise competed for reaction resources.

Progression through the following aptamer selection rounds showed the recurrent appearance of these PCR by-product sequences. Proceeding from one round to the next without by-product removal resulted in their appearance shortly after (Figure 3.7), suggesting that frequent library purification steps were imperative to prevent the accumulation of these sequence by-products. Of note, purifying the library more often proved effective at avoiding the formation of artefact sequence fragments of intermediate size between the larger by-products and the aptamer library. Given their small size difference compared to the sequences of the N42 aptamer library, the future removal of these sequences may have otherwise proved very challenging. To avoid the accumulation of by-products of different sizes, the libraries from every round were purified before proceeding to the next cycle of selection after the 7^{th} round.

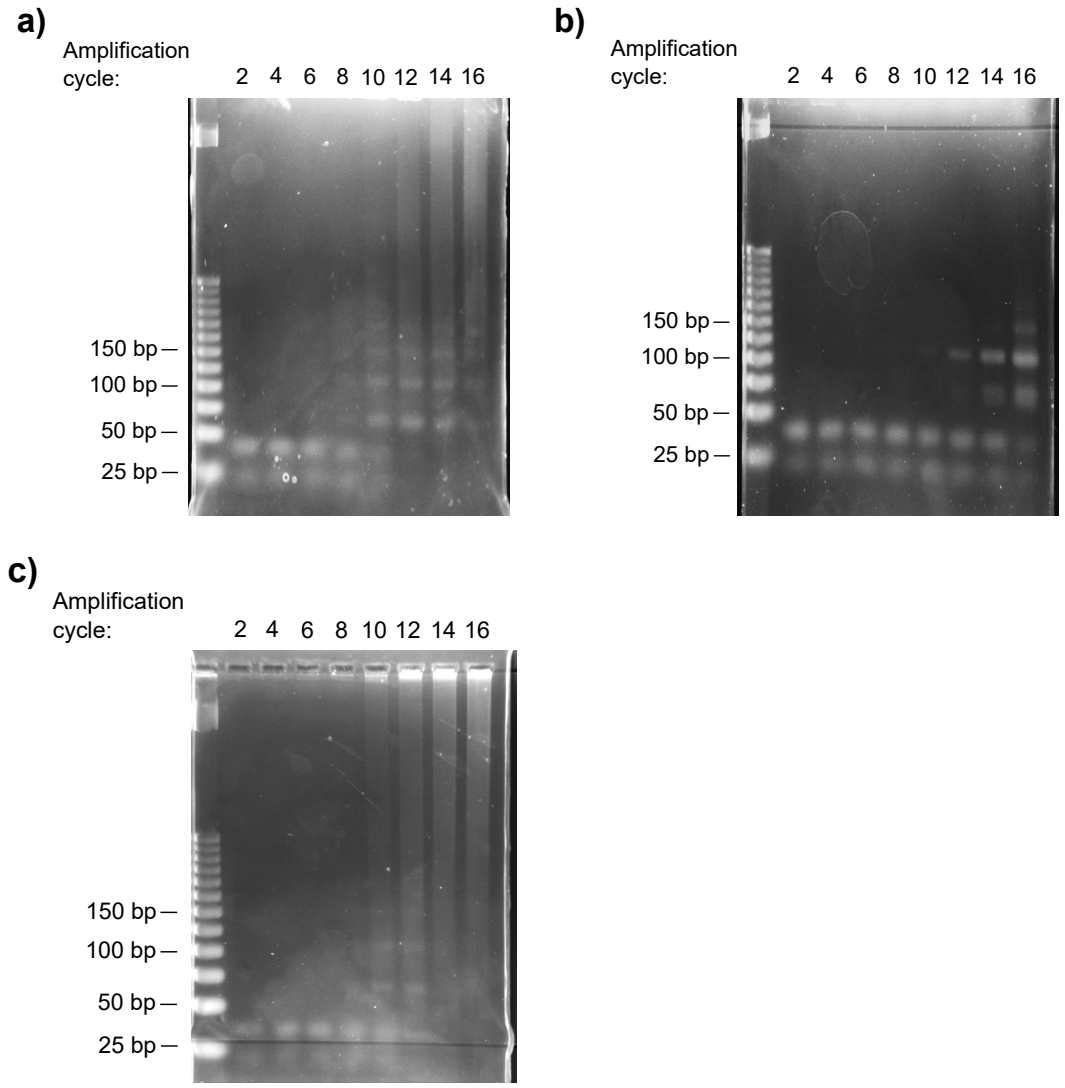


Figure 3.7: Electrophoresis analysis of the PCR products of the 4^{th} and 7^{th} libraries showing the formation of larger by-products, and their removal after symmetric amplification for 16 cycles. a) Non-specific by-product bands can be observed after symmetric amplification of the 4^{th} round library, together with the expected 111 nt-long library band, being formed after the same number of cycles that allow observation of the aptamer library band. b) Purification of the 4^{th} round library yields a much more intense aptamer library-sized band, and results in a delay in the formation of larger PCR by-products to later amplification cycles. c) Non-specific PCR by-products forming a smear of different sized bands after symmetric amplification of the seventh round library, after not having purified the library for one consecutive round (sixth round). Each lane corresponds to 2 cycles of symmetric PCR amplification. Visualisation by SYBR Gold staining; 3% agarose gel. Bands of Forward and Reverse primers can be seen at the bottom of the gels.

3.2.4 Progression of selection gave rise to a short ∼70 nt-long band

Interestingly, the recurrent appearance of an unexpected and unknown band of a smaller size than the N42 library sequences was observed upon test amplification of the 3^{rd} round library. From the 3^{rd} round (except for the 4^{th} round), purification of the aptamer pools prior to proceeding to the next selection round meant that PCR products that were both shorter and longer than the library sequences were being removed. However, particularly remarkable was the small number of PCR amplification cycles required for this ∼70 nt band to appear on a 3% agarose gel, which was sometimes smaller than that required to amplify the aptamer library, even after having purified the library prior to that round's incubation step. In the same way as with the larger by-products, the intensity of this band became stronger with increasing PCR cycles, and as selection progressed (Figure 3.8). Notably, this band was also seen to have an intensity that was equivalent or stronger than that of the band corresponding to the N42 aptamer library on an agarose gel even after a small number of PCR amplification cycles. However, library purification at every round as outlined above helped prevent the accumulation of the associated sequences, although the exceptionally quick regeneration of the sequence species responsible for that band even after purification of the previous round library escaped my understanding.

After performing the 7^{th} round of selection, the aptamer library was purified as usual, but this time the unknown band of ∼70nt in size was also excised with the aim of studying its composition. To investigate the origin of the sequences responsible for the formation of this recurrent band and clarify whether these sequences may have been selected against the target peptide, a round of selection was performed with the sequences of this excised band in the absence of the N42 aptamer library. Surprisingly, only 12 cycles of PCR amplification were required to observe the product band on an agarose gel upon test amplification (Figure 3.9), suggesting a high sequence recovery which may be indicative of this sequence pool having affinity for the αSyn_{1-25} peptide.

A further selection round was carried out with this sequence pool in which conditions were altered to increase the stringency of selection (Figure 3.9). In this round, the binding complex was washed three times compared to the two washes carried out in the previous round. In addition, these sequences were first negative-selected against SA-Mag beads and counter-selected against the γSyn_{1-25} peptide (to

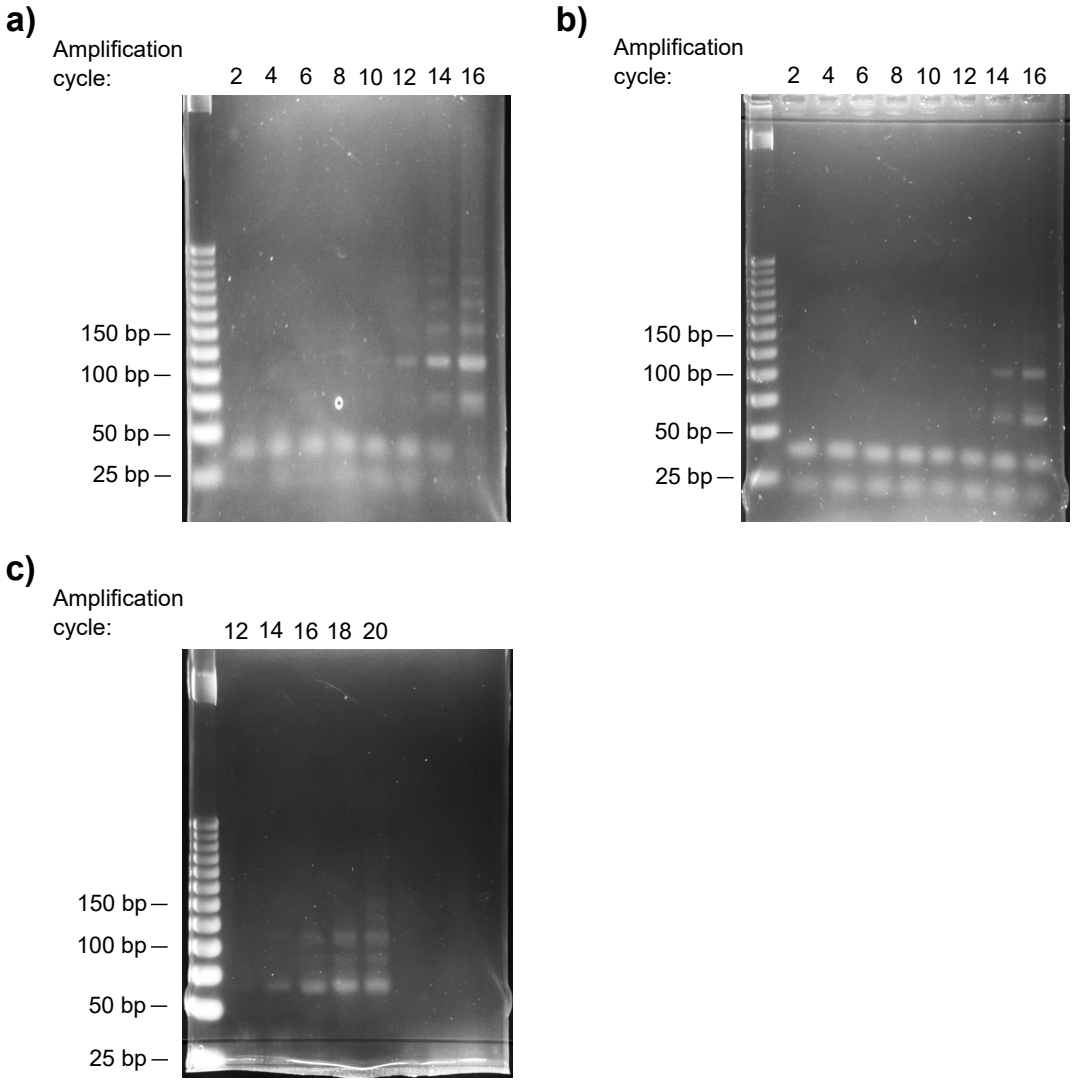


Figure 3.8: Electrophoresis analysis of the PCR products of the 3^{rd}, 5^{th} and 8^{th} libraries showing the presence of the $\sim$70 nt band throughout aptamer selection, compared to the expected 111 nt-long aptamer-library band. The intensity and hence abundance of the forming species increases each selection round, slowly outcompeting the amplification of the aptamer library band. a) 3^{rd} round library symmetric PCR amplification. b) 5^{th} round library symmetric PCR amplification. c) 8^{th} round library symmetric PCR amplification. Each lane corresponds to 2 cycles of symmetric PCR amplification. Visualisation by SYBR Gold staining; 3% agarose gel. Bands of Forward and Reverse primers can be seen at the bottom of the gels.

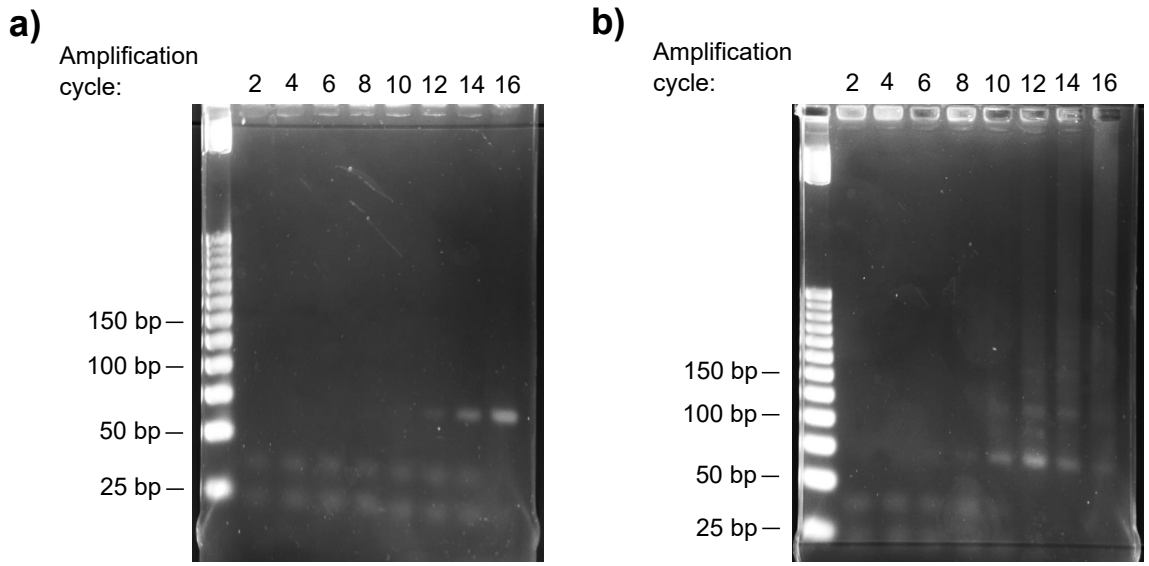


Figure 3.9: Electrophoresis analysis of the PCR products after purification of the ∼70 nt band. a) First round of selection performed with the purified ∼70 nt band. The band can be observed on an agarose gel after 12 cycles of amplification. b) Second round of selection performed with the ∼70 nt band, where a counter selection step against the SA-Mg beads and the γSyn_{1-25} peptide was incorporated. The band can be observed after only 10 cycles of amplification. Each lane corresponds to 2 cycles of symmetric PCR amplification. Visualisation by SYBR Gold staining; 3% agarose gel. Bands of Forward and Reverse primers can be seen at the bottom of the gels.

both discard any sequences that may be binding to the immobilisation beads and test the sequences' specificity for αSyn_{1-25} through incubation with the γSyn peptide), prior to incubation with αSyn_{1-25} to select for binders to the target peptide. Similar to the results from the previous selection round, test amplification after partitioning and sequence recovery showed a small number of amplification cycles being required to observe the ∼70 nt product band on an agarose gel (10 cycles), suggesting binding affinity of this sequence pool for the αSyn_{1-25} peptide, but not for the negative- and counter-selected molecules (SA-Mag beads and γSyn_{1-25}). Towards the correct interpretation of the remaining results from this section, it is important to know that sequencing revealed that this band is composed of only one sequence species, which is formed by the sequences of the forward primer and the reverse complement of the reverse primer together. As a reference to its size, this sequence species was named 65ntSeq.

Despite streptavidin being removed from the incubation mixture after SELEX was modified and partitioning was done by NCM filtering, bands corresponding to large PCR by-products and 65ntSeq were

still observed upon test amplification. Similarly, even though the aptamer library was purified after each ssDNA generation step before the following round of NCM-SELEX, large PCR by-products as well as 65ntSeq sequences were still being formed upon test amplification of the next round. The reason for the recurrent appearance of these sequences in the library of every round remained unknown, however, given that their putative affinity for streptavidin was thought to be driving their formation. To investigate the elusive origin of the 65ntSeq sequence, an alternative DNA polymerase to Taq was used to amplify the aptamer library (Figure 3.10). Taq polymerase is known to possess terminal transferase activity which adds a single deoxyadenosine (dA) overhang to the 3' end of a blunt double-stranded DNA sequence (i.e. PCR product) in a non-templated manner [509]. A single 'A' overhang on the 3' end of the forward primer may allow annealing of the reverse primer, resulting in the amplification and formation of 65ntSeq. To test this, Q5 polymerase, which does not have terminal transferase activity, was used upon test amplification of the 14^{th} round library of NCM-SELEX. Interestingly, amplification of the library with the Q5 polymerase resulted in a band pattern on an agarose gel that was similar to that observed upon amplification with Taq polymerase (Figure 3.10a and b), suggesting that the addition of this overhang 3' dA is not responsible for the fusion of the sequences of both primers into 65ntSeq.

The effect of primer annealing temperature was also studied to shed further light on the molecular mechanism giving rise to 65ntSeq and in large PCR by-product formation. This was altered from 45 ºC to 56 ºC, which was the calculated annealing temperature for the forward and reverse primers. To analyse this, the library of the 15^{th} round of NCM-SELEX was test amplified using 45 ºC and 56 ºC as PCR annealing temperatures. Results from the test amplification of the library showed the appearance of the band corresponding to 65ntSeq at both temperatures studied (Figure 3.10c and d), suggesting that annealing temperature has no effect on the formation of 65ntSeq. Comparison of the test amplification results revealed a similar amplification efficiency, with 4 cycles of PCR being required for the N42 aptamer library band to appear on an agarose gel at both annealing temperatures tested. Notably, the band corresponding to the N42 aptamer library was observed to appear slightly earlier in terms of PCR cycles at an annealing temperature of 56 ºC, compared to that corresponding to 65ntSeq. Despite the likely insignificance of this minimally positive result, amplification of the

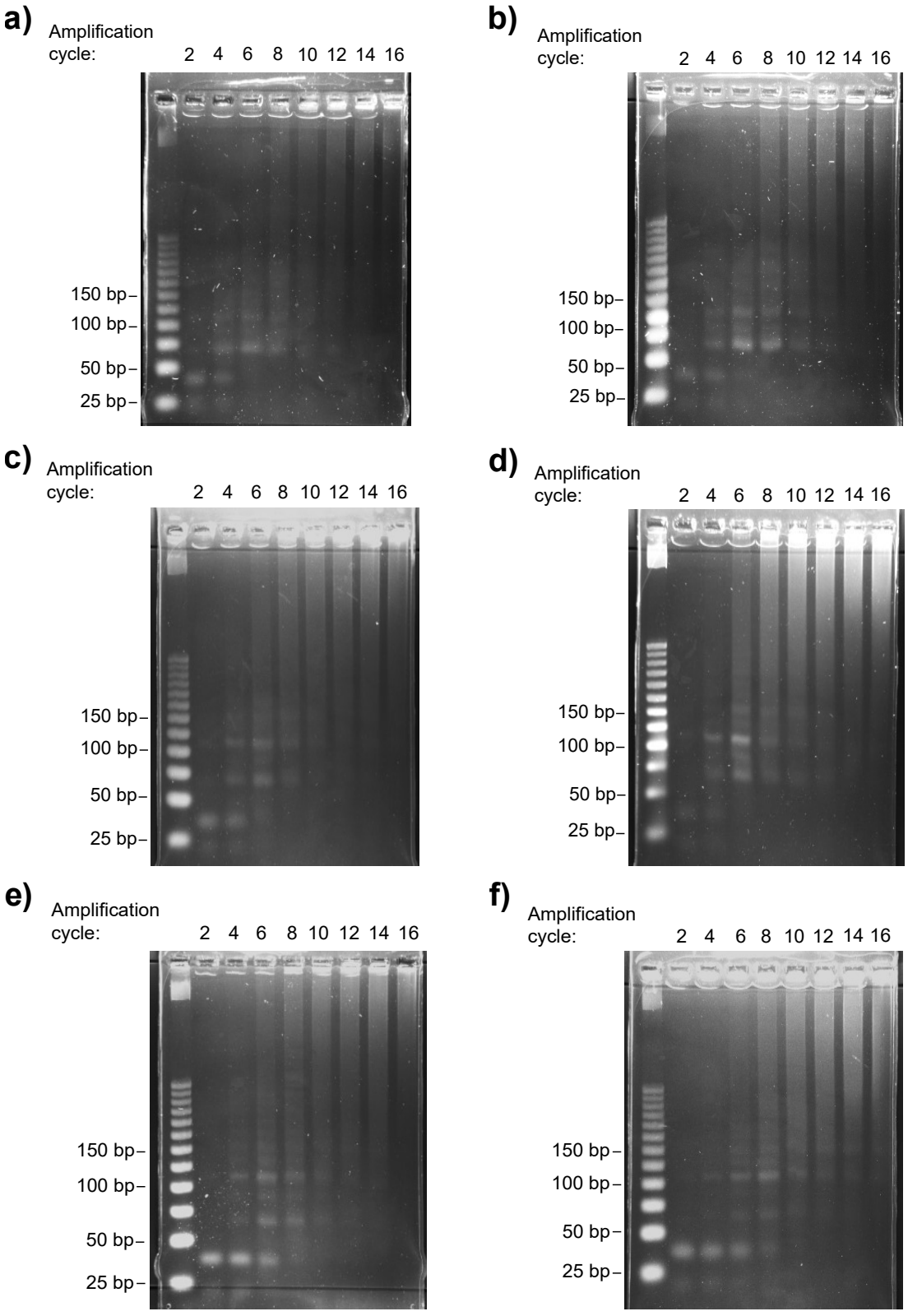


Figure 3.10: Electrophoresis analysis of the PCR products after amplification of the 14^{th}, 15^{th} and 16^{th} round NCM libraries upon modification of the selection conditions to prevent the formation of primer-derived sequences. a) 14^{th} round NCM library after PCR amplification with OneTaq DNA

Figure 3.10: polymerase. b) 14^{th} round NCM library after PCR amplification using Q5 DNA polymerase. c) Products of the 15^{th} round NCM library after PCR amplification using an annealing temperature of 45 ºC. d) 15^{th} round NCM library after amplification using an annealing temperature of 56 ºC. e) 16^{th} round NCM library amplified by PCR using the conventional reverse primer. f) Products of the 16^{th} round NCM library amplified using the truncated form of the reverse primer. Each lane corresponds to 2 cycles of symmetric PCR amplification. Visualisation by SYBR Gold staining; 3% agarose gel. Bands of forward and reverse primers can be seen at the bottom of the gels.

following NCM-SELEX rounds was carried out at an annealing temperature of 56 ºC, with the aim of minimising the formation of 65ntSeq.

Given that the sequence of 65ntSeq is composed of a fusion (no overlapping of complementary bases) of the sequences from the forward primer and the reverse complement of the reverse primer, it was hypothesised that the 'AA' bases at the 5' or 3' end of the reverse primer may be playing a role in the generation of the 65ntSeq sequence by complementarily binding to the 3'-terminal 'A' base of the forward primer. To investigate whether the recurrent formation of this sequence was the result of non-specific annealing and amplification of the primers, test amplification of the library from the 16^{th} round of NCM-SELEX was carried out using a truncated form of the reverse primer lacking both 5'- and 3'-terminal 'AA' bases. This showed an indistinguishable effect in the appearance of the bands corresponding to 65ntSeq and larger PCR by-products compared to test amplification using the full-length version of the reverse primer (Figure 3.10e and f), suggesting that 65ntSeq is not being formed through the annealing of any of these two pairs of terminal adenosine bases of the reverse primer with the single adenosine base at the 3' end of the forward primer.

Additionally, 6 cycles of test PCR amplification using the truncated form of the reverse primer, compared to only 4 cycles when using the full-length primer, were required to amplify the aptamer library products to form a band of similar intensity on an agarose gel. These results suggest that the single-base complementarity between the forward and reverse primers does not drive the formation of 65ntSeq and indicate that removal of the 5' and 3' "AA" from the reverse primer only slows down library amplification, as product-primer annealing is compromised.

3.2.5 Sequencing of different selection libraries revealed a high abundance of primer-derived sequence and the presence of sequences with random core regions

Following the progress made in selection of the aptamer library and the results from the selection rounds involving the ∼70 nt-long band sequence pool, the aptamer library was cloned and sequenced after 8 rounds of selection, as well as the ∼70 nt band sequence pool after the two separate selection rounds performed with it. This was done with the aim of shedding light on the origin of the sequence species giving rise to the ∼70 nt band and to have a deeper understanding of the enrichment progress that may have happened in the aptamer library.

After cloning the sequence pools, 77 clones from the 8^{th} round library were selected for sequencing, together with 10 clones from the second selection round pool carried out with the ∼70 nt band. Strikingly, sequencing results from the 8^{th} round library revealed that those clones analysed did not consist of DNA sequences with random core regions as it would have been expected from the design of the original N42 random library. Instead, the clones sequenced had central regions that were formed by truncations of the forward and reverse complement of the reverse primer, suggesting that those sequences may have been derived and formed directly from the primer sequences used in amplification and not from the N42 random library (Figure 3.11). Particularly interesting was also the fact that the sequenced clones did not have a full-length forward primer-binding site, but featured instead a forward primer-binding site lacking bases 'AATTC' at the 3' end, which resembles the sequence of the forward primer (the 3' terminal 'ATTC' is a distinguishing feature of the forward primer-binding site compared to the sequence of the forward primer, where these 3' extra bases are missing). Additionally, cloned sequences of different lengths were observed, with some being shorter and other longer than the 111 nt-long original N42 aptamer library. Out of the 77 clones, 18 sequences (23.4% of the total number of sequenced clones) were approximately 111 nucleotides long, whilst the rest were shorter or longer, possibly representing products of nonspecific PCR recombination events (Figure 3.12).

Interestingly, 11 clones from the sequenced 8^{th} round library (14.3%) were 65 nt long and corre-

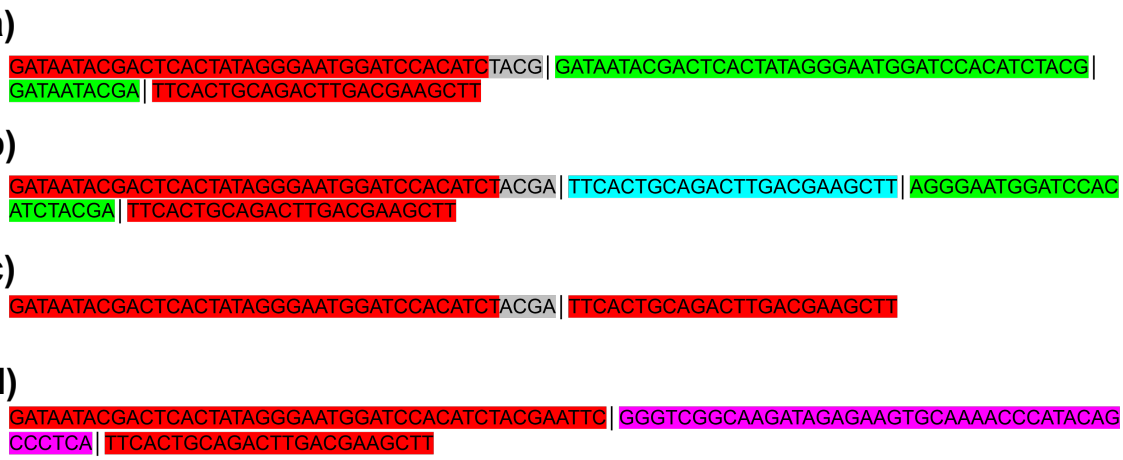


Figure 3.11: Comparison of primer-derived and N42 library aptamer sequences. Primer-derived sequences, like FSeq1 and 65ntSeq, are formed by a truncated forward primer-binding region that lacks -ATTC at the 3' end and which resembles the sequence of the forward primer. A series of alternating truncations of either primer is followed by the full-length reverse complement of the reverse primer at the 3' end of the sequence. Aptamer sequences originating from the initial N42 library have a random core region that is flanked by full-length forward and reverse primer-binding sites. Bases highlighted in red at the 5' end represent the forward primer-binding site, whilst bases highlighted in red at the 3' end represent the reverse primer-binding site. Bases highlighted in grey at the 3' end of the forward-primer binding site show the lack of the terminal -ATTC-3' bases characteristic of the forward-primer binding site. a) Sequence of FSeq1 as a representation of primer-derived sequences formed by alternating truncations of different regions of the forward primer (green) flanked by primer-binding sites. b) Representative sequence whose core consists of a combination of reverse primer truncations (cyan) and forward primer truncations (green). c) 65ntSeq consisting of a full-length forward primer, lacking the primer-binding site's characteristic -ATTC bases at the 3' end, followed by the full-length complementary of the reverse primer. d) Sequence of R12S91 as a depiction of sequences with full-length forward and reverse primer-binding sites, and with a random core derived from the N42 random library (purple). Small vertical bars separate the primer-binding sites from the core regions in each sequence.

sponded to the sequences from the forward primer and reverse complement of the reverse primer fused together (Figure 3.12). Of note, 60% of the sequenced clones from the purified unknown ~70 nt band sequence pool was also 65 nt long and had the same nucleotide sequence as the 65 nt-long sequences, which in turn represented a 14% of the sequenced clones from the 8^{th} round library. This sequence, which was called 65ntSeq, most likely corresponds to the sole sequence species giving rise to the unknown band seen on agarose gels which was initially thought to be approximately 70 nt in length. The remaining 40% of sequences was a mixture of clones that had either failed at sequencing stage, probably as a result of contamination with truncated sequences, or were truncated versions of 65ntSeq.

To gain a deeper understanding of the progress of binder enrichment of the aptamer library and further study if any the sequencing results from the 8^{th} round library contained sequences whose abundance had been influenced by selective pressures, the library of an earlier selection round was sequenced. For this, 34 clones were selected from the 6^{th} round library, which was considered to be far enough from the start of selection where diversity may still be very high, and not too close to the library from the 8^{th} round, to allow for changes in library composition to be observed. Sequencing of the 6^{th} round library involved an additional library purification step prior to library cloning, in which the double-stranded aptamer library band was excised from a 3% agarose gel, purified, and used as a PCR product for TOPO cloning. This additional library purification step was carried out to minimise the abundance of PCR artefacts corresponding to sequences that may have formed through primer recombination, which made up almost 60% of the sequenced clones from the 8^{th} round library. Sequencing of the clones from the 6^{th} round library revealed 13 sequences of approximately 111 nt in length. Importantly, 3 of these sequences (8.80% of the total number of clones sequenced) consisted of unique random core regions (not primer-derived), flanked by intact full-length primer-binding regions. The remaining 21 sequences were similar to those found in the cloned sequences from the 8^{th} round library, in that their core regions were composed of truncations of the primers, and the forward primer-binding region lacked the 3'-terminal 'AATTC' or 'ATTC'.

Four additional rounds of selection were carried out, after which the library was sequenced to search for sequence enrichment. To increase the stringency and select for high affinity binders, two steps of negative selection against SA-Mag beads and counter selection against γSyn_{1-25} were introduced, together with an increase in the number of washes of the target-aptamer complex from 3 to 4. Sequencing of 103 clones from the 12^{th} round library revealed that 20.4% of the sequences showed a similar length to the N42 aptamer library sequences but featured truncated primer-derived cores with forward primer-binding regions of compromised length and intact reverse primer-binding sites (Figure 3.12). Interestingly, 6 of the sequenced clones (5.83%) consisted of full-length primer-binding regions flanking a random core region, indicating that these sequences originate from the random N42 aptamer library. However, no two copies of the same sequence with a random core region were found within the sequenced clones. Importantly, these 6 sequences were all different to those non-

primer-derived sequences bearing random central regions found upon sequencing of the 6^{th} round library. Of note, sequencing of a pool of 40 additional clones from the 12^{th} round library identified only one new aptamer sequence (2.50% of the total number of newly sequenced clones of this pool), which was proportionately lower than the number of sequences found in the first sequenced pool from the 12^{th} round library.

Sequencing of the aptamer libraries of the 15^{th}, 17^{th} and 20^{th} rounds was done to obtain further information on aptamer enrichment and sequence population distribution. With an increasing number of selection rounds, a larger number of N42 library-derived sequences is commonly expected to be identified as an indication of aptamer enrichment. Surprisingly, sequencing of these three rounds failed at showing an increase in the proportion of the population of N42 aptamers with random cores, compared to the results from the previously sequenced 12^{th} round (except for the 15^{th} round library). In fact, sequencing of each round showed a gradual reduction in the proportion of sequences with random core regions with increasing selection rounds. From the sequenced pool of the 15^{th} round library, only three aptamer sequences belonging to the random N42 library were identified (7.50%), whilst only one (5%) and two (1.90%) of such sequences were isolated from the 17^{th} and 20^{th} round libraries, respectively. The rest of the identified clones from these sequenced pools corresponded to primer-derived sequences. Interestingly, out of all aptamer sequences with random core regions identified throughout selection, R15S15 was the only sequence isolated that was observed in more than one clone, although the two copies of it were isolated from the same round library and not from the sequenced pool of two different libraries.

Particularly surprising were the sequencing results from 18^{th} round library after having carried out NCM-SELEX for six rounds. From a sequenced pool of 51 clones, 28 aptamer sequences were identified as having full-length primer-binding regions and random cores, which accounted for almost 55% of the clones in the sequenced pool (Figure 3.12). Of note, single copies of each sequence were identified, with none of them being repeated within the same sequenced pool. These findings suggest that this library features a high sequence diversity even at advanced selection stages, together with a dramatically smaller proportion of primer-derived sequences, compared to the libraries generated

from SELEX involving exclusively SA-Mag beads as a partitioning method.

a)

	SELEX Library Rounds							
	6th		**8th**		**12th**		**15th**	
Total Number of Clones Sequenced	34	-	77	-	143	-	40	-
Primer-derived Sequences	24	70.6%	63	81.8%	109	76.2%	25	62.5%
N42 Library Sequences	3	8.8%	0	0%	7	4.9%	3	7.5%
Contamination/Low Sequencing Quality	7	20.6%	14	18.2%	27	18.9%	12	30.0%

	SELEX Library Rounds					
	17th		**20th**		**18th NCM**	
Total Number of Clones Sequenced	20	-	105	-	51	-
Primer-derived Sequences	14	70.0%	55	52.4%	9	17.6%
N42 Library Sequences	1	5.0%	2	1.9%	28	54.9%
Contamination/Low Sequencing Quality	5	25.0%	48	45.7%	14	27.5%

b)

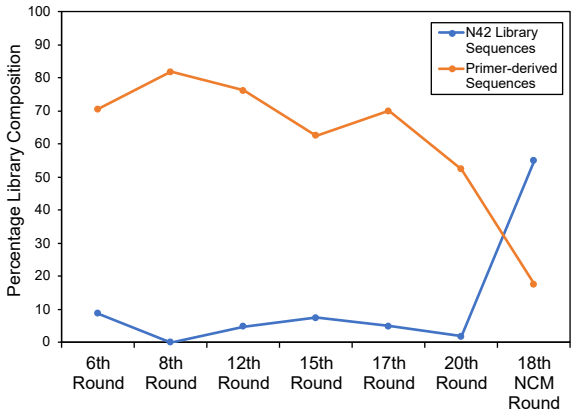


Figure 3.12: SELEX library sequencing statistics. Breakout of the different sequence species identified in the population of the sequenced libraries. *Primer-derived Sequences* refers to those sequences in which the core is formed by truncations of the forward and reverse primers and have an incomplete forward primer-binding site. These sequences are all 90-130 nt long, and hence considered potential aptamer sequences. *PCR Artefacts* refers to those sequences which are shorter or longer than the primer-derived sequences, and which are hence considered to have probably been formed as a result of non-specific PCR amplification and recombination of the primer-derived sequences. *N42 Library Sequences* represent the number of cloned sequences that had a random core, full length forward primer-binding site and which are hence considered to belong to the originally designed N42 aptamer library. *Contamination/Low Sequencing Quality* engulfs all clones that could not be properly sequenced, either as a result of contamination with other clones or errors in the sequencing process. Percentages of each category are shown beside the absolute abundance in each sequenced library, to allow a relative comparison between the sequenced populations.

3.3 Discussion

The highly hydrophobic regions of αSyn oligomers work in synergy to perturb the structure of biological membranes by establishing detrimental protein-membrane interactions. In particular, the lipophilic N-terminal segment of monomeric αSyn has been characterised as having an essential role

in the membrane binding ability of αSyn oligomers. The interaction of this lipophilic element with the membrane represents the first mechanistic step in the process of membrane disruption, as it permits the insertion of the highly hydrophobic oligomeric core into the membrane and the perturbation of the lipid organisation. Efforts to supress the toxicity associated with αSyn are hindered by its structurally dynamic nature, which lacks defined structural motifs, as well as its localisation within the brain, which is protected by a difficult-to-surpass BBB [510]. In this regard, nucleic acid aptamers have emerged as promising therapeutic alternatives to small molecule drugs and antibody-based therapies to target the aberrant cellular interactions of αSyn in PD [259, 260, 261].

The results of the efforts to select DNA aptamers against the lipophilic N-terminal segment of αSyn involved in oligomer membrane binding are discussed below in this subsection.

The conditions of any given aptamer selection are crucial for ensuring the isolation of sequence binders with high affinity and specificity for a given target. For this reason, the initial conditions of the selection of aptamers against αSyn_{1-25} required optimisation of key parameters, namely the ratio between αSyn_{1-25} and aptamer library, the amount of target-capturing SA-Mag beads and the temperature of incubation of these components, based on previous knowledge of aptamer selection [511].

Firstly, the effect of the temperature of incubation on the binding of the library sequences to the target was assessed in terms of the recovery and number of PCR cycles that were required to amplify the library upon test amplification. An incubation temperature of 37 ºC was studied given that the selected aptamers were intended to be used as therapeutic molecules within the human body, of which the average temperature is 37 ºC. Indeed, selecting aptamers at a temperature at which they may eventually be used in the clinic facilitates the identification of candidates that have structural stability at that given temperature and dramatically reduces the possibility of variations in their binding profile, which may be affected by changes in the thermodynamics of the reaction. The significantly smaller number of PCR cycles required to test-amplify the aptamer library after carrying out the selection step at RT, compared to at 37 ºC, suggested a higher recovery of bound sequences after partitioning of

the target-bound aptamers. This may be explained by the increase in protein flexibility and dynamics associated with an increase in temperature, which, combined with the highly flexible conformation of ssDNA molecules and the natively disordered nature of γSyn, renders the chances of a binding event between two highly flexible molecules in an environment with enhanced thermodynamics particularly low. These findings were especially important to establish the incubation temperature for the initial rounds of selection, as a low sequence recovery associated to a high temperature of incubation could be indicative of a small number of target-binding events at early stages of selection, which may lead to the rapid loss of sequence diversity from the initial library. Therefore, a low sequence recovery, especially in the initial rounds of selection, may compromise sequence diversity too early in the selection process, thereby jeopardising the successful identification of binders.

Unexpectedly, optimisation tests involving incubation at molar ratios of 1:1 and 1:50 of target to aptamer library revealed the recovery of a smaller fraction of target-bound aptamer sequences after incubation at the former ratio. Particularly interesting is the fact that a higher recovery was observed after incubation at a 1:50 molar ratio, despite the higher level of competition between sequences for target binding events. This is consistent with the observation that an excess of SA-Mag beads results in a larger number of PCR cycles being required for library amplification, suggesting that large amounts of magnetic particles may be hindering target binding and therefore the recovery of sequences with affinity for the target. Indeed, a molar ratio of incubation of 1:50 effectively requires a smaller amount of SA-Mag beads compared to what is required for a 1:1 incubation ratio, as a smaller amount of peptide target is used and hence required to be captured. The high concentration of bulky particles in the reaction mixture may physically interfere with the establishment of interaction events between the target and the library sequences, thereby preventing the recovery of as many bound aptamers in the presence of large amounts of SA-Mag beads as when smaller amounts are present. This is consistent with the results from the amplification tests involving a 1-, 5- and 10-fold amount of SA-Mag beads relative to that of the peptide target, which showed that an excess of magnetic particles compromised the recovery of bound sequences.

Following the results from the optimisation tests using γSyn_{1-25} as a target peptide and considering

the first rounds of selection against αSyn_{1-25}, the initial aptamer selection conditions were set to a 1:100 molar ratio of target:library at RT, using a 1-fold amount of SA-Mag beads to that of peptide to be captured (no excess). Despite the optimisation of the initial conditions and of the PCR amplification cycles on a roundly basis, the formation of nonspecific PCR by-products in the form of both longer and shorter sequence products was observed after only a few rounds of selection. These sequences arise as a result of primer-product and product-product annealing during iterative cycles of PCR amplification, especially of libraries composed of sequences bearing random regions [507], like aptamer libraries. Through the disruption of the sequences of the primer-binding regions, as well as the core random regions of aptamers, these PCR artefacts may ultimately populate the library and outcompete aptamer sequences for resources such as dNTPs and primers. As a result, PCR by-products of libraries that are carried over onto consecutive rounds of *in vitro* evolution are considered to be "parasitic" [507], as they may compromise the enrichment of high-affinity binders.

As observed in the results from the test amplification experiments from each round of selection, regular purification of the libraries to remove these non-aptamer PCR by-products is essential to prevent them from overrepresenting the sequence population and jeopardising selection. Removal of these by-products through ssDNA purification at every round after PCR amplification led to a higher recovery of aptamer-sized products at the following round, as shown by single library bands on an agarose gel upon test amplification. This prevented the accumulation of by-products and permitted the artefact-free progression of further selection rounds. Given that the generation of unwanted PCR artefacts is known to be a common pitfall of aptamer selection strategies involving large cycles of PCR amplification, alternative methods to minimise by-product formation have been proposed, such as specific primer design or emulsion PCR [512]. Here, water-oil separation creates droplets which behave as compartments with single sequence templates within them, thereby dramatically reducing the chances of primer-product and product-product hybridisation.

Throughout the various rounds carried out, selection was made more stringent by mainly increasing the total volume of buffer washes of the target-bound complex. Similarly, by increasing the ratio of incubation between the target and the library, sequences are forced to compete for binding to the tar-

get peptide, resulting in only the ones with the highest affinities being able to establish an interaction event. In NCM-SELEX, stringency of selection was also tuned by effectively increasing the molar ratio of incubation between the target and library, but not the volume of buffer washes. Given the low amount of protein target used and its characteristically small, disordered structure, αSyn may not adsorb onto the NCM as well as a large globular protein. A larger number of washes could therefore subject the bound complex immobilised on the NCM to a greater mechanical stress that may consequently lead to the loss of target and any bound sequences. Instead, the time of incubation between target and library was gradually decreased to favour the binding of ligands with faster association kinetics and remove low-affinity binders.

Negative and counter selection steps were also introduced as a means of removing nonspecific binders, with the aim of increasing the selectivity and affinity of the binding aptamer sequences [513, 514, 515]. By using counter-target analogues that closely resemble the desired target in either structure or sequence (as is γSyn_{1-25} to αSyn_{1-25}), every sequence that shows binding affinity for γSyn_{1-25} will be effectively removed from the library, thereby increasing the binding specificity for αSyn_{1-25} [516, 513, 514]. Conceptually similar to counter selection, negative selection uses molecular components that are unavoidably present in the selective environment, such as SA-Mag beads or NCM, to discard binders that nonspecifically interact and are adsorbed by the matrix support used for immobilisation of the selection target. Indeed, negative selection has been shown to result in the isolation of sequence binders that have a 10-fold higher binding affinity compared to those sequences identified without any negative selection cycles [516, 515].

Particularly surprising was the formation of 65ntSeq at every round of selection, given that the constant primer-binding sites of the N42 random library, as well as the primers used for amplification, were established sequences that had previously been used in the selection of aptamers against different targets [511]. The 65ntSeq sequence, named after obtaining further information on its composition following sequencing results, was first observed upon electrophoresis analysis of the library of the 3^{rd} round of selection. As shown by the increasing intensity of its band on an agarose gel upon test amplification, its relative abundance appeared to increase as selection progressed and with rising

PCR amplification cycles. These observations suggested that the sequences responsible for such a band contained, at least partially, primer-binding regions to which the primers that were being used during amplification could anneal and exponentially amplify that band, which was later confirmed by sequencing. The fact that 65ntSeq is most likely the only sequence species responsible for the ∼70 nt band observed in agarose gels, together with its characteristic sequence composition, suggest that this sequence is being formed independently of the selection of the aptamer library and that this likely happens as a result of sequence complementarity and amplification. Alternatively, putative innate binding affinity of the individual primers for the target or the SA-Mag beads may have promoted a close primer interaction, thereby facilitating the formation of 65ntSeq.

Results from PCR amplification tests in which the annealing temperature was increased from 45 to 56 ºC failed at preventing the formation of the bands corresponding to 65ntSeq and larger by-products. This change in PCR conditions was studied with the aim of minimising nonspecific annealing events. Similarly, the use of a truncated form of the reverse primer lacking both terminal 'AA' bases did not show a reduction in the formation of 65ntSeq, suggesting that it is unlikely that this sequence is being generated through the complementary annealing of the truncated terminal bases of the reverse primer to the 3' deoxyadenosine from the forward primer.

The non-template-dependent terminal transferase activity of Taq polymerase, by which a single dA is added to the 3' end of PCR products, was also studied as an alternative possible mechanism responsible for the formation of 65ntSeq without base overlap between the sequences of the forward and reverse primers. Prior to amplification by PCR, primers are present at a comparatively high concentration in the amplification mixture relative to the library sequences recovered after a selection round. It has therefore been hypothesised that during the first few PCR amplification cycles, Taq polymerase may be recognising the primers as sequences to be amplified, given their wide availability compared to the library sequences, which may result in the addition of 3' overhang single dA's on double-stranded primer products. This overhang base at the 3' end of a forward primer may have complementarily annealed to the reverse complement of the reverse primer, thereby forming a construct composed of the sequence of the forward primer followed by that of the reverse primer, without the need for

base complementarity between their own sequences. This mechanism could predictably explain the formation of 65ntSeq, by which both primers come together into a new sequence with the final base count being the sum of the base counts of the individual sequences. In the absence of an additional overhang base mediating complementary sequence hybridisation (3' A from the forward primer and 5' T from the reverse primer), annealing and amplification of the forward and reverse primers would result in a sequence with a base count sum smaller than the sum of their individual base counts, as a result of the necessary overlapping of their sequences.

Results from a test amplification carried out using Q5 polymerase, which lacks 3' dA transferase activity, rejected the proposed mechanism, as the band corresponding to the 65ntSeq sequence was still observed. It is worth noting that the effect on the formation of 65ntSeq of amplification by Q5 polymerase using the truncated form of the reverse primer was not studied. By combining these two changes in the amplification conditions, the addition of terminal dA overhangs may have been hindered, minimising the possibility of resulting in the annealing of the forward and reverse primers. It should be noted, however, that changes in the sequence of the reverse primer at advanced stages of selection may not have an effect in the formation of 65ntSeq, given that the aptamer library is already contaminated by even low copy numbers of such a sequence. This means that using the truncated form of the reverse primer for test-amplifying a library containing even low copy numbers of the 65ntSeq within the pool may result in the truncated form of the primer still amplifying these few copies of 65ntSeq, which may then act as precursors for further amplification.

Sequencing results from the 6^{th}, 8^{th} and 12^{th} round libraries showed a high abundance of sequences formed by truncations of the forward and reverse primers. These results suggest that these sequences may form the bulk of the library, instead of the sequences with random core regions which are the ones that would have been expected to populate the sequence pool based on the design of the N42 random library. These sequence species, some of which were longer, similar or shorter in size than the expected 111 nt-long aptamer library products may correspond to the PCR by-product bands observed upon electrophoresis at every selection round. Their formation may have been triggered by the accumulation of products of recombination from primer-product or product-product annealing throughout

iterative rounds of selection and amplification. Purification of the library at every round successfully removed the sequence artefacts that were longer than the N42 library sequences, but failed at removing those sequences that may have been formed by primer truncations and which had a similar size to the library sequences, as these were indistinguishable from the aptamer library sequences in terms of size. These sequences, which may have therefore remained in the library "disguised", may have acted as precursor seeds for the further elongation of primer-derived sequences in following rounds of selection. The fact that these sequences are formed by truncations of the primers used for amplification may have given them an evolutionary advantage compared to the N42 library sequences, as the readily available primers in every amplification reaction may have contributed to their ease of amplification (PCR bias).

Particularly interesting was the fact that primer-derived sequences could be divided into two subgroups: those whose core regions begin with truncations of the forward primer at the 5' end, following the forward primer-binding region, and those whose core regions start with truncations from the reverse complement of the reverse primer. These characteristic truncation patterns may have been a result of random recombination events, where the formation of particular sequence patterns may have depended on the availability of the primers to serve as templates. Indeed, the fact that sequences identified have similar truncation patterns but different lengths further supports the notion that PCR recombination events are responsible for the formation of primer-derived sequences. Similarly, the fact that multiple copies of some of these primer-derived sequences were observed may be the result of some being more readily amplifiable than others, due to variations in the particular conditions of the reaction mixture (e.g., differences in the abundance of certain dNTPs).

Three sequences bearing random core regions and full-length primer-binding regions were identified upon sequencing of the 6^{th} round library. This suggests that these sequences originate from the starting N42 library and not as a result of primer recombination. Interestingly, this finding strongly contrasts to the sequencing results from the 8^{th} round library, where no sequences with random core regions were found, despite the comparatively larger sequencing sample. This may at least partly be explained by the purification of the dsDNA sequences from 6^{th} round library prior to cloning,

which made aptamer-sized products more readily available for ligation with the pCR™2.1-TOPO vector. For this reason, the lack of a purification step of the 8^{th} round library to remove large PCR by-products prior to sequencing may have provided an unrealistic estimate of the library composition, by overestimating the presence of sequences with truncated primer regions, whilst also underestimating the abundance of N42 library sequences. Additionally, the aptamer sequences bearing random core regions that were identified after sequencing of the 6^{th} round library were not observed upon sequencing of the 8^{th} round library, possibly as a result of the expected reduction in sequence diversity that comes with an increasing number of selection cycles. Sequences showing low binding affinity for the target – as may have been the case with these identified aptamer sequences – may have been lost from the library as a result of the selective pressures from the two additional rounds of selection.

However, the fact that only primer-derived sequences were identified upon sequencing of the 8^{th} round library suggests that these sequences may represent the dominating sequence population. These may have outcompeted the population of N42 library aptamers and compromised their selection as a result of the enhanced ease of amplification of primer-derived sequences in the presence of a primer supply. Of note, all primer-derived sequences from the 8^{th} round library have truncated forward primer-binding regions, where the 3' end 'ATTC', or sometimes 'AATTC', was missing. Indeed, these 3' terminal bases represent a distinguishing feature that is only present in the sequence of the forward primer-binding site of the N42 library sequences and not in that of the forward primer. This indicates that this 5' region observed in primer-derived sequences most likely corresponds to the sequence of the forward primer, rather than to the forward primer-binding site flanking at the 5' end of the randomised core of the N42 aptamer library, suggesting that the forward primer may have acted as a template for the initiation of amplification of primer-derived sequences. Therefore, even if these sequences have a similar length to that of the 111 nt-long aptamer sequences, they possibly formed through nonspecific recombination events during the amplification reaction itself, in which the forward primer acted as a seed for their generation, instead of having been selected for their affinity for the target from the initial combinatorial N42 library.

Remarkably, none of the N42 aptamer sequences with random core regions that were isolated from

the 12^{th} round library corresponded to any of the 3 sequences that were identified upon sequencing of the 6^{th} round library. This observation was most likely a consequence of the small sequencing sample size, which may have largely underestimated sequence diversity, as an estimated 10^{15} DNA molecules are predicted to form a selection library. Importantly, the amplification advantage of primer-derived sequences may have masked the population contribution of sequences that are not as readily amplified, such as those with random core regions, thereby making them be easily missed upon sequencing as a result of their low copy number. The seven sequences identified after 12 rounds of selection may have predictably been selected throughout the selection rounds for their affinity to the αSyn_{1-25} target peptide. The consequent enrichment of these sequences may have yielded enough copy numbers for them to be observed upon sequencing of a small sample size, suggesting that these aptamers may constitute a subpopulation with higher affinity than the sequences identified in the 6^{th} round library, which may have been outcompeted for their binding affinity to the target during these additional six rounds of selection.

However, it is highly likely that other sequences belonging to the N42 library with random core regions are also present in the 12^{th} round library, which may have not been observed as a result of the small sequencing sample size. Interestingly, sequencing of 40 additional clones of the 12^{th} round library revealed a lower proportion of aptamer sequences with random core regions compared to the first pool that was sequenced from the 12^{th} round library. This finding may be explained by the fact that the newly sequenced pool was obtained by reamplifying an existing stock of the 12^{th} round library, which may have therefore favoured the formation of primer-derived sequences following iterative PCR amplification. The very small difference in the relative proportion of aptamer sequences identified in the two sequenced pools may be a product of chance, however, given the large error associated with the small sequencing sample size that was used to inform on the population distribution of the entire library.

Sequencing of several round libraries throughout SELEX was done as a way to monitor selection and aptamer enrichment. However, sequencing data failed to show the enrichment of target-binding aptamers with increasing selection rounds, by which an increase in the copy numbers of sequences with

affinity for the target and their assembly into clusters were expected to be observed. Instead, sequence diversity remained high until later stages in selection, indicating a lack of sequence enrichment. Comparatively, the libraries from the 6^{th}, 12^{th} and 15^{th} rounds contained the largest proportion of aptamer sequences, based on sequencing data. Interestingly, later rounds of selection were associated with a decrease in the proportion of these sequences in their libraries, whilst that of primer-derived sequences was observed to increase, suggesting that aptamer enrichment may have been compromised by an excessively large number of selection rounds that had been carried out on the library. Given the high sequence diversity observed in the libraries of rounds 6, 12 and 15, it is likely that the affinity peak might have been reached in some library at this approximate stage of selection, with those sequences showing the highest binding affinities for the target having been enriched up to that library. The affinities of these sequences, however high, may have not been able to withstand the increase in selective pressures that were introduced at later rounds, which may have resulted in their loss from the library. This would explain the extremely low abundance of aptamer sequences and the large proportion of primer-derived sequences in the libraries of the 17^{th} and 20^{th} round, compared to previous sequenced libraries. However, the error associated with sequencing small sample sizes makes estimating the population distribution of a particular library especially challenging, suggesting that differences in the proportion of identified aptamer sequences between all sequenced libraries may not be significant and may just be a product of variation.

Particularly intriguing is the fact that sequence subpopulations were not identified upon sequencing of the 6^{th}, 12^{th} and 15^{th} round libraries. The establishment of sequence clusters within a sequence pool usually indicates the enrichment of a subpopulation of sequences with affinity for the target [504]. Instead, single copies were observed of the sequences that were identified, except for R15S15. Whilst it is true that no signs of aptamer enrichment were detected throughout selection and sequencing, the small size of the sequenced sample of each round library may have skewed the observed results. Therefore, the presence of multiple copy numbers of binding aptamers within the sequence pool may have been underestimated in favour of the more abundant primer-derived sequences, for which next-generation sequencing may have provided further insights.

Modifying the method of partitioning during selection, by which SA-Mag beads were substituted by an NCM, had a dramatic effect in the sequence composition of the library. Surprisingly, more than half of the identified sequences from the 18^{th} round library after NCM-SELEX were estimated to correspond to aptamer sequences belonging to the N42 library featuring random core regions. Despite the large number of selection rounds performed, sequence diversity was still exceptionally high, and no sequence was observed to be repeated within the sequenced clones, suggesting that aptamer enrichment had not occurred. Interestingly, the identified 28 different aptamer sequences must have already been present in the 6^{th}, 8^{th}, and 12^{th} round libraries of SELEX performed with SA-Mag beads, suggesting that these sequences had previously not been detected possibly because they had been masked by the more abundant primer-derived sequences, as well as a result of the small size of the sequenced pool. Indeed, the fact that these sequences were only detected after 18 rounds of selection shows that they were able to withstand the imposed selective pressures, suggesting binding affinity for the target αSyn_{1-25} or αSyn. Remarkably, the reduction in the population proportion of primer-derived sequences in the 18^{th} round library may correlate with the removal of SA-Mag beads from the selection environment, indicating that these sequences or the constituting individual primers themselves may have affinity for streptavidin.

Aptamer Characterisation

4.1 Introduction

Nucleic acid aptamers have recently emerged as promising therapeutic agents by constituting a class of high affinity recognition molecules, which have similar characteristics to antibodies but are also able to overcome some of the hurdles of this technology. Their small size and low immunogenicity make aptamers ideal candidates as potential therapeutic molecules that can bind to targets which are challenging to reach, as are, for instance, protein aggregates in the brain, where a robust BBB prevents the entry of bulky macromolecules. In this sense, aptamers must have a high affinity comparable to that of antibodies (in the nM to pM range) to be able to recognise binding moieties.

As a result of their innate ability to complementary base pair, single-stranded nucleic acid sequences can fold back on themselves and adopt specific three-dimensional structures that can recognise specific target motifs. To establish these interaction events, they form networks of electrostatic salt-bridges, hydrogen bonds, Van der Waals and pi-stacking interactions that give them their characteristic secondary and tertiary conformations (stem loops, hairpin, pseudoknot and G-quadruplex) [236]. The combination of sequence composition and base distribution, as well as solution conditions such as temperature, ionic strength and the presence of specific ions that aid in the folding process like Mg^{2+} forms the structural basis of the recognition surfaces of aptamers, which dictate the affinity and

specificity of their binding.

To date, two research groups have successfully reported the selection of high-affinity aptamers against αSyn [259, 260, 261]. The first DNA aptamer showing affinity for both αSyn monomers and oligomers was generated by Tsukakoshi et al [261]. Later, by using a modified selection strategy, the same group identified eight aptamers that showed affinity for β-sheet-rich architectures present in both αSyn and Aβ oligomers [260]. Similarly, Zheng et al. were recently successful at isolating two high affinity DNA aptamer sequences against monomeric αSyn, which were shown to reverse aggregation and trigger the degradation of αSyn aggregates *in vitro* [259].

Whilst these findings are remarkable and mean a stepping stone in the field of aptamer selection for neurodegenerative diseases, such aptamer selection strategies against αSyn did not bear structural considerations in their design. Selection of aptamers against protein oligomers has the risk of isolating sequences that may have affinity for a specific oligomeric conformation, but which may not recognise a different oligomeric species of the same protein with the same affinity. This variability comes as a result of the intrinsic heterogeneity associated with the conformation of different strains of a specific protein aggregate oligomeric species. These may be formed by a varying number of monomeric copies of a specific protein, or may simply have a different conformation depending on the recombinant expression protocol used for their production or whether they might have been isolated from cultured cells or *in vivo* tissue. In fact, the conformation of oligomeric aptatopes may at the same time be different for the same protein species but also similar for oligomers of different proteins as a result of shared structural motifs (e.g., β-sheet-rich structures) that may lead to cross-reaction of selected aptamers.

The elusive nature of these toxic agents renders the generation of therapeutic molecules for neurodegenerative diseases like PD particularly difficult. As discussed in the introduction Chapter of this thesis, the N-terminal region of monomeric αSyn appears to be critical in the establishment of aberrant interactions of αSyn oligomers with membranes [82], which can lead to their disruption and ultimately cause cytotoxicity in neurons. Therefore, by exploiting the structural knowledge of the

mechanism of toxicity of αSyn oligomeric aggregates, it may be possible to select aptamers that bind to a structural moiety that may be key for the generation of toxicity in all αSyn oligomeric species.

In this effort, aptamers that are selected against the critical lipophilic N-terminal segment of αSyn (first 25 residues) must have their binding characterised, to provide information on the binding modes and interacting residues within the whole protein sequence.

4.2 Results

With the aim of obtaining a better understanding of the sequencing results and assessing the performance of the DNA sequences as aptamers, the sequences isolated from the different SELEX round libraries that were sequenced were characterised for the binding to both αSyn_{1-25} and full-length αSyn. The binding of the candidate aptamers was first measured using ELONA. Here, modified aptamer sequences carrying a 5'-fluorescein dT modification were incubated with the immobilised αSyn_{1-25} on streptavidin, and the extent of retention and, therefore binding, was measured in the form of absorbance at 450 nm by using an anti-fluorescein-HRP antibody, which reacts with TMB substrate to give a colourimetric output (Figure 4.1b). Protein NMR was used alongside ELONA to provide residue-specific information on the binding of the aptamer sequences that showed the most remarkable binding curves with the highest dissociation constants. Binding was also assessed using FRET in a setting in which aptamers and αSyn were free in solution in the absence of an immobilisation platform. The characterisation of the isolated aptamer sequences is outlined here organised by the different round libraries from which they were identified.

4.2.1 8^{th} Round

Out of all sequences identified after cloning and sequencing 77 clones from the 8^{th} round library, two sequences that were considered representative of the sequenced pool were chosen to be synthesised: FSeq1 and 65ntSeq (Table 2.1). FSeq1 is composed of truncations of the forward primer, whilst 65ntSeq is formed by the joint sequences of the forward primer and the reverse complement of the reverse primer. The sequence 65ntSeq was particularly interesting, as it is thought to exclusively

contribute to the formation of the non-library band that was observed to repeatedly form and that was visible just under the 70 nt ladder mark after analysing each round library by gel electrophoresis.

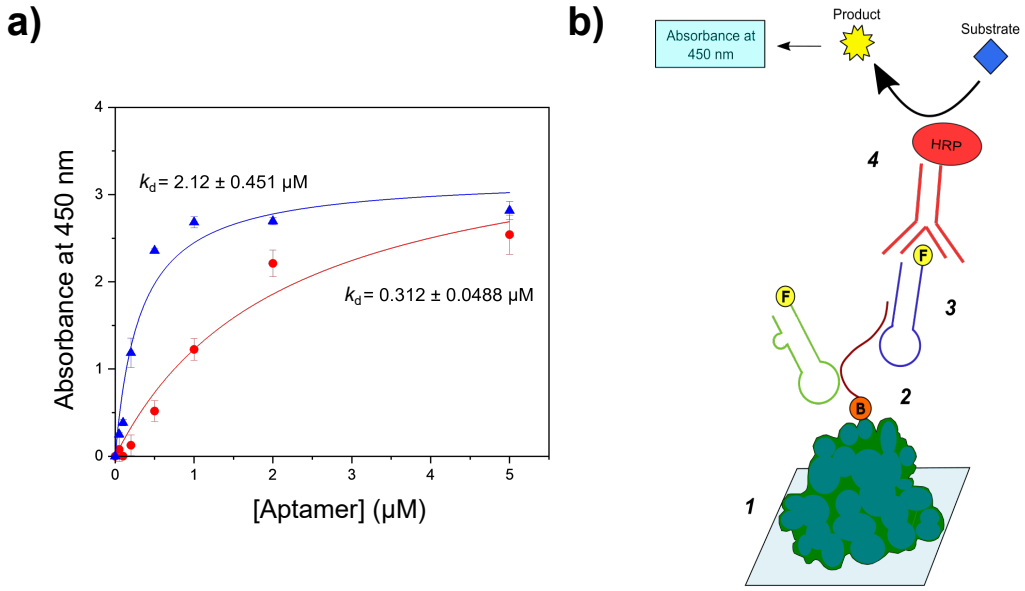


Figure 4.1: Characterisation of the binding of the primer-derived FSeq1 and 65ntSeq identified upon sequencing of the 8^{th} round library. a) Binding of FSeq1 (red) and 65ntSeq (dark blue) in the presence of αSyn_{1-25} measured with ELONA. b) Schematic of the ELONA binding set-up involving streptavidin (1) coated on a transparent 96-well plate, the biotinylated αSyn_{1-25} peptide target (2), 5'-fluorescein-coupled aptamer sequences (3), and an anti-fluorescein-HRP antibody (4) that catalyses the reaction of TMB to give a colourimetric output. k_d values for each condition are specified. ELONA was performed at RT in ABB. Error bars represent the standard error in the measurements.

The binding of the sequences FSeq1 and 65ntSeq to αSyn_{1-25} was assessed by ELONA, which showed that their binding curves produced affinities in the low μM range (Figure 4.1). Interestingly, 65ntSeq was identified as having the highest affinity, with a calculated dissociation constant, k_d, of 0.312 ± 0.0488 μM, about an order of magnitude higher than FSeq1, in the mid-lower nM range. FSeq1 presented a slightly higher binding constant of 2.12 ± 0.451 μM, corresponding to a lower binding affinity. Calculation of the k_d of FSeq1 most likely did not represent the actual binding constant of the interaction, given that a plateau indicating saturation of binding was not reached, as seen by the gradual and steady increase in absorbance values beyond aptamer concentrations of 5 μM. In contrast, the binding curve of 65ntSeq almost reached an absorbance plateau, which indicated a reduced effect in the recorded absorbance from an increase in the concentration of aptamer, thereby representing a better fit to the binding model.

A negative control in which the 65ntSeq sequence was incubated in streptavidin-coated plates in the absence of αSyn_{1-25} peptide was carried out to obtain further information on the binding mode of 65ntSeq (Figure 4.2a). This resulted in a binding curve that was almost superimposable to that in the presence of αSyn_{1-25}, indicating a very similar binding mode. This suggests that 65ntSeq may be binding exclusively to either streptavidin or nonspecifically to the walls of the plate, rather than to the peptide target, given that its dissociation constant under these two conditions was almost identical.

With the aim of obtaining further information on the binding partner of 65ntSeq and investigate the putative lack of binding affinity for the αSyn_{1-25} peptide, ELONA was performed in the absence of streptavidin (Figure 4.3a). A clear MaxiSorp™ 96-well plate was coated and blocked with BSA blocking solution and the 65ntSeq sequence was incubated following the usual protocol, after which the absorbance of the HRP-TMB reaction was read. This resulted in maximum absorbance values that were one-third smaller than those observed after incubation of 65ntSeq with streptavidin or streptavidin and αSyn_{1-25}, suggesting that sequence retention was greatly reduced in the absence of streptavidin. The binding curves appeared to slowly plateau at higher aptamer concentrations, although this probably does not reflect the actual binding mode. Instead, absorbance data seem to follow a linear increase characteristic of nonspecific binding, which were forced through the model and generated binding curves that appear to reach saturation at a low absorbance output. These findings indicate that 65ntSeq most likely specifically binds to streptavidin, and not αSyn_{1-25} or the walls of the plate nonspecifically.

To investigate the effect of the anti-fluorescein-HRP antibody dilution on absorbance signal output, this experiment was carried out using two different antibody dilutions, namely 1:500 and 1:1000 (Figure 4.3). The higher dilution, as expected, generated lower absorbance readings with a smaller distribution in the data repeats, compared to an antibody dilution of 500. However, the error in each point meant that both datasets could be superimposed and that there was no effective difference between the two. This indicated that, within this dilution range, a noticeable increase in nonspecific sequence binding was not detected and confirmed that the 1:500 dilution used in the standard ELONA protocol was adequate for measuring the dissociation constants of the various isolated aptamer sequences.

To confirm that 65ntSeq does not show binding affinity for αSyn_{1-25}, ^{1}H-^{15}N HSQC NMR spectra were collected of the full-length αSyn in the presence of the 65ntSeq sequence at various molar ratios

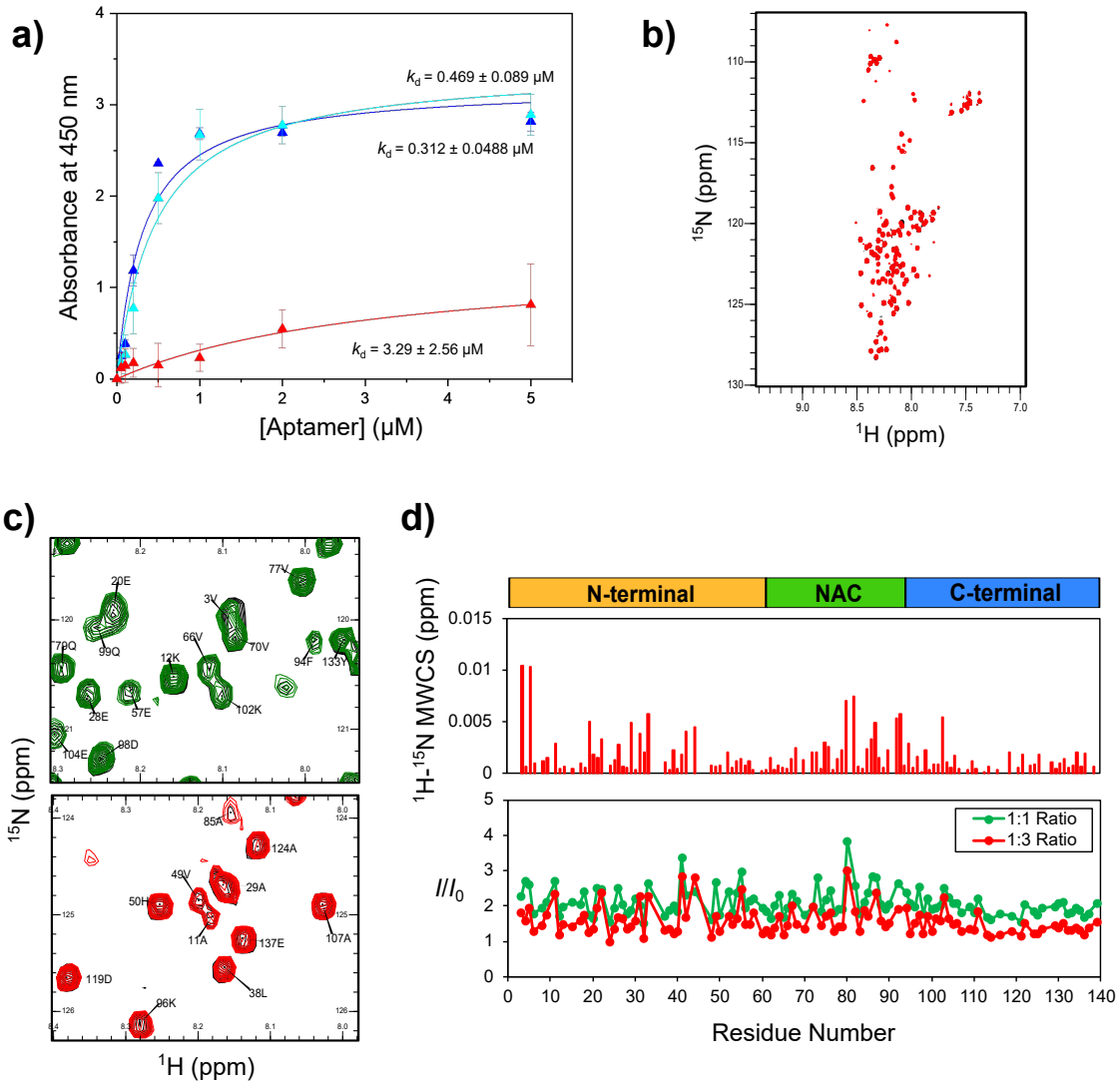


Figure 4.2: Characterisation of the binding of 65ntSeq. a) Binding of 65ntSeq in the presence (dark blue) and absence (light blue) of αSyn_{1-25}, and in the absense of streptavidin (red) measured with ELONA. k_d values for each condition are specified. ELONA was performed using streptavidin-coated 96-well plates to which the biotinylated αSyn_{1-25} peptide was bound, whilst binding assays not involving streptavidin were carried out using standard MaxiSorp 96-well plates. ELONA was performed at RT in ABB. b) Overlay of ^{1}H-^{15}N HSQC spectra of αSyn (50 μM) in the absence (black) and presence (red) of a molar ratio of 1:3 of αSyn to 65ntSeq (150 μM), showing no significant changes in the chemical shifts or intensities of the residue cross-peaks. c) Representative close-ups of αSyn residue cross-peaks showing the absence of significant changes upon incubation with a 1- (green) and 3-fold (red) molar excess of R12S91. d) ^{1}H-^{15}N MWCS of αSyn in the presence of 65ntSeq at a 1:3 molar ratio (50:150 μM) and I/I_0 of αSyn residue cross-peaks upon incubation with 65ntSeq at a 1:1 and 1:3 molar ratio (50:150 μM). Experiments were recorded at 25 ºC using αSyn in ABB. Error bars represent the standard error in the measurements.

(Figure 4.2b-d). This experiment provides residue-specific information and therefore constitutes a more sensitive method to probe any interaction events that may be occurring between 65ntSeq and the first 25 residues of αSyn against which the DNA library is being selected. Monomeric full-length αSyn and aptamer were incubated at 1:1 and 1:3 molar ratios of protein:aptamer. Analysis of the recorded spectra revealed an almost perfect overlay in the presence and absence of 65ntSeq. Changes in the intensity of some of the peaks were observed, although the magnitude of these is probably not indicative of a binding interaction (Figure 4.2c and d). Particularly interesting is the systematic increase in peak intensity upon incubation of αSyn with 65ntSeq at both incubation ratios compared to free protein, observed along the entire length of the protein in exception of the C-terminal region, whose residues did not experience peak intensity changes under any of the two incubation ratios investigated.

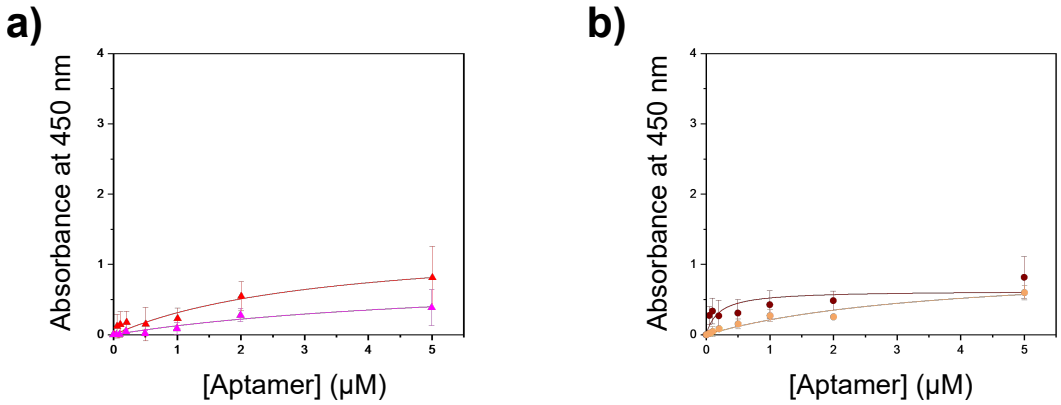


Figure 4.3: Characterisation of the binding of 65ntSeq and R12S91 in the absence of streptavidin using different antibody dilutions. a) Binding curve of 65ntSeq in the absence of streptavidin, using a 1:500 (red) and a 1:1000 (magenta) dilution of the anti-fluorescein-HRP antibody. b) Binding curve of R12S91 in the absence of streptavidin, using a 1:500 (wine red) and a 1:1000 (light orange) dilution of the anti-fluorescein-HRP antibody. Neither of the two sequences showed specific binding affinity to the plates in the absence of streptavidin. No major difference was observed in the absorbance after incubation of an anti-fluorescein-HRP antibody at the different dilutions tested. The sequences were incubated in clear 96-well Maxisorp plates that had been blocked with BSA blocker solution. ELONA was performed at RT in ABB.

Indeed, the spectrum recorded at the highest protein:aptamer ratio of 1:3 did not show any differences in the magnitude or extent of peak intensity or chemical shift changes compared to that recorded at an equimolar incubation ratio, despite a higher concentration of 65ntSeq sequence being present. Changes in the residue chemical shifts were seen concentrated around the mid N-terminal and NAC regions, although these were all extremely small under 0.01 MWCS. Overall, this indicated the ab-

sence of a specific binding interaction, with minimal changes in peak intensities and chemical shifts being most likely attributed to pH changes upon sequence addition or nonspecific isolated electrostatic interactions of αSyn with the highly negatively charged DNA backbone. Consistently, the changes observed in the recorded NMR spectra do not correspond to a measured dissociation constant of ∼300 nM and, together with the results from ELONA in the absence of αSyn_{1-25} and streptavidin, these findings confirm that 65ntSeq does not bind αSyn_{1-25} or αSyn, and therefore most likely interacts with streptavidin.

4.2.2 12^{th} Round

Sequencing of the library after 12 rounds of selection revealed several aptamer sequences containing a random core region, as well as many that were composed of primer truncations. The binding affinity of six aptamer sequences with random core regions most likely belonging to the initial N42 library was assessed by ELONA (Figure 4.4). Out of these six sequences, R12S91 and R12S24 showed moderate affinity in the presence of the αSyn_{1-25} peptide (k_d= 0.596 ± 0.112 μM and k_d= 1.05 ± 0.311 μM, respectively). In particular, binding data of R12S91 produced a binding curve that fits to the hyperbolic binding model that was used better than R12S24. The rest of the sequences investigated had calculated dissociation constants in the range of 2 μM or higher. To validate these results and confirm the binding interaction of R12S91 with αSyn_{1-25}, a negative control was carried out in which binding of R12S91 was measured in the absence of the peptide target. This resulted in a slight decrease in affinity (k_d= 1.61 ± 0.379 μM), which suggests that R12S91 may be interacting with αSyn_{1-25} (Figure 4.4g). In the absence of αSyn_{1-25}, the rest of the investigated sequences showed similar dissociation constants compared to in the presence of the peptide target, suggesting a lack of specific affinity for αSyn_{1-25}. Of note, incubation of R12S16 and R12S55 with streptavidin in the absence of the peptide target resulted in smaller dissociation constants, indicative of a lack of binding for αSyn_{1-25}. Interestingly, R12S15 and R12S24 presented larger k_d values, showing an impaired binding in the absence of the target peptide, and hence suggesting binding affinity for αSyn_{1-25}.

To discard nonspecific binding of R12S91 with the walls of the plate wells, its binding affinity was investigated in the absence of both αSyn_{1-25} (Figure 4.5a) and streptavidin (Figure 4.3b and 4.5a).

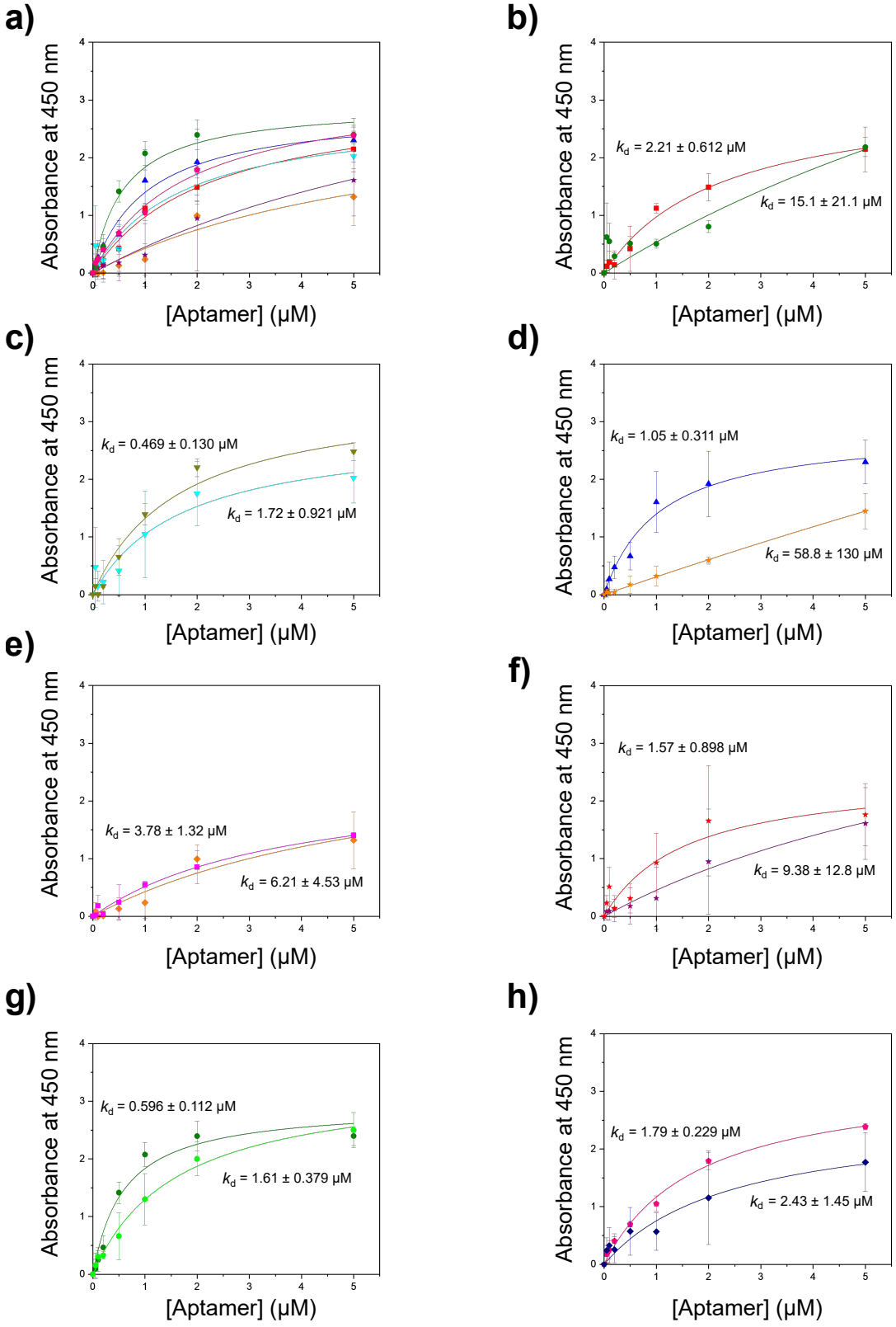


Figure 4.4: Characterisation of the binding of the six aptamer sequences identified upon sequencing of the 12^{th} round library. a) Binding of R12S15 (red), R12S16 (light blue), R12S24 (dark blue), R12S29 (orange), R12S55 (purple), R12S91 (dark green) and R12S93 (pink) in the presence of αSyn_{1-25}. b) Individual binding curves of R12S15 in the presence (red) and absence of αSyn_{1-25} (dark green). c) Individual binding curves of R12S16 in the presence (light blue) and absence of αSyn_{1-25} (olive green). d) Individual binding curves of R12S24 in the presence (dark blue) and absence of αSyn_{1-25}

Figure 4.4: (orange). e) Individual binding curves of R12S29 in the presence (orange) and absence of αSyn_{1-25} (magenta). f) Individual binding curves of R12S55 in the presence (purple) and absence of αSyn_{1-25} (red). g) Individual binding curves of R12S91 in the presence (dark green) and absence of αSyn_{1-25} (light green). h) Individual binding curves of R12S93 in the presence (pink) and absence of αSyn_{1-25} (navy). k_d values for each condition are specified. ELONA was performed using streptavidin-coated 96-well plates to which the biotinylated αSyn_{1-25} peptide was bound. ELONA was performed at RT in ABB. Error bars represent the standard error in the measurements.

Binding data revealed a linear dependency in which absorbance increased with increasing aptamer concentration, together with a reduction of approximately one-third of the maximum absorbance values, compared to in the presence of streptavidin or streptavidin and αSyn_{1-25}. Two anti-fluorescein-HRP antibody dilutions of 1:500 and 1:1000 were used to investigate any nonspecific effect the antibody dilution may have in this concentration range in the colourimetric output recorded. The fact that the binding curves produced under both conditions were almost identical was consistent with the results from the two antibody dilutions investigated in the binding of 65ntSeq to the plate, thereby discarding any antibody dilution-dependent artefacts on the absorbance values recorded. At the same time, these data validated the adequacy of these antibody concentrations for other ELONA experiments. Although the binding data were forced into the model in order to produce a binding curve, the observed linearity and the fact that a binding saturation plateau was not reached indicate that the calculated dissociation constants for the binding in the absence of streptavidin at both a 1:500 and 1:1000 antibody dilution do not reflect the actual affinity of the binding interaction (k_d= 0.199 ± 0.121 μM and k_d= 3.70 ± 1.47 μM, respectively). These findings indicate that R12S91 is not binding nonspecifically to the walls of the 96-well plates where ELONA is carried out, and suggest that its observed binding affinity is possibly a result of binding events with αSyn_{1-25}, streptavidin or a combination of both molecules.

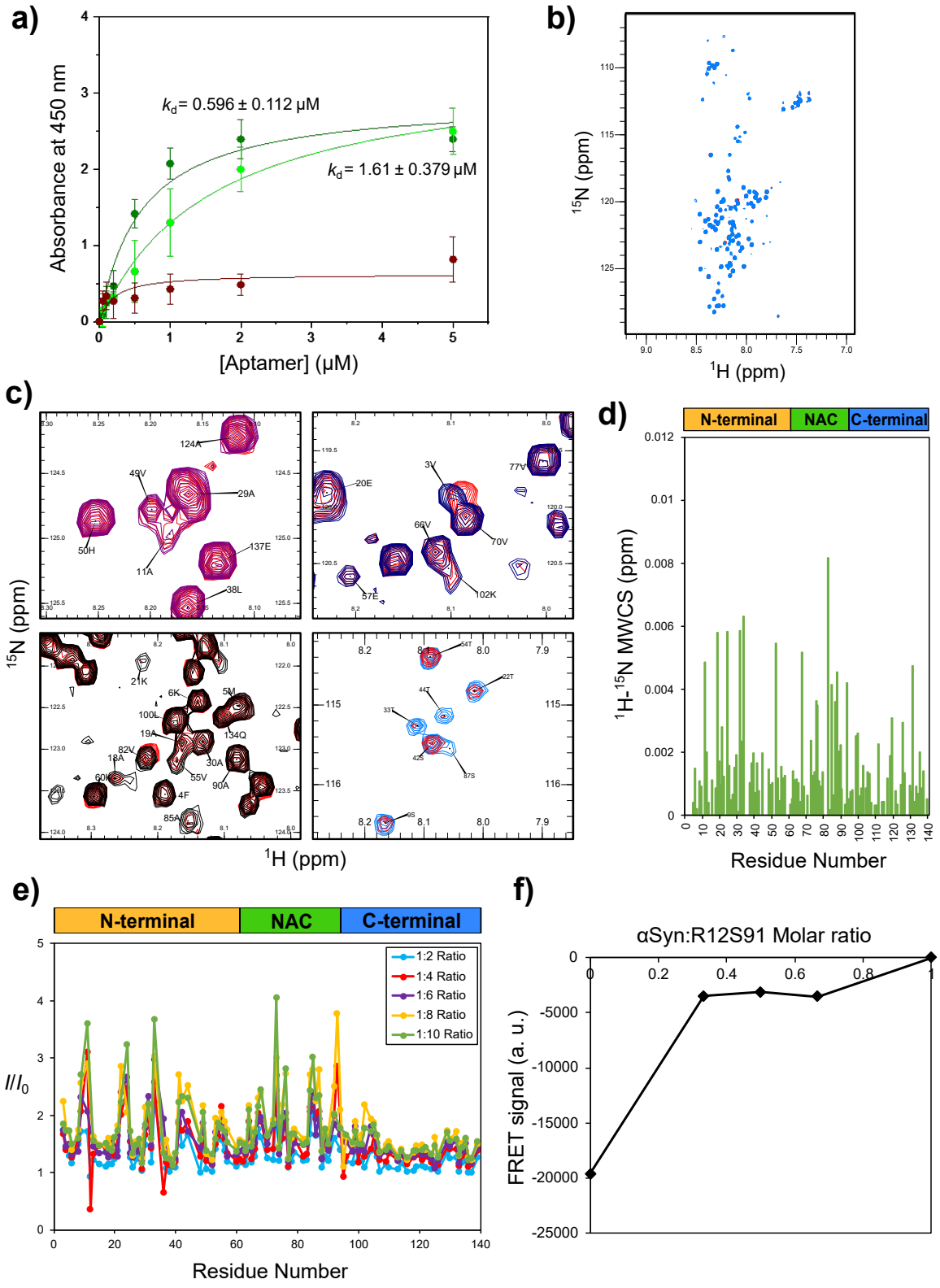


Figure 4.5: Characterisation of the binding of R12S91. a) Binding of R12S91 in the presence (dark green) and absence (light green) of αSyn$_{1-25}$, and in the absense of streptavidin (brown) measured with ELONA. k_d values for each condition are specified. ELONA was performed using streptavidin-coated 96-well plates to which the biotinylated αSyn$_{1-25}$ peptide was bound, whilst binding assays not involving streptavidin were carried out using standard MaxiSorp 96-well plates. ELONA was

Figure 4.5: performed at RT in ABB. b) Overlay of ^{1}H-^{15}N HSQC spectra of αSyn (50 μM) in the absence (red) and presence (light blue) of a molar ratio of 1:10 of αSyn to R12S91 (500 μM). c) Representative close-ups of αSyn residue cross-peaks (red) showing small chemical shift and intensity changes upon incubation with a 2- (purple), 6- (dark blue), 8- (black) and 10-fold (light blue) molar excess of R12S91. d) ^{1}H-^{15}N MWCS of αSyn in the presence of R12S91 at a 1:10 molar ratio (50:500 μM). e) I/I_0 of αSyn residue cross-peaks upon incubation with R12S91 at a 1:10 molar ratio (50:500 μM). Experiments were recorded at 25 ºC using αSyn in ABB. f) Job plot reporting FRET fluorescence for the interaction between R12S91 and aSyn. FRET was carried out in ABB. Error bars represent the standard error in the measurements.

To further characterise the binding of R12S91 with αSyn, an NMR titration was done in which several ^{1}H-^{15}N HSQC experiments were recorded of full-length ^{15}N αSyn in the presence of R12S91 at 1:2, 1:4, 1:6, 1:8 and 1:10 protein:aptamer ratios (Figure 4.5b-e). Overall, the collected spectra surprisingly revealed a steady increase in the intensity of some of the cross-peaks with increasing aptamer concentration, which could be indicative of stabilising interaction events. Analysis of the intensity changes of each spectrum at the different protein:aptamer ratios that were probed showed an increase in the intensity of the peaks corresponding to the residues of segments of the N-terminal (9-44) and NAC regions (68-87) (Figure 4.5e). Interestingly, the peaks of the C-terminal residues did not experience changes in their intensity in the presence of R12S91 at any concentration, compared to free protein. Similarly, the regions previous to residue 9 and between residues 50-65 did not show an increase in the intensity of their cross-peaks with increasing aptamer concentration.

Perturbations to the chemical shifts of the peaks were also analysed at the highest protein:aptamer ratio of incubation (Figure 4.5d). These findings correlated with the intensity change patterns observed, with residues at the mid-section of the N-terminal and in the NAC regions being the most affected, and those at the C-terminal region experiencing the least changes in chemical shifts. It should be noted, however, that changes in cross-peak chemical shifts were systematically of a smaller magnitude compared to the changes observed in peak intensities. Additionally, even though the regions with the largest number of peaks with the strongest chemical shift deviations could be identified as being located in the N-terminal and NAC regions, these were not as well-defined as those observed having the largest intensity changes, with some residues showing discrepancies in the extent of their perturbation in the presence of different aptamer concentrations (e.g., Gln24, Thr33, Gly41). Consistent with the observed changes in intensity, the residues from the C-terminal region as well as those

around positions 1-10 and 50-65 showed the smallest perturbations in chemical shifts. These findings suggest a nonspecific interaction between R12S91 and αSyn, where changes in the NMR parameters measured are not indicative of a ∼600 nM affinity, as it was calculated by ELONA. Indeed, the recorded increase in peak intensity with increasing aptamer concentration resembles the NMR binding data from αSyn in the presence of 65ntSeq. This therefore suggests that the observed changes may correspond to nonspecific electrostatic interactions with the negatively charged DNA backbone, which may be affecting different regions of αSyn.

The structure of R12S91 was modelled (Figure 4.6) to gain further insights into the structural basis of an interaction event with αSyn or streptavidin. Under the conditions used during the selection process, including a 150 mM Na^+ and 5 mM Mg^{2+} ionic strength at 298K, 2D and 3D models revealed the formation of a stable secondary structure with a predicted ΔG of -3.95 kcal/mol. This consists of hairpin stem-loop spanning bases 1-30 that contains an internal loop. Bases 31-42 are not predicted to form any secondary structure under the specified conditions. For this reason, it was hypothesised that this unstructured segment may be hindering the interaction between R12S91 and αSyn_{1-25}/αSyn by not contributing to the binding thermodynamics and instead sterically obstructing a closer binding mode. With this in mind, a truncated version of R12S91, TR12S91, which lacks bases 31-42, was made and its binding to αSyn_{1-25} was tested by ELONA.

Surprisingly, deletion of bases 31-42 dramatically reduced binding (Figure 4.7), which suggests that this predictably unstructured region may be playing a critical role in the binding mode of R12S91. Maximal absorbance values were three times lower than that observed upon binding of R12S91, indicating a low aptamer retention with the measured absorbance being most likely the result of nonspecific binding. Even though the hyperbolic binding model was forced onto the data obtained from ELONA, the binding curves produced did not resemble hyperbolic binding functions indicative of specific binding and the binding affinities in the high nM range that were calculated for both in the presence and absence of αSyn_{1-25}. The fact that the recorded binding traces in the presence and absence of αSyn_{1-25} were practically superimposable suggests that TR12S91 has no affinity for the αSyn_{1-25} peptide or streptavidin.

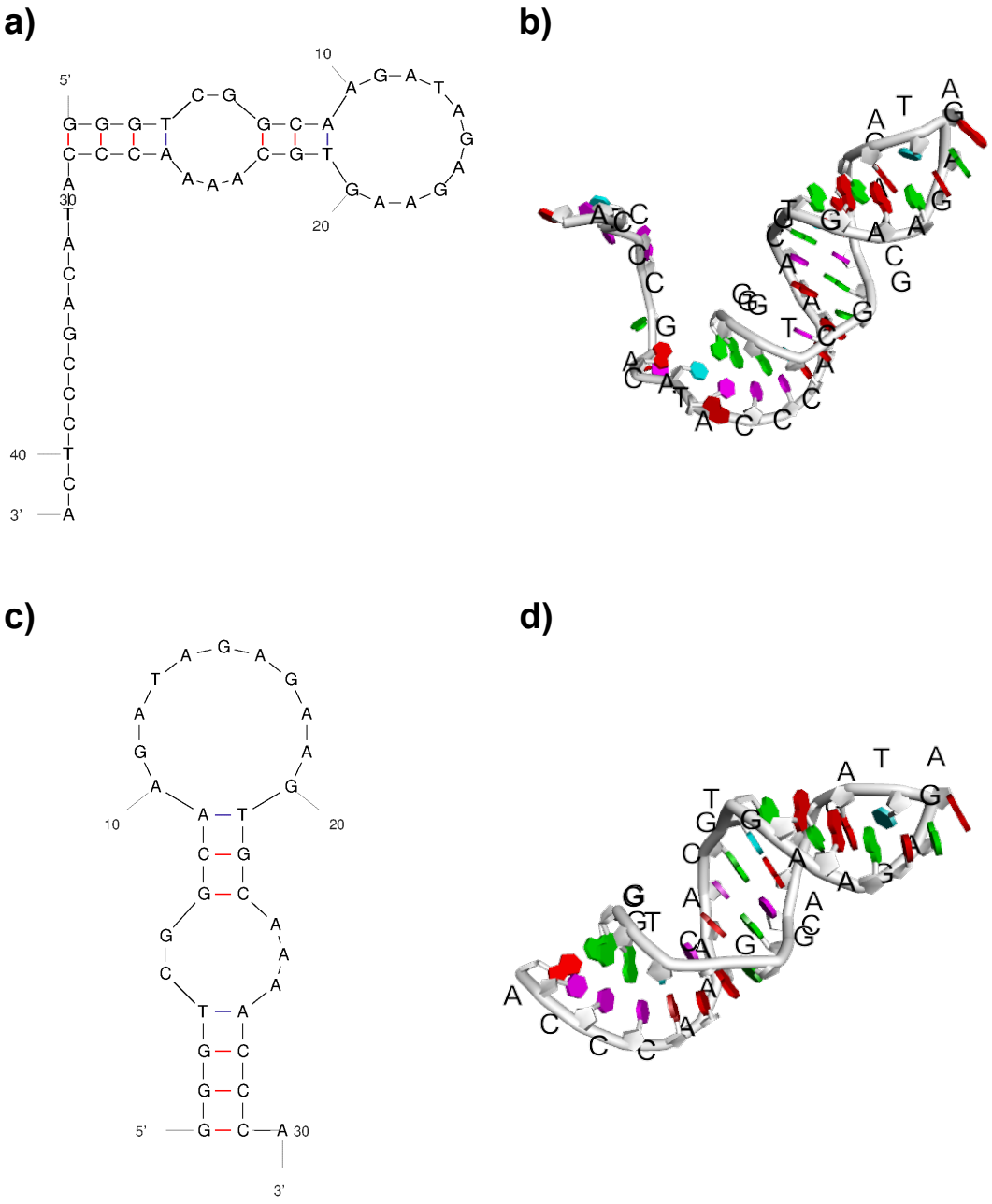


Figure 4.6: Structural prediction of the R12S91 and TR12S91 sequences. a) 2D prediction of the structure of R12S91. b) 3D structural model of the structure of R12S91. c) 2D prediction of the structure of the truncated form of R12S91, TR12S91. d) 3D structural model of the structure of TR12S91. e) Sequences of R12S91 and TR12S91. The 2D structural prediction was generated using the Mfold web server with the following specified conditions: 150 mM [Na^{+}] and 0.5 mM [Mg^{2+}] at 25 ºC. The predicted ΔG's for the 2D structures of R12S91 and TR12S91 are -3.95 kcal/mol. The 3D models were generated through an energy minimisation procedure outlined in Chapter 2.

As a control, the binding of R12S91 was newly tested by ELONA alongside that of TR12S91. Binding data of R12S91 in the presence and absence of the αSyn_{1-25} peptide was this time almost superimposable (Figure 4.7a), suggesting that the small differences in binding that had previously been observed (k_d= 0.596 ± 0.112 µM and k_d= 1.61 ± 0.379 µM in the presence and absence of αSyn_{1-25}, respectively) may be accounted for by experimental variation and not by a specific binding event between R12S91 and αSyn_{1-25}.

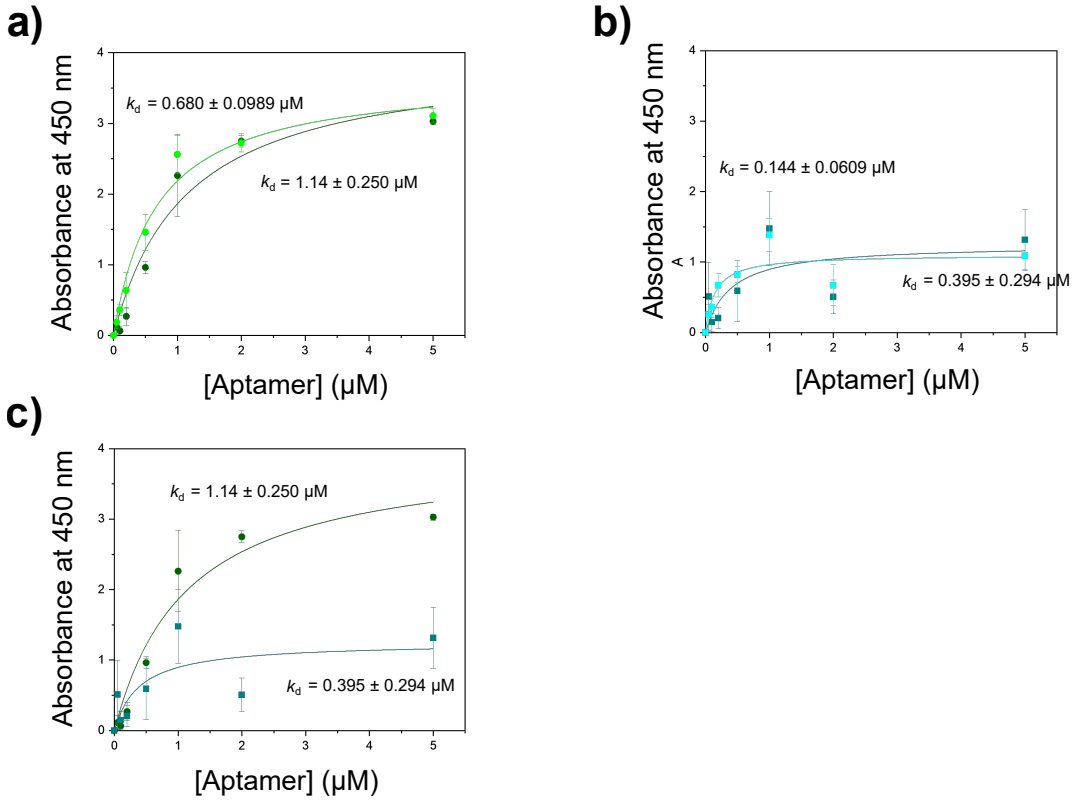


Figure 4.7: Comparison of the binding of R12S91 and TR12S91 to αSyn_{1-25}. a) Newly tested binding of R12S91 in the presence (dark green) and absence (light green) of αSyn_{1-25}. b) Binding of TR12S91 in the presence (teal) and absence (cyan) of αSyn_{1-25}. c) Comparison of the binding curves of R12S91 (dark green) and TR12S91 (teal) in the presence of αSyn_{1-25}. k_d values for each condition are specified. ELONA was performed at RT in ABB using streptavidin-coated 96-well plates to which the biotinylated αSyn_{1-25} peptide was bound.

4.2.3 15^{th} Round

After 15 rounds of selection, SELEX was expected to have resulted in the enrichment of a pool of sequences that have affinity for the target αSyn_{1-25} peptide and whose dissociation constants would be lower than those of the sequences found in the previous round libraries. However, analysis of the binding affinities of R15S2 and R15S15 isolated from the 15^{th} round library featured binding curves characteristic of nonspecific binding in the presence of αSyn_{1-25} immobilised on streptavidin (Figure 4.8a, d and e). Given that the data do not follow the applied binding model, the calculated dissociation constants are just estimates. These findings therefore indicate that these two sequences do not bind to αSyn_{1-25}. Unexpectedly, both sequences presented a worse binding profile in the presence of αSyn_{1-25} compared to the sequences identified in the library from the 12^{th} round of selection, despite the three additional rounds of selection that would have been expected to enrich target binders. Surprisingly, binding data from R15S15 in the absence of αSyn_{1-25} indicated a better binding profile compared to in the presence of the peptide, suggesting affinity for streptavidin (k_d= 2.56 ± 1.11 μM) but not for αSyn_{1-25}, although large experimental error bars may also be indicative of nonspecificity. Binding data of R15S2 in the absence of αSyn_{1-25} was very similar to that in the presence of αSyn_{1-25}, suggesting a lack of binding affinity for the target peptide.

4.2.4 17^{th} Round

Binding of R17S17, the only sequence identified from the 17^{th} round library with a random core region, resulted in very similar binding curves and calculated dissociation constants in both the presence (k_d= 5.18 ± 2.56 μM) and absence (7.18 ± 3.16 μM) of αSyn_{1-25} (Figure 4.8b and f). These findings, together with the fact that maximum absorbance values are low even after incubation of R17S17 with the peptide at a 5 μM concentration suggest a low binding affinity for streptavidin, but not αSyn_{1-25}.

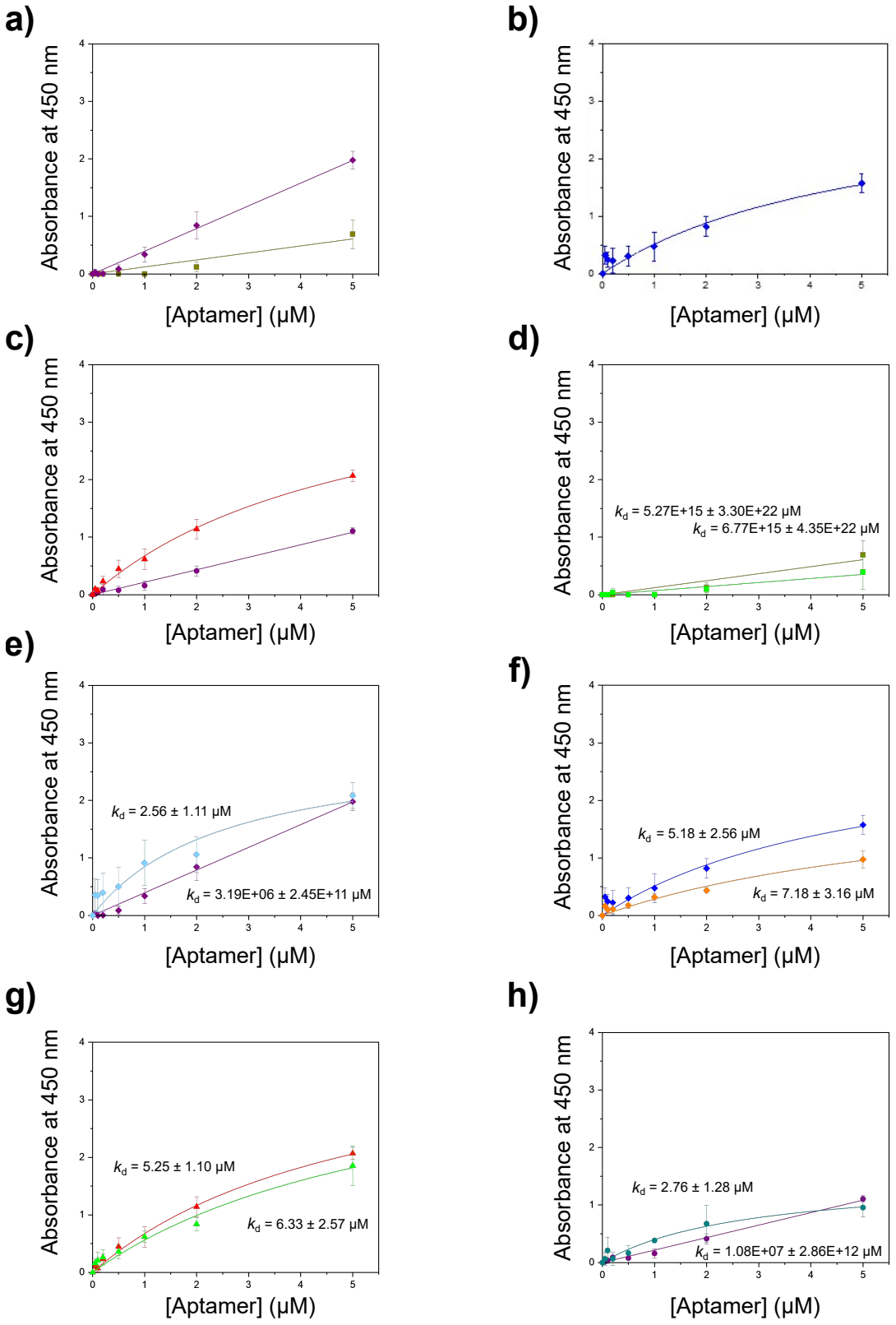


Figure 4.8: Characterisation of the binding of the aptamer sequences identified upon sequencing of the 15^{th}, 17^{th} and 20^{th} round libraries. a) Binding of the aptamer sequences identified from the 15^{th} round in the presence of αSyn_{1-25}: R15S2 (olive green) and R15S15 (purple). b) Binding of the sole aptamer sequence identified from the 17^{th} round in the presence of αSyn_{1-25}: R17S17 (dark blue). c) Binding of the aptamer sequences identified from the 20^{th} round in the presence of αSyn_{1-25}:

Figure 4.8: R20S35 (red) and R20S38 (purple). d) Individual binding curves of R15S2 in the presence (olive green) and absence of αSyn_{1-25} (light green). e) Individual binding curves of R15S15 in the presence (purple) and absence of αSyn_{1-25} (cyan). f) Individual binding curves of R17S17 in the presence (dark blue) and absence of αSyn_{1-25} (orange). g) Individual binding curves of R20S35 in the presence (red) and absence of αSyn_{1-25} (light green). h) Individual binding curves of R20S38 in the presence (purple) and absence of αSyn_{1-25} (dark cyan). k_d values for each condition are specified. ELONA was performed using streptavidin-coated 96-well plates to which the biotinylated αSyn_{1-25} peptide was bound. ELONA was performed at RT in ABB. Error bars represent the standard error in the measurements.

4.2.5 20^{th} Round

Data from ELONA revealed marked differences in the binding affinities of R20S35 and R20S38, despite both sequences having been identified in a late-stage library of the selection process (Figure 4.8c, g and h). The binding of R20S35 resulted in dissociation constants that were very similar in both the presence (k_d= 5.25 ± 1.10 μM) and absence (k_d= 6.33 ± 2.57 μM) of αSyn_{1-25}. Remarkably, data appear to follow the binding model, suggesting a specific interaction between R20S35 and streptavidin, but not αSyn_{1-25}. Binding saturation was, however, not reached even at high aptamer concentrations of 5 μM. This resulted in calculated dissociation constants in the low μM range and thus not indicative of high affinity binding events. In contrast, binding data from R20S38 in the presence of αSyn_{1-25} did not converge to fitting into the model, which suggests nonspecific binding. In the absence of the target peptide in the incubation mixture, binding data from R20S38 did converge into the binding model (k_d= 2.76 ± 1.28 μM), although low absorbance values and a slow increase in absorbance with aptamer concentration, as observed in the modelled binding curve, suggest a low retention of the binding aptamer sequence. These results indicate that R20S38 may be binding to streptavidin with an affinity lower than that of R20S35.

Altogether, the data from the binding assays of all aptamer sequences identified during SA-Mag bead-SELEX suggest that the aptamers may have inadvertently been selected against streptavidin, instead of αSyn_{1-25}, despite the negative selection rounds that were incorporated throughout the selection process.

As mentioned in Chapter 3, the selection strategy was modified to use the DNA library from the 12^{th}

round as a starting library for NCM-SELEX, with the aim of selecting aptamer sequences against full-length αSyn, under the assumption that there may be sequences in this library with affinity for the αSyn_{1-25} peptide which will then be further enriched for their binding to αSyn. The library was cloned and further sequenced after a total of 18 rounds of selection (12 rounds of selection against αSyn_{1-25} and 6 additional rounds of selection against αSyn) and the results reported below.

4.2.6 18^{th} Round

Sequencing of the 18^{th} round library of the modified selection revealed that a high content of sequences containing random core regions constituted the bulk of the sequenced pool, in contrast to what had previously been observed upon sequencing of the other DNA libraries, where sequences formed by truncations of the forward and reverse primers had dominated the library sequence population. Out of all 28 sequences identified carrying random core regions, a subset of six of them was chosen in order to assess their binding affinity and estimate the binding enrichment of the library. This was done based on a multiple sequence alignment of all newly identified sequences, which was displayed in the form of a phylogenetic tree to identify possible sequence clusters with similar binding affinities (Figure 4.9). For this reason, the six sequences whose affinity was studied each belong to a different cluster and are therefore expected to serve as a representation of the binding affinity of the sequences in a particular sequence family.

The binding affinities of R18S10N, R18S16N, R18S17N, R18S25, R18S30 and R18S41 for αSyn_{1-25} were first assessed. Unexpectedly, all six sequences showed a binding profile featuring a linear or almost linear binding curve indicating nonspecificity, as the recorded absorbance increased linearly with the incubated aptamer concentration (Figure 4.10a). Whilst the binding model did calculate dissociation constants for some of them in the low μM range, these must be observed with caution, as the binding curves have been forced to fit the binding model and the calculated k_ds most likely do not reflect the true binding constant. Therefore, these results showed that the sequences investigated do not have binding affinity for αSyn_{1-25} or streptavidin.

A more suitable binding assay to assess the affinity of these six sequences identified during the last six

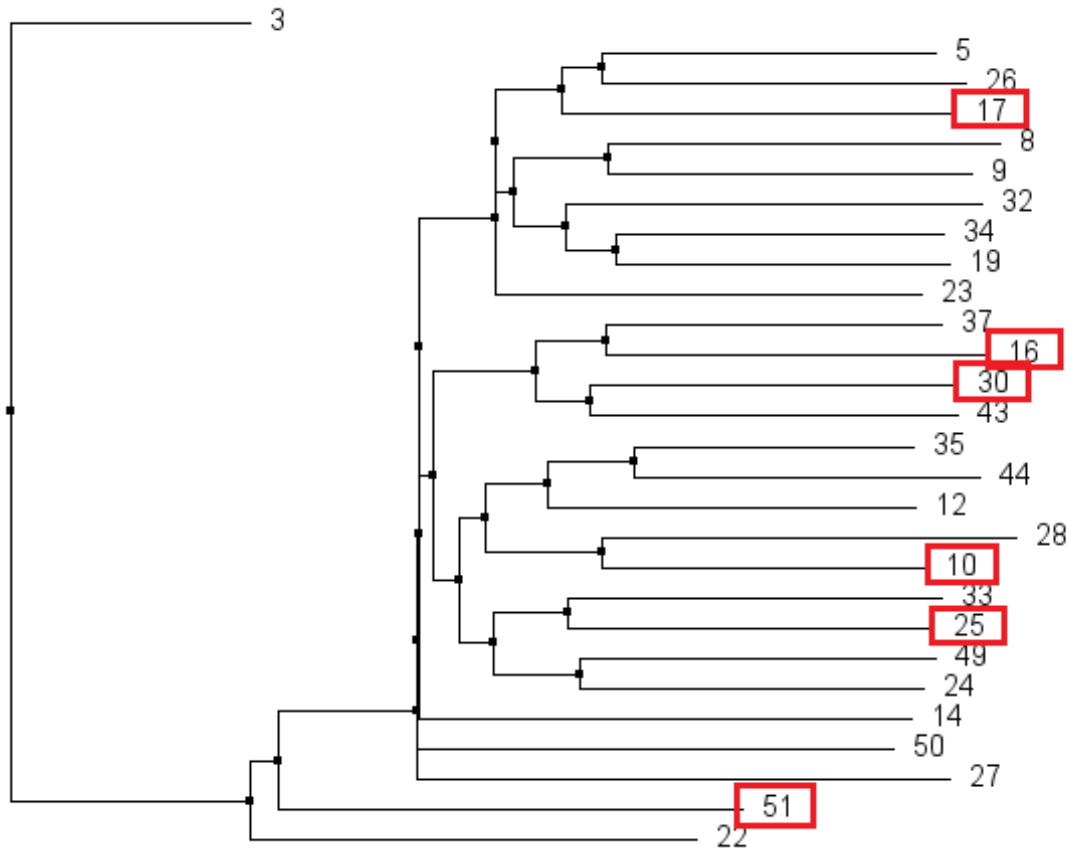


Figure 4.9: Phylogenetic tree of the different aptamer sequences identified from the 18th round NCM library illustrating different groups of aptamers with sequence similarity. The clustering of different aptamers into sequence families guided the selection of multiple sequences from different clusters. Six representative sequences, highlighted in red, were chosen and tested for their affinity to αSyn_{1-25} and αSyn. The phylogenetic tree was generated with Jalview [517] using multiple sequence alignment output.

SELEX rounds would be one in which the aptamers are incubated with the whole-length αSyn protein in solution, which would resemble the conditions used during NCM-SELEX. Therefore, to obtain further information on a possible interaction event between the DNA aptamer sequences from the 18^{th} round and αSyn, FRET was carried out. To do this, the 5'-fluorescein-labelled aptamer sequences were incubated with αSyn in solution, which had previously been labelled with rhodamine. The spectral emission of fluorescein overlaps with the excitation profile of rhodamine, which makes the two fluorophores a FRET-active pair and an excellent reporter of proximity interactions and therefore molecular binding events. A series of experiments were carried out in which the ratio of αSyn:DNA was altered to try to characterise the binding mode of action and the stoichiometry of the interaction between the 18^{th} round sequences and αSyn. Additionally, the binding of R12S91 was also assessed

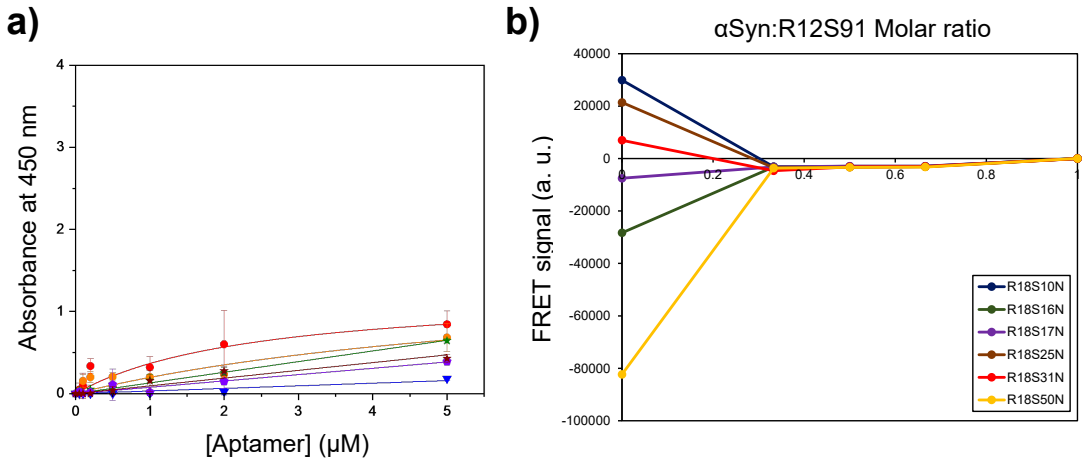


Figure 4.10: Characterisation of the binding of six sequences identified from the 18^{th} round library of NCM-SELEX. a) Binding of R18S10N (dark blue), R18S16N (dark green), R18S17N (violet), R18S25N (brown), R18S30N (red) and R18S51N (yellow) in the presence of αSyn_{1-25}. ELONA was performed using streptavidin-coated 96-well plates to which the biotinylated αSyn_{1-25} peptide was bound. ELONA was carried out in ABB at RT. b) Job plot reporting FRET fluorescence for the interaction between R18S10N, R18S16N, R18S17N, R18S25N, R18S30N, R18S51N and αSyn. FRET was carried out in ABB at RT. Error bars represent standard error. Error bars are comparatively small and therefore not visible in the plot reporting FRET fluorescence.

with FRET, to gain further insights into potential binding events with αSyn free in solution and complement the available ELONA and NMR data. The incubation mixtures were excited at different wavelengths to obtain the individual spectral contribution of fluorescein and rhodamine, and then excited at a wavelength range to induce a FRET signal.

Analysis of the emitted fluorescence from the acceptor rhodamine-αSyn and the donor fluorescein-DNA of all sequences being investigated revealed a profile that was particularly invariant upon an increase in the molar ratio of αSyn, indicating a lack of spatial proximity between the fluorophores and therefore of binding (Figure 4.10b and 4.5f). In the case of R18S10N, R18S17N, R18S31N, R18S50N and R12S91, a molar ratio of αSyn:DNA sequence of 0:1 produced the highest fluorescence signal, indicating that FRET did not occur upon incubation of these sequences with αSyn. Sequences R18S16N and R18S25N produced negative fluorescence FRET outputs after the measured emission signal was subtracted the fluorescence contribution from the acceptor and donor fluorophores, suggesting that FRET had not happened in the presence of R12S16N and R18S25N. A negative signal output indicates a lack of signal recorded at the wavelength range probed. Incuba-

tion of rhodamine-αSyn with all seven different sequences produced a similarly quick reduction in emitted fluorescence signal upon reduction of the present fluorescein-DNA sequences, which drops to zero as the amount of donor fluorescein decreases and that of the acceptor rhodamine increases. The fact that the highest recorded signal upon incubation with some sequences was in the absence of acceptor rhodamine-αSyn, together with a sharp decrease in fluorescence to almost zero when the ratio of donor fluorescein-DNA to acceptor rhodamine-αSyn drops by a third from 1 to 0.666 indicate that these sequences have no binding affinity for αSyn, which is consistent with the binding data from ELONA and NMR presented earlier in this Chapter.

Taken together, a summary of the binding affinities for αSyn_{1-25} of all aptamers considered here are specified in Table 4.1.

	k_d (αSyn 1-25 Peptide) (μM)	k_d (No αSyn 1-25 Peptide) (μM)
8th Round		
FSeq1	2.12 ± 0.451	-
65ntSeq	0.312 ± 0.0488	0.469 ± 0.0893
12th Round		
R12S15	2.21 ± 0.612	15.1 ± 21.1
R12S16	1.72 ± 0.921	0.469 ± 0.130
R12S24	1.05 ± 0.311	58.8 ± 130
R12S29	6.21 ± 4.53	3.78 ± 1.32
R12S55	9.38 ± 12.8	1.57 ± 0.898
R12S91	0.596 ± 0.112	1.61 ± 0.379
TR12S91	10.3 ± 9.47	
	0.394 ± 0.294	0.144 ± 0.0609
R12S93	1.79 ± 0.229	2.43 ± 1.45
15th Round		
R15S2	5.27E+15 ± 3.30E+22	6.77E+15 ± 4.35E+22
R15S15	3.19E+06 ± 2.45E+11	2.56 ± 1.11
17th Round		
R17S17	5.18 ± 2.56	7.18 ± 3.16
20th Round		
R20S35	5.25 ± 1.10	6.33 ± 2.57
R20S38	1.08E+07 ± 2.86E+12	2.76 ± 1.28
18th Round NCM		
R18S10N	9.73E+18 ± 6.43E+25	-
R18S16N	44.9 ± 58.9	-
R18S17N	2.38E+07 ± 5.40E+13	-
R18S25N	5.11 ± 2.38	-
R18S30N	2.42 ± 1.45	-
R18S51N	6.86 ± 5.41	-

Table 4.1: Affinities of the aptamer sequences identified and tested for αSyn_{1-25}.

4.3 Discussion

The results of this Chapter provide a comprehensive characterisation of the binding properties of the DNA aptamer sequences identified throughout the different rounds of selection performed during this work. The available pieces of evidence supporting the binding modes of each sequence, together with their suitability as a potential inhibitor of the membrane binding ability of αSyn is discussed below.

Given the large abundance of sequences formed by primer truncations in the first sequenced round library (8^{th} round), it was hypothesised that primer-derived sequences may have been selected for their binding to αSyn_{1-25}. To investigate this, the binding affinity of two of these sequences which were believed to be representative of the sequencing results was assessed: FSeq1 and 65ntSeq. FSeq1 is formed by the forward primer lacking the last adenosine base at the 3' end, followed by a truncation of the first 10 bases of the forward primer sequence. Similarly, 65ntSeq is formed by a full-length forward primer followed by the reverse complement of the reverse primer. ELONA binding assays were performed by which the binding affinity of both sequences was measured for αSyn_{1-25}, which was immobilised on streptavidin-coated 96-well plates. Binding results revealed that 65ntSeq has the highest binding affinity of the two sequences, with its dissociation constant being in the mid-nM range. However, 65ntSeq did not appear to specifically bind αSyn_{1-25}, since a similar dissociation constant was calculated after assessing its binding in the absence of αSyn_{1-25} and in the presence of streptavidin.

To obtain a better picture of the binding mode of 65ntSeq that may explain its low dissociation constant and its high abundance in the sequenced libraries, ^{1}H-^{15}N HSQC experiments of αSyn in the presence of 65ntSeq at molar ratios of 1:1 and 1:3 were recorded. The collected spectra of the free protein and in the presence of the 65ntSeq sequence at both molar ratios were almost identical. Furthermore, no significant differences were observed in the intensity and chemical shifts of the residue cross-peaks even after increasing the molar ratio of incubation from 1:1 to 1:3, indicating that 65ntSeq was not interacting with αSyn. This is consistent with binding data from ELONA, which demonstrated that 65ntSeq had an almost identical dissociation constant regardless of the pres-

ence of αSyn$_{1-25}$. Particularly interesting was the systematic increase in amide peak intensities that was observed along the protein sequence in exception of the C-terminal region upon incubation with 65ntSeq, compared to free protein. This may be explained by an artefactual effect caused by the electrostatic interactions between the highly negatively charged backbone of the 65ntSeq sequence and αSyn. Electrostatic repulsion with the acidic C-terminal region may have led to the release of native intramolecular interactions that hold the N-terminal and NAC regions in close proximity with the C-terminal region of αSyn. This may have resulted in the residues of the N-terminal and NAC regions experiencing a different environment featuring an increased exchange with the solvent, and hence an increase in the peak intensities. This observed effect may have also been affected by changes in the local pH as a result of the acidic DNA backbone. However, these results are not indicative of a specific binding event, as especially fuzzy interactions characterised by peak broadening of the residues involved would have been expected from binding events with an IDP such as αSyn.

To shed light onto the binding interactions driving the formation of 65ntSeq that may help explain its persistently high abundance in the libraries sequenced, an ELONA was carried out in the absence of αSyn$_{1-25}$ and streptavidin. In this way, every macromolecule the 65ntSeq may have been binding to during the selection process was removed from the binding reaction. The results from this experiment showed a drastic reduction in HRP-developed signal, suggesting a lack of sequence retention in the 96-well plate where the incubation was carried out, and hence a lack of binding. The data were forced to fit into the binding model and so the binding curves and calculated dissociation constants do not likely reflect the actual binding properties of the sequence in those conditions. In fact, the binding data resembled a linear binding profile featuring an increase in the absorbance that was almost proportional to the increase in aptamer concentration, which is characteristic of a nonspecific binding mode. The fact that nonspecific binding is observed in the absence of streptavidin suggests that 65ntSeq has binding affinity to streptavidin, given that previous binding data had demonstrated a lack of binding to αSyn$_{1-25}$. This finding suggests that either one of the individual primers (which together form 65ntSeq) or both may have native affinity for streptavidin, which may explain why the sequence interacts with streptavidin even without undergoing *in vitro* evolution. Indeed, the fact that the primers used during PCR amplification share the same sequence may have further biased the amplification of

65ntSeq as a result of the readily available priming sequences in solution. At the same time, the native affinity for streptavidin, together with the high concentration of priming sequences within the library, may have driven the generation of the primer-derived sequences formed by primer truncations through random recombination events. The combination of these effects predictably accounts for the fact that most of the sequenced clones correspond to primer-derived sequences, as their native affinity for streptavidin may have favoured their retention during the SELEX partitioning steps.

Comparison between the N42 library sequences identified from all sequenced round libraries revealed an intriguing base pattern composition. Intriguingly, many sequences are formed by stretches of the same base of different lengths (e.g., seven consecutive A's in R20S38) (Table 2.1). This was at first thought to be important for target recognition and binding, although later binding assays failed at showing affinity of the sequences tested for either αSyn_{1-25} or αSyn, suggesting that an alternative mechanism may have been responsible for the selection of these sequence motifs.

Sequencing of the 12^{th} round library identified seven N42 library clones that were not formed by truncations of the forward and reverse primers. Their binding was assessed by ELONA, which revealed that all had different dissociation constants in the mid-nM to mid-μM range. R12S91, in particular, was the sequence that showed the highest affinity. A decrease in its dissociation constant in the absence of αSyn_{1-25} suggested a binding interaction involving the αSyn_{1-25} peptide. The fact that the magnitude of the reduction in affinity is small may point at a binding mode spanning αSyn_{1-25} and streptavidin together, where removal of the αSyn_{1-25} peptide may perturb the binding interaction with R12S91. R12S24 also showed a reduction in affinity in the absence of αSyn_{1-25}, although its dissociation constant in the presence of the αSyn peptide was not as low as that of R12S91.

^{1}H-^{15}N HSQC spectra were recorded of αSyn in the presence of R12S91 at several molar ratios to provide further information on the binding of R12S91. Analysis of the collected spectra revealed an increase in the peak intensities of the mid N-terminal (residues 9-44) and NAC (residues 68-87) regions. Of note, the intensities of the peaks corresponding to the acidic residues of the C-terminal region did not experience alterations even after incubation at the highest molar ratio of 1:10

of αSyn:R12S91. This may have possibly been a result of the absence of a binding event with the highly negatively charged DNA backbone or a nonspecific electrostatic repulsion between the two net negatively charged molecules. Interestingly, the region prior to residue 10 and between residues 50-65 did not experience an increase in peak intensities, suggesting that this effect may be specific, as opposed to that observed upon incubation with 65ntSeq, which resulted in a systematic increase of the peak intensities throughout the sequence of the protein except for the C-terminal region. Regions around 10-45 and 70-90 are particularly rich in hydrophobic and aliphatic amino acids, which suggests that nonspecific interactions between these highly hydrophobic regions of αSyn and the hydrophobic DNA bases may be responsible for the observed changes in peak intensities. In fact, the basis of binding events between protein and DNA mostly consists of contacts between the target amino acid residues and the nucleotide bases, rather than solely the negatively charged DNA phosphate backbone [518].

Similarly, the fact that the increase in peak intensities appears to correlate with a higher molar ratio of R12S91 to αSyn suggests that this effect may be accounted for by a nonspecific low-affinity interaction. This correlated increase in peak intensity with ligand concentration was not observed with 65ntSeq, although this may partly be explained by the higher molar ratios of R12S91 to αSyn used during the titration experiment. Alternatively, R12S91 may be causing a non-specific disruption of the long-range intramolecular contacts within αSyn through electrostatic repulsion of the C-terminal region, which may lead to the release of the N-terminal and NAC regions and the enhancement of the signal of the local residues that were involved in maintaining these long-range contacts. However, a binding event between αSyn and R12S91 would be expected to lead to a reduction in the peak intensities of the residues involved in the interaction as a result of linewidth broadening, and not to an increase. Indeed, the changes observed in the recorded spectra do not correspond to what is expected from an intermolecular interaction where the dissociation constant was calculated to be approximately 600 nM by ELONA. The localised increase in peak intensities, coupled with a lack of change in the residue peaks of the C-terminal region, make these results particularly difficult to interpret. Whilst these spectra were recorded of αSyn alone in the absence of streptavidin, streptavidin may possibly be required to establish a putative three-way binding event, in which αSyn may be minimally involved.

These findings are consistent with FRET data that were recorded of fluorescein-labelled R12S91 (the donor) and rhodamine-labelled αSyn (the acceptor) in solution. These experiments failed at showing an interaction between αSyn and R12S91, given that an increase in the proximity of the donor and acceptor fluorophores that is required for FRET to occur was not recorded. It should be noted, however, that previous knowledge of the binding features between two binding partners is required for the correct performance of this experiment and the accurate analysis of these results, where the concentration of the individual molecular components is to be at least 10-fold higher than that of the calculated dissociation constant. In this case, the dissociation constant between R12S91 and αSyn was assumed to be the same as that between R12S91 and αSyn_{1-25} in the presence of streptavidin as calculated by ELONA, i.e., in the range of 600 nM. A protein and DNA concentration of 20 μM each should in theory fulfil this experimental requirement, although an incorrect calculation of the dissociation constant (e.g. actual binding affinity in the absence of streptavidin not being that high or no binding interaction at all) may have biased FRET calculations. R12S91 and αSyn were incubated at different molar ratios with the aim of determining the stoichiometry of the interaction, with the highest FRET signal recorded theoretically corresponding to the molar ratio at which the binding event occurs. The lack of a recorded FRET fluorescence signal, combined with the NMR and ELONA data indicate that R12S91 does not bind αSyn with high affinity with a dissociation constant in the order of the 600 nM as calculated with ELONA. These findings also suggest that R12S91 has not been selected to bind to αSyn_{1-25} but may have been inadvertently selected against streptavidin, or perhaps the αSyn_{1-25}-streptavidin complex, although the contribution of the αSyn peptide to the binding may be minimal.

Structural knowledge of an aptamer sequence is known to be critical to the design of strategies for the purpose of selectively modifying desired molecular properties, such as affinity, specificity or toxicity [505, 506, 519]. In particular, smaller truncated versions of aptamers frequently have lower dissociation constants than their original longer counterparts [520, 521]. For this reason, modelling of the structure of R12S91 was done with the aim of identifying regions within the sequence that may be subject to modification in order to attempt at increasing the binding affinity of R12S91. The 2D and 3D models generated of the sequence revealed the folding into a prominent hairpin stem-loop

involving bases 1-30, and an unstructured region from bases 31-42 under the experimental conditions employed during selection. This unstructured region was truncated to generate TR12S91, with the aim of removing unstructured motifs that may interfere with the binding mode of R12S91.

Interestingly, truncation of this portion of the sequence abolished binding of TR12S91 in both the presence and absence of αSyn_{1-25}, suggesting that this predictably unstructured portion of the sequence is critical for the binding of R12S91. By forcing the data into the binding model, a binding curve and a dissociation constant were obtained, although these most likely falsely represent the binding properties of the sequence, as a reduction in maximal absorbance and the linearity of the data compared to the binding results from R12S91 indicate the nonspecificity of this interaction. These findings may be explained by the fact that even if this portion of the sequence is predicted to lack a defined structure, it may still contribute to the binding of the aptamer by directly interacting with the target. Structural modelling of a dynamic molecule as is a single strand of DNA will likely show the structure of the free state in solution and will sometimes fail to provide a representative depiction of the molecule upon partner binding, where the dynamics of the individual molecules and complex may impose a particular fold on the binding molecules. Bases 31-40 may therefore be predicted to lack a specific structure but which may adopt a particular conformation upon interaction that may be essential for the binding of R12S91. In a similar way, the predicted hairpin stem-loop structure formed by bases 1-30 may unfold and adopt a different "induced" conformation upon interacting with a binding partner.

Analysis of the binding of the sequences identified in the libraries from further rounds, namely the 15^{th}, 17^{th} and 20^{th} rounds revealed a lack of specific binding to αSyn_{1-25}. Particularly interesting is the binding mode of some sequences, which showed binding curves characteristic of specific binding in the absence and not in the presence of αSyn_{1-25}. These aptamer sequences, whose affinity may decrease in the presence of αSyn_{1-25}, may have been selected to bind, at least partly, to the biotin binding site of streptavidin. The high-affinity interaction between the biotin-conjugated peptide and streptavidin may disrupt the binding of these aptamer sequences by displacing them from their binding site, with which they interact with an affinity lower than that of the streptavidin-biotin interaction.

Altogether, the data of binding assays performed with the identified sequences suggest that aptamers may have not been selected for their binding to αSyn_{1-25}, but rather for their binding affinity to streptavidin. The fact that no high affinity binders to streptavidin were observed among the sequences whose affinities were assessed may be explained by the negative selection rounds that were incorporated to remove streptavidin binders. In this way, only sequences showing low affinity to streptavidin may have survived in the libraries of advanced rounds of selection, as they may have escaped their removal through negative selection. Therefore, the results from the various assays suggest that the selection process involved in this work has most likely selected for low-affinity binders to streptavidin, rather than to αSyn_{1-25}.

The difficulty in identifying high-affinity aptamer binders to αSyn_{1-25} may be explained by the structural properties of the target peptide used and the environmental conditions in which SELEX was carried out. Specifically, αSyn is an IDP that exists as a dynamic conformational ensemble, meaning that it transiently adopts a plethora of different conformations which are difficult to individually isolate. αSyn_{1-25} likely adopts a variety of different conformations representative of the dynamic nature of the full-length protein [522] that therefore renders the selection and evolution of aptamers that bind to any specific conformation extremely challenging. Additionally, the size of the αSyn_{1-25} peptide target (2.6 kDa) is more than a 20-fold smaller than that of the streptavidin tetramer (approximately 60 kDa) used for immobilising the biotinylated peptide, and therefore constitutes a bulky complex formed by globular domains with defined structural motifs. The particularly dynamic structural properties of αSyn, coupled with the relatively small size of the peptide target compared to that of streptavidin may have therefore favoured the preferential selection of aptamer sequences that bind to well-defined structural moieties and binding sites on the surface of the streptavidin molecules.

Assessment of the binding of the sequences identified in the 18^{th} round library after 6 rounds of NCM-SELEX against full-length αSyn failed at showing binding affinity for either αSyn_{1-25} or streptavidin by ELONA. To correctly assess the binding properties of these sequences in a setting that better resembled the conditions used during the selection process, FRET experiments were performed, in which different molar ratios of fluorescein-labelled DNA sequences and rhodamine-αSyn were incu-

bated and the emitted fluorescence recorded. At the different protein and DNA concentrations used, this assay failed to record FRET. FRET occurs when the emission spectrum of a donor fluorophore overlaps with the absorption of an acceptor fluorophore and the distance between the two is 8-10 nm or less. The fact that no FRET was detected therefore shows that neither of the six aptamer sequences tested came closer than 10 nm in space to αSyn, indicating the absence of a binding event between them, which is consistent with the data obtained from ELONA indicating a lack of binding.

As mentioned earlier in this discussion, previous knowledge of the dissociation constant of a particular binding event is required for correctly performing this FRET assay. Given that nonspecific binding was observed between the six sequences from the 18^{th} round library and αSyn_{1-25} by ELONA, it was not possible to obtain binding affinity estimates that would guide the correct set-up of this experiment. Therefore, the experimental conditions used here may have biased these FRET results by not showing low-affinity binding events that may occur and which were not observed at the low concentrations of DNA and αSyn used. However, despite the large number of aptamer sequences identified in the 18^{th} round library, a lack of binding to αSyn may be explained, at least in part, by the selection of binding aptamers to the NCM used in the partitioning step. Since nitrocellulose consists of a large and stable scaffold, aptamer sequences may have evolved throughout the rounds by binding and being selected against NCM and not αSyn. This possible preferential binding, combined with the dynamic nature of αSyn, may have prevented aptamer sequences from tightly binding to the target and being selected as binders.

Interactions with Metal Ions

5.1 Introduction

The aetiology of PD is considered multifactorial, in which genetic and environmental factors modulate the onset and development of the disease. Although a detailed understanding of the interplay of the many molecular mechanisms that give rise to pathology in PD is still lacking, the misfolding and aggregation of αSyn has been recognised as a key event in the generation of the associated pathology [293, 19, 32, 523, 9, 58, 294, 68, 73, 295, 296, 297]. The misfolding of αSyn can be triggered by several mechanisms, including post-translational modifications, oxidative stress and interactions with metal ions, amongst others. Until recently, aberrant interactions with metal ions had been overseen as an important factor in the development of PD, although evidence from extensive research studies from the past two decades suggests that they might represent a prominent mechanistic pathway contributing to αSyn aggregation [300, 301, 302, 303, 304, 305].

Metal ions are ubiquitously present in the brain, given their essential roles in neurotransmission and normal neuronal physiological function [301, 309]. Apart from providing positive counterions that can help keep charge neutrality, metal ions also act as important electron carriers and catalytic centres in the form of cofactors for proteins, as a result of their ability to undergo reduction and oxidation cycles. As an example, Cu^{2+} acts as an essential catalytic cofactor for the detoxifying protein SOD1

involved in ROS breakdown. As a result of its two oxidation states (I and II), Cu^{2+} acts as an acceptor for electrons coming from superoxide ions, and is therefore reduced, in the process of oxygen radical removal [299]. One of the inarguably most important metals in the brain is calcium, which plays a critical role in neurotransmission [524]. Given action potentials required for neurotransmission are coupled with intracellular calcium fluctuations at the presynaptic terminal, it has been proposed that Ca^{2+} might act as an important modulator of the physiological function of αSyn. Indeed, binding of Ca^{2+} to the anionic C-terminal tail of αSyn dramatically alters the charge distribution of the C-terminal region by masking the negatively charged density associated with Glu and Asp residues. This charge neutralisation, in turn, allows the binding of the C-terminal tail of αSyn to lipids in cellular membranes, in what is thought to be a key aspect of its physiological role [37].

Whilst metal ions are required for the normal functioning of the body and brain in particular, evidence from epidemiological studies and research on the interactions between αSyn and cations suggests an important role in inducing αSyn aggregation and toxicity. Indeed, αSyn aggregation has been observed to be induced by numerous cations, such as Ca^{2+} [91], Mn^{2+} [430, 428], Zn^{2+} [401], Cu^{2+} [319] and Cu^{+} [382]. In a complex, multifactorial landscape that attempts at understanding the aetiology of PD, increasing age becomes the main risk factor for the development of neurodegenerative diseases. Amounting evidence has demonstrated a link between aging and elevated levels of metal ions in the brain [307, 308]. It has therefore been hypothesised that a perturbation in the homeostasis of brain metal ion levels and their interaction with key proteins involved might be a putative factor in the development of multiple age-related neurodegenerative disorders. In the case of PD, several early studies pointed at zinc as an important toxic modulator of αSyn, as abnormally high levels of zinc have been found in the parkinsonian substantia nigra of patients [310, 312, 36, 313]. The co-localisation of elevated concentrations of zinc and αSyn has been observed in post-mortem examinations of the olfactory bulb [315], as well as high levels of copper in the cerebrospinal fluid of PD patients [316].

As previously reviewed in the introduction section of this thesis, excessive levels of intracellular calcium upon a dysregulation of its homeostasis can have detrimental effects by disrupting a variety

of cellular processes. By interacting with αSyn, a conformational change is believed to modulate the binding to synaptic vesicles, which has also been observed to result in the clustering of synaptic vesicles *in vitro* and *ex vivo* [37], as well as aggregation of αSyn into short fibrils [363] in the presence of abnormal levels of Ca^{2+}. In fact, epidemiological studies have shown a correlation between a prolonged exposure to certain environments rich in copper, manganese or zinc and a higher predisposition to develop PD later in life [317]. Chronic occupational exposure to environments rich in manganese including fumes from welding, mining and smelting is considered particularly relevant for the early development of PD symptoms [436, 437, 438, 439, 446, 440, 441, 442, 443, 444, 445]. To confirm the *ex vivo* findings, much research has been done to elucidate the precise role metal ions might play in the aggregation of αSyn and subsequent associated cellular toxicity. Indeed, interactions with metal ions have been found to alter the aggregation kinetics of αSyn [430, 305, 306], in what has been described to be a positive correlation between metal ion binding affinity and the ability to modulate aggregation kinetics [327, 328, 329, 330, 333, 331, 332].

Interestingly, the variety of post-translational modifications that decorate αSyn as well as the different pathological genetic variants add an extra layer of complexity to the interaction network with metal ions [93, 321]. For instance, Cu^{2+} has been shown to be the most efficient at promoting fibrillation of non-acetylated αSyn *in vitro* at physiologically relevant micromolar concentrations [319, 320], but not of the acetylated form. Whilst metal ion binding may alter the amyloid assembly pathways and aggregation kinetics of αSyn, a sole binding event might not be sufficient to induce aggregation, but it may require the induction of a structural transition. This might explain why binding of Cu^{2+} to the familial A53T αSyn variant does not directly translate into a noticeable alteration of its aggregation rate [321]. A similar effect in which the aggregation kinetics are accelerated *in vitro* is observed with Zn^{2+} [36, 313, 323, 324, 325, 326], which specifically interacts with His50 and the C-terminal region of αSyn [309]. In contrast, the interaction between Mn^{2+} and αSyn was characterised by non-specificity and low-affinity to the acidic C-terminal tail of αSyn.

Another way in which redox metals can result in pathology is through their ability to catalyse the generation of ROS as a result of their various oxidation states [334]. Highly reactive hydroxyl rad-

icals can lead to the oxidation of DNA, protein and lipids, and result in cytotoxicity and eventually dopaminergic neuronal death in PD. The perturbation of copper homeostasis has been frequently reported to contribute to the levels of oxidative stress in the cell. Complex formation between Cu^{+} and αSyn has been found to undergo cycles of oxidation and reduction, which leads to the detrimental release of H_2O_2 and other ROS that result in dopaminergic neuron demise [381]. Importantly, generation of oxygen radicals through redox cycling of copper ions can exacerbate the aggregation process of αSyn and favour the formation of stable oligomers by resulting in site-specific copper-catalysed oxidation of amino acids in the vicinity of the coordination site [285, 384, 385, 386, 387, 323].

Under physiological conditions, αSyn exists as a monomer as part of a dynamic ensemble of interconverting conformational states with no residual secondary structure. The three different regions that can be identified in αSyn (N-terminal, NAC and C-terminal regions) have distinct physical properties and functions that can be described as being independent. Evidence shows that this modular organisation promotes intramolecular long-range interactions that are electrostatic in character between the highly-negatively charged C-terminal region and the partially positively charged N-terminal portion, and hydrophobic between the C-terminal and NAC regions. This leads to the stabilisation of conformations that inhibit self-assembly, by protecting the aggregation-prone NAC region from exposure to the solvent and other αSyn monomers, ultimately preventing self-association and amyloid formation [94, 39, 283, 284, 285, 286, 40, 41, 42, 43]. Indeed, the properties of intrinsically disordered proteins are exquisitely sensitive to changes in the environment, where binding to different metals could cause local or global changes in the conformation and behaviour of the protein and therefore its aggregation propensity. Given that αSyn is highly dependent on an unequal charge distribution along its sequence for the maintenance of a stable aggregation auto-inhibited conformation [41, 40], interactions with metal ions might lead to the local neutralisation of charge clusters, and the potential collapse of the long-range weak protective contacts, leading to the full exposure of the NAC region to the solvent.

In this Chapter, I present a comprehensive investigation of how the binding of the metals Ca^{2+}, Zn^{2+}, Cu^{+}, Cu^{2+} and Mn^{2+} affect the conformation and dynamics of monomeric αSyn in a unified picture. To probe changes in the exposure of the different regions and therefore in the hydration sphere of

the protein, a series of CLEANEX NMR experiments were carried out where the exchange between labile backbone amide protons and solvent water protons was recorded. Additionally, I also measured αSyn dynamics in the presence of the various metals at different timescales to provide details that, together with the hydrogen exchange data, suggest conformational changes that occur in the protein which might point at hints of how metal ions might affect αSyn aggregation kinetics.

5.2 Results

To firstly determine the regions and residues of αSyn involved in the binding with the different metal ions of concern, details of the binding sites of Ca^{2+}, Zn^{2+}, Cu^{+}, Cu^{2+} and Mn^{2+} were explored at single-residue resolution by recording ^{1}H-^{15}N HSQC experiments. The high resolution of this methodology provides a means for mapping the binding sites of the metals on αSyn by studying chemical shift perturbations (CSPs). Amide proton exchange with the solvent (hydrogen-hydrogen) provided information on slow conformational dynamics of αSyn in the ms timescale, which was complemented with ^{15}N relaxation to probe faster backbone dynamics. These studies were carried out using non-acetylated as well as acetylated αSyn (apart from ^{15}N relaxation experiments, which were only recorded on Ac-αSyn) to discern any possible physiologically relevant effect that acetylation may have on the protein upon metal complexation. This Chapter is therefore divided into individual subsections corresponding to the different metals investigated, where a detailed explanation of the results from the different probes used to study conformation and dynamics is provided.

5.2.1 Calcium

Consistent with previous findings from other research groups, chemical shift data obtained from the ^{1}H-^{15}N HSQCs recorded here of non-acetylated αSyn and Ac-αSyn showed a clear perturbation at the C-terminal region of the protein upon incubation with Ca^{2+} (Figure 5.1a and c). Differences in the chemical shifts of αSyn in the absence and presence of 10 mM Ca^{2+} were largest in the region of residues 95-140. The CSP profile of Ac-αSyn and non-acetylated αSyn were nearly superimposable, suggesting that N-terminal acetylation does not influence the chemical environment experienced by

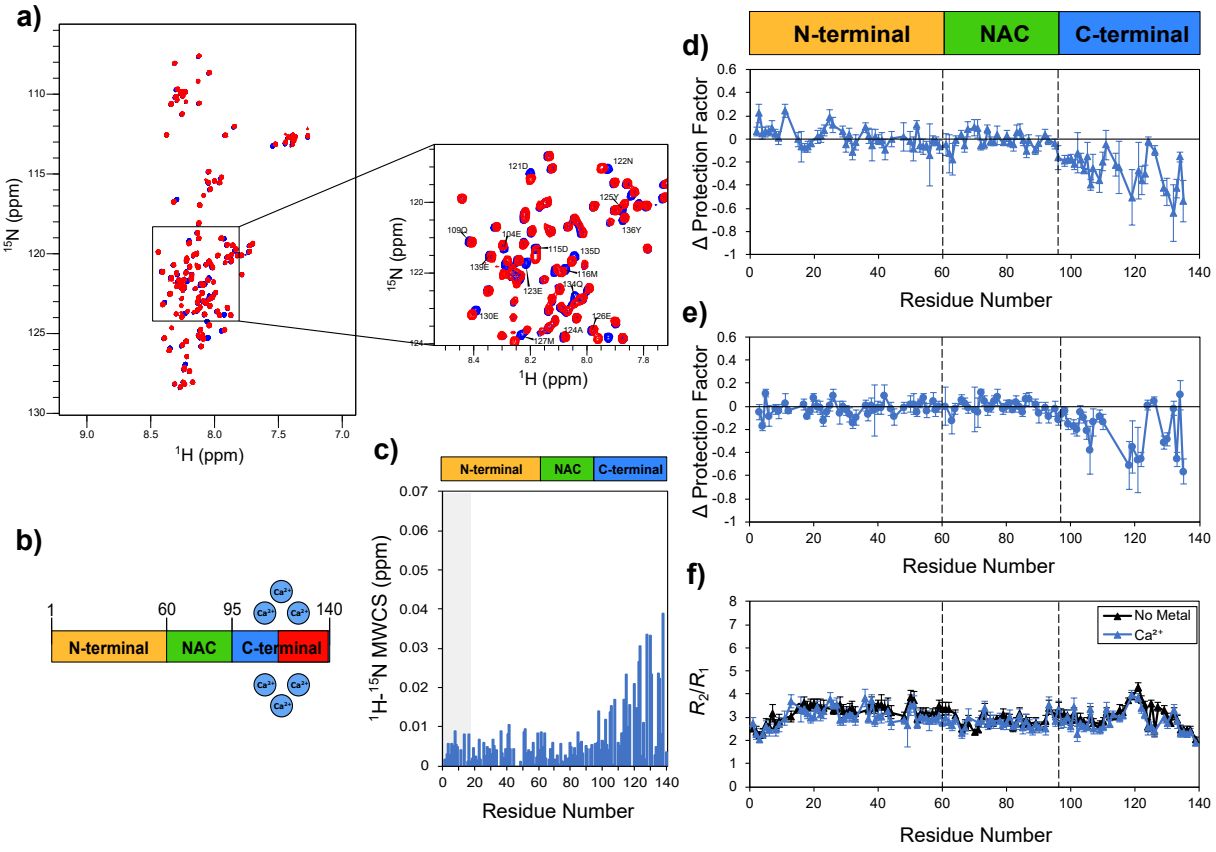


Figure 5.1: NMR analysis of Ca^{2+} binding to αSyn. a) Overlay of ^{1}H-^{15}N HSQC spectra of Ac-αSyn in the absence (red) and presence of Ca^{2+} (blue). The close-up of the spectra shows the most representative affected residues belonging to the C-terminal region of Ac-αSyn. b) Schematic depicting the Ca^{2+}-binding properties of Ac-αSyn. The C-terminal region harbours the low affinity and non-specific metal binding site featuring the DPDNEA sequence motif between residues 119 and 125. However, as a result of the high density of acidic Glu and Asp residues, αSyn has multiple Ca^{2+}-binding sites in the C-terminal region (represented as blue spheres). Highlighted in red is the segment of Ac-αSyn most affected by Ca^{2+} binding. c) ^{1}H-^{15}N MWCS of Ac-αSyn (415 μM) in the presence of Ca^{2+} (10 mM). The grey box denotes the first 15 residues of Ac-αSyn. d) Change in the protection factor along the sequence of Ac-αSyn in the presence of Ca^{2+} compared to free protein, as a measure of amide backbone hydrogen exchange. This is calculated as the log$P$ function of the k_{int}/k_{ex} ratio of each residue. A positive change in protection factor represents an increase in protection of that segment against backbone amide hydrogen exchange, whilst a negative change illustrates a deprotection. Calculated error bars represent the fitting error in the calculation of the k_{ex} for each residue. e) Change in the protection factor along the sequence of non-acetylated αSyn in the presence of Ca^{2+} compared to free protein. f) R_2/R_1 ^{15}N relaxation data of Ac-αSyn in the absence (black) and presence (blue) of Ca^{2+}. No significant alteration in R_2/R_1 along the sequence upon Ca^{2+} complexation suggests that the metal interaction does not induce specific conformational transitions in the intermediate NMR timescale. Error bars represent the sum of the fitting errors in the calculation of R_1 and R_2 along the series of relaxation delays. Dotted lines represent the interface of the different regions along the sequence of Ac-αSyn. The different regions of Ac-αSyn are defined by the following colour scheme: orange represents the N-terminal region; green depicts the NAC; and blue illustrates the C-terminal region. Experiments were recorded at 10 ºC using Ac-αSyn (415 μM) in the absence and presence of Ca^{2+} (10 mM) in 25 mM Tris, pH 7.0.

the residues along the sequence upon binding to Ca^{2+}. This affected portion of the protein coincides with the C-terminal region, which features a net negative charge as a result of a high density of Asp and Glu residues. An electrostatic attraction between the negatively charged residues and the positively charged Ca^{2+} possibly forms the basis of the interaction.

To demonstrate the principle of hydrogen-exchange experiments using the CLEANEX pulse sequence, Figure 5.2 is presented here. By recording these experiments at different mixing times (5 ms, 10 ms, 15 ms, 20 ms, 25 ms), the signal that was allowed to evolve generated NMR spectra with residue peaks presenting increasing associated intensities corresponding to an increase in the mixing time. This change in peak intensity over time can provide information on the rate of chemical exchange, k_{ex}, between amide protons and water hydrogens from the surrounding solvent. Correspondingly, residues showing sharper rises in peak intensities with increasing mixing time will present faster k_{ex} rates and therefore represent residues that are in a fast exchange regime with water hydrogens and hence more exposed (deprotected) to the solvent. In contrast, residue peaks presenting smaller increases in intensity over the increase in mixing time will have slower k_{ex} rates, their amide hydrogens will be less available for exchange with protons from nearby water molecules and will therefore be less exposed (more protected) to the surrounding solvent.

As explained in Chapter 2 (section 2.14) in more detail, the log function of the ratio of the intrinsic exchange rate constant of an individual residue to the chemical exchange rate of that particular residue provides the protection factor value for that residue as a measure of solvent exposure. Furthermore, to demonstrate that the observed results corresponded to effects in the protein upon metal ion interaction and not due to monomer depletion and oligomerisation of the sample during CLEANEX, ^{1}H-^{15}N HSQC spectra recorded before and after performing the NMR experiments confirmed the structural integrity of monomeric αSyn throughout the duration of CLEANEX (Figure 5.3).

CLEANEX NMR experiments were recorded to report on hydrogen exchange of free non-acetylated and acetylated αSyn (Figure 5.4). In both, protection of the C-terminal region was observed in the form of higher protection factor values of up to almost 2.5 compared to the protection factor baseline

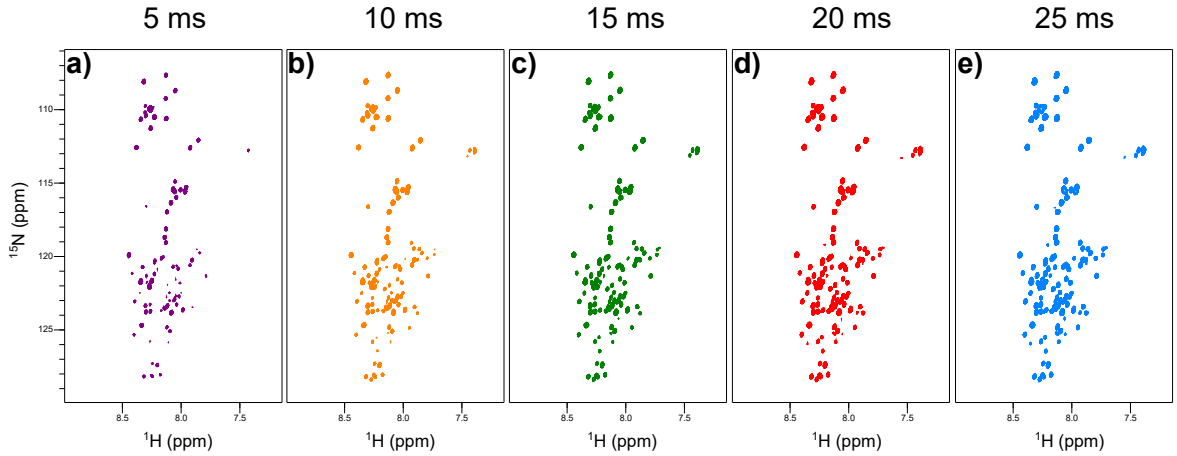


Figure 5.2: Collection of Ac-αSyn CLEANEX NMR spectra recorded at different mixing times. Spectra of free Ac-αSyn recorded at different mixing times (5 ms, 10 ms, 15 ms, 20 ms, 25 ms), showing an increase in the cross-peak intensity with increasing mixing time. Differently coloured spectra represent the recorded signal after a specific mixing time. Experiments were recorded at 10 ºC using Ac-αSyn (415 µM) in 25 mM Tris, pH 7.0.

of the protein. The rest of the sequence did not show significant changes in protection apart from a slight deprotection, and hence higher exposure to the aqueous solvent, observed between residues 35 and 50. Comparison between the protection factor profiles of non-acetylated αSyn and Ac-αSyn did not show any noticeable difference between them, suggesting that the N-terminal acetyl group does not induce significant changes in the conformation of the protein for them to be detected through solvent exposure experiments.

However, binding of Ca^{2+} induced profound alterations in the protection profile of both non-acetylated αSyn and Ac-αSyn (Figure 5.1d and e). Differences in the protection factors along the sequence showed a significant deprotection of the C-terminal region associated with a reduction in log$P$ values of up to 0.6, which is in stark contrast to the strong protection observed for the same region in the absence of Ca^{2+}, indicating a possible conformational transition. A decreased protection of the C-terminal region as observed by faster k_{ex} rates in the presence of calcium relative to uncomplexed protein suggests an enhanced exposure to the solvent (Figure 5.5). Interestingly, comparison between the protection factor profiles of non-acetylated αSyn and Ac-αSyn reveals hints of a small increase in the protection of the first 9 residues closest to the N-terminus of the acetylated protein compared to non-acetylated αSyn. Although not sustained over all residues of this segment of the protein sequence, this increase in protection can be seen to extend up to residue 40, with protection gradually

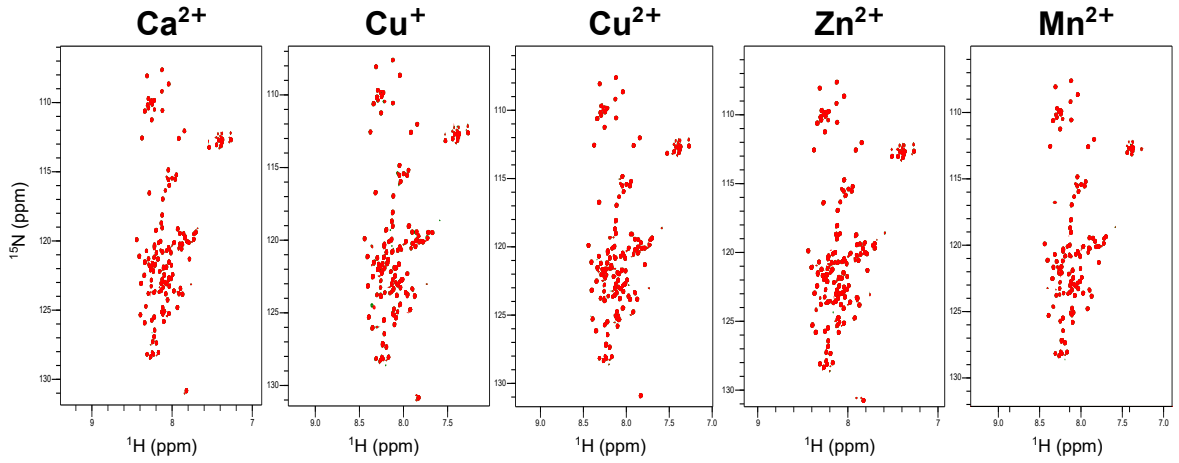


Figure 5.3: Overlay of ^{1}H-^{15}N HSQC spectra of Ac-αSyn in the presence of the various metal ions tested before and after CLEANEX. Red spectra represent Ac-αSyn in combination with each metal ion specified prior to performing CLEANEX. Spectra post-CLEANEX of Ac-αSyn in combination with Ca^{2+}, Cu^{+}, Cu^{2+}, Zn^{2+} and Mn^{2+} are coloured green. The duration of CLEANEX experiments was approximately 18 hours. The absence of differences in cross-peak intensity and distribution in the overlayed spectra of Ac-αSyn before and after CLEANEX confirms the monomeric integrity of the protein and indicates that observed experimental changes are due to the interactions of Ac-αSyn with the metals being tested, and not as a result of metal-induced protein oligomerisation in the samples that may have occurred whilst the experiment was being performed. ^{1}H-^{15}N HSQC and CLEANEX spectra were recorded at 10 ºC in 25 mM Tris in the presence of each respective metal.

decreasing along the sequence. This differential protection of the N-terminal region may be accounted for by the acetylation of the N-terminus of αSyn.

To further investigate the conformational dynamics in a different regime, ^{15}N relaxation was probed as a way of identifying changes in the rigidity and conformation of the protein upon binding events with Ca^{2+}. Given that the protection profiles of non-acetylated αSyn and Ac-αSyn in the presence of Ca^{2+} did not feature large differences, relaxation studies were recorded only on samples of Ac-αSyn, which is thought to be the most physiologically relevant form in which αSyn is found inside the cell. The free form of Ac-αSyn was incubated with 1 mM EDTA to remove any unwanted metal traces from the reference sample spectrum. Comparison between the ^{1}H-^{15}N HSQC spectra of Ac-αSyn in the absence and presence of EDTA failed to show any visible changes in the cross-peaks, indicating that changes observed in the HSQC spectra of Ac-αSyn upon incubation with the different metals considered here are indicative of specific interaction events and not artefacts caused by any residual traces of unknown metal (Figure 5.7c and d). ^{15}N backbone amide longitudinal and transverse relaxation measurements were recorded to inform on the fast-dynamics of the protein in the ps-µs

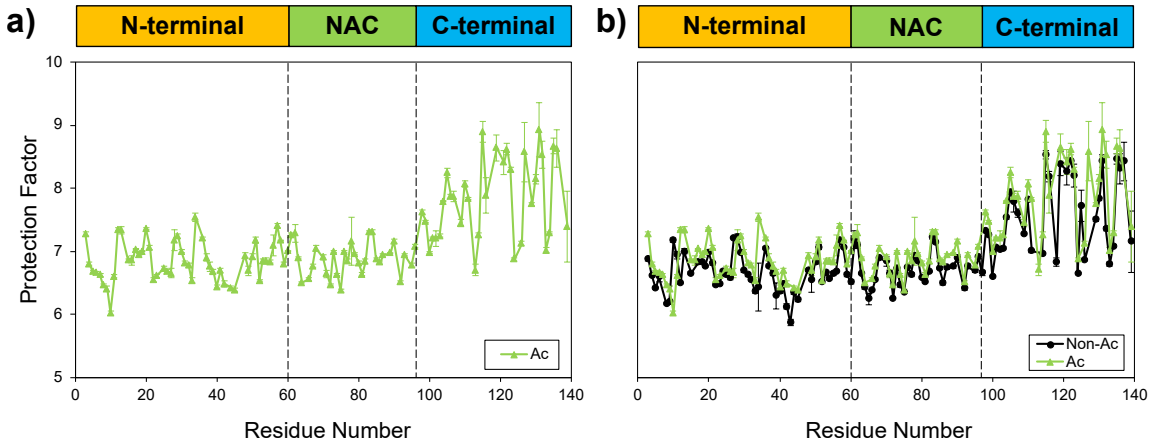


Figure 5.4: Protection factor profile of αSyn as measured by CLEANEX. a) Protection factor values of the residues along the sequence of Ac-αSyn. A strong protection of the C-terminal region is detected in comparison to the rest of the protein. b) Overlay of the protection factor values of the residues along the sequence of Ac-αSyn (green) and non-acetylated αSyn (black). Comparison between the protection factor profiles of Ac-αSyn and non-acetylated αSyn does not reveal significant changes, indicating that N-terminal acetylation has no effect on the protection factor profile of free Ac-αSyn. Dotted lines represent the interface of the different regions along the sequence of Ac-αSyn. The different regions of Ac-αSyn are defined by a colour scheme: orange represents the N-terminal region; green depicts the NAC; and blue illustrates the C-terminal region. Experiments were recorded at 10 ºC using Ac-αSyn (415 μM) and non-acetylated αSyn (415 μM) in 25 mM Tris, pH 7.0.

timescale (Figure 5.6a). These were first performed on the free unbound state of Ac-αSyn. Lower R_1 and R_2 relaxation rates were observed at the termini relative to the rest of the protein. R_1 rates showed lower relaxation values for the C-terminal region in relation to the central segment of the protein, which uniformly ranged between 1.5-2.1 s^{-1}. Remarkably, the R_2 relaxation rate profile seemed to be partitioned into two plateaus, with the N-terminal region having R_2 rates ranging between 5.3-7.6 s^{-1}, and lower relaxation values extending from the NAC to the C-terminal region, which ranged between 3.8-6.7 s^{-1}. This indicates that Ac-αSyn is characterised by a highly flexible conformation, which features dynamic internal motions of the NAC and C-terminal regions with increased local sampling compared to the N-terminal portion of the protein.

Binding of Ca^{2+} did not show a significant alteration of the R_2/R_1 ratio along the protein, including of the C-terminal region, suggesting that interaction with Ca^{2+} does not induce a specific conformational exchange in the intermediate NMR timescale (μs to ms) (Figure 5.1f). It is worth noting that Ca^{2+} binding resulted in a small increase in the R_1 values of the C-terminal region of Ac-αSyn (Figure 5.6a), which is consistent with the region showing the strongest CSPs and largest reductions in log$P$

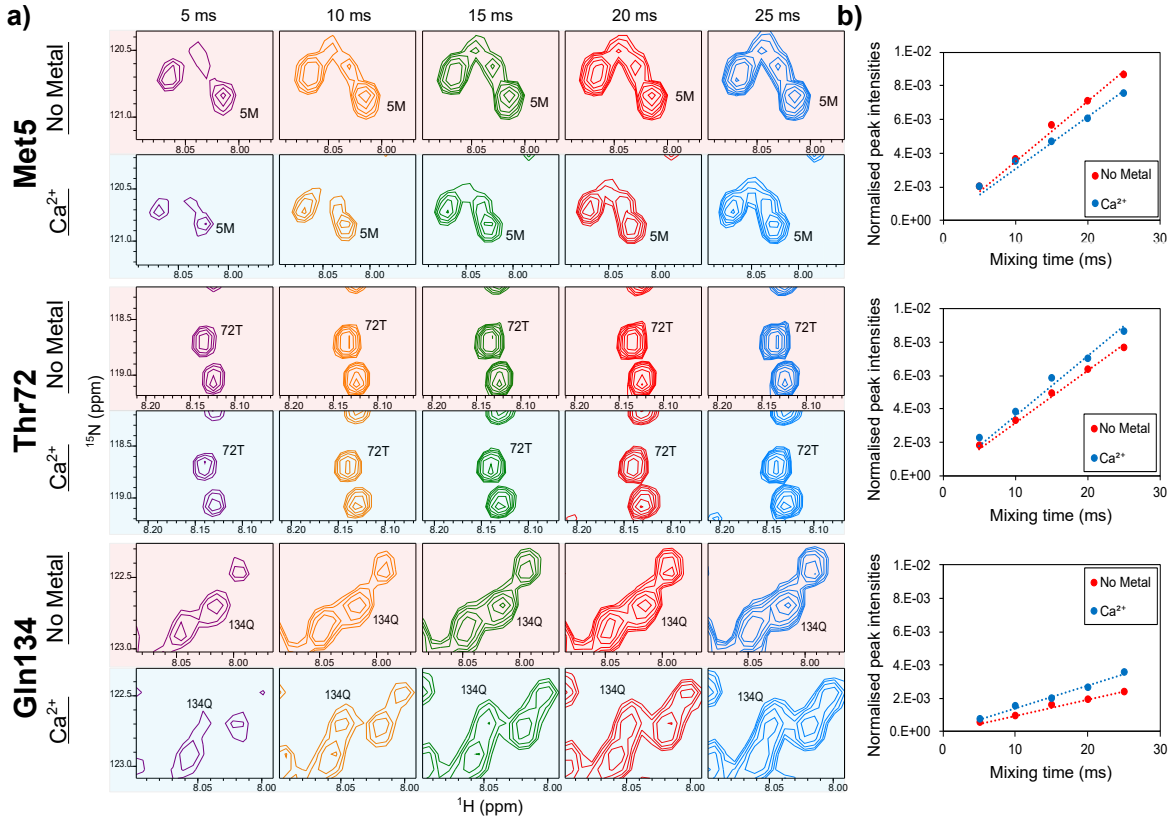


Figure 5.5: Representative example of peak intensity changes recorded with CLEANEX at different mixing times. a) Spectrum close-ups of representative residues of Ac-αSyn in the absence (red background) and presence (blue background) of Ca^{2+} (Met5, Thr72 and Gln134). Higher mixing times are seen to increase the intensity of the peaks of the residues to different extents. b) Quantitative comparison of the peak intensities of Met5, Thr72 and Gln134 at the different mixing times probed during CLEANEX, in the absence (red) and presence (blue) of Ca^{2+}. The slope of the plots is equal to the k_{ex} of each residue, which indicates the rate of hydrogen exchange with the solvent. The intensities were normalised by dividing the recorded peak intensity for each residue at every mixing time by the peak intensity of that residue in a ^{1}H-^{15}N HSQC spectrum. Experiments were recorded at 10 ºC using Ac-αSyn (415 μM) in the absence and presence of Ca^{2+} (10 mM) in 25 mM Tris, pH 7.0.

upon interaction with calcium. This was observed in the NMR spectra as an increase in linewidth broadening, correlating with the highest reduction in intensity of the spectrum peaks of the residues in the C-terminal tail, relative to in the absence of Ca^{2+}. An increase in the values of R_1 of the C-terminal region may suggest restricted local motion sampling in the ns timescale and therefore a higher degree of conformational order in this portion of the Ac-αSyn-Ca^{2+} complex relative to free protein. In this way, binding of an excess of calcium to the C-terminal region may lead to a more constricted C-terminal tail that is able to exchange with the solvent more freely. Interestingly, R_2 relaxation data did not reveal changes in the rigidity of Ac-αSyn upon binding of calcium (Figure 5.6a). Of note, even though relaxation data from non-acetylated αSyn is not available in the same

conditions for comparison, higher R_1 and R_2 values of the first five residues of the sequence relative to that of the next immediate residues suggests an increased rigidity in the very first few residues, which is consistent with an enhanced propensity for the acetylated N-terminus of αSyn to dynamically and transiently probe helical states.

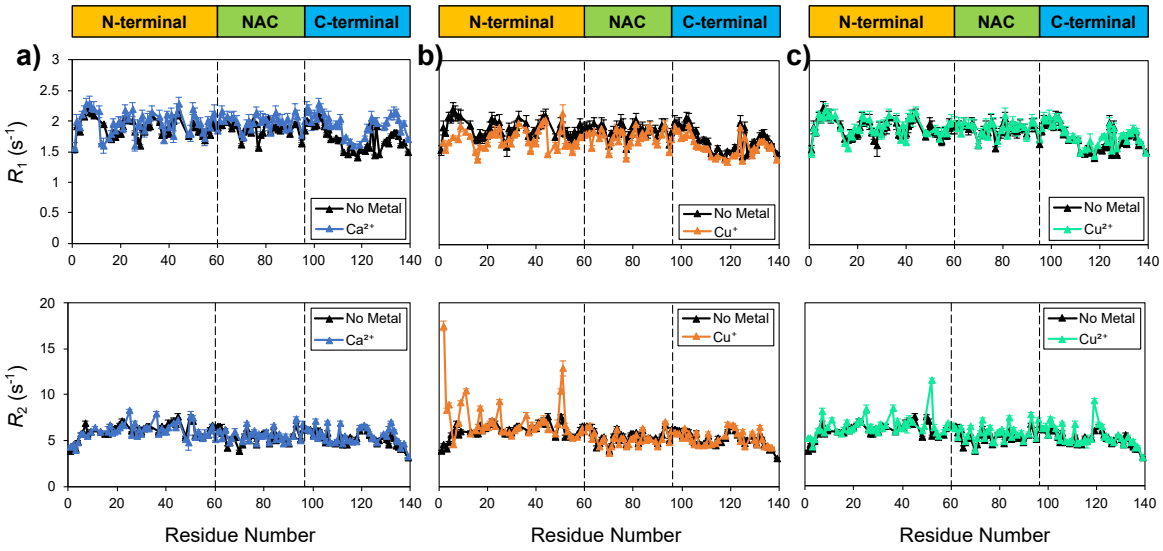


Figure 5.6: ^{15}N relaxation of Ac-αSyn complexed with Ca^{2+}, Cu^{+} and Cu^{2+}. a) R_1 and R_2 relaxation data of Ac-αSyn in the absence (black) and presence (blue) of Ca^{2+}. A slight increase in the R_1 values of the residues of the C-terminal region can be detected, whilst no change was observed in transverse relaxation along the sequence of Ac-αSyn. b) R_1 and R_2 relaxation profiles of Ac-αSyn in the absence (black) and presence (orange) of Cu^{+}. A slight reduction in the R_1 values up to residue 15 of the N-terminal region can be detected. A strong perturbation of R_2 relaxation is observed at the N-terminus of Ac-αSyn and in the proximity of His50, which is consistent with these regions showing the strongest CSPs. c) R_1 and R_2 relaxation data of Ac-αSyn in the absence (black) and presence (turquoise) of Cu^{2+}. No significant changes are seen in the longitudinal or transverse relaxation of Ac-αSyn, except in the R_2 values in the proximity of His50 and Asp121. Error bars represent the sum of the fitting errors in the calculation of R_1 and R_2 along the series of relaxation delays. Dotted lines represent the interface of the different regions along the sequence of Ac-αSyn. The different regions of Ac-αSyn are defined by the following colour scheme: orange represents the N-terminal region; green depicts the NAC; and blue illustrates the C-terminal region. Experiments were recorded at 10 ºC using Ac-αSyn (415 μM) in the absence and presence of Ca^{2+} (10 mM), Cu^{+} (85 μM) and Cu^{2+} (85 μM) in 25 mM Tris, pH 7.0.

Therefore, these data indicate that Ca^{2+} binding perturbs the conformational ensemble of αSyn by destabilising a closed conformation featuring the transient intramolecular contacts between the N- and C-terminal regions, and resulting in a reduction in log$P$ in the acidic C-terminal tail.

5.2.2 Copper

Evidence shows a strong link between copper and αSyn aggregation, which makes the molecular mechanisms of this interaction worth studying [525, 526, 527, 319, 387, 305, 528, 284, 529]. Given the reducing environment inside the cell, copper most likely exists in a dynamic redox state cycling between Cu^{+} and Cu^{2+}. To map the binding sites of the transient interactions of αSyn with the two physiological oxidation sates of copper, chemical shifts of non-acetylated αSyn and Ac-αSyn in the presence and absence of Cu^{+} and Cu^{2+} were measured. In order to ensure full reduction of Cu^{2+} to Cu^{+}, an excess of 10 mM sodium ascorbate was added to the reaction. This was not found to induce any conformational changes in αSyn, as seen by an unperturbed ^{1}H-^{15}N HSQC spectrum of the protein in the presence of the reducing agent (Figure 5.7a and b).

The largest perturbations to the chemical shifts of the amino acid residues of αSyn in the presence of copper were observed to occur in three different regions: the N-terminus, residues centred around His50 in the N-terminal region, and the C-terminal region (Figure 5.8b). The electron spin relaxation from the paramagnetic Cu^{2+} and diamagnetic Cu^{+} ions resulted in differential broadening of amide proton resonances in the vicinity of the para- or diamagnetic centres by through-bond or through-space interactions. However, it should be noted that chemical shift data for some residues in these regions that may probably be involved in binding were missing as a result of line broadening due to excessive paramagnetic and diamagnetic effects from Cu^{2+} and Cu^{+} ions, respectively. A low 1:5 ratio of copper to αSyn (85 μM:415 μM) was used when investigating these interactions, although this still seemed to lead to broadening and the disappearing of specific peak signals of certain residues.

Particularly surprising was the profound effect of Cu^{+} complexation on the chemical shifts of the residues of Ac-αSyn (Figure 5.8b). Whilst the chemical environment experienced by nuclei in the C-terminal region and around His50 in Ac-αSyn was very similar to that experienced by nuclei of non-acetylated αSyn, dramatic chemical shift deviations can be observed upon Cu^{+} binding at the N-terminus. Consistently, the three regions where Cu^{+} and Cu^{2+} appear to bind are conserved in Ac-αSyn, although the magnitude of the chemical shift differences seen for the N-terminus of Ac-αSyn in the presence of Cu^{+} is drastically higher. These dramatically larger perturbations in the chemical

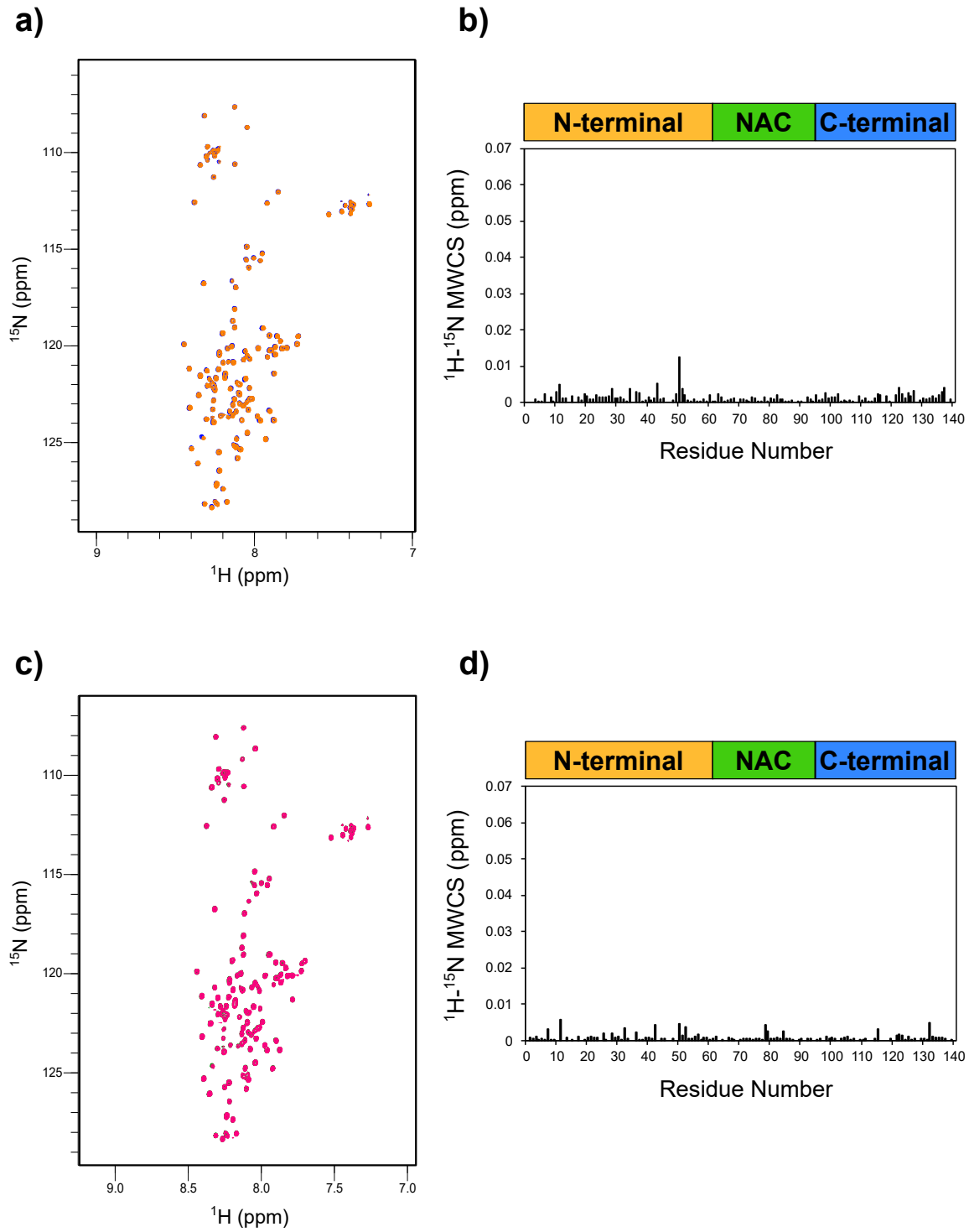


Figure 5.7: Effect of addition of Na-ascorbate and EDTA on αSyn and Ac-αSyn, respectively. a) Overlay of ^{1}H-^{15}N HSQC spectra of αSyn (415 μM) in the absence (green) and presence of Na-ascorbate (10 mM) (pink). b) ^{1}H-^{15}N MWCS of αSyn (415 μMM) in the presence of Na-ascorbate (10 mM), showing no significant effect in the chemical environments of the nuclei along the sequence. This indicates that the effect seen upon addition of Cu^{+} (85 μM) corresponds to the binding interaction of the metal ion, and not of the reducing agent used to reduce Cu^{2+} to Cu^{+}. A subtle perturbation of the chemical environment of His50 likely corresponds to a slight change in pH upon ascorbate addition. c) Overlay of ^{1}H-^{15}N HSQC spectra of Ac-αSyn (415 μM) in the absence (dark blue) and presence of EDTA (1 mM) (orange). d) MWCS of Ac-αSyn (415 μM) in the presence of EDTA

Figure 5.7: (1 mM), showing no effect in the chemical environments of the nuclei along the protein sequence. This indicates that there were no trace amounts of metal ions present in free Ac-αSyn that may have influenced the effect seen upon binding of the metal ions studied. Experiments were recorded at 10 ºC using Ac-αSyn in 25 mM Tris, pH 7.0.

shifts of the first 13 residues of the protein suggest a change in the local chemical environment of the nuclei of this region that might represent structural motions beyond a sole metal ion binding event. At the same time, N-terminal acetylation is associated with a small reduction in the CSPs observed at the N-terminus upon binding of Cu^{2+} to Ac-αSyn, compared to non-acetylated αSyn.

To investigate how the binding of Cu^{+} and Cu^{2+} to these three localised regions might affect the folding of the protein and its exposure to the solvent, CLEANEX experiments were recorded. As shown in Figures 5.8c and 5.8d, no big changes can be observed in the exposure to the solvent of non-acetylated αSyn and Ac-αSyn upon binding of Cu^{+}. However, a small increase in 0.3 in log$P$ values of the protection factors of the residues in the N-terminus was observed upon Cu^{+} binding to Ac-αSyn. Indeed, the protection factor of the first residue for which exchange data is available, Val3, is almost 0.4 higher in Ac-αSyn relative to non-acetylated αSyn. The interpretation of this finding is cumbersome because exchange data for Met1 and Asp2 are not available, most likely as a result of the diamagnetic properties of Cu^{+}, which induced line broadening. However, by observing the difference in protection of 3Val, it can be envisioned that the protection factors of the two first residues closest to the N-terminus of the protein might experience a similar enhanced protection relative to the rest of the protein. This could therefore be indicative of a decrease in the exposure to the solvent of the N-terminus of αSyn when Met1 is acetylated. Missing data as a result of line broadening effects, which are also particularly noticeable in the C-terminal region of the protein, prevented the detailed characterisation of the hydrogen exchange rate profiles of the regions involved in Cu^{+} binding. Subtle fluctuations of deviations of around 0.1 in the log$P$ values of some residues are likely to be the result of variations in solvent conditions.

Binding of Cu^{2+} did not result in large changes in the protection factor profiles of either non-acetylated or Ac-αSyn. No significant differences could be identified between the hydrogen exchange rates of residues in Ac-αSyn relative to non-acetylated αSyn. As with complexation with Cu^{+}, paramagnetic

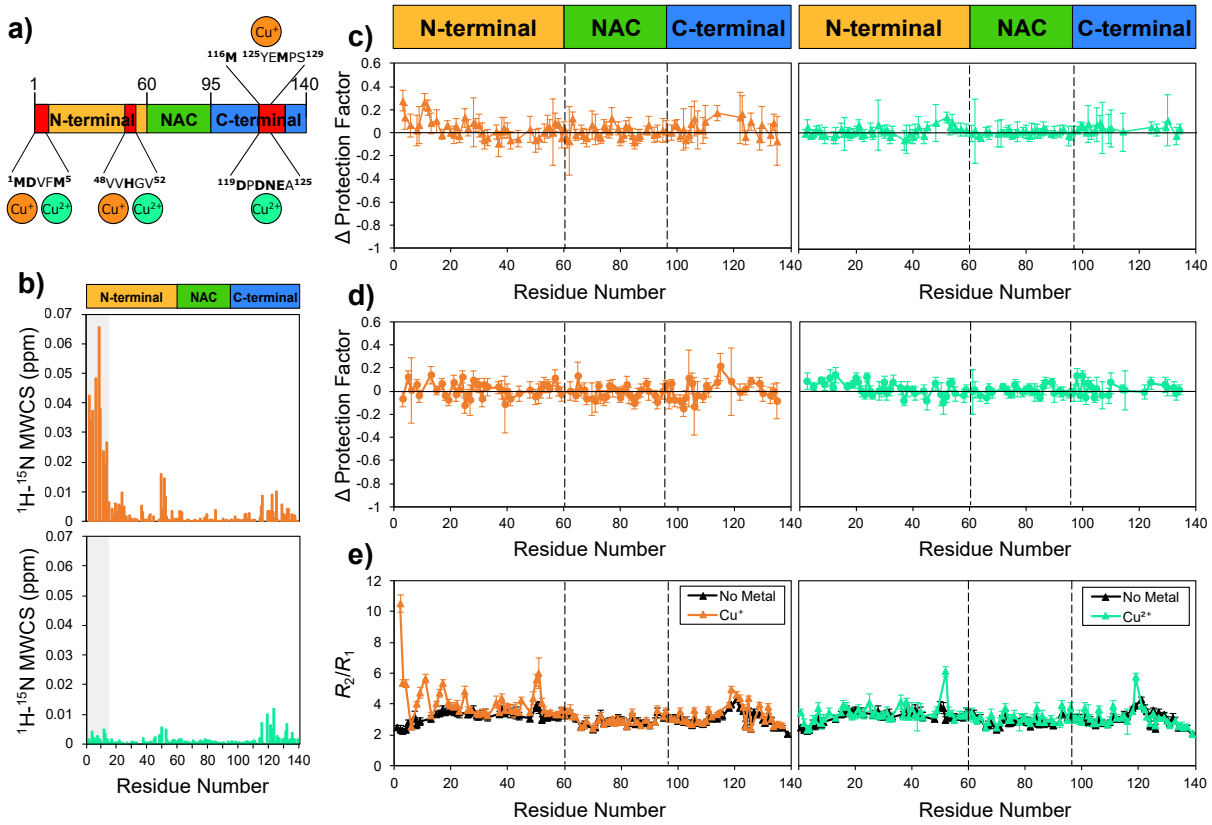


Figure 5.8: NMR analysis of copper binding to Ac-αSyn. a) Schematic depiction of the Cu^{2+}- and Cu^{+}-binding sites of Ac-αSyn. The sequence of Ac-αSyn has three independent binding sites for copper with different binding affinities: (1) the N-terminus is the high affinity binding site and is mediated by Met1, Asp2 and Met5, which form the MDVFM binding motif. This binding site in Ac-αSyn is highly specific for Cu^{+}, but not Cu^{2+}, whose binding at this site is only seen in non-acetylated αSyn. (2) The imidazole ring of His50 constitutes the second binding site of Cu^{+} and Cu^{2+}, which bind with a lower affinity than at the N-terminus. (3) The C-terminal region corresponds to the low affinity site of copper and has two sequence motifs responsible for copper coordination: Cu^{+} binding is mediated by the sulfur atoms in Met116 and Met127, whilst Cu^{2+} binds to Asp119, Asp121, Gln122 and Glu123 in the DPDNEA motif spanning residues 119 and 125. Parts of the schematic coloured in red display the segment of Ac-αSyn most affected by Cu^{+} and Cu^{2+} binding. Binding of Cu^{+} along the sequence of Ac-αSyn is shown by orange spheres, whilst Cu^{2+} coordination is displayed as turquoise balls. b) ^{1}H-^{15}N MWCS of Ac-αSyn in the presence of Cu^{+} (orange) and Cu^{2+} (turquoise). The grey box denotes the first 15 residues of Ac-αSyn. c) Change in the protection factor along the sequence of Ac-αSyn in the presence of Cu^{+} (orange) and Cu^{2+} (turquoise) compared to free protein. No significant alterations to the protection factors of Ac-αSyn were observed upon copper binding, apart from a slight increase detected at the N-terminus upon Cu^{+} coordination. Calculated error bars represent the fitting error in the calculation of the k_{ex} for each residue. d) Change in the protection factor along the sequence of non-acetylated αSyn in the presence of Cu^{+} (orange) and Cu^{2+} (turquoise) compared to free protein. e) R_2/R_1 ^{15}N relaxation data of Ac-αSyn in the absence (black) and presence of Cu^{+} (orange) and Cu^{2+} (turquoise). An increase in the R_2/R_1 values of the residues in the N-terminus and in the proximity of His50 upon Cu^{2+} coordination indicates that interaction with Cu^{+} induces a conformational exchange in the intermediate timescale. Binding of Cu^{2+} did not induce in significant changes in R_2/R_1 values, except in proximity of His50 and Asp121. Error bars represent the sum of the fitting errors in the calculation of R_1 and R_2 along the series of

Figure 5.8: relaxation delays. Dotted lines represent the interface of the different regions along the sequence of Ac-αSyn. Binding of copper in both oxidation states showed paramagnetic broadening in the C-terminal region, which made the interpretation of the solvent exposure properties of this segment of Ac-αSyn challenging. Binding data from Cu^{+} and Cu^{2+} are displayed in orange and turquoise, respectively. The different regions of Ac-αSyn are defined by the following colour scheme: orange represents the N-terminal region; green depicts the NAC; and blue illustrates the C-terminal region. Experiments were recorded at 10 ºC using Ac-αSyn (415 μM) in the absence and presence of Cu^{+} or Cu^{2+} (85 μM) in 25 mM Tris, pH 7.0.

effects and large fitting error led to missing data particularly in the C-terminal region, which made interpretation difficult of the solvent exposure of this segment of the protein. Overall, binding of copper in both oxidation states did not induce large changes in the protection of the residues of either non-acetylated or Ac-αSyn against hydrogen exchange with the solvent.

Fast motion R_1 and R_2 relaxation dynamics were measured with the aim of studying transient conformational changes and local motions that may result from the binding of copper (Figure 5.8e, and 5.6b and c). As with calcium, relaxation experiments were recorded using Ac-αSyn, and not non-acetylated αSyn, given their similar solvent protection factor profiles. Particularly remarkable was the difference observed upon complexation of Cu^{+} in the R_1 and R_2 values of the N-terminus (Figure 5.6b). Analysis of the relaxation properties of αSyn in the presence of Cu^{+} revealed a strong increase in R_2/R_1 values in the N-terminus and, to a lesser extent, in the proximity of His50 (Figure 5.8e), indicating that interaction with Cu^{+} induced a conformational exchange in the intermediate timescale. Binding of Cu^{+} also induced a significant increase in the R_2 values of the residues in the N-terminus of Ac-αSyn up to around residue 15, compared to free protein, suggesting a large structural rearrangement. This alteration in the relaxation properties of these regions is consistent with the strong CSPs observed and the small increase in protection factor values detected for the N-terminus.

R_1 relaxation showed a small perturbation in the dynamics of the N-terminus of the protein too, with a reduction in the R_1 values compared to free protein. Indeed, no large deviations were observed in the R_1 and R_2 relaxation values along the rest of the protein, suggesting that this striking difference in N-terminal dynamics upon Cu^{+} binding is a result of a localised, specific interaction (Figure 5.6b). A small increase in the R_2 values in the region around His50 upon binding of Cu^{+} might also suggest an

increased degree of rigidity, although the fact that it is only two isolated amino acid residues the ones presenting higher R_2 values within a local region that possesses lower relaxation rates urges caution on the interpretation of this finding. A generally faster R_1 as seen throughout the whole sequence of Ac-αSyn when complexed with Cu^{+} may be explained by diamagnetic effects in the solvent that might affect relaxation rates of the whole polypeptide.

Interestingly, no remarkable changes were observed in relaxation measurements of Ac-αSyn in the presence of Cu^{2+} (Figure 5.6c and 5.8e). Whilst complexation with Cu^{2+} did not induce changes in the dynamics of the protein detectable in the ps-ns timescale by R_1 relaxation experiments, a higher R_2 value for residue His50 and Asp121 might raise the question of whether this might suggest a higher restricted structural sampling in these two regions, which have been shown to be copper binding sites. However, the fact that these are two isolated data points argues against the robustness of this proposed mechanism.

5.2.3 Zinc

Analysis of the chemical shifts corresponding to the residues of non-acetylated αSyn and Ac-αSyn in the presence of Zn^{2+} identified the largest CSPs around residue H50 and the C-terminal region, with the largest differences centred around Asp121 (Figure 5.9a and c). These data therefore identified two binding sites for Zn^{2+} involving His50 in the far N-terminal region and Asp121 in the C-terminal region, which are in agreement with previous studies on the binding mode of Zn^{2+} with αSyn [309]. No changes were observed upon comparison of the CSP pattern of non-acetylated αSyn and Ac-αSyn as a result of acetylation.

In a similar way to calcium, addition of an excess of Zn^{2+} induced a large reduction in the log$P$ values of up to 0.5 in the protection factors of the residues in the C-terminal region (Figure 5.9d and e). Zinc therefore seems to induce the deprotection of the C-terminal tail and thus enhance its exposure to the solvent. This corresponds to a remarkable difference compared to the uncomplexed protection profile of both non-acetylated αSyn and Ac-αSyn. In terms of the N-terminal region, a small increase in the protection of residues against solvent exposure can be observed along the entirety of the N-terminal segment up to the NAC region, with protection gradually decreasing along the sequence. While this can also be seen in the protection profile of non-acetylated αSyn, this effect seems to be attenuated in the absence of N-terminal acetylation. This small increase in protection is followed by a subtle reduction, which coincides with the start of the NAC region, and which then extends to the larger extent of exposure observed over the whole C-terminal region.

The dynamics of Ac-αSyn complexed with Zn^{2+} were then probed by recording R_1 and R_2, with the aim of shining light on possible local conformational transition events that may take place in the fast regime to allow the deprotection of the C-terminal region. ^{15}N relaxation measurements were carried out using only Ac-αSyn, as a representation of the most physiologically available form of αSyn. Binding of Zn^{2+} was found to strongly perturb the relaxation properties of αSyn, with significant alterations of R_2/R_1 in the proximity of His50 and Asp121, indicating conformational exchange in the intermediate timescale in these regions (Figure 5.9f). These data are in agreement with a large increase in the R_2 values of these two localised regions upon Zn^{2+} binding (Figure 5.10a). Higher R_2 values

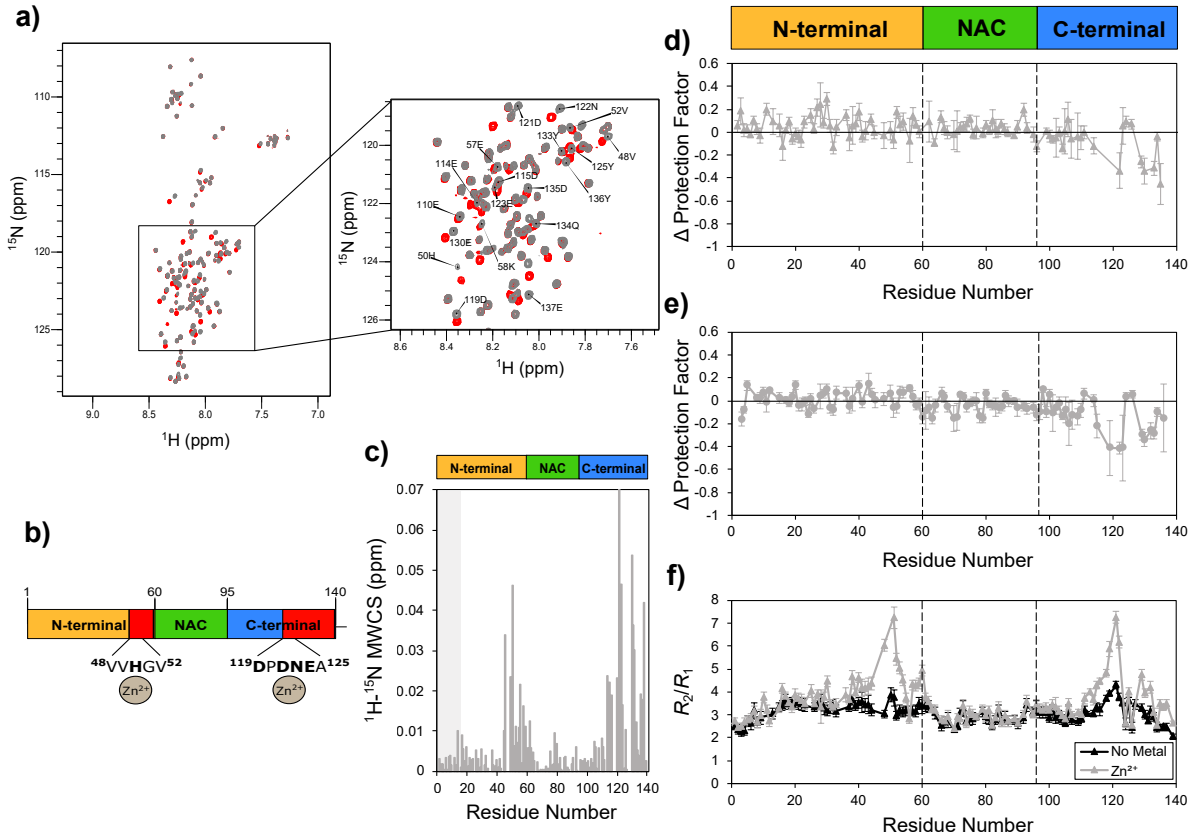


Figure 5.9: NMR analysis of Zn^{2+} binding to Ac-αSyn. a) Overlay of ^{1}H-^{15}N HSQC spectra of Ac-αSyn in the absence (red) and presence of Zn^{2+} (grey). The close-up of the spectra shows some of the most representative affected residues. b) Schematic depicting the Zn^{2+}-binding properties of Ac-αSyn. The sequence of αSyn displays two binding sites for Zn^{2+}: (1) His50 in the N-terminal region as part of the motif VVHGV between residues 48 and 52; and (2) the C-terminal region involving Asp119, Asp121, Gln122 and Glu123 within the sequence motif DPDNEA spanning residues 119 and 125. Binding of Zn2+ at these binding sites is represented as grey spheres. Red displays the segments of Ac-αSyn most affected by Zn^{2+} binding. c) ^{1}H-^{15}N MWCS of Ac-αSyn in the presence of Zn^{2+}. The grey box denotes the first 15 residues of Ac-αSyn. MWCS data for the strong perturbation detected at Asp121 reached 0.086 but was capped at 0.07 to allow the unbiased interpretation of the data for the different residues involved in the interaction with Zn^{2+}. d) Change in the protection factor along the sequence of Ac-αSyn in the presence of Zn^{2+} compared to free protein, as a measure of amide backbone hydrogen exchange. A negative change in protection factor illustrates an enhanced solvent exchange of the residues in the C-terminal region of Ac-αSyn. Calculated error bars represent the fitting error in the calculation of the k_{ex} for each residue. e) Change in the protection factor along the sequence of non-acetylated αSyn in the presence of Zn^{2+} compared to free protein. f) R_2/R_1 ^{15}N relaxation data of Ac-αSyn in the absence (black) and presence (grey) of Zn^{2+}. A strong perturbation of the R_2/R_1 relaxation properties of Ac-αSyn in the proximity of His50 and Asp121 indicate a conformational exchange in the intermediate NMR timescale. Error bars represent the sum of the fitting errors in the calculation of R_1 and R_2 along the series of relaxation delays. Dotted lines represent the interface of the different regions along the sequence of Ac-αSyn. The different regions of Ac-αSyn are defined by the following colour scheme: orange represents the N-terminal region; green depicts the NAC; and blue illustrates the C-terminal region. Experiments were recorded at 10 ºC using Ac-αSyn (415 µM) in the absence and presence of Zn^{2+} (2.1 mM) in 25 mM Tris, pH 7.0.

are indicative of a faster loss of magnetisation, which translates into a shorter-lived FID and broader spectrum peaks. This shows that these two regions experience an enhanced conformational ordering compared to the rest of the protein and therefore suggests the existence of a local conformational change upon Zn^{2+} binding. These findings are consistent with these regions showing the strongest perturbations in chemical shifts and largest reduction in the protection factors of the C-terminal region. This enhanced restriction in the local sampling of the C-terminal region is therefore coupled with a higher exposure to the solvent observed upon coordination to Zn^{2+}. However, it should be noted that the increased rigidity experienced by the region around residue H50 cannot be explained by the results from the CLEANEX studies, which fail to show an apparent change in hydrogen exchange rates of this segment of the protein, and therefore solvent exposure. Interestingly, longitudinal relaxation values probing for faster motions in the subnanosecond time regime were unperturbed upon the addition of Zn^{2+}, as shown in Figure 5.10a.

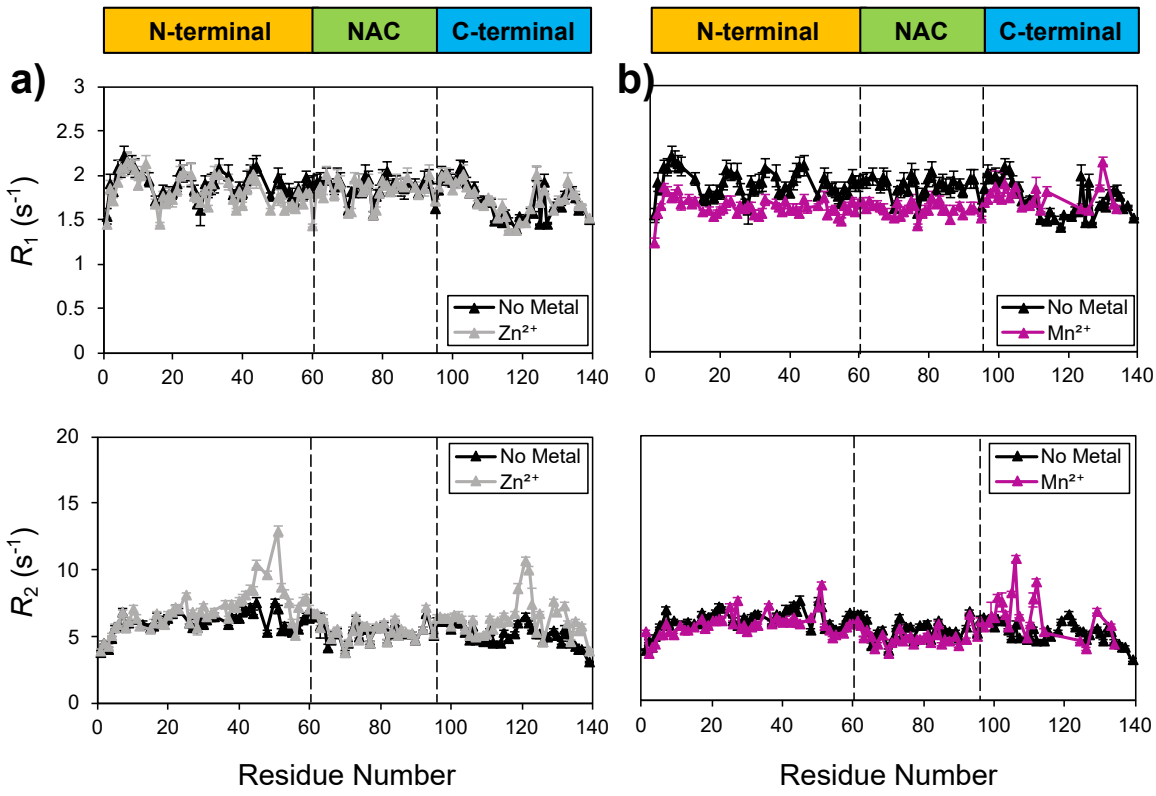


Figure 5.10: ^{15}N relaxation of Ac-αSyn complexed with Zn^{2+} and Mn^{2+}. a) R_1 and R_2 relaxation profiles of Ac-αSyn in the absence (black) and presence (grey) of Zn^{2+}. No significant changes are detected in the R_1 values of Ac-αSyn. However, a strong perturbation in the transverse relaxation of the regions around His50 and Asp121 can be detected, indicative of a conformational exchange. This is consistent with these regions showing the largest CSPs and a reduction in log$P$ at the C-terminal region. b) R_1 and R_2 relaxation data of Ac-αSyn in the absence (black) and presence (grey) of Mn^{2+}. It is worth noting that a the general reduction in R_1 values except for those of the C-terminal region may be induced by Mn^{2+} as a result of the paramagnetic effect on the Ac-αSyn resonances. A slight increase in the R_2 values of the residues 100-120 of the C-terminal region can be detected. Extensive line broadening in the relaxation spectra of Ac-αSyn as a result of the strong paramagnetic properties of Mn^{2+} allowed only the measurement of the R_1 and R_2 values of a few residues in the C-terminal region of Ac-αSyn. Error bars represent the sum of the fitting errors in the calculation of R_1 and R_2 along the series of relaxation delays. Dotted lines represent the interface of the different regions along the sequence of Ac-αSyn. The different regions of Ac-αSyn are defined by the following colour scheme: orange represents the N-terminal region; green depicts the NAC; and blue illustrates the C-terminal region. Experiments were recorded at 10 ºC using Ac-αSyn (415 μM) in the absence and presence of Zn^{2+} (2.1 mM) and Mn^{2+} (55 μM) in 25 mM Tris, pH 7.0.

5.2.4 Manganese

As with the other metals reported in this Chapter, chemical shift data was extracted from ^{1}H-^{15}N HSQCs recorded of non-acetylated αSyn and Ac-αSyn in the presence of Mn^{2+} to characterise the binding site of Mn^{2+} on the sequence of αSyn (Figure 5.11b). Even though an incubation ratio of 1:7.5 (55 μM Mn^{2+} to 415 μM αSyn) was used, extensive line broadening was observed in the spectra of non-acetylated αSyn and Ac-αSyn upon incubation with manganese as a result of the metal's paramagnetic properties. As shown, the C-terminal tail of αSyn is the only region where significant perturbations to the chemical shifts of the amino acids were recorded. Together with the fact that the largest extent of peak broadening leading to the disappearing of peaks occurred in this region, suggests that the C-terminal region may be the only binding site of Mn^{2+} in αSyn. No differences were seen in terms of the localisation of major CSPs in Ac-αSyn compared to non-acetylated αSyn. A slightly larger number of data points revealing disturbances in the chemical shifts of residues of the C-terminal region of non-acetylated αSyn compared to Ac-αSyn is most likely the result of experimental variation, and not of a decrease in the binding of Mn^{2+} resulting in less linewidth broadening.

Measurement of hydrogen exchange along the sequence of non-acetylated αSyn and Ac-αSyn in the presence of Mn^{2+} was again hindered by strong broadening effects of the resonances of the residues in the vicinity of the binding site (Figure 5.11c and d). Consistent with chemical shift results, the largest number of missing peaks concentrates at the C-terminal region. It is therefore particularly challenging to make conclusive judgements on the effect of Mn^{2+} on the hydration sphere and folding of the protein. However, the recorded data suggest a general lack of perturbation to the local solvent exchange of the residues of non-acetylated αSyn and Ac-αSyn as shown by the unambiguously uniform protection factor profiles.

Relaxation of αSyn was measured to probe any effect on fast backbone dynamics of the binding of Mn^{2+} that may not be detected in slower protein motional samplings as measured with amide hydrogen exchange. In the same way as with the other metals discussed in this Chapter, relaxation experiments were only measured on Ac-αSyn. Interestingly, enhanced R_2/R_1 values were observed in residues M1, G25, A27, G36, G51, Q99, L100, G101, K102, N103, E104, E105, A107, E110,

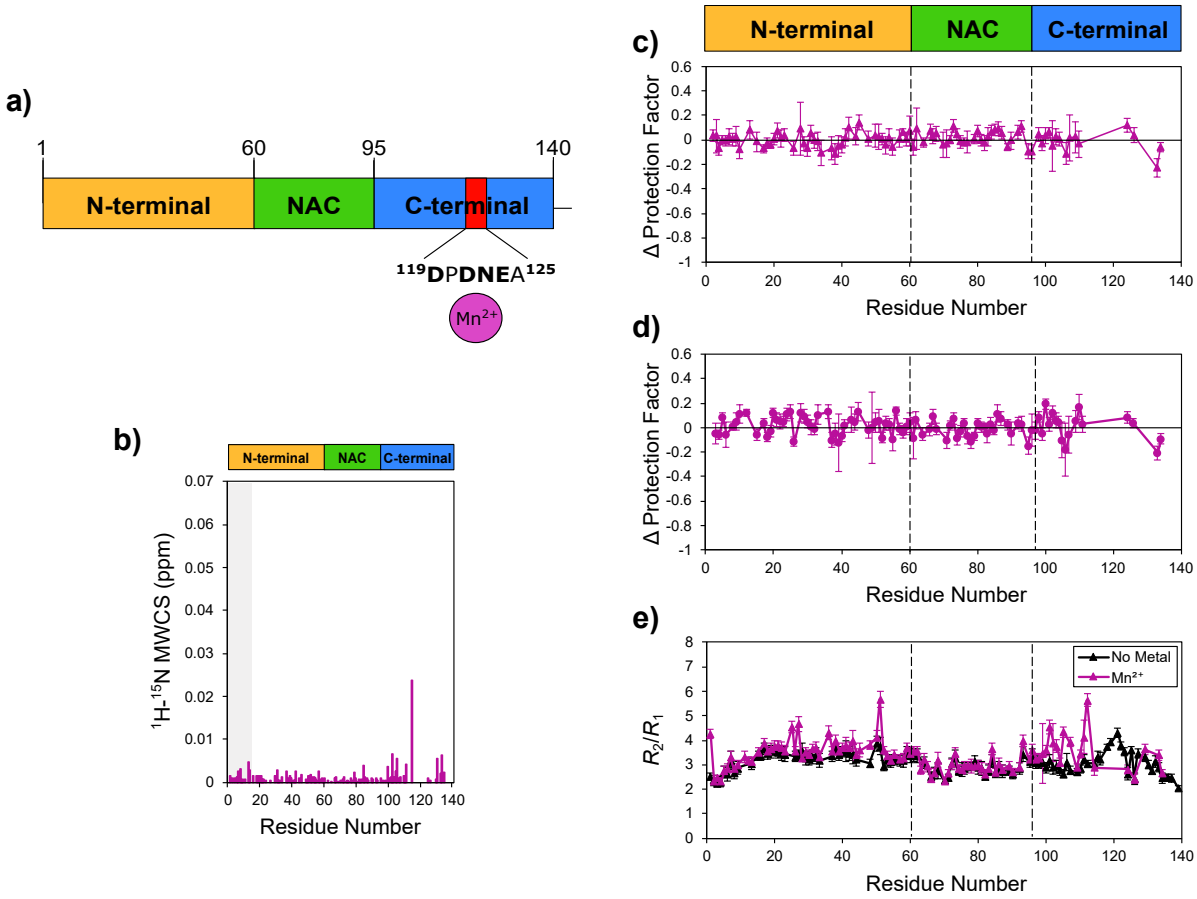


Figure 5.11: NMR analysis of Mn^{2+} binding to Ac-αSyn. a) Schematic depiction of the Mn^{2+}-binding properties of Ac-αSyn. The C-terminal region features a low affinity and non-specific metal binding site featuring the DPDNEA sequence motif between residues 119 and 125. Mn^{2+} binding at the C-terminal region is represented by purple spheres. Red displays the segment of Ac-αSyn most affected by Mn^{2+} binding. b) ^{1}H-^{15}N MWCS of Ac-αSyn in the presence of Mn^{2+}. The grey box denotes the first 15 residues of Ac-αSyn. c) Change in the protection factor along the sequence of Ac-αSyn in the presence of Mn^{2+} compared to free protein. Protection factor data are only available for a few residues as a result of broadening effects, although no perturbation to the local solvent exchange is observed in those residues for which data are present. Calculated error bars represent the fitting error in the calculation of the k_{ex} for each residue. d) Change in the protection factor along the sequence of non-acetylated αSyn in the presence of Mn^{2+} compared to free protein. e) R_2/R_1 ^{15}N relaxation data of Ac-αSyn in the absence (black) and presence (purple) of Mn^{2+}. Enhanced R_2/R_1 values can be observed in some residues located in the mid N-terminal segment and C-terminal region of Ac-αSyn. Error bars represent the sum of the fitting errors in the calculation of R_1 and R_2 along the series of relaxation delays. Dotted lines represent the interface of the different regions along the sequence of Ac-αSyn. Extensive line broadening was observed in the spectra recorded of Ac-αSyn in the presence of Mn^{2+} as a result of the metal's paramagnetic properties, making the detailed interpretation of the residues involved in the interaction challenging. The different regions of Ac-αSyn are defined by the following colour scheme: orange represents the N-terminal region; green depicts the NAC; and blue illustrates the C-terminal region. Experiments were recorded at 10 ºC using Ac-αSyn (415 μM) in the absence and presence of Mn^{2+} (55 μM) in 25 mM Tris, pH 7.0.

G111 and I112 along the protein (Figure 5.11e). Fast motion R_1 data showed a generalised decrease in the relaxation values along almost the entirety of the protein sequence up to approximately residue 95 (Figure 5.10b). It is worth noting that this effect is believed to have probably been caused by paramagnetic effects, which may have influenced R_2/R_1 values. However, the same effect was not observed in R_2 relaxation data (Figure 5.10b). Particularly intriguing are the relaxation properties of the C-terminal region in both measures of dynamics. Complexation with Mn^{2+} resulted in a small increase in the R_2 relaxation rates of this region, suggesting a higher degree of internal motion restriction. Whilst this effect is not as apparent from R_1 relaxation rates of the residues of the C-terminal region, the generalised decrease in R_1 values seen along the polypeptide chain up to residue 95 is not observed in the C-terminal portion of the protein, which might hint at a small conformational transition in the fast NMR timescale being induced by Mn^{2+} in this region.

5.3 Discussion

Transient intramolecular long-range contacts between the C-terminal and N-terminal regions, as well as the C-terminal region and the NAC maintain αSyn in its soluble monomeric form [288, 530, 531, 41, 385, 532, 533, 534, 535, 40]. Alteration of these interactions can lead to conformational transitions which can have an influence in the aggregation propensity of αSyn. Despite extensive evidence, the underlying mechanisms linking metal dyshomeostasis and the neurotoxicity of PD are not fully understood and remain strongly debated. In this Chapter, I have provided a detailed exploration of structural probes using CSPs, hydrogen exchange and ^{15}N relaxation dynamics of αSyn in the presence of various metal ions, to assess structural transitions that may disrupt the long-range intramolecular contacts and skew the distribution of the dynamic conformational ensemble.

Chemical shift data collected from ^{1}H-^{15}N HSQC experiments of αSyn in the presence of Ca^{2+}, Zn^{2+}, Cu^{+}, Cu^{2+} and Mn^{2+} identified perturbations in three localised sites along the sequence of the protein that seemed to be shared by the different metal ions investigated: (1) the very first few residues of the N-terminal region, (2) His50 in the N-terminal region and the surrounding residues and (3) the C-terminal region. The large CSPs observed in these regions are the result of direct interactions between the metal ions and αSyn and can therefore be described as the metal ion binding sites.

Consistent with previous studies of metal ion binding to αSyn, copper interacts with the protein at the three sites identified here with different affinities [285]. In particular, the first few residues of the N-terminal region constitute the high affinity binding site for Cu^{+} and Cu^{2+} in non-acetylated αSyn, where the motif MDVFM has been shown to be a key structural determinant for copper binding [284]. Binding of copper to His50 and the C-terminal region of αSyn is also well documented in the literature, with the binding affinity for the identified binding sites here is (1)>(2)>(3) [284, 285]. To explain this binding mode, the formation of a macrochelate has been widely speculated [536, 537], in which Cu^{2+} would coordinate the intramolecular binding of the imidazole nitrogen from His50 to the N-terminal binding site. However, recent efforts have shown that this is highly unlikely, probably as a result of the significant ordering necessary across 50 residues. Instead, the formation of a ternary complex involving the binding of the N-terminus to the His50 of a second αSyn molecule, mediated by the coordination of a Cu^{2+} ion, has been suggested to be possible but only at high protein concentrations [538].

CSP analysis also identified His50 as an anchoring site for Zn^{2+} coordination. These findings suggest a particularly important role for the imidazole ring of His50 as a metal anchoring group for Cu^{+}, Cu^{2+} and Zn^{2+}, which may be especially relevant in disease. One of the missense genetic mutations in the SNCA gene associated with the development of familial PD corresponds to H50Q [60, 59, 539], which has been shown to accelerate αSyn fibrillation *in vitro* [540] whilst compromising its solubility [541]. In a study using CD and NMR aimed at characterising the pathological implications of the H50Q mutation, Khalaf et. al found that this familial variant did not have an effect on either the structure of the free or membrane-bound state of the αSyn monomer, nor did it affect its ability to interact with metals or the formation of the long-range intramolecular interactions observed in αSyn [542]. However, they identified an increase in aggregation *in vitro*, compared to wild-type αSyn.

Whilst upon binding of Cu^{2+} the His50 coordination site was lost, as illustrated by a lack of peak broadening in NMR, the N- and C-terminal binding sites were conserved in a similar way to that of the wild-type protein. Of note, they also observed an increase in the secretion of αSyn from SHSY5Y cells into the culture medium, as well as exogenous toxicity compared to wild-type αSyn

[542]. Consistently, another group investigating the role of H50Q in the binding of Cu^{2+} to αSyn demonstrated a loss of copper coordination at this binding site, whilst binding to the N-terminal site was conserved [59]. H50Q mutation did not appear to impair copper binding, which suggests that His50 is not an essential anchoring residue for Cu^{2+} and highlights the role of the N-terminus as a high affinity binding site. Interestingly, mutation of His to Gln at position 50 in Ac-αSyn resulted in a compromised binding ability of Cu^{2+} [543], indicating a secondary role for His50 in the binding of Cu^{2+} that becomes essential when αSyn is N-terminally acetylated, which lacks the high affinity N-terminal Cu^{2+} binding site [283, 543]. These results highlight the importance of the N-terminal and His50 binding sites for Cu^{2+} and suggest that the low affinity binding site at the C-terminal region has little effect in preserving Cu^{2+} coordination.

Particularly intriguing are the findings from Villar-Pique et al., who investigated the effect of Cu^{2+} on the aggregation propensity of a panel of αSyn pathological mutations, as well as wild-type αSyn [544]. They found that in the presence of Cu^{2+}, H50Q is the only mutant that results in the formation of aggregates and even showed an enhanced propensity to form fibrils compared to wild-type αSyn. These findings suggest that conformational transitions leading to self-assembly may follow a different misfolding mechanism in H50Q αSyn compared to the wild-type protein. Although the reason for this difference in aggregation propensity escapes our knowledge, it has been proposed that the spatial localisation of His50 around the centre of the protein sequence may favour β-sheet nucleation [545]. Another possibility may involve an enhanced flexibility of the C-terminal region observed in the H50Q mutant, which could affect the Cu^{2+}-binding properties of this segment of the protein and affect aggregation kinetics [546].

The induction of transient conformational changes in the structure of αSyn as a result of metal binding may lead to a shift in the conformational ensemble of the protein [547]. By using electrospray ionisation-ion mobility spectrometry-mass spectrometry, Mason et al. found that binding of Cu^{2+} to non-acetylated αSyn results in an enhanced occupation of compact conformational states that may show an increased aggregation propensity [543, 430]. Binding of Cu^{2+} to non-acetylated H50Q αSyn resulted in the same conformational population distribution, suggesting that H50 does not play an im-

portant role in the shifting of αSyn to a more compact conformation. This conformational shift was not observed upon acetylation of the H50Q mutant, which instead resulted in an impaired ability to bind Cu^{2+} and a higher populational occupation of extended conformational states. Consistently, by studying aggregation kinetics using thioflavin T, αSyn bearing the H50Q mutation showed a higher aggregation propensity than the wild-type protein, which further increased in the presence of Cu^{2+}. In contrast, acetylated H50Q αSyn demonstrated the same enhancement in aggregation kinetics as the non-acetylated mutant, with no change upon Cu^{2+} binding [543].

Particularly interesting is the role of the C-terminal region in metal binding. All metals investigated here interacted with the C-terminal region, with some to a larger extent than others. Given the high net negative charge of this αSyn segment, it is not surprising that positively charged metal ions may interact with this region of the protein. Indeed, the C-terminal region is commonly described as a "sink for metal ions" for its ability to electrostatically attract cations. Nonspecific electrostatic interactions are probably responsible for attracting metal ions to the close proximity of the C-terminal region of αSyn in the first instance, although specific interactions with certain amino acid residues may account for the differences in magnitude observed in the CSPs caused by the different metal ions. Binding of Cu^{+} and Cu^{2+} only produce modest perturbations to the chemical shifts of the C-terminal region compared to those observed upon binding of Ca^{2+}, Zn^{2+} and Mn^{2+}. Whilst the smaller magnitude in CSPs of the affected C-terminal residues may be a result of the smaller ratios of incubation used in the presence of copper compared to an excess of Ca^{2+} and Zn^{2+}, the C-terminal region has been shown to correspond to the binding site to which copper binds with the least affinity [95, 93].

Different binding modes have been described for the different metal ions studied at the C-terminal binding site, which could translate into different structural consequences. For instance, Cu^{+} specifically binds to Met116 and Met127 [285], whilst Cu^{2+} appears to interact nonspecifically with negatively charged residues at the C-terminal region [528]. In contrast, Zn^{2+} was observed to specifically interact with the negatively charged Asp121, whose cross-peak experienced a large shift in chemical environment in the presence of Zn^{2+}, as well as with Ser129 and Glu137 to a lesser extent. Binding of Ca^{2+} and Mn^{2+}, on the other hand, led to perturbations in the chemical shifts of the cross-peaks

of several acidic residues, including Asp115, Asp119, Asp121, Glu123, Ser129, Glu137 and Glu139, which indicates a multitude of binding partners that are responsible for metal ion coordination. These findings are in agreement with previous studies that have suggested that certain cations like Ca^{2+} may bind to multiple sites along the C-terminal region via electrostatic contacts in a series of weak binding modes, as opposed to a tight binding interaction with specific amino acid residues. This is in line with the physiologically relevant interaction between αSyn and Ca^{2+} [37], where transient binding to the C-terminal region enhances the membrane binding ability of the C-terminal tail, which seems to be essential for the role of αSyn in vesicle trafficking at the pre-synaptic terminal.

Acetylation of the N-terminus of αSyn is believed to be ubiquitously found *in vivo* [99], which makes studying the interaction of metal ions with both non-acetylated and acetylated αSyn imperative. Given that N-terminal acetylation has been shown to enhance the sampling of α-helical conformations of the N-terminus of αSyn, the largest changes in metal ion binding upon N-terminal acetylation were expected to involve those cations interacting with the N-terminal region. Indeed, no significant changes were detected in the CSP profiles of Ac-αSyn upon binding of Ca^{2+}, Zn^{2+} and Mn^{2+} compared to upon binding to non-acetylated αSyn, indicating that acetylation at the N-terminus does not have long-range effects by affecting the binding to these metals in the mid-N-terminal and C-terminal regions. In contrast, the dramatic increase in CSPs observed upon binding of Cu^{+} to the high affinity N-terminus binding site in Ac-αSyn is in agreement with previous findings reporting a profound conformational change of the first N-terminal residues upon coordination with Cu^{+}, which corresponds to the stabilisation of an α-helical conformation at this binding site [95]. This highlights the importance of studying the physiological and pathological implications of N-terminal acetylation of αSyn.

An increase in the number of cross-peaks of residues at the N-terminus was observed in the recorded ^{1}H-^{15}N HSQC spectra upon incubation of Cu^{2+} with Ac-αSyn compared to non-acetylated αSyn, which indicated a reduction in the binding at the N-terminus associated with N-terminal acetylation. This is consistent with an observed loss of binding of Cu^{2+} to the N-terminal binding site in Ac-αSyn *in vitro*, together with a perturbation in metal-induced conformational transitions [283, 543]. This is in agreement with ThT aggregation assays, which show an enhancement in fibrillation kinetics for

non-acetylated αSyn in the presence of equimolar concentrations of Cu^{2+} *in vitro* [328, 548], whilst much higher stoichiometric levels are required to modulate Ac-αSyn aggregation [283]. In turn, the increase in CSPs of the residues of the C-terminal region of αSyn may account for an increased availability of Cu^{2+} for binding at this site upon N-terminal acetylation.

Hydrogen-hydrogen exchange was measured to probe the extent of solvent exposure of the regions of αSyn upon metal ion binding, to gain further insights into changes to the protein's intramolecular long-range contacts. Previous CLEANEX analyses involving αSyn confirmed that the chemical exchange of the residues follows an EX2 exchange regime with a dependence on pH [549, 550]. In addition, previous measurements of proton exchange of αSyn with the solvent water in *E. coli* have shown that the cellular environment does not alter the rates of exchange and that the structural disorder of the protein persists inside the crowded cellular interior [551]. By measuring the rates of amide hydrogen exchange, protection factors of the individual residues along αSyn could therefore be determined. Backbone amide exchange is indeed specifically sensitive to slow backbone dynamics in proteins and perturbations in this process can provide evidence of key conformational changes in IDPs.

An enhanced protection of the N-terminal region of free non-acetylated and Ac-αSyn was not observed, which would have been expected to compensate the strong protection recorded of the C-terminal region against hydrogen exchange with the solvent. This was also the case in [552], whilst another group investigating the effect of pH on hydrogen exchange of αSyn observed a higher protection for the residues at the N-terminus that is consistent with the proposed model of long-range intramolecular contacts [549]. Two reasons may explain the observation of a lack of an unshielded N-terminal, together with a protected C-terminal region: (1) The high concentration of residues with rapidly exchanging hydroxyl and amine side chains in the N-terminus (Lys (15), Thr (10) and Ser (3)) may be causing some of the solvent dephasing to be transferred by hydrogen exchange and then to other residues in the vicinity through NOEs, effectively increasing the apparent exchange rates and reducing relaxation times [553, 554]; (2) the high density of negative charges in the C-terminal region may be increasing the pH of the microenvironment in the vicinity of the protein in relation to

the bulk solution, whilst also shielding that region from reactive H_3O^+ an OH^- ions that are known to catalyse hydrogen exchange reactions in the absence of salt in the buffer, as is the case with the reported experiments in this Chapter [555, 556].

Additionally, the low ionic strength of the solution buffer may have contributed to an electrostatic-mediated enhancement of the protection of the amide protons at the acidic C-terminal domain. Indeed, a high salt content was shown to lead to an increase in the hydrogen exchange rates throughout the sequence of αSyn, whilst residue chemical shifts were unaffected, suggesting that the high protection observed at the C-terminal region at low ionic strength may partly be a result of the high density of unshielded charges and not of conformational exchange [552]. In line with the results from Okazaki et al., hydrogen exchange data presented here failed at identifying a higher protection at the NAC region, despite long-range contacts between this segment and the C-terminal tail having previously been reported [40, 41]. Local regions featuring a high concentration of residues with rapidly exchanging side chains may account for small fluctuations observed in protection along the protein sequence, as seen between residues 35-50. The fact that no significant differences were observed between the protection factor profiles of non-acetylated αSyn and Ac-αSyn strengthens the assumption that the observed hydrogen exchange rates for the N-terminal region are a result of fast amide proton exchange and not of conformational exchange.

Aberrant interactions following an unbalance in the homeostasis of metal ions has been linked to cellular toxicity and especially αSyn aggregation and faster fibrillation kinetics. As observed in the results of this study, different metal ions have different effects in the hydrogen exchange profiles of αSyn. This finding suggests that, although all metal ions probed here have been shown to accelerate aggregation of αSyn in previous studies [528, 306, 304, 300, 91, 529, 428, 319, 36], multiple mechanisms may exist depending on the nature of the metal ion involved that lead to a final shared outcome of an increase in αSyn aggregation. Binding of Ca^{2+} and Zn^{2+} seem to cause a strong deprotection of the C-terminus, which was also coupled with a small increase in the protection of the N-terminal region in Ac-αSyn. This observed deprotection is most likely a result of the disruption of the long-range contacts between the C-terminal and N-terminal regions, following the charge neutralisation of the

negative charges of the C-terminal tail. This collapse in the intramolecular interactions may lead to the release of the N-terminal region, which may promote an enhanced transient sampling of α-helical conformations in Ac-αSyn and a resulting increase in protection from exchange. This is in line with a gradual reduction in protection enhancement seen along the sequence as distance from the acetylated N-terminus increases. A reduction in the electrostatic repulsion upon Ca^{2+} binding may also result at the same time in enhanced intra- and intermolecular hydrophobic interactions between the C-terminal region and the NAC, which have previously been shown to constitute aggregation-prone conformations [533, 430, 557, 558, 559].

The N-terminus of non-acetylated αSyn was observed to be marginally exposed by -0.1 log$P$ upon binding of Ca^{2+}, whilst a small enhancement of the protection of the N-terminus was detected in Ac-αSyn upon Ca^{2+} binding. These data are in apparent contrast with previous mass spectrometry analyses [91], which used a combination of H/D exchange- and native nano electrospray ionisation-mass spectrometry to study intramolecular contacts within αSyn. An increase in solvent exposure of the N-terminal region of non-acetylated αSyn was instead observed upon Ca^{2+} binding, together with the release of long-range contacts with the C-terminal tail [91]. However, both strategies – CLEANEX and H/D exchange-mass spectrometry – together indicate that calcium binding disrupts the electrostatically-driven transient interactions between the N-terminal and C-terminal regions of αSyn [41]. Indeed, they also found that different αSyn mutants and PTMs together influence the extent of N-terminal exposure and the distribution of the conformational ensemble of αSyn species [91], which are both main determinants of protein aggregation propensity.

Stephens et al. also indicated that aggregation propensity of αSyn upon Ca^{2+} binding cannot be explained by a sole charge neutralisation effect at the C-terminal region, as wild-type and familial αSyn mutants, which all happen in the N-terminal region, have different aggregation kinetics [91]. Rather, these findings suggest that the increased propensity to aggregate may be the result of altered and different long-range interactions with the C-terminus, given that it is the residues in the N-terminal region which may undergo mutation the ones interacting with the calcium-binding regions in the C-terminal tail. This is consistent with other studies, which observed differences in the aggregation

kinetics of αSyn after altering the sequence and binding properties of the N-terminal region, supporting the hypothesis that this portion of the protein plays a key role in modulating self-assembly [560, 561, 562, 563, 564, 565]. Indeed, the formation of altered long-range interactions in mutant variants compared to wild-type αSyn has been widely reported [40, 566, 567, 568, 329].

In contrast to the enhanced hydrogen exchange rates observed at the C-terminal region upon binding of Ca^{2+} and Zn^{2+}, Cu^{+} binding results in a slight increase in the protection of the N-terminus of Ac-αSyn, relative to non-acetylated αSyn. Looking at these data together, this may indicate that an enhanced protection in the N-terminal region, either as a result of a direct binding event as is the case with Cu^{+}, or through a disruption of long-range interactions as seen with Ca^{2+} and Zn^{2+}, may correspond to a key initial step towards an altered misfolding pathway that favours αSyn self-aggregation.

To understand how changes in the protection factor profile of αSyn in the presence of metal ions correlate with fast protein dynamics, ^{15}N relaxation experiments were recorded. A small increase in R_1 relaxation rates of the residues at the C-terminal region of Ac-αSyn in the presence of Ca^{2+} was detected, suggesting an increase in conformational order in the ns timescale. The collapse of the electrostatic contacts with the net positively charged N-terminal region as a result of negative charge neutralisation leads to the release of the C-terminal tail, which may experience an enhanced motional restriction as it wraps around the bound Ca^{2+} ions whilst trying to bring interacting residues closer together in space to aid in metal ion coordination. This, in turn, leads to an increase in exposure to the solvent, allowing C-terminal amide protons to exchange with the solvent more freely. This proposed model accounts for a deprotection of the C-terminal region, whilst accommodating for an increase in conformational order. An enhanced exposure of the N-terminal and NAC regions upon disruption of long-range contacts was, however, not observed. This is in contrast to previous studies that report a structural transition of αSyn into an ensemble of extended conformations where the exposure of the NAC region seems a key event in promoting aggregation [569]. The binding of Ca^{2+} to αSyn has been described to follow positive cooperativity, which suggests that the main driving force in this interaction may not be a sole charge and electrostatic attraction, but rather hints at a specific binding

mode [91].

However, the fact that no changes were observed in the R_2/R_1 values of the residues of the C-terminal region upon binding of Ca^{2+} indicates a conformational transition which may not happen in the intermediate timescale. Consistently, enhanced R_2 rates detected along the N-terminal and NAC regions in both the presence and absence of Ca^{2+} suggests the existence of residual structure corresponding to slower transient motions as the conformational ensemble probed is skewed towards α-helical structures in Ac-αSyn. This is in line with the expected absence of an effect of calcium binding on the ability of the N-terminus to sample α-helical conformations, as data from CSPs did not suggest the existence of a binding site for Ca^{2+} in this region.

Interestingly, the results presented in this Chapter indicate that alterations in the local dynamics may not always be coupled to changes in the local exposure to the solvent. Indeed, changes in the local dynamics are seen to correlate with altered solvent exposure upon binding of Ca^{2+} and Zn^{2+} to the C-terminal region, but not upon binding of Zn^{2+} to His50 in the far N-terminal region. Even though binding of Zn^{2+} leads to a deprotection of the C-terminal region in non-acetylated and Ac-αSyn in the same way as Ca^{2+}, backbone dynamics greatly differs upon binding of the two divalent cations. Whilst R_1 relaxation rates of Ac-αSyn were found to be unperturbed upon binding of Zn^{2+}, R_2/R_1 and R_1 values experienced a significant increase in the two regions of Ac-αSyn corresponding to the binding sites of Zn^{2+}. This finding is especially remarkable not only because of an increase in rigidity observed around residues His50 and Asp121, but because these two regions correlate with the binding sites of Zn^{2+} but not with changes in the local protection factors of αSyn. This therefore suggests that changes in the hydrogen exchange rates along the protein may be, at least to some extent, uncoupled to conformational transitions that may occur upon metal binding. The fact that a conformational transition is not accompanied by changes in solvent exposure may be the result of differences in the flexibility of the different regions of the protein. The termini, which form intramolecular contacts, may have a higher inherent flexibility compared to the central part of the polypeptide, which is thought to be mostly solvent protected and the least dynamic segment of the protein.

The fact that Zn^{2+} specifically binds to His50 and Asp121 [309] in αSyn may suggest the formation of a coordination mode involving neighbouring residues, which would impose a certain degree of entropic penalty to allow their proximity in space. This may especially be the case regarding binding to His50. Coordination to the C-terminal Asp121 may follow a similar mechanism to that proposed for Ca^{2+}: Neutralisation of the strong net negative charge of Asp121, which is centrally located in the C-terminal region, as well as of other acidic residues which Zn^{2+} may loosely interact with, may alter the long-range contacts with the N-terminal region. This disruption in the electrostatic contacts may, in turn, induce a transient restriction of local motion sampling, as residues of the C-terminal tail come in close proximity to coordinate Zn^{2+}. In this case, a deprotection of the C-terminal region as that seen upon binding of Ca^{2+} may not effectively involve changes in the solvent exposure of the N-terminal region as a result of the different binding mode of Zn^{2+}, which is localised around Asp121, compared to Ca^{2+}, which binds at multiple sites along the entire stretch of acidic residues of the C-terminal tail [569, 37]. Consistently, the fact that Zn^{2+} binds to the C-terminal region, which has been described as being motionally restricted around residues 115-119 and 125-129 using residual dipolar couplings, suggests that a specific spatial organisation around residues 121-123 may result from the adoption of an adequate orientation of the side chain coordination moieties to favour metal binding [309]. This further supports the idea that metal ion interactions with the C-terminal region may not be exclusively driven by electrostatic forces, but may instead be strongly modulated by the intrinsic conformation of the protein region. The structural and dynamic features of the C-terminal tail may therefore constitute a modulator of the preferential binding of divalent metal ions to this common low-affinity binding site.

A lack of significant changes in the hydrogen exchange rates along the sequence of non-acetylated αSyn and Ac-αSyn upon binding of Cu^{2+} is consistent with the absence of ^{15}N relaxation cues that indicate conformational exchange. The observation of faster R_2 and R_2/R_1 relaxation rates for the residues His50 and Asp121 upon binding of Cu^{2+} may be accounted for by a restriction in the motion of the torsion and dihedral angles of those residues upon metal ion coordination, although conformational ordering is not detected in neighbouring residues. These findings disagree with previous studies using a combination of CD and EPR, which showed a gain in α-helical content and an induced com-

paction of αSyn upon addition of Cu^{2+} [548, 306]. Whilst a conformational transition may not be detected in the form of a change in solvent exposure along the sequence, relaxation data presented in this Chapter may not agree with an enhanced extent of α-helical structure because relaxation experiments were recorded using Ac-αSyn, whose N-terminal acetylation has been shown to compromise Cu^{2+} binding at the N-terminal binding site [283].

In contrast, the strong perturbation in R_2/R_1 and R_2 relaxation rates of the N-terminal region of the Ac-αSyn-Cu^{+} complex up to residue 25 may help explain the small enhancement in protection against exposure to the solvent of the same region of the protein. Cu^{+} binding may induce a higher degree of restricted local sampling in the acetylated N-terminus, which already has an enhanced propensity to probe α-helical conformational ensembles. An enhanced occupation of α-helical states may shield some residues involved in helical structure formation from hydrogen exchange with the solvent. This may explain the lack of uniformity in the increase in protection along the N-terminus of Ac-αSyn, where some highly protected residues flank areas observing a lack in enhanced protection. This is in line with the previously reported observation of small and large increases in R_1 and R_2, respectively, for the 1-10 amino acid segment in Ac-αSyn upon binding of Cu^{+} [95], indicative of an enhanced conformational order in the first 15 residues compared to free protein. Consistently, this highlights the importance of N-terminal acetylation in inducing a local helical conformation upon binding of Cu^{+}, which may be explained through the formation of a hydrogen bond network resulting from the removal of the positive N-terminal alpha amino positive charge upon acetylation and Cu^{+} complexation, which may induce a spatial reorganisation of the coordination side chain moieties of Met1 and Met5.

Interpretation of the protection factor profile of the C-terminal region of αSyn upon binding of Mn^{2+} has proven to be difficult as a result of the paramagnetic properties of Mn^{2+}, whose binding quenched residue resonances in its binding site and led to missing cross-peaks in the collected CLEANEX spectra. Available data hint at a small perturbation of the hydrogen exchange rates of the residues in this region relative to the rest of the protein, although the extent, as well as residue-specific information on this perturbation, failed to be measured. Predictably, any changes to the local exposure to the

solvent may happen in the C-terminal region, where Mn^{2+} ions are observed to bind. This would be expected as a result of the lack of significant differences between the protection factor profiles of non-acetylated αSyn and Ac-αSyn, indicating that Mn^{2+} does not interact with the N-terminal region and its binding is probably therefore not affected by N-terminal acetylation.

C-terminal binding of Mn^{2+} seems to induce some degree of conformational ordering on this part of αSyn, as seen by a small increase in the R_1 and R_2 relaxation rates of some residues of this region of the protein. The general decrease in R_1 rates along the sequence of Ac-αSyn compared to free protein suggests a global effect on the relaxation that is most likely a result of the paramagnetic properties of Mn^{2+}. Despite being difficult to draw any reliable conclusions because of missing data, the fact that the generalised decrease in R_1 rates is not observed in the C-terminal region suggests that a change in backbone rigidity in this portion of the protein may be an effect of direct Mn^{2+} binding. This is in line with a small increase in the R_2/R_1 values and R_2 rates of some residues of the C-terminal region, which further suggest that Mn^{2+} binding may induce a small conformational transition in this region of αSyn. Whether this increased degree of conformational order is coupled to either an enhanced protection or deprotection from solvent exposure of the C-terminal region escapes the interpretation of the results presented in this Chapter, given the extent of missing data as a result of paramagnetic effects.

As discussed in section 2.17.6, relaxation rates are strongly dependent on the large magnetic moment associated with paramagnetic metal ions, like Cu^{2+} and Mn^{2+}. The large gyromagnetic ratios of species bearing unpaired electrons enhance the relaxation of neighbouring nuclei spins through dipolar coupling. Indeed, the product of the gyromagnetic ratios of Cu^{2+} or Mn^{2+} and hydrogen nuclei promotes the fast relaxation of protons in the vicinity of the metal ion binding site, which is observed as short T_2 times and higher ^{15}N R_2 rates of the interacting residues. This mechanism is responsible for the enhanced R_2 relaxation rates recorded of H50 and the C-terminus upon incubation with Cu^{2+}, and of residues in the C-terminus in the presence of Mn^{2+}. Importantly, the stronger magnetic moment of Mn^{2+} compared to Cu^{2+} as a result of the larger number of unpaired electrons (5 vs. 2, respectively) further enhances the relaxation rate of the interacting nuclei spins in comparison,

resulting in a faster signal decay and a larger extent of residue peak intensity loss.

In addition, the proximity of the paramagnetic species to NH protons also dictates the extent of relaxation enhancement, which is given by $1/r^6$, where r is the distance between the paramagnetic species and the amide protons. Therefore, the enhancing effect on relaxation rapidly reduces as the distance between the two increases, providing a measure of the occupation of the binding site by the paramagnetic ions. Similarly, the relaxation enhancing effect of Mn^{2+} has a wider spatial reach than Cu^{2+} as a result of the larger associated gyromagnetic ratio, which is observed as a greater extent of missing peak intensities around the metal interacting site.

In summary, the extent of metal-induced conformational transitions in αSyn seems to be relatively small compared to those of a folded globular protein. Indeed, this is a result of the dynamic nature of monomeric αSyn, which samples a vast set of conformations that feature minimal structural changes. However, small perturbations in the long-range intramolecular contacts of αSyn may lead to transient changes in solvent exposure of certain protein regions that may be enough to tip the balance of the conformational ensemble towards aggregation-prone conformations. The fact that different effects in the solvent exposure and dynamics of αSyn were observed upon binding of different metal ions strengthens the hypothesis that different mechanisms exist by which the conformational ensemble is perturbed and the sampled population biased towards aggregation-prone conformers. Understanding the nature of these mechanisms is therefore critical to reveal the connection between metal dyshomeostasis and αSyn aggregation in the context of PD.

Discussion

This final Chapter begins by discussing the main findings and conclusions that can be drawn from the work presented in this thesis. Afterwards, possible future directions that may be explored are proposed, with the aim of addressing the shortcomings and further questions concerning this research.

6.1 Aptamer selection

The process of aptamer selection relies on the gradual enrichment of nucleic acid sequences with affinity for the target from an initial randomised library that contains single copies of each sequence. Throughout selection, conditions must constantly be tuned to ensure the enrichment of only those sequences with the highest affinity and specificity, whilst also avoiding compromising sequence diversity by increasing the stringency too quickly and risking the loss of sequences with low copy number at early stages of selection. This balance is therefore crucial for ensuring the success of high affinity aptamer binders, whilst minimising diversity loss and formation of PCR artefacts as a result of repeated amplification cycles. The results of this thesis demonstrate that optimisation of selection conditions is essential to ensure an adequate recovery of aptamer sequences with affinity for the target, in order to allow the gradual enrichment of binding candidates. Similarly, amplification tests at every selection round allowed the adjustment of PCR amplification cycles which minimised the build-up of parasitic PCR by-products.

Despite the constant optimisation of the conditions of selection, the PCR artefact sequence 65ntSeq was observed to form after only three selection rounds. Given its increasing abundance and the fact that a high sequence recovery was observed after incubation with the target, affinity of this sequence for αSyn_{1-25} was at first postulated. However, the combined binding affinity results from ELONA and NMR demonstrated a lack of binding affinity for αSyn_{1-25} or αSyn. Instead, the sequence was observed to interact with streptavidin with a calculated binding affinity of 300 nM, indicating that 65ntSeq may have interacted with the SA-Mag beads during the selection process. The fact that this sequence does not originate from a combinatorial library, together with its recurrent re-formation despite insistent library purification efforts suggest, however, that 65ntSeq has not been selected for its affinity to the streptavidin molecules present in the selection environment. Instead, the primers used for library amplification may coincidentally have innate affinity for streptavidin, which may have driven their annealing and the subsequent formation of 65ntSeq. Given its characteristic sequence composition, the large availability of primer sequences during the PCR amplification steps at each selection round may have fuelled its formation.

Efforts to understand the precise mechanism responsible for the formation of the 65ntSeq sequence involved the use of a truncated reverse primer lacking the terminal 'AA' bases, an alternative DNA polymerase without terminal transferase activity and a higher primer annealing temperature. These approaches aimed at interfering with the hypothesised complementary annealing of the 3' end adenine from the forward primer with a putative thymidine from the reverse primer that would allow the formation of 65ntSeq. Given that 65ntSeq has the same number of nucleotides as that of the forward and reverse primers combined, the proposed complementary annealing event is believed to happen through an additionally ligated adenine (thymidine in the reverse complement of the reverse primer) that does not form part of the sequence of the reverse or forward primers. It is worth noting that although these different approaches failed at preventing the recurrent formation of 65ntSeq, further changes in the selection conditions may have proven ineffective at preventing its reamplification. Indeed, low copy numbers of the 65ntSeq that may have escaped library purification may still act as seeds for the generation of 65ntSeq sequences in subsequent amplification steps in the presence of a primer supply. Therefore, even though these results demonstrate that the putative single-base

complementarity mechanism proposed is not driving the generation of 65ntSeq, it may be likely that the initial formation of this sequence in libraries of earlier rounds may have perpetuated its presence under a supply of the amplification primers.

Presumably, the binding affinity of either or both individual primers for streptavidin may have positioned them in close spatial proximity, which may have favoured their amplification by Taq polymerase even upon annealing through a single base. The affinity of 65ntSeq for streptavidin, together with the fact that library sequence recovery was always observed to be low, may have caused Taq polymerase to recognise the primer sequences, which were present at a higher concentration during the initial amplification cycles compared to the N42 library sequences, as sequences to be amplified, thereby making them template their own amplification. A combination of these mechanisms possibly resulted in the generation of the 65ntSeq sequence, which, together with binding data, demonstrate that this primer-derived sequence represents a false positive aptamer candidate that is most likely a product of primer innate affinity to streptavidin and PCR artefactual formation.

Similarly, sequencing results demonstrated the widespread presence of other primer-derived sequences of different lengths in the cloned round libraries from SA-Mag beads-SELEX. PCR by-products that are longer than the aptamer library may have predictably been formed as a result of both the innate affinity of the primer sequences for streptavidin and the artefactual amplification of the primers. In fact, it is highly likely that the origin of 65ntSeq and of other primer-derived sequences that are formed by truncations of the primer sequences is inherently interrelated, with the formation of one species favouring that of the other in a feed-forward loop. As opposed to the theory governing aptamer selection, the proportion of primer-derived sequences in the library increased with increasing rounds of selection, accompanied by a waning proportion of N42 aptamer sequences. Indeed, the characteristic composition of these sequences may have given them an evolutionary advantage compared to N42 library sequences, which may have increased their ease of amplification fuelled by the supply of complementary priming sequences. The fact that primer-derived sequences of different lengths were identified, together with the lack of binding of FSeq1 for αSyn_{1-25}, highlights that the high abundance of these sequences is a result of recombination events that favoured their amplification, and not

of the fact that they were enriched for their affinity to the target.

Whilst the 12^{th} round library was the sequenced library with the highest proportion of identified N42 aptamer sequences from SA-Mag beads-SELEX, binding data from the six sequences tested did not reveal high binding affinity for the αSyn_{1-25} target. Sequences R12S91 and R12S24 showed the highest affinities amongst the sequences tested at preliminary binding assays. However, data from ELONA assays and NMR titrations on the binding of R12S91 to αSyn revealed a lack of high affinity binding, which suggested that this sequence may have been selected for its affinity for streptavidin, and not αSyn_{1-25}. HSQC spectra recorded at various molar ratios of αSyn:R12S91 failed to show CSP and specific cross-peak intensity changes even at the highest concentrations, demonstrating a lack of binding affinity of R12S91 for full-length αSyn. In fact, additional binding assays failed to record FRET, which confirmed the lack of spatial proximity between R12S91 and αSyn, thereby demonstrating a lack of binding interaction in the range of 600 nM as calculated by ELONA, consistent with previous results. These data therefore demonstrate that R12S91 likely evolved and remained in the selection library as a result of its binding affinity for streptavidin and not αSyn_{1-25}.

Surprisingly, these sequences were identified after 12 rounds of selection, which initially suggested that they may have binding affinity for the target αSyn_{1-25}. Later rounds of selection did not identify sequence clusters, and instead revealed sequences that performed worse at binding assays for αSyn_{1-25}, compared to sequences identified in previous rounds. Sequencing and binding data suggest that a combination of overselection of the library sequences, which may have dismissed superior aptamers, together with the persistent contamination with primer-derived PCR by-products may have compromised the selection of aptamers against αSyn_{1-25}. The small size and extremely dynamic nature of the target may have favoured the preferential binding of aptamer sequences to better defined structural motifs on the surface of the bulkier streptavidin, which may have outcompeted any putative sequences that may have been selected for their binding to αSyn_{1-25} throughout selection.

The fact that the structures of the aptagens (the aptamer equivalents of antigens) on the αSyn_{1-25} target are likely to be constantly changing may have prevented sequences that had affinity for one par-

ticular conformation from being selected for and being enriched, as a different conformation would have not been recognised with the same affinity as a previous conformation by any particular aptamer. However, the stable structure of a large globular protein like streptavidin predictably acts as a beacon which facilitates binding and selection of sequences with affinity for it. Even if systematic sequencing of the round libraries had been carried out by NGS, it may have been challenging to identify subclusters of sequences binding αSyn_{1-25}, as these may have been masked by clusters of sequences with affinity for streptavidin. The fact that no high affinity binders for streptavidin were identified, however, may be explained by the rounds of negative selection carried out during SELEX, which may have removed those sequences with the tightest kinetics. Therefore, only sequences showing low affinity for streptavidin may have survived throughout selection, as these may have escaped the effect of negative selection rounds. As a result, the selection process may have unintendedly selected for primarily low-affinity binders to streptavidin, and not to αSyn_{1-25}.

Modification of SELEX to include NCM as a partitioning method demonstrated a striking increase in the library proportion of N42 aptamer sequences. Considering that primer-derived sequences represented a smaller proportion of the sequenced library after 6 rounds of NCM-SELEX compared to in SA-Mag beads-SELEX round libraries, these findings further support the hypothesis that these sequence species were found to repeatedly form as a result of the innate affinity of the primer sequences for streptavidin. Those sequences formed by truncations of the primer sequences may have escaped library purification as a result of having a similar size to the N42 library sequences which made their separation by electrophoresis indistinguishable, and which were being amplified given the primer supply at every amplification step. Whilst numerous new aptamer sequences were identified from NCM-SELEX, no two copies of the same sequence were identified, suggesting a high sequence diversity and a lack of enrichment even after 18 rounds of selection.

The high sequence diversity observed in the 12^{th} round library (initial library of NCM-SELEX) suggested the presence of a high number of sequences with potential binding affinity for αSyn. Surprisingly, binding assays failed at demonstrating affinity of the six sequences that were tested from this newly identified sequence pool for αSyn_{1-25} or αSyn. Predictably, sequences with affinity for

αSyn$_{1-25}$ may had already been lost in previous selection rounds, with only sequences with affinity for streptavidin populating the library. Indeed, sequences in the library may have interacted through non-specific interactions with SA-Mag beads first during SA-Mag beads-SELEX, which may have allowed them to withstand the evolutionary pressures of selection. A lack of binding of the N42 library sequences identified during NCM-SELEX for αSyn$_{1-25}$ and αSyn may partly be explained by the selection of aptamer sequences for their affinity to the NCM used in the partitioning steps through non-specific hydrophobic interactions. Given that nitrocellulose forms of a large and stable polymeric scaffold, aptamer sequences may have evolved and been selected throughout the rounds of NCM-SELEX against NCM and not αSyn. This possible preferential binding, combined with the dynamic nature and comparatively small size of αSyn, may have prevented aptamer sequences from tightly binding to the target and being selected as binders.

In summary, the results from this thesis provide a detailed description and interpretation of the challenging process of aptamer selection against the small, disordered peptide αSyn$_{1-25}$ and the characterisation of the identified aptamers. The combination of SA-Mag beads and NCM-SELEX was intended to surpass the limitations associated with each method, as well as the experimental hurdles encountered throughout selection, with these being mostly the recurrent formation of primer-derived sequences (PCR by-products) and the lack of affinity of the identified aptamers for the target. The findings of this work therefore highlight the difficulties of aptamer selection against a small, disordered protein target and the extremely crucial role that the selection environment plays in the success of selection, and provide, too, solutions to solve some common problems that may be encountered throughout aptamer selection campaigns.

6.2 Interactions with metal ions

Imbalances in the homeostatic levels of metal ions in the brain have been linked to an acceleration of the aggregation kinetics of αSyn [430] and an associated rise in cellular toxicity [307, 308, 529, 36, 92]. The results of this thesis demonstrate that different divalent cations have different effects on the conformation and the extent of solvent exposure of αSyn. The findings of this research demonstrate that a variety of mechanisms exist that govern the conformational effects of metal ion binding with

αSyn which converge to a common increased propensity of aggregation that is modulated by the nature of the metal ion involved. The binding of different metal ions and the variety of PTMs together influence the extent of local exposure and the distribution of the conformational ensemble of αSyn, therefore making them both critical determinants of protein aggregation propensity.

6.2.1 Calcium

Consistent with previous published work [91], the results of this thesis demonstrate a clear binding of Ca^{2+} to the C-terminal region of both αSyn and Ac-αSyn, with the N-terminal acetyl group not having an effect on this binding interaction. Chemical exchange rates between backbone amide protons and water hydrogens from the surrounding solvent were measured along the sequence of the protein as a measure of slow dynamics, to provide information on the effects of Ca^{2+} binding on the intramolecular long-range contacts of αSyn. These results showed a stark deprotection of the C-terminal region of Ac-αSyn and αSyn compared to free protein, suggesting that Ca^{2+} binding causes a collapse of the intramolecular contacts between the C- and N-terminal regions as a result of the neutralisation of the negative charges in the C-terminal tail, enhancing its exposure to the solvent.

Additionally, faster exchange rates at the N-terminus indicate an increased protection in this region in Ac-αSyn, possibly as a result of the higher propensity to sample local helical conformations upon N-terminal acetylation. The conformational equilibrium is predictably shifted to a higher helical content upon collapse of the long-range contacts with the C-terminal region. Interestingly, a conformational transition was not detected in the intermediate timescale, although an increased exposure to the solvent of the C-terminal tail is accompanied by a small increase in local rigidity of this region in the fast ns timescale, which may result from a local structural transition by which residues involved in the binding to Ca^{2+} are brought together in close spatial proximity to aid in metal coordination.

6.2.2 Copper

Chemical shift mapping, chemical exchange and relaxation data presented in this thesis demonstrate the differential effect of binding of copper in its two oxidation states on the conformation of αSyn. In line with previous work, binding of Cu^{+} and Cu^{2+} to Ac-αSyn and αSyn is observed in three

localised regions of the protein, namely the N-terminus, His50 and its proximity in the N-terminal region, and the C-terminal region. Remarkably, complexation of Cu^{+} with Ac-αSyn is associated with a dramatically large perturbation of the chemical environment of the residues in the N-terminus, whilst the other two copper-binding regions were unaffected upon N-terminal acetylation. In contrast, a large decrease in Cu^{2+} binding was observed at the N-terminus upon acetylation. Consistently, binding of Cu^{+} induced an increase in the protection of the N-terminus of Ac-αSyn associated with an enhanced increase in propensity to sample α-helical conformations [95]. Indeed, deviations in the relaxation properties upon binding of Cu^{+} demonstrated a large increase in conformational order at the N-terminus of Ac-αSyn indicative of a conformational transition.

On the other hand, complexation with Cu^{2+} did not result in either changes in the local exposure to the solvent of the regions of Ac-αSyn or αSyn, nor significant alterations in the conformational ensemble. Considering that most αSyn is believed to be N-terminally acetylated [99] and that copper most likely exists as Cu^{+} inside the reducing environment of the cell [570], these findings are therefore particularly relevant in understanding the physiological behaviour of αSyn upon binding of copper and the effect on its aggregation propensity, whose importance in disease development may have been overlooked until now.

6.2.3 Zinc

Binding of Zn^{2+}, in contrast to Ca^{2+}, seemed to involve both the C-terminal and N-terminal regions of αSyn, with the largest perturbations recorded in the chemical environments of His50 and Asp121. Binding of Zn^{2+} to the C-terminal region is coupled to an enhanced local exposure to the solvent, although the same is not observed for the N-terminal region in the proximity of His50. Instead, a slight enhancement in the protection of the N-terminus of Ac-αSyn and αSyn may reflect the collapse of the intramolecular long-range contacts. Although stronger in the acetylated variant, this increase in protection wanes along the sequence, indicating that binding to His50 does not have a direct effect on the local exposure to the solvent.

The binding regions of Zn^{2+} are consistent with ^{15}N relaxation data, which show a significant increase

in conformational order associated with an induced conformational transition around His50 and the C-terminal region centred on Asp121. Indeed, the observed strong deprotection of the C-terminal region, coupled to a decrease in local conformational flexibility, may be explained by the multi-residue coordination of Zn^{2+} ions. However, the fact that the decrease in motional flexibility around His50 is not coupled to changes in the chemical exchange with the solvent may indicate the establishment of hydrophobic intramolecular contacts with the N-terminal region that compensate the collapse of the interactions with the C-terminal segment.

6.2.4 Manganese

The strong relaxation enhancement observed upon incubation with Mn^{2+} shows that binding to Ac-αSyn and αSyn happens in the C-terminal tail. Considering that this region is commonly described as a "sink" for metal ions as a result of the abundance of negative charges that attract a variety of metal cations, interactions of Mn^{2+} ions are expected to be nonspecific in nature. Changes in the solvent exposure of αSyn upon Mn^{2+} binding were difficult to interpret as a result of paramagnetic effects, although available data hint at a lack of significant perturbations to the chemical exchange rates of the residues in the C-terminal region relative to the rest of the protein. Small changes in the relaxation properties of Ac-αSyn upon binding of Mn^{2+} suggested some degree of local structural ordering in the form of a small conformational transition. However, whether this subtle increase in conformational order is coupled to either a change in solvent exposure or a lack of perturbation escapes the interpretation of the results presented in this chapter as a result of missing data.

Understanding the ensemble of long-range interactions that maintain αSyn soluble and in monomeric state together with the effect of environmental factors on the complexity of the sampled dynamic conformations is vital to gain insights into the different ways in which they may be perturbed in favour of aggregation. The dynamic nature of αSyn makes the study of specific aggregation-prone and disease-relevant conformations particularly challenging. By analysing the effect of binding of different relevant metal ions on the submolecular structure of αSyn, a skewed populational ensemble was recorded, which provided structural information that can be used to infer misfolding mechanisms that may explain differences in aggregation propensity under different conditions.

Indeed, the results of this thesis show that the imidazole ring of His50 constitute an important common anchoring site for Cu^{+}, Cu^{2+} and Zn^{2+} which can have profound effects in the dynamics of the protein. In fact, His50 has been observed to be mutated to Gln50 by missense genetic mutations in the SNCA gene linked to familial PD, and is associated with an increased rate of αSyn aggregation *in vitro* [60, 539, 59]. The effect of such a mutation on aggregation may be exacerbated by metal ion binding and PTMs that may change the normal behaviour of the protein. For instance, loss of Cu^{2+} coordination at the N-terminus upon acetylation [283] and at the His50 site upon H50Q mutation [59] may alter the binding of copper at the remaining C-terminal site and have profound effects in the long-range interactions within αSyn that may affect its conformational ensemble [543]. Therefore, different combinations of interactions with metal ions and PTMs may have different effects on the structural stability of monomeric αSyn and may induce different misfolding mechanisms.

Different metal binding modes therefore translate into a variety of structural and dynamic consequences which may dramatically influence the misfolding pathway that is followed. At the same time, the findings on metal binding to N-terminally acetylated αSyn highlight the importance of PTMs in modulating the function and conformation of the protein, which are particularly relevant given their ubiquity within the cell. Importantly, the work presented here indicate that an increased propensity to aggregate may be the result of alterations in the long-range intramolecular interactions with the C-terminal region. A collapse of these contacts as a result of charge neutralisation may result in changes in the conformational equilibrium of the N-terminal region, where all known mutations linked to increased aggregation rates and familial PD are found [91]. Specifically, the extent of solvent exposure and conformational stability of the N-terminus may therefore play a key role in self-assembly by lying on a thin balance between protein function and pathology, which may be disturbed by excessive metal ion binding upon metal dyshomeostasis and may constitute a key initial step in an altered misfolding pathway [560, 561, 562, 563, 564, 565]. Indeed, the shielding of charges in the N- and C-terminal regions through metal ion binding promotes an enhancement of the hydrophobic interactions that may favour self-assembly and permit a more energetically favourable packing into fibrils [328, 571].

Taken together, understanding the mechanisms of the deleterious interactions between metal ions and

αSyn is therefore essential to reveal the connection between metal dyshomeostasis, an enhancement in the aggregation of αSyn and an increased neurotoxicity in PD. A key challenge in this research area will be the characterisation of the synergistic effects of different metal ions in their multiple interactions with αSyn, and determining how these are related with the various phases of the pathological neuronal activity.

6.3 Future Work

6.3.1 Aptamer selection

To select high binding affinity DNA aptamers against the crucial membrane-binding segment of αSyn, a rethinking of the experimental method is required. The results of this thesis have demonstrated the high sensitivity of SELEX to the unintended selection of aptamers against large molecules with well-defined motifs that may be present in the selection environment, compared to small targets lacking a well-defined conformation. Therefore, a new strategy is required to make the αSyn_{1-25} target peptide be the only molecule present at high concentration during the SELEX incubation step. In this regard, many variations of the conventional SELEX protocol exist that have been adapted for the selection of targets with different physicochemical properties. For instance, capture-SELEX has been shown to succeed at selecting aptamers against small molecule targets of less than 1 kDa in size [572]. Here, the single-stranded library of sequences is immobilised (instead of the target) by hybridisation to a complementary oligonucleotide. Sequences involved in a binding interaction with the target will experience an induced conformational change that may break the hydrogen bonds keeping the library sequences hybridised to the capture-oligonucleotides, thereby releasing those sequences with affinity for the target from the immobilised library and making them available for subsequent PCR amplification. This approach therefore provides a much more sensitive selection method that exploits small target-induced structural changes in aptamer sequences as a way of identifying binding sequences.

Alternatively, affinity chromatography SELEX involves the modification of a column matrix to covalently immobilise the target molecules [573]. By passing a combinatorial library through the affinity column, those sequences with affinity for the target will not be washed off and will instead be re-

tained, eluted and reamplified for subsequent selection rounds. Whilst appropriate negative selection rounds would be required to prevent the selection of aptamers with affinity for the column matrix, the small size of the target peptide will not be a limiting factor for this experimental setup given that the target would be covalently attached to the matrix.

The results of the work presented in this thesis show that innate binding affinity of the PCR amplification primers for non-target molecules in the selection environment that are not the target can have detrimental effects in the outcome of selection. To avoid this, it is imperative to test the primer sequences for affinity to any possible interfering molecules/material prior to selection. Alternatively, various test selections may be carried out for a few rounds using different sets of amplification primers, with the aim of identifying an optimal sequence pair. Persistent generation of PCR by-products and the appearance of unexpected bands may signal the inadequacy of a primer pair, although sequencing of the library is recommended to be able to make an informed quantitative decision.

Sequencing efforts involving Sanger sequencing of a combinatorial library may identify aptamers with low affinity or specificity and overlook superior aptamers. Therefore, NGS of the aptamer library selected against αSyn_{1-25} could identify sequence clusters that may indicate enrichment of aptamers for affinity to the target. Additionally, frequent sequencing of the round libraries by NGS may provide information on the progress of sequence enrichment, which may aid in identifying the best aptamer candidates.

Since the methods used to investigate target binding in this work are heavily material-consuming and labour-intensive, capacity for performing further binding experiments was limited to studying the binding of those sequences showing the highest affinity in preliminary assays. Therefore, studying the interaction of additional N42 library sequences, such as R12S24, may have helped identify aptamer candidates with affinity for αSyn_{1-25}.

To address the issues presented in this thesis, SELEX will therefore need to be optimised further for the selection of aptamers against the small, disordered αSyn_{1-25} peptide target, which lacks a stable

and well-defined structure. To do this, selection strategies should avoid the use of bulky molecules in the selection environment, together with primers that may have innate affinity for any of the components used in selection. Additionally, strategies that involve the high-throughput sequencing of the aptamer library will aid in following the progress of selection and will provide crucial information that may facilitate the challenging endeavours of selecting aptamers against a highly flexible target.

6.3.2 Interactions with metal ions

The second part of the work presented in this thesis highlights the relevance of metal ion binding in inducing structural transitions and changes in the local solvent exposure of regions of αSyn, which may influence both protein function and aggregation propensity. Whilst a comprehensive analysis of the effects a variety of different metal ions is provided here, other less well characterised metals have been observed to establish putative binding events with αSyn, which may have implications in physiology and pathology [529]. For instance, studying the structural and dynamic properties of αSyn upon binding of metals ions such as, Fe^{2+}, Fe^{3+}, Mg^{2+}, as well as non-essential metals like Co^{2+}, Ni^{2+}, Pb^{2+} and Al^{3+} is crucially important for establishing a complete view of the different binding modes of metal cations, and their role in αSyn misfolding and PD development.

Idiopathic and age-related PD involving the accumulation of inclusions of wild-type αSyn account for around 90-95% of the total number of cases, with the rest being attributed to genetic defects [72]. Despite their small proportion, these cases are associated with early-onset disease development and a rapid progression. The study of the effect of the mutations involved on the structural and dynamic properties of αSyn is therefore essential to understand the underlying molecular mechanisms responsible for these phenotypic differences. Indeed, investigating the effect of metal ion binding to these αSyn variants may provide further information of the pathological implications of their interplay. Additionally, as demonstrated by the results of this thesis, PTMs modulate the effect of metal ion binding by interfering with their binding mode. In fact, αSyn is subjected to extensive PTMs that decorate its sequence, including N-terminal acetylation, ubiquitination, nitration, phosphorylation and SUMOylation, among others [574], indicating large physiological and pathological implications which warrant further exploration. Studying the combined effect of the binding of the different metal

ions, the plethora of different PTMs and the various genetic variants of αSyn may provide a deeper understanding of the conformational behaviour of αSyn in physiology that may lead to different misfolding pathways being triggered by different combinations of external factors.

Whilst an excess of calcium and zinc has been used in this work to unambiguously study their effect on the conformational properties of αSyn, physiological concentrations of Zn^{2+} in the mammalian brain, for instance, are in the 10-20 nM range [398], whilst increases of up to only 50% have been detected in the substantia nigra of patients with PD [310, 311, 312]. Indeed, evidence showing an increased rate of fibrillation of αSyn upon Zn^{2+} binding suggests that mM concentrations are required to accelerate aggregation kinetics [36, 313, 323, 324, 325, 326], which challenge the biological significance of these results in the aetiology of PD. Therefore, it is imperative to study the conformational implications of metal binding to αSyn at different physiologically relevant concentrations and compare the results with those obtained under an excess of metal, to be able to draw reliable conclusions of the molecular pathways that may unravel in the cell to induce the misfolding and aggregation of monomeric αSyn. Additionally, different concentrations of paramagnetic ions such as Cu^{2+} and Mn^{2+} will aid in inferring changes in the protein that may have been overlooked in this study as a result of linewidth broadening.

To understand the molecular interplay between genetic and environmental factors, such as metal ion binding and PTMs, an exhaustive investigation of the conformational properties of αSyn and the associated rate of aggregation is therefore critical. This will help in establishing a connection between metal dyshomeostasis and perturbations to the conformational ensemble of αSyn, to understand the molecular mechanisms underlying differences in the induced misfolding pathways and provide respective clues for therapeutic intervention.

Bibliography

[1] Lonneke de Lau M.L. and Monique M. B. Breteler. Epidemiology of parkinson's disease. *The Lancet Neurology*, 5(6):525–535, 2006.

[2] Carl E. Clarke and A. Peter Moore. Parkinson's disease. *BMJ clinical evidence*, 2007:1203, Aug 1 2007.

[3] Parkinson disease - world health organization, June 13, 2022.

[4] E. Ray Dorsey, Todd Sherer, Michael S. Okun, and Bastiaan R. Bloem. The emerging evidence of the parkinson pandemic. *Journal of Parkinson's disease*, 8(s1):S3–S8, 2018.

[5] Rodolfo Savica, Brandon R. Grossardt, Walter A. Rocca, and James H. Bower. Parkinson disease with and without dementia: A prevalence study and future projections. *Movement disorders : official journal of the Movement Disorder Society*, 33(4):537–543, Apr 2018.

[6] J. Burre. The synaptic function of alpha-synuclein. *Journal of Parkinson's disease*, 5(4):699–713, 2015.

[7] Lingjia Xu and Jiali Pu. Alpha-synuclein in parkinson's disease: From pathogenetic dysfunction to potential clinical application. *Parkinson's disease*, 2016:1720621; 1720621–1720621, 2016.

[8] V. Ghiglieri, V. Calabrese, and P. Calabresi. Alpha-synuclein: From early synaptic dysfunction to neurodegeneration. *Frontiers in neurology*, 9:295, May 4 2018.

[9] M. H. Polymeropoulos, C. Lavedan, E. Leroy, S. E. Ide, A. Dehejia, A. Dutra, B. Pike, H. Root, J. Rubenstein, R. Boyer, E. S. Stenroos, S. Chandrasekharappa, A. Athanassiadou, T. Papapetropoulos, W. G. Johnson, A. M. Lazzarini, R. C. Duvoisin, G. Di Iorio, L. I. Golbe, and R. L. Nussbaum. Mutation in the alpha-synuclein gene identified in families with parkinson's disease. *Science (New York, N.Y.)*, 276(5321):2045–2047, Jun 27 1997.

[10] E. Mezey, A. M. Dehejia, G. Harta, N. Tresser, S. F. Suchy, R. L. Nussbaum, M. J. Brownstein, and M. H. Polymeropoulos. Alpha synuclein is present in lewy bodies in sporadic parkinson's disease. *Molecular psychiatry*, 3(6):493–499, Nov 1998.

[11] Koichi Wakabayashi, Kunikazu Tanji, Saori Odagiri, Yasuo Miki, Fumiaki Mori, and Hitoshi Takahashi. The lewy body in parkinson's disease and related neurodegenerative disorders. *Molecular neurobiology*, 47(2):495–508, Apr 2013.

[12] W. P. Gai, H. X. Yuan, X. Q. Li, J. T. Power, P. C. Blumbergs, and P. H. Jensen. *In situ* and *in vitro* study of colocalization and segregation of alpha-synuclein, ubiquitin, and lipids in lewy bodies. *Experimental neurology*, 166(2):324–333, Dec 2000.

[13] W. A. den Jager. Sphingomyelin in lewy inclusion bodies in parkinson's disease. *Archives of Neurology*, 21(6):615–619, Dec 1969.

[14] L. S. Forno, L. E. DeLanney, I. Irwin, and J. W. Langston. Electron microscopy of lewy bodies in the amygdala-parahippocampal region. comparison with inclusion bodies in the mptp-treated squirrel monkey. *Advances in Neurology*, 69:217–228, 1996.

[15] L. S. Forno and R. L. Norville. Ultrastructure of lewy bodies in the stellate ganglion. *Acta Neuropathologica*, 34(3):183–197, Mar 30 1976.

[16] K. Hayashida, S. Oyanagi, Y. Mizutani, and M. Yokochi. An early cytoplasmic change before lewy body maturation: an ultrastructural study of the substantia nigra from an autopsy case of juvenile parkinsonism. *Acta Neuropathologica*, 85(4):445–448, 1993.

[17] Lysia S. Forno, J. W. Langston, Louis E. DeLanney, Ian Irwin, and George A. Ricaurte. Locus

ceruleus lesions and eosinophilic inclusions in mptp-treated monkeys. *Annals of Neurology*, 20(4):449–455, 1986.

[18] K. Wakabayashi, H. Takahashi, S. Takeda, E. Ohama, and F. Ikuta. Parkinson's disease: the presence of lewy bodies in auerbach's and meissner's plexuses. *Acta Neuropathologica*, 76(3):217–221, 1988.

[19] M. G. Spillantini, M. L. Schmidt, V. M. Lee, J. Q. Trojanowski, R. Jakes, and M. Goedert. Alpha-synuclein in lewy bodies. *Nature*, 388(6645):839–840, Aug 28 1997.

[20] M. Baba, S. Nakajo, P. H. Tu, T. Tomita, K. Nakaya, V. M. Lee, J. Q. Trojanowski, and T. Iwatsubo. Aggregation of alpha-synuclein in lewy bodies of sporadic parkinson's disease and dementia with lewy bodies. *The American journal of pathology*, 152(4):879–884, Apr 1998.

[21] Michel Goedert, Bernardino Ghetti, and Maria Grazia Spillantini. Frontotemporal dementia: implications for understanding alzheimer disease. *Cold Spring Harbor perspectives in medicine*, 2(2):a006254, Feb 2012.

[22] Sigurlaug Sveinbjornsdottir. The clinical symptoms of parkinson's disease. *Journal of neurochemistry*, 139 Suppl 1:318–324, Oct 2016.

[23] C. H. Williams-Gray, T. Foltynie, C. E. G. Brayne, T. W. Robbins, and R. A. Barker. Evolution of cognitive dysfunction in an incident parkinson's disease cohort. *Brain : a journal of neurology*, 130(Pt 7):1787–1798, Jul 2007.

[24] P. K. Auluck, G. Caraveo, and S. Lindquist. Alpha-synuclein: membrane interactions and toxicity in parkinson's disease. *Annual Review of Cell and Developmental Biology*, 26:211–233, 2010.

[25] Thomas B. Stoker and Roger A. Barker. Recent developments in the treatment of parkinson's disease. *F1000Research*, 9:10.12688/f1000research.25634.1. eCollection 2020, Jul 31 2020.

[26] Joseph Jankovic and L. Giselle Aguilar. Current approaches to the treatment of parkinson's disease. *Neuropsychiatric disease and treatment*, 4(4):743–757, Aug 2008.

[27] L. Maroteaux, J. T. Campanelli, and R. H. Scheller. Synuclein: a neuron-specific protein localized to the nucleus and presynaptic nerve terminal. *The Journal of neuroscience : the official journal of the Society for Neuroscience*, 8(8):2804–2815, Aug 1988.

[28] Marco Bisaglia, Isabella Tessari, Luca Pinato, Massimo Bellanda, Sabrina Giraudo, Mauro Fasano, Elisabetta Bergantino, Luigi Bubacco, and Stefano Mammi. A topological model of the interaction between alpha-synuclein and sodium dodecyl sulfate micelles. *Biochemistry*, 44(1):329–339, Jan 11 2005.

[29] Christine C. Jao, Ani Der-Sarkissian, Jeannie Chen, and Ralf Langen. Structure of membrane-bound alpha-synuclein studied by site-directed spin labeling. *Proceedings of the National Academy of Sciences of the United States of America*, 101(22):8331–8336, Jun 1 2004.

[30] S. Chandra, X. Chen, J. Rizo, R. Jahn, and T. C. Sudhof. A broken alpha-helix in folded alpha-synuclein. *The Journal of biological chemistry*, 278(17):15313–15318, Apr 25 2003.

[31] B. I. Giasson, I. V. Murray, J. Q. Trojanowski, and V. M. Lee. A hydrophobic stretch of 12 amino acid residues in the middle of alpha-synuclein is essential for filament assembly. *The Journal of biological chemistry*, 276(4):2380–2386, Jan 26 2001.

[32] M. G. Spillantini, R. A. Crowther, R. Jakes, M. Hasegawa, and M. Goedert. Alpha-synuclein in filamentous inclusions of lewy bodies from parkinson's disease and dementia with lewy bodies. *Proceedings of the National Academy of Sciences of the United States of America*, 95(11):6469–6473, May 26 1998.

[33] Claudio O. Fernández, Wolfgang Hoyer, Markus Zweckstetter, Elizabeth A. Jares-Erijman, Vinod Subramaniam, Christian Griesinger, and Thomas M. Jovin. Nmr of alpha-synuclein-polyamine complexes elucidates the mechanism and kinetics of induced aggregation. *The EMBO journal*, 23(10):2039–2046, May 19 2004.

[34] Wolfgang Hoyer, Dmitry Cherny, Vinod Subramaniam, and Thomas M. Jovin. Rapid self-assembly of alpha-synuclein observed by *in situ* atomic force microscopy. *Journal of Molecular Biology*, 340(1):127–139, Jun 25 2004.

[35] G. Fusco, A. De Simone, T. Gopinath, V. Vostrikov, M. Vendruscolo, C. M. Dobson, and G. Veglia. Direct observation of the three regions in alpha-synuclein that determine its membrane-bound behaviour. *Nature communications*, 5:3827, May 29 2014.

[36] Leonid Breydo, Jessica W. Wu, and Vladimir N. Uversky. α-synuclein misfolding and parkinson's disease. *Biochimica et biophysica acta*, 1822(2):261–285, Feb 2012.

[37] Janin Lautenschläger, Amberley D. Stephens, Giuliana Fusco, Florian Ströhl, Nathan Curry, Maria Zacharopoulou, Claire H. Michel, Romain Laine, Nadezhda Nespovitaya, Marcus Fantham, Dorothea Pinotsi, Wagner Zago, Paul Fraser, Anurag Tandon, Peter St George-Hyslop, Eric Rees, Jonathan J. Phillips, Alfonso De Simone, Clemens F. Kaminski, and Gabriele S. Kaminski Schierle. C-terminal calcium binding of α-synuclein modulates synaptic vesicle interaction. *Nature Communications*, 9(1):712, 2018.

[38] G. Fusco, M. Sanz-Hernandez, and A. De Simone. Order and disorder in the physiological membrane binding of alpha-synuclein. *Current opinion in structural biology*, 48:49–57, Feb 2018.

[39] Alexander S. Maltsev, Jinfa Ying, and Ad Bax. Impact of n-terminal acetylation of α-synuclein on its random coil and lipid binding properties. *Biochemistry*, 51(25):5004–5013, Jun 26, 2012.

[40] Carlos W. Bertoncini, Young-Sang Jung, Claudio O. Fernandez, Wolfgang Hoyer, Christian Griesinger, Thomas M. Jovin, Markus Zweckstetter, and Gregory A. Petsko. Release of long-range tertiary interactions potentiates aggregation of natively unstructured α-synuclein. *Proceedings of the National Academy of Sciences - PNAS*, 102(5):1430–1435, Feb 01, 2005.

[41] Matthew M. Dedmon, Kresten Lindorff-Larsen, John Christodoulou, Michele Vendruscolo, and Christopher M. Dobson. Mapping long-range interactions in α-synuclein using spin-label nmr and ensemble molecular dynamics simulations. *Journal of the American Chemical Society*, 127(2):476–477, Jan 19, 2005.

[42] Jennifer C. Lee, Harry B. Gray, and Jay R. Winkler. Tertiary contact formation in α-synuclein probed by electron transfer. *Journal of the American Chemical Society*, 127(47):16388–16389,

Nov 30, 2005.

[43] Jennifer C. Lee, Bert T. Lai, John J. Kozak, Harry B. Gray, and Jay R. Winkler. α-synuclein tertiary contact dynamics. *The journal of physical chemistry. B*, 111(8):2107–2112, Mar 01, 2007.

[44] Valeria Losasso, Adriana Pietropaolo, Claudio Zannoni, Stefano Gustincich, and Paolo Carloni. Structural role of compensatory amino acid replacements in the α-synuclein protein. *Biochemistry*, 50(32):6994–7001, Aug 16 2011.

[45] Fernando E. Herrera, Alessandra Chesi, Katerina E. Paleologou, Adrian Schmid, Adriana Munoz, Michele Vendruscolo, Stefano Gustincich, Hilal A. Lashuel, and Paolo Carloni. Inhibition of alpha-synuclein fibrillization by dopamine is mediated by interactions with five c-terminal residues and with e83 in the nac region. *PloS one*, 3(10):e3394, 2008.

[46] A. K. Dunker, Z. Obradovic, P. Romero, E. C. Garner, and C. J. Brown. Intrinsic protein disorder in complete genomes. *Genome informatics.Workshop on Genome Informatics*, 11:161–171, 2000.

[47] James M Krieger, Giuliana Fusco, Marc Lewitzky, Philip C Simister, Jan Marchant, Carlo Camilloni, Stephan M Feller, and Alfonso De Simone. Conformational recognition of an intrinsically disordered protein. *Biophysical Journal*, 106(8):1771–1779, Apr 15, 2014.

[48] J. H. Soper, S. Roy, A. Stieber, E. Lee, R. B. Wilson, J. Q. Trojanowski, C. G. Burd, and V. M. Lee. Alpha-synuclein-induced aggregation of cytoplasmic vesicles in saccharomyces cerevisiae. *Molecular biology of the cell*, 19(3):1093–1103, Mar 2008.

[49] Aaron D. Gitler, Brooke J. Bevis, James Shorter, Katherine E. Strathearn, Shusei Hamamichi, Linhui Julie Su, Kim A. Caldwell, Guy A. Caldwell, Jean-Christophe Rochet, J. M. McCaffery, Charles Barlowe, and Susan Lindquist. The parkinson's disease protein α-synuclein disrupts cellular rab homeostasis. *Proc Natl Acad Sci USA*, 105(1):145, 2008.

[50] Giuliana Fusco, Tillmann Pape, Amberley D. Stephens, Pierre Mahou, Ana Rita Costa,

Clemens F. Kaminski, Gabriele S. Kaminski Schierle, Michele Vendruscolo, Gianluigi Veglia, Christopher M. Dobson, and Alfonso De Simone. Structural basis of synaptic vesicle assembly promoted by α-synuclein. *Nature Communications*, 7:12563, 2016.

[51] S. Wislet-Gendebien, C. D'Souza, T. Kawarai, P. St George-Hyslop, D. Westaway, P. Fraser, and A. Tandon. Cytosolic proteins regulate alpha-synuclein dissociation from presynaptic membranes. *The Journal of biological chemistry*, 281(43):32148–32155, Oct 27 2006.

[52] Antony A. Cooper, Aaron D. Gitler, Anil Cashikar, Cole M. Haynes, Kathryn J. Hill, Bhupinder Bhullar, Kangning Liu, Kexiang Xu, Katherine E. Strathearn, Fang Liu, Songsong Cao, Kim A. Caldwell, Guy A. Caldwell, Gerald Marsischky, Richard D. Kolodner, Joshua Labaer, Jean-Christophe Rochet, Nancy M. Bonini, and Susan Lindquist. Alpha-synuclein blocks ergolgi traffic and rab1 rescues neuron loss in parkinson's models. *Science (New York, N.Y.)*, 313(5785):324–328, Jul 21 2006.

[53] Wing K. Man, Bogachan Tahirbegi, Michail D. Vrettas, Swapan Preet, Liming Ying, Michele Vendruscolo, Alfonso De Simone, and Giuliana Fusco. The docking of synaptic vesicles on the presynaptic membrane induced by α-synuclein is modulated by lipid composition. *Nature Communications*, 12(1):927, 2021.

[54] J. Burre, M. Sharma, and T. C. Sudhof. Definition of a molecular pathway mediating alpha-synuclein neurotoxicity. *The Journal of neuroscience : the official journal of the Society for Neuroscience*, 35(13):5221–5232, Apr 1 2015.

[55] S. Chandra, G. Gallardo, R. Fernandez-Chacon, O. M. Schluter, and T. C. Sudhof. Alpha-synuclein cooperates with cspα in preventing neurodegeneration. *Cell*, 123(3):383–396, Nov 4 2005.

[56] N. M. Bonini and B. I. Giasson. Snaring the function of alpha-synuclein. *Cell*, 123(3):359–361, Nov 4 2005.

[57] R. Krüger, W. Kuhn, T. Müller, D. Woitalla, M. Graeber, S. Kösel, H. Przuntek, J. T. Epplen, L. Schöls, and O. Riess. Ala30pro mutation in the gene encoding alpha-synuclein in parkin-

son's disease. *Nature genetics*, 18(2):106–108, Feb 1998.

[58] Juan J. Zarranz, Javier Alegre, Juan C. Gómez-Esteban, Elena Lezcano, Raquel Ros, Israel Ampuero, Lídice Vidal, Janet Hoenicka, Olga Rodriguez, Begoña Atarés, Verónica Llorens, Estrella Gomez Tortosa, Teodoro del Ser, David G. Muñoz, and Justo G. de Yebenes. The new mutation, e46k, of α-synuclein causes parkinson and lewy body dementia. *Annals of neurology*, 55(2):164–173, Feb 2004.

[59] C. Proukakis, C. G. Dudzik, T. Brier, D. S. MacKay, J. M. Cooper, G. L. Millhauser, H. Houlden, and A. H. Schapira. A novel alpha-synuclein missense mutation in parkinson disease. *Neurology*, 80(11):1062–1064, Mar 12 2013.

[60] Silke Appel-Cresswell, Carles Vilarino-Guell, Mary Encarnacion, Holly Sherman, Irene Yu, Brinda Shah, David Weir, Christina Thompson, Chelsea Szu-Tu, Joanne Trinh, Jan O. Aasly, Alex Rajput, Ali H. Rajput, A. Jon Stoessl, and Matthew J. Farrer. Alpha-synuclein p.h50q, a novel pathogenic mutation for parkinson's disease. *Movement disorders : official journal of the Movement Disorder Society*, 28(6):811–813, Jun 2013.

[61] S. Lesage, M. Anheim, F. Letournel, L. Bousset, A. Honore, N. Rozas, L. Pieri, K. Madiona, A. Durr, R. Melki, C. Verny, A. Brice, and French Parkinson's Disease Genetics Study Group. G51d alpha-synuclein mutation causes a novel parkinsonian-pyramidal syndrome. *Annals of Neurology*, 73(4):459–471, Apr 2013.

[62] P. Pasanen, L. Myllykangas, M. Siitonen, A. Raunio, S. Kaakkola, J. Lyytinen, P. J. Tienari, M. Poyhonen, and A. Paetau. Novel alpha-synuclein mutation a53e associated with atypical multiple system atrophy and parkinson's disease-type pathology. *Neurobiology of aging*, 35(9):2180.e1–2180.e5, Sep 2014.

[63] L. Breydo, J. W. Wu, and V. N. Uversky. Alpha-synuclein misfolding and parkinson's disease. *Biochimica et biophysica acta*, 1822(2):261–285, Feb 2012.

[64] G. Zhang, Y. Xia, F. Wan, K. Ma, X. Guo, L. Kou, S. Yin, C. Han, L. Liu, J. Huang, N. Xiong, and T. Wang. New perspectives on roles of alpha-synuclein in parkinson's disease. *Frontiers*

in aging neuroscience, 10:370, Nov 22 2018.

[65] J. J. Zarranz, J. Alegre, J. C. Gomez-Esteban, E. Lezcano, R. Ros, I. Ampuero, L. Vidal, J. Hoenicka, O. Rodriguez, B. Atares, V. Llorens, E. Gomez Tortosa, T. del Ser, D. G. Munoz, and J. G. de Yebenes. The new mutation, e46k, of alpha-synuclein causes parkinson and lewy body dementia. *Annals of Neurology*, 55(2):164–173, Feb 2004.

[66] M. Farrer, J. Kachergus, L. Forno, S. Lincoln, D. S. Wang, M. Hulihan, D. Maraganore, K. Gwinn-Hardy, Z. Wszolek, D. Dickson, and J. W. Langston. Comparison of kindreds with parkinsonism and alpha-synuclein genomic multiplications. *Annals of Neurology*, 55(2):174–179, Feb 2004.

[67] Hilal A. Lashuel, Cassia R. Overk, Abid Oueslati, and Eliezer Masliah. The many faces of α-synuclein: from structure and toxicity to therapeutic target. *Nature reviews. Neuroscience*, 14(1):38–48, Jan 01, 2013.

[68] A. B. Singleton, M. Farrer, J. Johnson, A. Singleton, S. Hague, J. Kachergus, M. Hulihan, T. Peuralinna, A. Dutra, R. Nussbaum, S. Lincoln, A. Crawley, M. Hanson, D. Maraganore, C. Adler, M. R. Cookson, M. Muenter, M. Baptista, D. Miller, J. Blancato, J. Hardy, and K. Gwinn-Hardy. α-synuclein locus triplication causes parkinson's disease. *Science (American Association for the Advancement of Science)*, 302(5646):841, Oct 31, 2003.

[69] M. C. Chartier-Harlin, J. Kachergus, C. Roumier, V. Mouroux, X. Douay, S. Lincoln, C. Levecque, L. Larvor, J. Andrieux, M. Hulihan, N. Waucquier, L. Defebvre, P. Amouyel, M. Farrer, and A. Destee. Alpha-synuclein locus duplication as a cause of familial parkinson's disease. *Lancet (London, England)*, 364(9440):1167–1169, 2004.

[70] P. Ibanez, A. M. Bonnet, B. Debarges, E. Lohmann, F. Tison, P. Pollak, Y. Agid, A. Durr, and A. Brice. Causal relation between alpha-synuclein gene duplication and familial parkinson's disease. *Lancet (London, England)*, 364(9440):1169–1171, 2004.

[71] E. Kara, A. P. Kiely, C. Proukakis, N. Giffin, S. Love, J. Hehir, K. Rantell, A. Pandraud, D. G. Hernandez, E. Nacheva, A. M. Pittman, M. A. Nalls, A. B. Singleton, T. Revesz, K. P. Bhatia,

N. Quinn, J. Hardy, J. L. Holton, and H. Houlden. A 6.4 mb duplication of the alpha-synuclein locus causing frontotemporal dementia and parkinsonism: phenotype-genotype correlations. *JAMA neurology*, 71(9):1162–1171, Sep 2014.

[72] Christina M. Lill. Genetics of parkinson's disease. *Molecular and cellular probes*, 30(6):386–396, Dec 2016.

[73] M. B. Feany and W. W. Bender. A drosophila model of parkinson's disease. *Nature*, 404(6776):394–398, Mar 23 2000.

[74] Tjakko J. van Ham, Karen L. Thijssen, Rainer Breitling, Robert M. W. Hofstra, Ronald H. A. Plasterk, and Ellen A. A. Nollen. C. elegans model identifies genetic modifiers of α-synuclein inclusion formation during aging. *PLOS Genetics*, 4(3):e1000027, 2008.

[75] R. Betarbet, T. B. Sherer, G. MacKenzie, M. Garcia-Osuna, A. V. Panov, and J. T. Greenamyre. Chronic systemic pesticide exposure reproduces features of parkinson's disease. *Nature neuroscience*, 3(12):1301–1306, Dec 2000.

[76] C. Warren Olanow and Patrik Brundin. Parkinson's disease and alpha synuclein: is parkinson's disease a prion-like disorder? *Movement disorders : official journal of the Movement Disorder Society*, 28(1):31–40, Jan 2013.

[77] Heiko Braak, Kelly Del Tredici, Udo Rüb, Rob A. I. de Vos, Ernst N. H. Jansen Steur, and Eva Braak. Staging of brain pathology related to sporadic parkinson's disease. *Neurobiology of aging*, 24(2):197–211, 2003.

[78] Jia-Yi Li, Elisabet Englund, Janice L. Holton, Denis Soulet, Peter Hagell, Andrew J. Lees, Tammaryn Lashley, Niall P. Quinn, Stig Rehncrona, Anders Björklund, Håkan Widner, Tamas Revesz, Olle Lindvall, and Patrik Brundin. Lewy bodies in grafted neurons in subjects with parkinson's disease suggest host-to-graft disease propagation. *Nature medicine*, 14(5):501–503, May 2008.

[79] Jeffrey H. Kordower, Yaping Chu, Robert A. Hauser, Thomas B. Freeman, and C. Warren

Olanow. Lewy body-like pathology in long-term embryonic nigral transplants in parkinson's disease. *Nature medicine*, 14(5):504–506, May 2008.

[80] Laura A. Volpicelli-Daley, Kelvin C. Luk, Tapan P. Patel, Selcuk A. Tanik, Dawn M. Riddle, Anna Stieber, David F. Meaney, John Q. Trojanowski, and Virginia M-Y Lee. Exogenous α-synuclein fibrils induce lewy body pathology leading to synaptic dysfunction and neuron death. *Neuron*, 72(1):57–71, Oct 6 2011.

[81] David Sulzer and D. James Surmeier. Neuronal vulnerability, pathogenesis, and parkinson's disease. *Movement disorders : official journal of the Movement Disorder Society*, 28(1):41–50, Jan 2013.

[82] Giuliana Fusco, Alfonso De Simone, Paolo Arosio, Michele Vendruscolo, Gianluigi Veglia, and Christopher M. Dobson. Structural ensembles of membrane-bound α-synuclein reveal the molecular determinants of synaptic vesicle affinity. *Scientific Reports*, 6:27125, 2016.

[83] D. Eliezer, E. Kutluay, R. Bussell Jr, and G. Browne. Conformational properties of alpha-synuclein in its free and lipid-associated states. *Journal of Molecular Biology*, 307(4):1061–1073, Apr 6 2001.

[84] D. Snead and D. Eliezer. Alpha-synuclein function and dysfunction on cellular membranes. *Experimental neurobiology*, 23(4):292–313, Dec 2014.

[85] R. Bussell Jr and D. Eliezer. A structural and functional role for 11-mer repeats in alpha-synuclein and other exchangeable lipid binding proteins. *Journal of Molecular Biology*, 329(4):763–778, Jun 13 2003.

[86] W. S. Davidson, A. Jonas, D. F. Clayton, and J. M. George. Stabilization of alpha-synuclein secondary structure upon binding to synthetic membranes. *The Journal of biological chemistry*, 273(16):9443–9449, Apr 17 1998.

[87] R. Bussell Jr, T. F. Ramlall, and D. Eliezer. Helix periodicity, topology, and dynamics of membrane-associated alpha-synuclein. *Protein science : a publication of the Protein Society*,

14(4):862–872, Apr 2005.

[88] K. Vamvaca, M. J. Volles, and P. T. Lansbury Jr. The first n-terminal amino acids of alpha-synuclein are essential for alpha-helical structure formation *in vitro* and membrane binding in yeast. *Journal of Molecular Biology*, 389(2):413–424, Jun 5 2009.

[89] K. Ueda, H. Fukushima, E. Masliah, Y. Xia, A. Iwai, M. Yoshimoto, D. A. Otero, J. Kondo, Y. Ihara, and T. Saitoh. Molecular cloning of cdna encoding an unrecognized component of amyloid in alzheimer disease. *Proceedings of the National Academy of Sciences of the United States of America*, 90(23):11282–11286, Dec 1 1993.

[90] M. Grey, S. Linse, H. Nilsson, P. Brundin, and E. Sparr. Membrane interaction of alpha-synuclein in different aggregation states. *Journal of Parkinson's disease*, 1(4):359–371, 2011.

[91] Amberley D. Stephens, Maria Zacharopoulou, Rani Moons, Giuliana Fusco, Neeleema Seetaloo, Anass Chiki, Philippa J. Woodhams, Ioanna Mela, Hilal A. Lashuel, Jonathan J. Phillips, Alfonso De Simone, Frank Sobott, and Gabriele S. Kaminski Schierle. Extent of n-terminus exposure of monomeric alpha-synuclein determines its aggregation propensity. *Nature Communications*, 11(1):2820, 2020.

[92] Mario Gonzalez-Garcia, Giuliana Fusco, and Alfonso De Simone. Membrane interactions and toxicity by misfolded protein oligomers. *Frontiers in Cell and Developmental Biology*, 9:395, 2021.

[93] Nazareno González, Trinidad Arcos-López, Annekatrin König, Liliana Quintanar, Mauricio Menacho Márquez, Tiago F. Outeiro, and Claudio O. Fernández. Effects of alpha-synuclein post-translational modifications on metal binding. *Journal of neurochemistry*, 150(5):507–521, Sep 2019.

[94] Lijuan Kang, Gina M. Moriarty, Lucy A. Woods, Alison E. Ashcroft, Sheena E. Radford, and Jean Baum. N-terminal acetylation of α-synuclein induces increased transient helical propensity and decreased aggregation rates in the intrinsically disordered monomer. *Protein science*, 21(7):911–917, Jul 2012.

[95] Marco C. Miotto, Ariel A. Valiente-Gabioud, Giulia Rossetti, Markus Zweckstetter, Paolo Carloni, Philipp Selenko, Christian Griesinger, Andres Binolfi, and Claudio O. Fernández. Copper binding to the n-terminally acetylated, naturally occurring form of alpha-synuclein induces local helical folding. *Journal of the American Chemical Society*, 137(20):6444–6447, May 27, 2015.

[96] Gina M. Moriarty, Maria K. Janowska, Lijuan Kang, and Jean Baum. Exploring the accessible conformations of n-terminal acetylated α-synuclein. *FEBS letters*, 587(8):1128–1138, 2013.

[97] Matteo Runfola, Alfonso De Simone, Michele Vendruscolo, Christopher M. Dobson, and Giuliana Fusco. The n-terminal acetylation of α-synuclein changes the affinity for lipid membranes but not the structural properties of the bound state. *Scientific Reports*, 10(1):204, 2020.

[98] Matthew D. Watson and Jennifer C. Lee. N-terminal acetylation affects α-synuclein fibril polymorphism. *Biochemistry*, 58(35):3630–3633, 2019.

[99] Bruno Fauvet, Martial K. Mbefo, Mohamed-Bilal Fares, Carole Desobry, Sarah Michael, Mustafa T. Ardah, Elpida Tsika, Philippe Coune, Michel Prudent, Niels Lion, David Eliezer, Darren J. Moore, Bernard Schneider, Patrick Aebischer, Omar M. El-Agnaf, Eliezer Masliah, and Hilal A. Lashuel. α-synuclein in central nervous system and from erythrocytes, mammalian cells, and *Escherichia coli* exists predominantly as disordered monomer. *JOURNAL OF BIOLOGICAL CHEMISTRY*, 287(19):15345–15364, May 04, 2012.

[100] F. U. Hartl. Protein misfolding diseases. *Annual Review of Biochemistry*, 86(1):21–26, 2017.

[101] Beate Winner, Roberto Jappelli, Samir K. Maji, Paula A. Desplats, Leah Boyer, Stefan Aigner, Claudia Hetzer, Thomas Loher, Marçal Vilar, Silvia Campioni, Christos Tzitzilonis, Alice Soragni, Sebastian Jessberger, Helena Mira, Antonella Consiglio, Emiley Pham, Eliezer Masliah, Fred H. Gage, and Roland Riek. *In vivo* demonstration that α-synuclein oligomers are toxic. *Proceedings of the National Academy of Sciences - PNAS*, 108(10):4194–4199, Mar 08, 2011.

[102] M. Helwig, M. Klinkenberg, R. Rusconi, R. E. Musgrove, N. K. Majbour, O. M. El-Agnaf, A. Ulusoy, and D. A. Di Monte. Brain propagation of transduced alpha-synuclein involves

non-fibrillar protein species and is enhanced in alpha-synuclein null mice. *Brain : a journal of neurology*, 139(Pt 3):856–870, Mar 2016.

[103] R. Cascella, M. Perni, S. W. Chen, G. Fusco, C. Cecchi, M. Vendruscolo, F. Chiti, C. M. Dobson, and A. De Simone. Probing the origin of the toxicity of oligomeric aggregates of alpha-synuclein with antibodies. *ACS chemical biology*, 14(6):1352–1362, Jun 21 2019.

[104] B. J. Ryan, S. Hoek, E. A. Fon, and R. Wade-Martins. Mitochondrial dysfunction and mitophagy in parkinson's: from familial to sporadic disease. *Trends in biochemical sciences*, 40(4):200–210, Apr 2015.

[105] N. Plotegher, E. Gratton, and L. Bubacco. Number and brightness analysis of alpha-synuclein oligomerization and the associated mitochondrial morphology alterations in live cells. *Biochimica et biophysica acta*, 1840(6):2014–2024, Jun 2014.

[106] E. Colla, P. H. Jensen, O. Pletnikova, J. C. Troncoso, C. Glabe, and M. K. Lee. Accumulation of toxic alpha-synuclein oligomer within endoplasmic reticulum occurs in alpha-synucleinopathy *in vivo*. *The Journal of neuroscience : the official journal of the Society for Neuroscience*, 32(10):3301–3305, Mar 7 2012.

[107] E. Emmanouilidou, L. Stefanis, and K. Vekrellis. Cell-produced alpha-synuclein oligomers are targeted to, and impair, the 26s proteasome. *Neurobiology of aging*, 31(6):953–968, Jun 2010.

[108] Himanshu Chaudhary, Aditya Iyer, Vinod Subramaniam, and Mireille M. A. E. Claessens. α-synuclein oligomers stabilize pre-existing defects in supported bilayers and propagate membrane damage in a fractal-like pattern. *Langmuir*, 32(45):11827–11836, 2016.

[109] P. H. Nguyen, A. Ramamoorthy, B. R. Sahoo, J. Zheng, P. Faller, J. E. Straub, L. Dominguez, J. E. Shea, N. V. Dokholyan, A. De Simone, B. Ma, R. Nussinov, S. Najafi, S. T. Ngo, A. Loquet, M. Chiricotto, P. Ganguly, J. McCarty, M. S. Li, C. Hall, Y. Wang, Y. Miller, S. Melchionna, B. Habenstein, S. Timr, J. Chen, B. Hnath, B. Strodel, R. Kayed, S. Lesné, G. Wei, F. Sterpone, A. J. Doig, and P. Derreumaux. Amyloid oligomers: A joint experimental/computational perspective on alzheimer's disease, parkinson's disease, type ii diabetes, and

amyotrophic lateral sclerosis. *Chemical reviews*, 121(4):2545–2647, Feb 24 2021.

[110] K. M. Danzer, D. Haasen, A. R. Karow, S. Moussaud, M. Habeck, A. Giese, H. Kretzschmar, B. Hengerer, and M. Kostka. Different species of alpha-synuclein oligomers induce calcium influx and seeding. *The Journal of neuroscience : the official journal of the Society for Neuroscience*, 27(34):9220–9232, Aug 22 2007.

[111] Hai-Young Kim, Min-Kyu Cho, Ashutosh Kumar, Elke Maier, Carsten Siebenhaar, Stefan Becker, Claudio O. Fernandez, Hilal A. Lashuel, Roland Benz, Adam Lange, and Markus Zweckstetter. Structural properties of pore-forming oligomers of α-synuclein. *Journal of the American Chemical Society*, 131(47):17482–17489, 2009.

[112] Laura Tosatto, Alberto O. Andrighetti, Nicoletta Plotegher, Valeria Antonini, Isabella Tessari, Leonardo Ricci, Luigi Bubacco, and Mauro Dalla Serra. Alpha-synuclein pore forming activity upon membrane association. *Biochimica et Biophysica Acta (BBA) - Biomembranes*, 1818(11):2876–2883, 2012.

[113] Edward Rockenstein, Silke Nuber, Cassia R. Overk, Kiren Ubhi, Michael Mante, Christina Patrick, Anthony Adame, Margarita Trejo-Morales, Juan Gerez, Paola Picotti, Poul H. Jensen, Silvia Campioni, Roland Riek, Jürgen Winkler, Fred H. Gage, Beate Winner, and Eliezer Masliah. Accumulation of oligomer-prone α-synuclein exacerbates synaptic and neuronal degeneration *in vivo*. *Brain : a journal of neurology*, 137(Pt 5):1496–1513, May 2014.

[114] T. P. Knowles, M. Vendruscolo, and C. M. Dobson. The amyloid state and its association with protein misfolding diseases. *Nature reviews.Molecular cell biology*, 15(6):384–396, Jun 2014.

[115] Farah El Turk, Erwin De Genst, Tim Guilliams, Bruno Fauvet, Mirva Hejjaoui, Justin Di Trani, Anass Chiki, Anthony Mittermaier, Michele Vendruscolo, Hilal A. Lashuel, and Christopher M. Dobson. Exploring the role of post-translational modifications in regulating α-synuclein interactions by studying the effects of phosphorylation on nanobody binding, 2018.

[116] Dominic M. Walsh and David B. Teplow. Alzheimer's disease and the amyloid β-protein. *Progress in molecular biology and translational science*, 107:101–124, 2012.

[117] Sarah M. Ward, Diana S. Himmelstein, Jody K. Lancia, and Lester I. Binder. Tau oligomers and tau toxicity in neurodegenerative disease. *Biochemical Society transactions*, 40(4):667–671, 2012.

[118] Andisheh Abedini, Annette Plesner, Ping Cao, Zachary Ridgway, Jinghua Zhang, Ling-Hsien Tu, Chris T. Middleton, Brian Chao, Daniel J. Sartori, Fanling Meng, Hui Wang, Amy G. Wong, Martin T. Zanni, C. B. Verchere, Daniel P. Raleigh, and Ann Marie Schmidt. Time-resolved studies define the nature of toxic iapp intermediates, providing insight for anti-amyloidosis therapeutics. *eLife*, 5:e12977, 2016.

[119] Federica Scollo and Carmelo La Rosa. Amyloidogenic intrinsically disordered proteins: New insights into their self-assembly and their interaction with membranes. *Life (Basel, Switzerland)*, 10(8):144, 2020.

[120] Benedetta Mannini, Estefania Mulvihill, Caterina Sgromo, Roberta Cascella, Reza Khodarahmi, Matteo Ramazzotti, Christopher M. Dobson, Cristina Cecchi, and Fabrizio Chiti. Toxicity of protein oligomers is rationalized by a function combining size and surface hydrophobicity. *ACS Chemical Biology*, 9(10):2309–2317, 2014.

[121] Mirella Vivoli Vega, Roberta Cascella, Serene W. Chen, Giuliana Fusco, Alfonso De Simone, Christopher M. Dobson, Cristina Cecchi, and Fabrizio Chiti. The toxicity of misfolded protein oligomers is independent of their secondary structure. *ACS Chemical Biology*, 14(7):1593–1600, 2019.

[122] Alfonso De Simone, Luciana Esposito, Carlo Pedone, and Luigi Vitagliano. Insights into stability and toxicity of amyloid-like oligomers by replica exchange molecular dynamics analyses. *Biophysical journal*, 95(4):1965–1973, 2008.

[123] Laura Pieri, Karine Madiona, and Ronald Melki. Structural and functional properties of prefibrillar α-synuclein oligomers. *Scientific Reports*, 6:24526, 2016.

[124] Giuliana Fusco, Serene W. Chen, Philip T. F. Williamson, Roberta Cascella, Michele Perni, James A. Jarvis, Cristina Cecchi, Michele Vendruscolo, Fabrizio Chiti, Nunilo Cremades, Lim-

ing Ying, Christopher M. Dobson, and Alfonso De Simone. Structural basis of membrane disruption and cellular toxicity by α-synuclein oligomers. *Science*, 358(6369):1440–1443, 2017.

[125] Michele F. M. Sciacca, Carmelo Tempra, Federica Scollo, Danilo Milardi, and Carmelo La Rosa. Amyloid growth and membrane damage: Current themes and emerging perspectives from theory and experiments on aβ and hiapp. *Biochimica et Biophysica Acta (BBA) - Biomembranes*, 1860(9):1625–1638, 2018.

[126] L. Boi, A. Pisanu, M. F. Palmas, G. Fusco, E. Carboni, M. A. Casu, V. Satta, M. Scherma, E. Janda, I. Mocci, G. Mulas, A. Ena, S. Spiga, P. Fadda, A. De Simone, and A. R. Carta. Modeling parkinson's disease neuropathology and symptoms by intranigral inoculation of preformed human α-synuclein oligomers. *International journal of molecular sciences*, 21(22):8535. doi: 10.3390/ijms21228535, Nov 12 2020.

[127] H. A. I. Lin, Rajinder Bhatia, and Ratneshwar Lal. Amyloid β protein forms ion channels: implications for alzheimer's disease pathophysiology. *The FASEB Journal*, 15(13):2433–2444, 2001.

[128] Plamena R. Angelova, Marthe H. R. Ludtmann, Mathew H. Horrocks, Alexander Negoda, Nunilo Cremades, David Klenerman, Christopher M. Dobson, Nicholas W. Wood, Evgeny V. Pavlov, Sonia Gandhi, and Andrey Y. Abramov. Ca2+ is a key factor in α-synuclein-induced neurotoxicity. *Journal of cell science*, 129(9):1792–1801, May 1 2016.

[129] Arjan Quist, Ivo Doudevski, Hai Lin, Rushana Azimova, Douglas Ng, Blas Frangione, Bruce Kagan, Jorge Ghiso, and Ratnesh Lal. Amyloid ion channels: A common structural link for protein-misfolding disease. *Proceedings of the National Academy of Sciences of the United States of America*, 102(30):10427–10432, 2005.

[130] Li Rebekah Feng, Howard J. Federoff, Stefano Vicini, and Kathleen Maguire-Zeiss. Alpha-synuclein mediates alterations in membrane conductance: a potential role for alpha-synuclein oligomers in cell vulnerability. *The European journal of neuroscience*, 32(1):10–17, 2010.

[131] Stephanie Wong Su, Andy Chieng, Jacob Parres-Gold, Megan Chang, and Yixian Wang. Real-

time determination of aggregated alpha-synuclein induced membrane disruption at neuroblastoma cells using scanning ion conductance microscopy. *Faraday discussions*, 210(0):131–143, 2018.

[132] Reinier Oropesa-Nuñez, Silvia Seghezza, Silvia Dante, Alberto Diaspro, Roberta Cascella, Cristina Cecchi, Massimo Stefani, Fabrizio Chiti, and Claudio Canale. Interaction of toxic and non-toxic hypf-n oligomers with lipid bilayers investigated at high resolution with atomic force microscopy. *Oncotarget*, 7(29):44991–45004, 2016.

[133] David C. Bode, Mark Freeley, Jon Nield, Matteo Palma, and John H. Viles. Amyloid-β oligomers have a profound detergent-like effect on lipid membrane bilayers, imaged by atomic force and electron microscopy. *The Journal of biological chemistry*, 294(19):7566–7572, 2019.

[134] Hyunbum Jang, Fernando Teran Arce, Srinivasan Ramachandran, Ricardo Capone, Rushana Azimova, Bruce L. Kagan, Ruth Nussinov, and Ratnesh Lal. Truncated β-amyloid peptide channels provide an alternative mechanism for alzheimer's disease and down syndrome. *Proceedings of the National Academy of Sciences*, 107(14):6538, 2010.

[135] Liu Liu, Hiroaki Komatsu, Ian V. J. Murray, and Paul H. Axelsen. Promotion of amyloid β protein misfolding and fibrillogenesis by a lipid oxidation product. *Journal of Molecular Biology*, 377(4):1236–1250, 2008.

[136] Minee L. Choi and Sonia Gandhi. Crucial role of protein oligomerization in the pathogenesis of alzheimer's and parkinson's diseases. *The FEBS Journal*, 285(19):3631–3644, 2018.

[137] Patrycja Michalska and Rafael León. When it comes to an end: Oxidative stress crosstalk with protein aggregation and neuroinflammation induce neurodegeneration. *Antioxidants (Basel, Switzerland)*, 9(8):740, 2020.

[138] Plamena R. Angelova, Noemi Esteras, and Andrey Y. Abramov. Mitochondria and lipid peroxidation in the mechanism of neurodegeneration: Finding ways for prevention. *Medicinal research reviews*, n/a, 2020.

[139] Esther Dalfó and Isidre Ferrer. Early alpha-synuclein lipoxidation in neocortex in lewy body diseases. *Neurobiology of aging*, 29(3):408–417, 2008.

[140] M. J. Picklo S. and T. J. Montine. Mitochondrial effects of lipid-derived neurotoxins. *J Alzheimers Dis*, 12(2):185–193, Sep 2007.

[141] Carmelo La Rosa, Silvia Scalisi, Fabio Lolicato, Martina Pannuzzo, and Antonio Raudino. Lipid-assisted protein transport: A diffusion-reaction model supported by kinetic experiments and molecular dynamics simulations. *The Journal of chemical physics*, 144(18):184901, 2016.

[142] Federica Scollo, Carmelo Tempra, Fabio Lolicato, Michele F. M. Sciacca, Antonio Raudino, Danilo Milardi, and Carmelo La Rosa. Phospholipids critical micellar concentrations trigger different mechanisms of intrinsically disordered proteins interaction with model membranes. *The Journal of Physical Chemistry Letters*, 9(17):5125–5129, 2018.

[143] Michele F. Sciacca, Fabio Lolicato, Carmelo Tempra, Federica Scollo, Bikash R. Sahoo, Matthew D. Watson, Sara García-Viñuales, Danilo Milardi, Antonio Raudino, Jennifer C. Lee, Ayyalusamy Ramamoorthy, and Carmelo La Rosa. Lipid-chaperone hypothesis: A common molecular mechanism of membrane disruption by intrinsically disordered proteins. *ACS Chemical Neuroscience*, 11(24):4336–4350, 2020.

[144] Giovanna Cenini, Ana Lloret, and Roberta Cascella. Oxidative stress in neurodegenerative diseases: From a mitochondrial point of view. *Oxidative Medicine and Cellular Longevity*, 2019:2105607, 2019.

[145] Leigh J. Hsu, Yutaka Sagara, Armando Arroyo, Edward Rockenstein, Abbyann Sisk, Margaret Mallory, Jeff Wong, Takato Takenouchi, Makoto Hashimoto, and Eliezer Masliah. α-synuclein promotes mitochondrial deficit and oxidative stress. *The American Journal of Pathology*, 157(2):401–410, 2000.

[146] Cristina Guardia-Laguarta, Estela Area-Gomez, Cornelia Rüb, Yuhui Liu, Jordi Magrané, Dorothea Becker, Wolfgang Voos, Eric A. Schon, and Serge Przedborski. α-synuclein is localized to mitochondria-associated er membranes. *The Journal of Neuroscience*, 34(1):249–259,

2014.

[147] Goutham K. Ganjam, Kathrin Bolte, Lina A. Matschke, Sandra Neitemeier, Amalia M. Dolga, Matthias Höllerhage, Günter U. Höglinger, Agata Adamczyk, Niels Decher, Wolfgang H. Oertel, and Carsten Culmsee. Mitochondrial damage by α-synuclein causes cell death in human dopaminergic neurons. *Cell Death & Disease*, 10(11):865, 2019.

[148] Hilal A. Lashuel. Membrane permeabilization: A common mechanism in protein-misfolding diseases. *Sci.Aging Knowl.Environ.*, 2005(38):pe28, 2005.

[149] Charles G. Glabe. Common mechanisms of amyloid oligomer pathogenesis in degenerative disease. *Neurobiology of aging*, 27(4):570–575, 2006.

[150] Maria Ylenia Farrugia, Mario Caruana, Stephanie Ghio, Angelique Camilleri, Claude Farrugia, Ruben J. Cauchi, Sara Cappelli, Fabrizio Chiti, and Neville Vassallo. Toxic oligomers of the amyloidogenic hypf-n protein form pores in mitochondrial membranes. *Scientific Reports*, 10(1):17733, 2020.

[151] Vincenzo Bonifati, Guido J. Breedveld, Ferdinando Squitieri, Nicola Vanacore, Pierluigi Brustenghi, Biswadjiet S. Harhangi, Pasquale Montagna, Milena Cannella, Giovanni Fabbrini, Patrizia Rizzu, Cornelia M. van Duijn, Ben A. Oostra, Giuseppe Meco, and Peter Heutink. Localization of autosomal recessive early-onset parkinsonism to chromosome 1p36 (park7) in an independent dataset. *Annals of Neurology*, 51(2):253–256, 2002.

[152] Enza Maria Valente, Patrick Abou-Sleiman, Viviana Caputo, Miratul M. K. Muqit, Kirsten Harvey, Suzana Gispert, Zeeshan Ali, Domenico Del Turco, Anna Rita Bentivoglio, Daniel G. Healy, Alberto Albanese, Robert Nussbaum, Rafael González-Maldonado, Thomas Deller, Sergio Salvi, Pietro Cortelli, William P. Gilks, David S. Latchman, Robert J. Harvey, Bruno Dallapiccola, Georg Auburger, and Nicholas W. Wood. Hereditary early-onset parkinson's disease caused by mutations in pink1. *Science*, 304(5674):1158–1160, 2004.

[153] William P. Gilks, Patrick Abou-Sleiman, Sonia Gandhi, Shushant Jain, Andrew Singleton, Andrew J. Lees, Karen Shaw, Kailash P. Bhatia, Vincenzo Bonifati, Niall P. Quinn, John Lynch,

Daniel G. Healy, Janice L. Holton, Tamas Revesz, and Nicholas W. Wood. A common lrrk2 mutation in idiopathic parkinson's disease. *The Lancet*, 365(9457):415–416, 2005.

[154] William C. Nichols, Nathan Pankratz, Dena Hernandez, Coro Paisán-Ruíz, Shushant Jain, Cheryl A. Halter, Veronika E. Michaels, Terry Reed, Alice Rudolph, Clifford W. Shults, Andrew Singleton, and Tatiana Foroud. Genetic screening for a single common lrrk2 mutation in familial parkinson's disease. *The Lancet*, 365(9457):410–412, 2005.

[155] Angelique Camilleri, Claire Zarb, Mario Caruana, Ulrike Ostermeier, Stephanie Ghio, Tobias Högen, Felix Schmidt, Armin Giese, and Neville Vassallo. Mitochondrial membrane permeabilisation by amyloid aggregates and protection by polyphenols. *Biochimica et Biophysica Acta (BBA) - Biomembranes*, 1828(11):2532–2543, 2013.

[156] Angelique Camilleri, Stephanie Ghio, Mario Caruana, Daniel Weckbecker, Felix Schmidt, Frits Kamp, Andrei Leonov, Sergey Ryazanov, Christian Griesinger, Armin Giese, Ruben J. Cauchi, and Neville Vassallo. Tau-induced mitochondrial membrane perturbation is dependent upon cardiolipin. *Biochimica et Biophysica Acta (BBA) - Biomembranes*, 1862(2):183064, 2020.

[157] Natalie C. Kegulian, Shalene Sankhagowit, Melania Apostolidou, Sajith A. Jayasinghe, Noah Malmstadt, Peter C. Butler, and Ralf Langen. Membrane curvature-sensing and curvature-inducing activity of islet amyloid polypeptide and its implications for membrane disruption. *The Journal of biological chemistry*, 290(43):25782–25793, 2015.

[158] Stephanie Ghio, Angelique Camilleri, Mario Caruana, Viktoria C. Ruf, Felix Schmidt, Andrei Leonov, Sergey Ryazanov, Christian Griesinger, Ruben J. Cauchi, Frits Kamp, Armin Giese, and Neville Vassallo. Cardiolipin promotes pore-forming activity of alpha-synuclein oligomers in mitochondrial membranes. *ACS Chemical Neuroscience*, 10(8):3815–3829, 2019.

[159] Susanne E. Horvath and Günther Daum. Lipids of mitochondria. *Progress in lipid research*, 52(4):590–614, 2013.

[160] Federico Elías-Wolff, Martin Lindén, Alexander P. Lyubartsev, and Erik G. Brandt. Curvature sensing by cardiolipin in simulated buckled membranes. *Soft Matter*, 15(4):792–802, 2019.

[161] Latha Devi, Vijayendran Raghavendran, Badanavalu M. Prabhu, Narayan G. Avadhani, and Hindupur K. Anandatheerthavarada. Mitochondrial import and accumulation of alpha-synuclein impair complex i in human dopaminergic neuronal cultures and parkinson disease brain. *The Journal of biological chemistry*, 283(14):9089–9100, 2008.

[162] Martin Klingenberg. Cardiolipin and mitochondrial carriers. *Biochimica et Biophysica Acta (BBA) - Biomembranes*, 1788(10):2048–2058, 2009.

[163] Ranit Pariary, Dipita Bhattacharyya, and Anirban Bhunia. Mitochondrial-membrane association of α-synuclein: Pros and cons in consequence of parkinson's disease pathophysiology. *Gene Reports*, 16:100423, 2019.

[164] M. T. Carrì, A. Ferri, A. Battistoni, L. Famhy, R. Gabbianelli, F. Poccia, and G. Rotilio. Expression of a cu,zn superoxide dismutase typical of familial amyotrophic lateral sclerosis induces mitochondrial alteration and increase of cytosolic ca2+ concentration in transfected neuroblastoma sh-sy5y cells. *FEBS Lett*, 414(2):365–368, Sep 8 1997.

[165] Fiona M. Menzies, Mark R. Cookson, Robert W. Taylor, Douglass M. Turnbull, Zofia M. A. Chrzanowska-Lightowlers, Lichun Dong, Denise A. Figlewicz, and Pamela J. Shaw. Mitochondrial dysfunction in a cell culture model of familial amyotrophic lateral sclerosis. *Brain*, 125(7):1522–1533, 2002.

[166] Cynthia M. J. Higgins, Cheolwha Jung, Hongliu Ding, and Zuoshang Xu. Mutant cu, zn superoxide dismutase that causes motoneuron degeneration is present in mitochondria in the cns. *The Journal of neuroscience : the official journal of the Society for Neuroscience*, 22(6):RC215, 2002.

[167] Marina Mattiazzi, Marilena D'Aurelio, Carl D. Gajewski, Katherine Martushova, Mahmoud Kiaei, M. F. Beal, and Giovanni Manfredi. Mutated human sod1 causes dysfunction of oxidative phosphorylation in mitochondria of transgenic mice. *Journal of Biological Chemistry*, 277(33):29626–29633, 2002.

[168] Russell H. Swerdlow, Janice K. Parks, David S. Cassarino, Patricia A. Trimmer, Scott W.

Miller, David J. Maguire, Jason P. Sheehan, Robyn S. Maguire, Gary Pattee, Vern C. Juel, Lawrence H. Phillips, Jeremy B. Tuttle, James P. Bennett, Robert E. Davis, and W. D. Parker. Mitochondria in sporadic amyotrophic lateral sclerosis. *Experimental neurology*, 153(1):135–142, 1998.

[169] Falk R. Wiedemann, Giovanni Manfredi, Christian Mawrin, M. F. Beal, and Eric A. Schon. Mitochondrial dna and respiratory chain function in spinal cords of als patients. *Journal of neurochemistry*, 80(4):616–625, 2002.

[170] Melissa Birol, Sunil Kumar, Elizabeth Rhoades, and Andrew D. Miranker. Conformational switching within dynamic oligomers underpins toxic gain-of-function by diabetes-associated amyloid. *Nature Communications*, 9(1):1312, 2018.

[171] Tatyana Gurlo, Sergey Ryazantsev, Chang jiang Huang, Michael W. Yeh, Howard A. Reber, O. J. Hines, Timothy D. O'Brien, Charles G. Glabe, and Peter C. Butler. Evidence for proteotoxicity in beta cells in type 2 diabetes: toxic islet amyloid polypeptide oligomers form intracellularly in the secretory pathway. *The American journal of pathology*, 176(2):861–869, 2010.

[172] Eric S. Luth, Irina G. Stavrovskaya, Tim Bartels, Bruce S. Kristal, and Dennis J. Selkoe. Soluble, prefibrillar α-synuclein oligomers promote complex i-dependent, ca^{2+}-induced mitochondrial dysfunction. *The Journal of biological chemistry*, 289(31):21490–21507, 2014.

[173] Todd B. Sherer, Ranjita Betarbet, Amy K. Stout, Serena Lund, Melisa Baptista, Alexander V. Panov, Mark R. Cookson, and J. T. Greenamyre. An *in vitro* model of parkinson's disease: linking mitochondrial impairment to altered alpha-synuclein metabolism and oxidative damage. *The Journal of neuroscience : the official journal of the Society for Neuroscience*, 22(16):7006–7015, 2002.

[174] Kalpita Banerjee, Maitrayee Sinha, Chi Le Lan Pham, Sirsendu Jana, Dalia Chanda, Roberto Cappai, and Sasanka Chakrabarti. α-synuclein induced membrane depolarization and loss of phosphorylation capacity of isolated rat brain mitochondria: Implications in parkinson's

disease. *FEBS letters*, 584(8):1571–1576, 2010.

[175] Ken Nakamura. α-synuclein and mitochondria: partners in crime? *Neurotherapeutics : the journal of the American Society for Experimental NeuroTherapeutics*, 10(3):391–399, 2013.

[176] R. Resende, E. Ferreiro, C. Pereira, and C. Resende de Oliveira. Neurotoxic effect of oligomeric and fibrillar species of amyloid-β peptide 1-42: Involvement of endoplasmic reticulum calcium release in oligomer-induced cell death. *Neuroscience*, 155(3):725–737, 2008.

[177] Tomohiro Umeda, Takami Tomiyama, Naomi Sakama, Saya Tanaka, Mary P. Lambert, William L. Klein, and Hiroshi Mori. Intraneuronal amyloid β oligomers cause cell death via endoplasmic reticulum stress, endosomal/lysosomal leakage, and mitochondrial dysfunction *in vivo*. *Journal of neuroscience research*, 89(7):1031–1042, 2011.

[178] Aashiq Hussain Bhat, Khalid Bashir Dar, Suhail Anees, Mohammad Afzal Zargar, Akbar Masood, Manzoor Ahmad Sofi, and Showkat Ahmad Ganie. Oxidative stress, mitochondrial dysfunction and neurodegenerative diseases; a mechanistic insight. *Biomedicine & Pharmacotherapy*, 74:101–110, 2015.

[179] P. H. Reddy. Role of mitochondria in neurodegenerative diseases: mitochondria as a therapeutic target in alzheimer's disease. *CNS spectrums*, 14(8):8–18, 2009.

[180] Ofek Oren, Shani Ben Zichri, Ran Taube, Raz Jelinek, and Niv Papo. Aβ42 double mutant inhibits aβ42-induced plasma and mitochondrial membrane disruption in artificial membranes, isolated organs, and intact cells. *ACS Chemical Neuroscience*, 11(7):1027–1037, 2020.

[181] Elizabeth M. Mutisya, Allen C. Bowling, and M. F. Beal. Cortical cytochrome oxidase activity is reduced in alzheimer's disease. *Journal of neurochemistry*, 63(6):2179–2184, 1994.

[182] C. S. Casley, L. Canevari, J. M. Land, J. B. Clark, and M. A. Sharpe. β-amyloid inhibits integrated mitochondrial respiration and key enzyme activities. *Journal of neurochemistry*, 80(1):91–100, 2002.

[183] Virginie Rhein, Xiaomin Song, Andreas Wiesner, Lars M. Ittner, Ginette Baysang, Fides Meier,

Laurence Ozmen, Horst Bluethmann, Stefan Dröse, Ulrich Brandt, Egemen Savaskan, Christian Czech, Jürgen Götz, and Anne Eckert. Amyloid-β and tau synergistically impair the oxidative phosphorylation system in triple transgenic alzheimer's disease mice. *Proceedings of the National Academy of Sciences of the United States of America*, 106(47):20057–20062, 2009.

[184] Christopher S. Casley, Viktor Lakics, Hyoung gon Lee, Lisa M. Broad, Theresa A. Day, Tricia Cluett, Mark A. Smith, Michael J. O'Neill, and Ann E. Kingston. Up-regulation of astrocyte metabotropic glutamate receptor 5 by amyloid-β peptide. *Brain research*, 1260:65–75, 2009.

[185] Dmitry Lim, Anand Iyer, Virginia Ronco, Ambra A. Grolla, Pier Luigi Canonico, Eleonora Aronica, and Armando A. Genazzani. Amyloid β deregulates astroglial mglur5-mediated calcium signaling via calcineurin and nf-kb. *Glia*, 61(7):1134–1145, 2013.

[186] Amulya Nidhi Shrivastava, Jacob M. Kowalewski, Marianne Renner, Luc Bousset, Annette Koulakoff, Ronald Melki, Christian Giaume, and Antoine Triller. β-amyloid and atp-induced diffusional trapping of astrocyte and neuronal metabotropic glutamate type-5 receptors. *Glia*, 61(10):1673–1686, 2013.

[187] Marianne Renner, Pascale N. Lacor, Pauline T. Velasco, Jian Xu, Anis Contractor, William L. Klein, and Antoine Triller. Deleterious effects of amyloid β oligomers acting as an extracellular scaffold for mglur5. *Neuron*, 66(5):739–754, 2010.

[188] Ji Won Um, Adam C. Kaufman, Mikhail Kostylev, Jacqueline K. Heiss, Massimiliano Stagi, Hideyuki Takahashi, Meghan E. Kerrisk, Alexander Vortmeyer, Thomas Wisniewski, Anthony J. Koleske, Erik C. Gunther, Haakon B. Nygaard, and Stephen M. Strittmatter. Metabotropic glutamate receptor 5 is a coreceptor for alzheimer aβ oligomer bound to cellular prion protein. *Neuron*, 79(5):887–902, 2013.

[189] R. Sanchez-Pernaute, J. Q. Wang, D. Kuruppu, L. Cao, W. Tueckmantel, A. Kozikowski, O. Isacson, and A. L. Brownell. Enhanced binding of metabotropic glutamate receptor type 5 (mglur5) pet tracers in the brain of parkinsonian primates. *NeuroImage*, 42(1):248–251, 2008.

[190] Diana L. Price, Edward Rockenstein, Kiren Ubhi, Van Phung, Natalie MacLean-Lewis, David Askay, Anna Cartier, Brian Spencer, Christina Patrick, Paula Desplats, Mark H. Ellisman, and Eliezer Masliah. Alterations in mglur5 expression and signaling in lewy body disease and in transgenic models of alpha-synucleinopathy–implications for excitotoxicity. *PloS one*, 5(11):e14020, 2010.

[191] Nicolas Morin, Laurent Grégoire, Marc Morissette, Sandrine Desrayaud, Baltazar Gomez-Mancilla, Fabrizio Gasparini, and Thérèse Di Paolo. Mpep, an mglu5 receptor antagonist, reduces the development of l-dopa-induced motor complications in de novo parkinsonian monkeys: Biochemical correlates. *Neuropharmacology*, 66:355–364, 2013.

[192] Fei Li and Joe Z. Tsien. Memory and the nmda receptors. *The New England journal of medicine*, 361(3):302–303, 2009.

[193] Elena Alberdi, Maria Victoria Sánchez-Gómez, Fabio Cavaliere, Alberto Pérez-Samartín, José Luis Zugaza, Ramón Trullas, María Domercq, and Carlos Matute. Amyloid β oligomers induce ca2+ dysregulation and neuronal death through activation of ionotropic glutamate receptors. *Cell calcium*, 47(3):264–272, 2010.

[194] Jingyi Liang, Don Kulasiri, and Sandhya Samarasinghe. Computational investigation of amyloid-β-induced location- and subunit-specific disturbances of nmdar at hippocampal dendritic spine in alzheimer's disease. *PLOS ONE*, 12(8):e0182743, 2017.

[195] Juha Laurén, David A. Gimbel, Haakon B. Nygaard, John W. Gilbert, and Stephen M. Strittmatter. Cellular prion protein mediates impairment of synaptic plasticity by amyloid-β oligomers. *Nature*, 457(7233):1128–1132, 2009.

[196] Santiago V. Salazar, Christopher Gallardo, Adam C. Kaufman, Charlotte S. Herber, Laura T. Haas, Sophie Robinson, Jean C. Manson, Michael K. Lee, and Stephen M. Strittmatter. Conditional deletion of prnp rescues behavioral and synaptic deficits after disease onset in transgenic alzheimer's disease. *The Journal of Neuroscience*, 37(38):9207–9221, 2017.

[197] A. H. Brody and Stephen M. Strittmatter. Synaptotoxic signaling by amyloid β oligomers in

alzheimer's disease through prion protein and mglur5. *Advances in Pharmacology (San Diego, Calif.)*, 82:293–323, 2018.

[198] Silvia A. Purro, Andrew J. Nicoll, and John Collinge. Prion protein as a toxic acceptor of amyloid-β oligomers. *Biological psychiatry*, 83(4):358–368, 2018.

[199] Yuan Zhang, Yanfang Zhao, Lei Zhang, Wanpeng Yu, Yu Wang, and Wenguang Chang. Cellular prion protein as a receptor of toxic amyloid-β42 oligomers is important for alzheimer's disease. *Frontiers in Cellular Neuroscience*, 13(339), 2019.

[200] Darragh B. Freir, Andrew J. Nicoll, Igor Klyubin, Silvia Panico, Jessica M. Mc Donald, Emmanuel Risse, Emmanuel A. Asante, Mark A. Farrow, Richard B. Sessions, Helen R. Saibil, Anthony R. Clarke, Michael J. Rowan, Dominic M. Walsh, and John Collinge. Interaction between prion protein and toxic amyloid β assemblies can be therapeutically targeted at multiple sites. *Nature communications*, 2:336, 2011.

[201] Laura T. Haas, Mikhail A. Kostylev, and Stephen M. Strittmatter. Therapeutic molecules and endogenous ligands regulate the interaction between brain cellular prion protein (prpc) and metabotropic glutamate receptor 5 (mglur5). *The Journal of biological chemistry*, 289(41):28460–28477, 2014.

[202] Laura T. Haas, Santiago V. Salazar, Mikhail A. Kostylev, Ji Won Um, Adam C. Kaufman, and Stephen M. Strittmatter. Metabotropic glutamate receptor 5 couples cellular prion protein to intracellular signalling in alzheimer's disease. *Brain : a journal of neurology*, 139:526–546, 2016.

[203] Neng-Wei Hu, Andrew J. Nicoll, Dainan Zhang, Alexandra J. Mably, Tiernan O'Malley, Silvia A. Purro, Cassandra Terry, John Collinge, Dominic M. Walsh, and Michael J. Rowan. mglu5 receptors and cellular prion protein mediate amyloid-β-facilitated synaptic long-term depression *in vivo*. *Nature communications*, 5:3374, 2014.

[204] Jo V. Rushworth, Heledd H. Griffiths, Nicole T. Watt, and Nigel M. Hooper. Prion protein-mediated toxicity of amyloid-β oligomers requires lipid rafts and the transmembrane lrp1. *The*

Journal of biological chemistry, 288(13):8935–8951, 2013.

[205] Jennifer N. Rauch, Gabriel Luna, Elmer Guzman, Morgane Audouard, Collin Challis, Youssef E. Sibih, Carolina Leshuk, Israel Hernandez, Susanne Wegmann, Bradley T. Hyman, Viviana Gradinaru, Martin Kampmann, and Kenneth S. Kosik. Lrp1 is a master regulator of tau uptake and spread. *Nature*, 580(7803):381–385, 2020.

[206] Diana G. Ferreira, Mariana Temido-Ferreira, Hugo Vicente Miranda, Vânia L. Batalha, Joana E. Coelho, Éva M. Szegö, In Marques-Morgado, Sandra H. Vaz, Jeong Seop Rhee, Matthias Schmitz, Inga Zerr, Luísa V. Lopes, and Tiago F. Outeiro. α-synuclein interacts with prpc to induce cognitive impairment through mglur5 and nmdar2b. *Nature neuroscience*, 20(11):1569–1579, 2017.

[207] Ji Won Um, Haakon B. Nygaard, Jacqueline K. Heiss, Mikhail A. Kostylev, Massimiliano Stagi, Alexander Vortmeyer, Thomas Wisniewski, Erik C. Gunther, and Stephen M. Strittmatter. Alzheimer amyloid-β oligomer bound to postsynaptic prion protein activates fyn to impair neurons. *Nature neuroscience*, 15(9):1227–1235, 2012.

[208] Chuanzhou Li and Jürgen Götz. Pyk2 is a novel tau tyrosine kinase that is regulated by the tyrosine kinase fyn. *Journal of Alzheimer's disease : JAD*, 64(1):205–221, 2018.

[209] K. Iqbal, F. Liu, C. X. Gong, and I. Grundke-Iqbal. Tau in alzheimer disease and related tauopathies. *Current Alzheimer research*, 7(8):656–664, 2010.

[210] Takayuki Ohnishi, Masako Yanazawa, Tomoya Sasahara, Yasuki Kitamura, Hidekazu Hiroaki, Yugo Fukazawa, Isao Kii, Takashi Nishiyama, Akiyoshi Kakita, Hiroyuki Takeda, Akihide Takeuchi, Yoshie Arai, Akane Ito, Hitomi Komura, Hajime Hirao, Kaori Satomura, Masafumi Inoue, Shin ichi Muramatsu, Ko Matsui, Mari Tada, Michio Sato, Eri Saijo, Yoshiki Shigemitsu, Satoko Sakai, Yoshitaka Umetsu, Natsuko Goda, Naomi Takino, Hitoshi Takahashi, Masatoshi Hagiwara, Tatsuya Sawasaki, Genji Iwasaki, Yu Nakamura, Yo ichi Nabeshima, David B. Teplow, and Minako Hoshi. Na, k-atpase α3 is a death target of alzheimer patient amyloid-β assembly. *Proceedings of the National Academy of Sciences of the United*

States of America, 112(32):E4465–E4474, 2015.

[211] Amulya Nidhi Shrivastava, Virginie Redeker, Nicolas Fritz, Laura Pieri, Leandro G. Almeida, Maria Spolidoro, Thomas Liebmann, Luc Bousset, Marianne Renner, Clément Léna, Anita Aperia, Ronald Melki, and Antoine Triller. α-synuclein assemblies sequester neuronal α3-na+/k+-atpase and impair na+ gradient. *The EMBO journal*, 34(19):2408–2423, 2015.

[212] Harald Hampel, M. M. Mesulam, A. C. Cuello, Martin R. Farlow, Ezio Giacobini, George T. Grossberg, Ara S. Khachaturian, Andrea Vergallo, Enrica Cavedo, Peter J. Snyder, and Zaven S. Khachaturian. The cholinergic system in the pathophysiology and treatment of alzheimer's disease. *Brain : a journal of neurology*, 141(7):1917–1933, 2018.

[213] Martin Sarter and Giovanna Paolone. Deficits in attentional control: cholinergic mechanisms and circuitry-based treatment approaches. *Behavioral neuroscience*, 125(6):825–835, 2011.

[214] Sara V. Maurer and Christina L. Williams. The cholinergic system modulates memory and hippocampal plasticity via its interactions with non-neuronal cells. *Frontiers in Immunology*, 8(1489), 2017.

[215] Dennis A. Burke, Pooneh Heshmati, Ehsan Kholdebarin, and Edward D. Levin. Decreasing nicotinic receptor activity and the spatial learning impairment caused by the nmda glutamate antagonist dizocilpine in rats. *European journal of pharmacology*, 741:132–139, 2014.

[216] Hoau-Yan Wang, Weiwei Li, Nancy J. Benedetti, and Daniel H. S. Lee. α7 nicotinic acetylcholine receptors mediate β-amyloid peptide-induced tau protein phosphorylation. *Journal of Biological Chemistry*, 278(34):31547–31553, 2003.

[217] Robert G. Nagele, Michael R. D'Andrea, H. Lee, Venkateswar Venkataraman, and Hoau-Yan Wang. Astrocytes accumulate aβ42 and give rise to astrocytic amyloid plaques in alzheimer disease brains. *Brain research*, 971(2):197–209, 2003.

[218] Kelly T. Dineley. β-amyloid peptide–nicotinic acetylcholine receptor interaction: the two faces of health and disease. *Frontiers in bioscience : a journal and virtual library*, 12:5030–5038,

Sep 1 2007.

[219] Jianxin Shen and Jie Wu. Nicotinic cholinergic mechanisms in alzheimer's disease. *International review of neurobiology*, 124, 2015.

[220] Jorge J. Palop and Lennart Mucke. Amyloid-β-induced neuronal dysfunction in alzheimer's disease: from synapses toward neural networks. *Nature neuroscience*, 13(7):812–818, 2010.

[221] Y. Liu, D. Wu, F. Song, C. Zhu, Y. Hui, Q. Zhu, J. Wu, W. Fan, and J. Hu. Activation of a7 nicotinic acetylcholine receptors prevents monosodium iodoacetate-induced osteoarthritis in rats. *Cellular Physiology and Biochemistry*, 35(2):627–638, 2015.

[222] Lingling Lu, Chunyan Zhang, Qing Cai, Qiang Lu, Chunli Duan, Yuangang Zhu, and Hui Yang. Voltage-dependent anion channel involved in the α-synuclein-induced dopaminergic neuron toxicity in rats. *Acta Biochimica et Biophysica Sinica*, 45(3):170–178, 2013.

[223] Tatiana K. Rostovtseva, Philip A. Gurnev, Olga Protchenko, David P. Hoogerheide, Thai Leong Yap, Caroline C. Philpott, Jennifer C. Lee, and Sergey M. Bezrukov. α-synuclein shows high affinity interaction with voltage-dependent anion channel, suggesting mechanisms of mitochondrial regulation and toxicity in parkinson disease. *The Journal of biological chemistry*, 290(30):18467–18477, 2015.

[224] Adrian Israelson, Nir Arbel, Sandrine Da Cruz, Hristelina Ilieva, Koji Yamanaka, Varda Shoshan-Barmatz, and Don W. Cleveland. Misfolded mutant sod1 directly inhibits vdac1 conductance in a mouse model of inherited als. *Neuron*, 67(4):575–587, 2010.

[225] Steve Pedrini, Daniela Sau, Stefania Guareschi, Marina Bogush, Robert H. Brown Jr., Nicole Naniche, Azadeh Kia, Davide Trotti, and Piera Pasinelli. Als-linked mutant sod1 damages mitochondria by promoting conformational changes in bcl-2. *Human molecular genetics*, 19(15):2974–2986, 2010.

[226] Francesco Tafuri, Dario Ronchi, Francesca Magri, Giacomo P. Comi, and Stefania Corti. Sod1 misplacing and mitochondrial dysfunction in amyotrophic lateral sclerosis pathogenesis. *Fron-*

tiers in cellular neuroscience, 9:336, 2015.

[227] Wenzhi Tan, Nicole Naniche, Alexey Bogush, Steve Pedrini, Davide Trotti, and Piera Pasinelli. Small peptides against the mutant sod1/bcl-2 toxic mitochondrial complex restore mitochondrial function and cell viability in mutant sod1-mediated als. *The Journal of neuroscience : the official journal of the Society for Neuroscience*, 33(28):11588–11598, 2013.

[228] Maria Damiano, Laurie Galvan, Nicole Déglon, and Emmanuel Brouillet. Mitochondria in huntington's disease. *Biochimica et Biophysica Acta (BBA) - Molecular Basis of Disease*, 1802(1):52–61, 2010.

[229] Yeun Su Choo, Gail V. W. Johnson, Marcy MacDonald, Peter J. Detloff, and Mathieu Lesort. Mutant huntingtin directly increases susceptibility of mitochondria to the calcium-induced permeability transition and cytochrome c release. *Human molecular genetics*, 13(14):1407–1420, 2004.

[230] Emmanuel Brouillet, Françoise Condé, M. F. Beal, and Philippe Hantraye. Replicating huntington's disease phenotype in experimental animals. *Progress in neurobiology*, 59(5):427–468, 1999.

[231] Maria Fouka, Panagiota Mavroeidi, Grigoria Tsaka, and Maria Xilouri. In search of effective treatments targeting α-synuclein toxicity in synucleinopathies: Pros and cons. *Frontiers in cell and developmental biology*, 8:559791, Sep 4 2020.

[232] C. Tuerk and L. Gold. Systematic evolution of ligands by exponential enrichment: Rna ligands to bacteriophage t4 dna polymerase. *Science (New York, N.Y.)*, 249(4968):505–510, Aug 3 1990.

[233] Andrew D. Ellington and Jack W. Szostak. *In vitro* selection of rna molecules that bind specific ligands. *Nature*, 346(6287):818–822, 1990.

[234] Michael Blind and Michael Blank. Aptamer selection technology and recent advances. *Molecular therapy.Nucleic acids*, 4(1):e223, 2015.

[235] Guillermo Aquino-Jarquin and Julia D. Toscano-Garibay. Rna aptamer evolution: two decades of selection. *International Journal of Molecular Sciences*, 12(12):9155–9171, Dec 01, 2011.

[236] J. Zhou and J. Rossi. Aptamers as targeted therapeutics: current potential and challenges. *Nature reviews.Drug discovery*, 16(3):181–202, Mar 2017.

[237] Z. Zhuo, Y. Yu, M. Wang, J. Li, Z. Zhang, J. Liu, X. Wu, A. Lu, G. Zhang, and B. Zhang. Recent advances in selex technology and aptamer applications in biomedicine. *International journal of molecular sciences*, 18(10):10.3390/ijms18102142, Oct 14 2017.

[238] F. Tolle and G. Mayer. Preparation of selex samples for next-generation sequencing, 2016.

[239] H. Kaur, J. G. Bruno, A. Kumar, and T. K. Sharma. Aptamers in the therapeutics and diagnostics pipelines. *Theranostics*, 8(15):4016–4032, Jul 1 2018.

[240] S. I. Hori, A. Herrera, J. J. Rossi, and J. Zhou. Current advances in aptamers for cancer diagnosis and therapy. *Cancers*, 10(1):10.3390/cancers10010009, Jan 3 2018.

[241] Y. Wan, Y. T. Kim, N. Li, S. K. Cho, R. Bachoo, A. D. Ellington, and S. M. Iqbal. Surface-immobilized aptamers for cancer cell isolation and microscopic cytology. *Cancer research*, 70(22):9371–9380, Nov 15 2010.

[242] M. C. Cowperthwaite and A. D. Ellington. Bioinformatic analysis of the contribution of primer sequences to aptamer structures. *Journal of Molecular Evolution*, 67(1):95–102, Jul 2008.

[243] S. Missailidis and A. Hardy. Aptamers as inhibitors of target proteins. *Expert opinion on therapeutic patents*, 19(8):1073–1082, Aug 2009.

[244] E. W. Ng, D. T. Shima, P. Calias, E. T. Cunningham Jr, D. R. Guyer, and A. P. Adamis. Pegaptanib, a targeted anti-vegf aptamer for ocular vascular disease. *Nature reviews.Drug discovery*, 5(2):123–132, Feb 2006.

[245] G. S. Baird. Where are all the aptamers? *American Journal of Clinical Pathology*, 134(4):529–531, Oct 2010.

[246] P. J. Bates, D. A. Laber, D. M. Miller, S. D. Thomas, and J. O. Trent. Discovery and development of the g-rich oligonucleotide as1411 as a novel treatment for cancer. *Experimental and molecular pathology*, 86(3):151–164, Jun 2009.

[247] D. A. Laber, B. S. Taft, G. H. Kloecker, P. J. Bates, J. O. Trent, and D. M. Miller. Extended phase i study of as1411 in renal and non-small cell lung cancers. *JCO*, 24(18):13098, 2006.

[248] Abhijeet Dhiman, Priya Kalra, Vipul Bansal, John G. Bruno, and Tarun Kumar Sharma. Aptamer-based point-of-care diagnostic platforms, 2017.

[249] P. Weerathunge, R. Ramanathan, R. Shukla, T. K. Sharma, and V. Bansal. Aptamer-controlled reversible inhibition of gold nanozyme activity for pesticide sensing. *Analytical Chemistry*, 86(24):11937–11941, Dec 16 2014.

[250] J. Qu, S. Yu, Y. Zheng, Y. Zheng, H. Yang, and J. Zhang. Aptamer and its applications in neurodegenerative diseases. *Cellular and molecular life sciences : CMLS*, 74(4):683–695, Feb 2017.

[251] A. Bouvier-Muller and F. Duconge. Nucleic acid aptamers for neurodegenerative diseases. *Biochimie*, 145:73–83, Feb 2018.

[252] O. Wolter and G. Mayer. Aptamers as valuable molecular tools in neurosciences. *The Journal of neuroscience : the official journal of the Society for Neuroscience*, 37(10):2517–2523, Mar 8 2017.

[253] F. Ylera, R. Lurz, V. A. Erdmann, and J. P. Furste. Selection of rna aptamers to the alzheimer's disease amyloid peptide. *Biochemical and biophysical research communications*, 290(5):1583–1588, Feb 8 2002.

[254] C. T. Farrar, C. M. William, E. Hudry, T. Hashimoto, and B. T. Hyman. Rna aptamer probes as optical imaging agents for the detection of amyloid plaques. *PloS one*, 9(2):e89901, Feb 26 2014.

[255] S. Weiss, D. Proske, M. Neumann, M. H. Groschup, H. A. Kretzschmar, M. Famulok, and E. L.

Winnacker. Rna aptamers specifically interact with the prion protein prp. *Journal of virology*, 71(11):8790–8797, Nov 1997.

[256] T. Takahashi, K. Tada, and H. Mihara. Rna aptamers selected against amyloid β-peptide (aβ) inhibit the aggregation of aβ. *Molecular bioSystems*, 5(9):986–991, Sep 2009.

[257] J. H. Kim, E. Kim, W. H. Choi, J. Lee, J. H. Lee, H. Lee, D. E. Kim, Y. H. Suh, and M. J. Lee. Inhibitory rna aptamers of tau oligomerization and their neuroprotective roles against proteotoxic stress. *Molecular pharmaceutics*, 13(6):2039–2048, Jun 6 2016.

[258] D. Proske, S. Gilch, F. Wopfner, H. M. Schatzl, E. L. Winnacker, and M. Famulok. Prion-protein-specific aptamer reduces prpsc formation. *Chembiochem : a European journal of chemical biology*, 3(8):717–725, Aug 2 2002.

[259] Y. Zheng, J. Qu, F. Xue, Y. Zheng, B. Yang, Y. Chang, H. Yang, and J. Zhang. Novel dna aptamers for parkinson's disease treatment inhibit alpha-synuclein aggregation and facilitate its degradation. *Molecular therapy.Nucleic acids*, 11:228–242, Jun 1 2018.

[260] K. Tsukakoshi, K. Abe, K. Sode, and K. Ikebukuro. Selection of dna aptamers that recognize alpha-synuclein oligomers using a competitive screening method. *Analytical Chemistry*, 84(13):5542–5547, Jul 3 2012.

[261] K. Tsukakoshi, R. Harada, K. Sode, and K. Ikebukuro. Screening of dna aptamer which binds to alpha-synuclein. *Biotechnology Letters*, 32(5):643–648, May 2010.

[262] M. Gonzalez Garcia. *Assessing The Neuroprotective Potential Of A DNA Aptamer Against Alpha-Synuclein*. Imperial College London, 2019.

[263] K. K. Pulicherla and M. K. Verma. Targeting therapeutics across the blood brain barrier (bbb), prerequisite towards thrombolytic therapy for cerebrovascular disorders-an overview and advancements. *AAPS PharmSciTech*, 16(2):223–233, Apr 2015.

[264] W. M. Pardridge. Blood-brain barrier biology and methodology. *Journal of neurovirology*, 5(6):556–569, Dec 1999.

[265] C. Cheng, Y. H. Chen, K. A. Lennox, M. A. Behlke, and B. L. Davidson. *In vivo* selex for identification of brain-penetrating aptamers. *Molecular therapy.Nucleic acids*, 2:e67, Jan 8 2013.

[266] J. M. Healy, S. D. Lewis, M. Kurz, R. M. Boomer, K. M. Thompson, C. Wilson, and T. G. McCauley. Pharmacokinetics and biodistribution of novel aptamer compositions. *Pharmaceutical research*, 21(12):2234–2246, Dec 2004.

[267] Melvin M. Evers, Lodewijk J. A. Toonen, and Willeke M. C. van Roon-Mom. Antisense oligonucleotides in therapy for neurodegenerative disorders, 2015.

[268] H. J. Lee, R. J. Boado, D. A. Braasch, D. R. Corey, and W. M. Pardridge. Imaging gene expression in the brain *in vivo* in a transgenic mouse model of huntington's disease with an antisense radiopharmaceutical and drug-targeting technology. *Journal of nuclear medicine : official publication, Society of Nuclear Medicine*, 43(7):948–956, Jul 2002.

[269] S. Kozlu, S. Caban, F. Yerlikaya, E. Fernandez-Megia, R. Novoa-Carballal, R. Riguera, M. Yemisci, Y. Gursoy-Ozdemir, T. Dalkara, P. Couvreur, and Y. Capan. An aquaporin 4 antisense oligonucleotide loaded, brain targeted nanoparticulate system design. *Die Pharmazie*, 69(5):340–345, May 2014.

[270] G. McClorey and S. Banerjee. Cell-penetrating peptides to enhance delivery of oligonucleotide-based therapeutics. *Biomedicines*, 6(2):51. doi: 10.3390/biomedicines6020051. eCollection 2018 Jun, May 5 2018.

[271] J. R. Kanwar, B. Sriramoju, and R. K. Kanwar. Neurological disorders and therapeutics targeted to surmount the blood-brain barrier. *International journal of nanomedicine*, 7:3259–3278, 2012.

[272] L. Du, R. Kayali, C. Bertoni, F. Fike, H. Hu, P. L. Iversen, and R. A. Gatti. Arginine-rich cell-penetrating peptide dramatically enhances amo-mediated atm aberrant splicing correction and enables delivery to brain and cerebellum. *Human molecular genetics*, 20(16):3151–3160, Aug 15 2011.

[273] S. Zeniya, H. Kuwahara, K. Daizo, A. Watari, M. Kondoh, K. Yoshida-Tanaka, H. Kaburagi, K. Asada, T. Nagata, M. Nagahama, K. Yagi, and T. Yokota. Angubindin-1 opens the blood-brain barrier *in vivo* for delivery of antisense oligonucleotide to the central nervous system. *Journal of controlled release : official journal of the Controlled Release Society*, 283:126–134, Aug 10 2018.

[274] S. I. Rapoport. Advances in osmotic opening of the blood-brain barrier to enhance cns chemotherapy. *Expert opinion on investigational drugs*, 10(10):1809–1818, Oct 2001.

[275] Guillaume van Niel, Gisela D'Angelo, and Graça Raposo. Shedding light on the cell biology of extracellular vesicles. *Nature reviews.Molecular cell biology*, 19(4):213–228, Apr 2018.

[276] Andrew F. Hill. Extracellular vesicles and neurodegenerative diseases. *The Journal of neuroscience : the official journal of the Society for Neuroscience*, 39(47):9269–9273, Nov 20 2019.

[277] Natasha Vassileff, Lesley Cheng, and Andrew F. Hill. Extracellular vesicles - propagators of neuropathology and sources of potential biomarkers and therapeutics for neurodegenerative diseases. *Journal of cell science*, 133(23):jcs243139. doi: 10.1242/jcs.243139, Dec 11 2020.

[278] Xiaoxi Ren, Yun Zhao, Fenqin Xue, Yan Zheng, Haixia Huang, Wei Wang, Yongchang Chang, Hui Yang, and Jianliang Zhang. Exosomal dna aptamer targeting α-synuclein aggregates reduced neuropathological deficits in a mouse parkinson's disease model. *Molecular therapy.Nucleic acids*, 17:726–740, Sep 6 2019.

[279] Christopher M. Dobson. Principles of protein folding, misfolding and aggregation. *Seminars in cell & developmental biology*, 15(1):3–16, Feb 01, 2004.

[280] Fabrizio Chiti and Christopher M. Dobson. Protein misfolding, functional amyloid, and human disease. *Annual review of biochemistry*, 75(1):333–366, Jan 01, 2006.

[281] Serene W. Chen, Srdja Drakulic, Emma Deas, Myriam Ouberai, Francesco A. Aprile, Rocío Arranz, Samuel Ness, Cintia Roodveldt, Tim Guilliams, Erwin De-Genst, David Klenerman,

Nicholas W. Wood, Tuomas P. J. Knowles, Carlos Alfonso, Germán Rivas, Andrey Y. Abramov, José María Valpuesta, Christopher M. Dobson, and Nunilo Cremades. Structural characterization of toxic oligomers that are kinetically trapped during α-synuclein fibril formation. *Proceedings of the National Academy of Sciences*, 112(16):E1994, 2015.

[282] James E. Galvin, Kunihiro Uryu, Virginia M.-Y. Lee, and John Q. Trojanowski. Axon pathology in parkinson's disease and lewy body dementia hippocampus contains α-, β-, and γ-synuclein. *Proceedings of the National Academy of Sciences - PNAS*, 96(23):13450–13455, Nov 09, 1999.

[283] Gina M. Moriarty, Conceiç ao A. S. A. Minetti, David P. Remeta, and Jean Baum. A revised picture of the cu(ii)α-synuclein complex: The role of n-terminal acetylation. *Biochemistry (Easton)*, 53(17):2815–2817, May 06, 2014.

[284] Andres Binolfi, Ariel A. Valiente-Gabioud, Rosario Duran, Markus Zweckstetter, Christian Griesinger, and Claudio O. Fernandez. Exploring the structural details of cu(i) binding to α-synuclein by nmr spectroscopy. *Journal of the American Chemical Society*, 133(2):194–196, Jan 19, 2011.

[285] Marco C. Miotto, Esaú E. Rodriguez, Ariel A. Valiente-Gabioud, Valentina Torres-Monserrat, Andrés Binolfi, Liliana Quintanar, Markus Zweckstetter, Christian Griesinger, and Claudio O. Fernández. Site-specific copper-catalyzed oxidation of α-synuclein: Tightening the link between metal binding and protein oxidative damage in parkinson's disease. *Inorganic chemistry*, 53(9):4350–4358, May 05, 2014.

[286] Wolfgang Bermel, Ivano Bertini, Veronika Csizmok, Isabella C. Felli, Roberta Pierattelli, and Peter Tompa. H-start for exclusively heteronuclear nmr spectroscopy: The case of intrinsically disordered proteins. *Journal of magnetic resonance (1997)*, 198(2):275–281, Jun 01, 2009.

[287] Vladimir N. Uversky, Jie Li, Pierre Souillac, Ian S. Millett, Sebastian Doniach, Ross Jakes, Michel Goedert, and Anthony L. Fink. Biophysical properties of the synucleins and their propensities to fibrillate. *The Journal of biological chemistry*, 277(14):11970–11978, Apr 05,

2002.

[288] Amberley D. Stephens, Maria Zacharopoulou, and Gabriele S. Kaminski Schierle. The cellular environment affects monomeric α-synuclein structure. *Trends in biochemical sciences (Amsterdam. Regular ed.)*, 44(5):453–466, May 2019.

[289] Kseniia Afitska, Anna Fucikova, Volodymyr V. Shvadchak, and Dmytro A. Yushchenko. Modification of c terminus provides new insights into the mechanism of α-synuclein aggregation. *Biophysical journal*, 113(10):2182–2191, Nov 21, 2017.

[290] Nataša Poklar Ulrih, Christopher H. Barry, and Anthony L. Fink. Impact of tyr to ala mutations on α-synuclein fibrillation and structural properties. *Biochimica et Biophysica Acta (BBA) - Molecular Basis of Disease*, 1782(10):581–585, Oct 01, 2008.

[291] Natalie Landeck, Katherine E. Strathearn, Daniel Ysselstein, Kerstin Buck, Sayan Dutta, Siddhartha Banerjee, Zhengjian Lv, John D. Hulleman, Jagadish Hindupur, Li-Kai Lin, Sonal Padalkar, Lia A. Stanciu, Yuri L. Lyubchenko, Deniz Kirik, and Jean-Christophe Rochet. Two c-terminal sequence variations determine differential neurotoxicity between human and mouse α-synuclein. *Molecular neurodegeneration*, 15(1):1–49, Sep 08, 2020.

[292] Anne-Laure Mahul-Mellier, Firat Altay Melek, Johannes Burtscher, Niran Maharjan, Nadine Ait-Bouziad, Anass Chiki, Siv Vingill, Richard Wade-Martins, Janice Holton, Catherine Strand, Caroline Haikal, Jia-Yi Li, Romain Hamelin, Marie Croisier, Graham Knott, Georges Mairet-Coello, Laura Weerens, Anne Michel, Patrick Downey, Martin Citron, and Hilal A. Lashuel. The making of a lewy body: the role of α-synuclein post-fibrillization modifications in regulating the formation and the maturation of pathological inclusions. *bioRxiv*, page 500058, 2018.

[293] M. Goedert. Alpha-synuclein and neurodegenerative diseases. *Nature reviews.Neuroscience*, 2(7):492–501, Jul 2001.

[294] Ian Martin, Valina L. Dawson, and Ted M. Dawson. Recent advances in the genetics of parkinson's disease. *Annual review of genomics and human genetics*, 12(1):301–325, Jan 01, 2011.

[295] Makoto Hashimoto, Kohichi Kawahara, Pazit Bar-On, Edward Rockenstein, Leslie Crews, and Eliezer Masliah. The role of α-synuclein assembly and metabolism in the pathogenesis of lewy body disease. *Journal of molecular neuroscience*, 24(3):343–352, Jan 01, 2004.

[296] E. Masliah, E. Rockenstein, I. Veinbergs, M. Mallory, M. Hashimoto, A. Takeda, Y. Sagara, A. Sisk, and L. Mucke. Dopaminergic loss and inclusion body formation in alpha-synuclein mice: implications for neurodegenerative disorders. *Science (New York, N.Y.)*, 287(5456):1265–1269, Feb 18 2000.

[297] Shusei Hamamichi, Renee N. Rivas, Adam L. Knight, Songsong Cao, Kim A. Caldwell, and Guy A. Caldwell. Hypothesis-based rnai screening identifies neuroprotective genes in a parkinson's disease model. *Proceedings of the National Academy of Sciences - PNAS*, 105(2):728–733, Jan 15, 2008.

[298] Shawn C. Burdette and Stephen J. Lippard. Meeting of the minds: Metalloneurochemistry. *Proceedings of the National Academy of Sciences*, 100(7):3605–3610, 2003.

[299] Richard W. Strange, Michael A. Hough, Svetlana V. Antonyuk, and S. Samar Hasnain. Structural evidence for a copper-bound carbonate intermediate in the peroxidase and dismutase activities of superoxide dismutase. *PLoS ONE*, 7(9):e44811, Sep 11, 2012.

[300] Anthony L. Fink. The aggregation and fibrillation of alpha-synuclein. *Accounts of Chemical Research*, 39(9):628–634, Sep 2006.

[301] A. I. Bush. Metals and neuroscience. *Current opinion in chemical biology*, 4(2):184–191, Apr 2000.

[302] Geir Bjorklund, Vera Stejskal, Mauricio A. Urbina, Maryam Dadar, Salvatore Chirumbolo, and Joachim Mutter. Metals and parkinson's disease: Mechanisms and biochemical processes. *Current medicinal chemistry*, 25(19):2198–2214, 2018.

[303] Jan Aaseth, Petr Dusek, and Per M. Roos. Prevention of progression in parkinson's disease. *Biometals*, 31(5):737–747, Oct 01, 2018.

[304] Emma Deas, Nunilo Cremades, Plamena R. Angelova, Marthe H. R. Ludtmann, Zhi Yao, Serene Chen, Mathew H. Horrocks, Blerida Banushi, Daniel Little, Michael J. Devine, Paul Gissen, David Klenerman, Christopher M. Dobson, Nicholas W. Wood, Sonia Gandhi, and Andrey Y. Abramov. Alpha-synuclein oligomers interact with metal ions to induce oxidative stress and neuronal death in parkinson's disease. *Antioxidants & redox signaling*, 24(7):376–391, Mar 1 2016.

[305] Andrés Binolfi, Liliana Quintanar, Carlos W. Bertoncini, Christian Griesinger, and Claudio O. Fernández. Bioinorganic chemistry of copper coordination to alpha-synuclein: Relevance to parkinson's disease. *Coordination chemistry reviews*, 256(19-20):2188–2201, Oct 2012.

[306] Andrés Binolfi, Esaú E. Rodriguez, Daniela Valensin, Nicola D'Amelio, Emiliano Ippoliti, Gonzalo Obal, Rosario Duran, Alessandra Magistrato, Otto Pritsch, Markus Zweckstetter, Gianni Valensin, Paolo Carloni, Liliana Quintanar, Christian Griesinger, and Claudio O. Fernández. Bioinorganic chemistry of parkinson's disease: structural determinants for the copper-mediated amyloid formation of alpha-synuclein. *Inorganic chemistry*, 49(22):10668–10679, Nov 15 2010.

[307] Elena Gaggelli, Henryk Kozlowski, Daniela Valensin, and Gianni Valensin. Copper homeostasis and neurodegenerative disorders (alzheimer's, prion, and parkinson's diseases and amyotrophic lateral sclerosis). *Chemical reviews*, 106(6):1995–2044, Jun 01, 2006.

[308] Henryk Kozłowski, David R. Brown, and Gianni Valensin. *Parkinson's Disease: Any Role for Metals*, pages 201 – 222. Metallochemistry of Neurodegeneration. The Royal Society of Chemistry, 2006.

[309] Ariel A. Valiente-Gabioud, Valentina Torres-Monserrat, Laura Molina-Rubino, Andres Binolfi, Christian Griesinger, and Claudio O. Fernández. Structural basis behind the interaction of zn2+ with the protein α-synuclein and the aβ peptide: A comparative analysis. *Journal of inorganic biochemistry*, 117:334–341, Dec 2012.

[310] D. T. Dexter, A. Carayon, F. Javoy-Agid, Y. Agid, F. R. Wells, S. E. Daniel, A. J. Lees, P. Jen-

ner, and C. D. Marsden. Alterations in the levels of iron, ferritin and other trace metals in parkinson's disease and other neurodegenerative diseases affecting the basal ganglia. *Brain : a journal of neurology*, 114 (Pt 4)(Pt 4):1953–1975, Aug 1991.

[311] Peter Riederer, Emin Sofic, Wolf-Dieter Rausch, Bruno Schmidt, Gavin P. Reynolds, Kurt Jellinger, and Moussa B. H. Youdim. Transition metals, ferritin, glutathione, and ascorbic acid in parkinsonian brains. *Journal of neurochemistry*, 52(2):515–520, Feb 1989.

[312] D. T. Dexter, F. R. Wells, A. J. Lee, F. Agid, Y. Agid, P. Jenner, and C. D. Marsden. Increased nigral iron content and alterations in other metal ions occurring in brain in parkinson's disease. *Journal of neurochemistry*, 52(6):1830–1836, Jun 1989.

[313] Leonid Breydo and Vladimir N. Uversky. Role of metal ions in aggregation of intrinsically disordered proteins in neurodegenerative diseases. *Metallomics : integrated biometal science*, 3(11):1163–1180, Nov 2011.

[314] R. J. Castellani, S. L. Siedlak, G. Perry, and M. A. Smith. Sequestration of iron by lewy bodies in parkinson's disease. *Acta Neuropathologica*, 100(2):111–114, Aug 2000.

[315] Bronwen Gardner, Birger V. Dieriks, Steve Cameron, Lakshini H. S. Mendis, Clinton Turner, Richard L. M. Faull, and Maurice A. Curtis. Metal concentrations and distributions in the human olfactory bulb in parkinson's disease, -09-05 2017.

[316] H. S. Pall, A. C. Williams, D. R. Blake, J. Lunec, J. M. Gutteridge, M. Hall, and A. Taylor. Raised cerebrospinal-fluid copper concentration in parkinson's disease. *Lancet (London, England)*, 2(8553):238–241, Aug 1 1987.

[317] J. M. Gorell, B. A. Rybicki, C. Cole Johnson, and E. L. Peterson. Occupational metal exposures and the risk of parkinson's disease. *Neuroepidemiology*, 18(6):303–308, 1999.

[318] Emma Lorentzon, Ranjeet Kumar, Istvan Horvath, and Pernilla Wittung-Stafshede. Differential effects of cu(2+) and fe(3+) ions on in vitro amyloid formation of biologically-relevant α-synuclein variants. *Biometals : an international journal on the role of metal ions in biology,*

biochemistry, and medicine, 33(2-3):97–106, Jun 2020.

[319] Sergio Montes, Susana Rivera-Mancia, Araceli Diaz-Ruiz, Luis Tristan-Lopez, and Camilo Rios. Copper and copper proteins in parkinson's disease. *Oxidative Medicine and Cellular Longevity*, 2014:147251–15, Jan 01, 2014.

[320] Katherine M. Davies, Julian F. B. Mercer, Nicholas Chen, and Kay L. Double. Copper dyshomoeostasis in parkinson's disease: implications for pathogenesis and indications for novel therapeutics. *Clinical science (London, England : 1979)*, 130(8):565–574, Apr 2016.

[321] Emma Lorentzon, Ranjeet Kumar, Istvan Horvath, and Pernilla Wittung-Stafshede. Differential effects of cu(2+) and fe(3+) ions on *in vitro* amyloid formation of biologically-relevant α-synuclein variants. *Biometals : an international journal on the role of metal ions in biology, biochemistry, and medicine*, 33(2-3):97–106, Jun 2020.

[322] Hangyu Zhang, Amy Griggs, Jean-Christophe Rochet, and Lia A Stanciu. *In vitro* study of α-synuclein protofibrils by cryo-em suggests a cu^{2+}-dependent aggregation pathway. *Biophysical Journal*, 104(12):2706–2713, Jun 18, 2013.

[323] Mark J. Hokenson, Vladimir N. Uversky, John Goers, Ghiam Yamin, Larissa A. Munishkina, and Anthony L. Fink. Role of individual methionines in the fibrillation of methionine-oxidized alpha-synuclein. *Biochemistry*, 43(15):4621–4633, Apr 20 2004.

[324] Claire André, Tong T. Truong, Jean Francois Robert, and Yves C. Guillaume. Effect of metals on herbicides-alpha-synuclein association: a possible factor in neurodegenerative disease studied by capillary electrophoresis. *Electrophoresis*, 26(17):3256–3264, Sep 2005.

[325] Thomas D. Kim, Seung R. Paik, Chul-Hak Yang, and Jongsun Kim. Structural changes in α-synuclein affect its chaperone-like activity *in vitro*. *Protein science*, 9(12):2489–2496, Dec 01, 2000.

[326] Ghiam Yamin, Charles B. Glaser, Vladimir N. Uversky, and Anthony L. Fink. Certain metals trigger fibrillation of methionine-oxidized α-synuclein. *The Journal of biological chemistry*,

278(30):27630, Jul 25, 2003.

[327] Rodolfo M. Rasia, Carlos W. Bertoncini, Derek Marsh, Wolfgang Hoyer, Dmitry Cherny, Markus Zweckstetter, Christian Griesinger, Thomas M. Jovin, Claudio O. Fernández, and Harry B. Gray. Structural characterization of copper(ii) binding to α-synuclein: Insights into the bioinorganic chemistry of parkinson's disease. *Proceedings of the National Academy of Sciences - PNAS*, 102(12):4294–4299, Mar 22, 2005.

[328] Andrés Binolfi, Rodolfo M. Rasia, Carlos W. Bertoncini, Marcelo Ceolin, Markus Zweckstetter, Christian Griesinger, Thomas M. Jovin, and Claudio O. Fernández. Interaction of alpha-synuclein with divalent metal ions reveals key differences: a link between structure, binding specificity and fibrillation enhancement. *Journal of the American Chemical Society*, 128(30):9893–9901, Aug 2 2006.

[329] Robert Bussell and David Eliezer. Residual structure and dynamics in parkinson's disease-associated mutants of α-synuclein. *The Journal of biological chemistry*, 276(49):45996–46003, Dec 07, 2001.

[330] Ivo F. Scheiber, Julian F. B. Mercer, and Ralf Dringen. Metabolism and functions of copper in brain. *Progress in neurobiology*, 116:33–57, May 01, 2014.

[331] Valerie L. Anderson, Trudy F. Ramlall, Carla C. Rospigliosi, Watt W. Webb, and David Eliezer. Identification of a helical intermediate in trifluoroethanol-induced alpha-synuclein aggregation. *Proceedings of the National Academy of Sciences of the United States of America*, 107(44):18850–18855, Nov 2 2010.

[332] Dhiman Ghosh, Pradeep K. Singh, Shruti Sahay, Narendra Nath Jha, Reeba S. Jacob, Shamik Sen, Ashutosh Kumar, Roland Riek, and Samir K. Maji. Structure based aggregation studies reveal the presence of helix-rich intermediate during α-synuclein aggregation. *Scientific reports*, 5:9228, Mar 18 2015.

[333] Maya Schushan, Yariv Barkan, Turkan Haliloglu, and Nir Ben-Tal. C(alpha)-trace model of the transmembrane domain of human copper transporter 1, motion and functional implica-

tions. *Proceedings of the National Academy of Sciences of the United States of America*, 107(24):10908–10913, Jun 15 2010.

[334] Eleonora Carboni and Paul Lingor. Insights on the interaction of alpha-synuclein and metals in the pathophysiology of parkinson's disease. *Metallomics : integrated biometal science*, 7(3):395–404, Mar 2015.

[335] Heather R. Lucas, Serena DeBeer, Myoung-Soon Hong, and Jennifer C. Lee. Evidence for copper-dioxygen reactivity during α-synuclein fibril formation. *Journal of the American Chemical Society*, 132(19):6636–6637, May 19, 2010.

[336] Manish K. Tiwari, Fabian Leinisch, Cagla Sahin, Ian Max Møller, Daniel E. Otzen, Michael J. Davies, and Morten J. Bjerrum. Early events in copper-ion catalyzed oxidation of α-synuclein. *Free radical biology & medicine*, 121:38–50, Jun 2018.

[337] Dinendra L. Abeyawardhane, Ricardo D. Fernández, Denver R. Heitger, Madeleine K. Crozier, Julia C. Wolver, and Heather R. Lucas. Copper induced radical dimerization of α-synuclein requires histidine. *Journal of the American Chemical Society*, 140(49):17086–17094, Dec 12, 2018.

[338] Hemi Dimant, Darius Ebrahimi-Fakhari, and Pamela J. McLean. Molecular chaperones and co-chaperones in parkinson disease. *The Neuroscientist : a review journal bringing neurobiology, neurology and psychiatry*, 18(6):589–601, Dec 2012.

[339] Vera Dias, Eunsung Junn, and M. Maral Mouradian. The role of oxidative stress in parkinson's disease. *Journal of Parkinson's disease*, 3(4):461–491, 2013.

[340] Michelle Smeyne and Richard Jay Smeyne. Glutathione metabolism and parkinson's disease. *Free radical biology & medicine*, 62:13–25, Sep 01, 2013.

[341] Mark P. Mattson. Calcium and neurodegeneration. *Aging cell*, 6(3):337–350, Jun 2007.

[342] Philippe Marambaud, Ute Dreses-Werringloer, and Valérie Vingtdeux. Calcium signaling in neurodegeneration. *Molecular Neurodegeneration*, 4(1):20, May 06, 2009.

[343] G. Schaafsma. *Calcium in Extracellular Fluid: Homeostasis*, pages 241–259. Calcium in Human Biology. Springer London, London, 1988.

[344] R. C. Foehring, X. F. Zhang, J. C. F. Lee, and J. C. Callaway. Endogenous calcium buffering capacity of substantia nigral dopamine neurons. *Journal of neurophysiology*, 102(4):2326–2333, Oct 2009.

[345] D. C. German, K. F. Manaye, P. K. Sonsalla, and B. A. Brooks. Midbrain dopaminergic cell loss in parkinson's disease and mptp-induced parkinsonism: sparing of calbindin-d28k-containing cells. *Annals of the New York Academy of Sciences*, 648:42–62, May 11 1992.

[346] Marisa Brini, Tito Calì, Denis Ottolini, and Ernesto Carafoli. Neuronal calcium signaling: function and dysfunction. *Cellular and molecular life sciences : CMLS*, 71(15):2787–2814, Aug 01, 2014.

[347] M. L. Michaelis, D. J. Bigelow, C. Schöneich, T. D. Williams, L. Ramonda, D. Yin, A. F. Hühmer, Y. Yao, J. Gao, and T. C. Squier. Decreased plasma membrane calcium transport activity in aging brain. *Life Sciences*, 59(5-6):405–412, 1996.

[348] S. P. Duckles, H. Tsai, and J. N. Buchholz. Evidence for decline in intracellular calcium buffering in adrenergic nerves of aged rats. *Life Sciences*, 58(22):2029–2035, 1996.

[349] Lidia Reznichenko, Qun Cheng, Krystal Nizar, Sergey L. Gratiy, Payam A. Saisan, Edward M. Rockenstein, Tanya González, Christina Patrick, Brian Spencer, Paula Desplats, Anders M. Dale, Anna Devor, and Eliezer Masliah. *In vivo* alterations in calcium buffering capacity in transgenic mouse model of synucleinopathy. *The Journal of neuroscience*, 32(29):9992–9998, Jul 18, 2012.

[350] Y. Kimula, M. Utsuyama, M. Yoshimura, and M. Tomonaga. Element analysis of lewy and adrenal bodies in parkinson's disease by electron probe microanalysis. *Acta Neuropathologica*, 59(3):233–236, 1983.

[351] Jordan Follett, Bonnie Darlow, Mathew B. Wong, Jacob Goodwin, and Dean L. Pountney.

Potassium depolarization and raised calcium induces α-synuclein aggregates. *Neurotoxicity research*, 23(4):378–392, May 01, 2013.

[352] S. Nath, J. Goodwin, Y. Engelborghs, and D. L. Pountney. Raised calcium promotes α-synuclein aggregate formation. *Molecular and cellular neurosciences*, 46(2):516–526, Feb 2011.

[353] Rachel Lowe, Dean L. Pountney, Poul Henning Jensen, Wei Ping Gai, and Nicolas H. Voelcker. Calcium(ii) selectively induces α-synuclein annular oligomers via interaction with the c-terminal domain. *Protein science*, 13(12):3245–3252, Dec 2004.

[354] Alex Rcom-H'cheo-Gauthier, Jacob Goodwin, and Dean L. Pountney. Interactions between calcium and alpha-synuclein in neurodegeneration. *Biomolecules*, 4(3):795–811, Aug 14, 2014.

[355] Agata Adamczyk and Joanna B. Strosznajder. Alpha-synuclein potentiates ca2+ influx through voltage-dependent ca2+ channels. *Neuroreport*, 17(18):1883–1886, Dec 18 2006.

[356] S. Büttner, L. Faes, W. N. Reichelt, F. Broeskamp, L. Habernig, S. Benke, N. Kourtis, D. Ruli, D. Carmona-Gutierrez, T. Eisenberg, P. D'hooge, R. Ghillebert, V. Franssens, A. Harger, T. R. Pieber, P. Freudenberger, G. Kroemer, S. J. Sigrist, J. Winderickx, G. Callewaert, N. Tavernarakis, and F. Madeo. The ca2+/mn2+ ion-pump pmr1 links elevation of cytosolic ca2+ levels to α-synuclein toxicity in parkinson's disease models. *CELL DEATH AND DIFFERENTIATION*, 20(3):465–477, Nov 16, 2012.

[357] Geert Callewaert, Petra D'hooge, Tien-Yang Ma, Mara Del Vecchio, Vincent Van Eyck, Vanessa Franssens, and Joris Winderickx. Decreased vacuolar ca(2+) storage and disrupted vesicle trafficking underlie alpha-synuclein-induced ca(2+) dysregulation in s. cerevisiae. *Frontiers in genetics*, 11:266, May 8 2020.

[358] Nishani T. Hettiarachchi, Andrew Parker, Mark L. Dallas, Kyla Pennington, Chao-Chun Hung, Hugh A. Pearson, John P. Boyle, Philip Robinson, and Chris Peers. α-synuclein modulation of ca2+ signaling in human neuroblastoma (sh-sy5y) cells. *Journal of neurochemistry*,

111(5):1192–1201, Dec 2009.

[359] Cristine Betzer, Louise Berkhoudt Lassen, Anders Olsen, Rikke Hahn Kofoed, Lasse Reimer, Emil Gregersen, Jin Zheng, Tito Calì, Wei-ping Gai, Tong Chen, Arne Moeller, Marisa Brini, Yuhong Fu, Glenda Halliday, Tomasz Brudek, Susana Aznar, Bente Pakkenberg, Jens Peter Andersen, and Poul Henning Jensen. Alpha-synuclein aggregates activate calcium pump serca leading to calcium dysregulation, -03-29 2018.

[360] Gabriela Caraveo, Pavan K. Auluck, Luke Whitesell, Chee Yeun Chung, Valeriya Baru, Eugene V. Mosharov, Xiaohui Yan, Manu Ben-Johny, Martin Soste, Paola Picotti, Hanna Kim, Kim A. Caldwell, Guy A. Caldwell, David Sulzer, David T. Yue, and Susan Lindquist. Calcineurin determines toxic versus beneficial responses to α-synuclein. *Proceedings of the National Academy of Sciences - PNAS*, 111(34):E3544–E3552, Aug 26, 2014.

[361] Ori J. Lieberman, Se Joon Choi, Ellen Kanter, Anastasia Saverchenko, Micah D. Frier, Giulia M. Fiore, Min Wu, Jyothisri Kondapalli, Enrico Zampese, D. James Surmeier, David Sulzer, and Eugene V. Mosharov. α-synuclein-dependent calcium entry underlies differential sensitivity of cultured sn and vta dopaminergic neurons to a parkinsonian neurotoxin, -11 2017.

[362] J. Goodwin, S. Nath, Y. Engelborghs, and D. L. Pountney. Raised calcium and oxidative stress cooperatively promote alpha-synuclein aggregate formation. *Neurochemistry international*, 62(5):703–711, Apr 2013.

[363] Shiori Tamamizu-Kato, Malathi G. Kosaraju, Hiroyuki Kato, Vincent Raussens, Jean-Marie Ruysschaert, and Vasanthy Narayanaswami. Calcium-triggered membrane interaction of the α-synuclein acidic tail. *Biochemistry (Easton)*, 45(36):10947–10956, Sep 12, 2006.

[364] Tiago F. Outeiro, Jochen Klucken, Kathryn Bercury, Julie Tetzlaff, Preeti Putcha, Luis M. A. Oliveira, Alexandre Quintas, Pamela J. McLean, and Bradley T. Hyman. Dopamine-induced conformational changes in alpha-synuclein. *PloS one*, 4(9):e6906, Sep 04, 2009.

[365] K. A. Conway, J. C. Rochet, R. M. Bieganski, and P. T. Jr Lansbury. Kinetic stabilization of the alpha-synuclein protofibril by a dopamine-alpha-synuclein adduct. *Science (New York, N.Y.)*,

294(5545):1346–1349, Nov 9 2001.

[366] Agata Rekas, Robert B. Knott, Anna Sokolova, Kevin J. Barnham, Keyla A. Perez, Colin L. Masters, Simon C. Drew, Roberto Cappai, Cyril C. Curtain, and Chi L. L. Pham. The structure of dopamine induced alpha-synuclein oligomers. *European biophysics journal : EBJ*, 39(10):1407–1419, Sep 2010.

[367] Eugene V. Mosharov, Kristin E. Larsen, Ellen Kanter, Kester A. Phillips, Krystal Wilson, Yvonne Schmitz, David E. Krantz, Kazuto Kobayashi, Robert H. Edwards, and David Sulzer. Interplay between cytosolic dopamine, calcium, and α-synuclein causes selective death of substantia nigra neurons. *Neuron*, 62(2):218–229, Apr 30, 2009.

[368] Wolfgang Oertel and Jörg B. Schulz. Current and experimental treatments of parkinson disease: A guide for neuroscientists, -08-30 2016.

[369] S. A. Schneider, M. Boettner, A. Alexoudi, D. Zorenkov, G. Deuschl, and T. Wedel. Can we use peripheral tissue biopsies to diagnose parkinson's disease? a review of the literature. *European journal of neurology*, 23(2):247–261, Feb 2016.

[370] C. Savio Chan, Jaime N. Guzman, Ema Ilijic, Jeff N. Mercer, Caroline Rick, Tatiana Tkatch, Gloria E. Meredith, and D. James Surmeier. 'rejuvenation' protects neurons in mouse models of parkinson's disease. *Nature*, 447(7148):1081–1086, Jun 28 2007.

[371] Svetlana Lutsenko, Ashima Bhattacharjee, and Ann L. Hubbard. Copper handling machinery of the brain. *Metallomics : integrated biometal science*, 2(9):596–608, Sep 2010.

[372] Edward B. Maryon, Shannon A. Molloy, Adriana M. Zimnicka, and Jack H. Kaplan. Copper entry into human cells: progress and unanswered questions. *Biometals : an international journal on the role of metal ions in biology, biochemistry, and medicine*, 20(3-4):355–364, Jun 2007.

[373] Igor Dikiy and David Eliezer. N-terminal acetylation stabilizes n-terminal helicity in lipid- and micelle-bound α-synuclein and increases its affinity for physiological membranes. *The Journal*

of biological chemistry, 289(6):3652–3665, Feb 07, 2014.

[374] Jianfeng Jiang, Istvan A. Nadas, M. A. Kim, and Katherine J. Franz. A mets motif peptide found in copper transport proteins selectively binds cu(i) with methionine-only coordination. *Inorganic chemistry*, 44(26):9787–9794, 2005.

[375] Jeffrey T. Rubino, Pamela Riggs-Gelasco, and Katherine J. Franz. Methionine motifs of copper transport proteins provide general and flexible thioether-only binding sites for cu(i) and ag(i). *Journal of biological inorganic chemistry*, 15(7):1033–1049, Sep 01, 2010.

[376] Benjamin G. Wilhelm, Sunit Mandad, Sven Truckenbrodt, Katharina Kröhnert, Christina Schäfer, Burkhard Rammner, Seong Joo Koo, Gala A. Claßen, Michael Krauss, Volker Haucke, Henning Urlaub, and Silvio O. Rizzoli. Composition of isolated synaptic boutons reveals the amounts of vesicle trafficking proteins. *Science (New York, N.Y.)*, 344(6187):1023–1028, May 30 2014.

[377] Alexander Hopt, Stefan Korte, Herbert Fink, Ulrich Panne, Reinhard Niessner, Reinhard Jahn, Hans Kretzschmar, and Jochen Herms. Methods for studying synaptosomal copper release, -09 2003.

[378] Annadurai Anandhan, Humberto Rodriguez-Rocha, Iryna Bohovych, Amy M. Griggs, Laura Zavala-Flores, Elsa M. Reyes-Reyes, Javier Seravalli, Lia A. Stanciu, Jaekwon Lee, Jean-Christophe Rochet, Oleh Khalimonchuk, and Rodrigo Franco. Overexpression of alpha-synuclein at non-toxic levels increases dopaminergic cell death induced by copper exposure via modulation of protein degradation pathways. *Neurobiology of disease*, 81:76–92, Sep 01, 2015.

[379] Cecilia Chavarría and José M. Souza. Oxidation and nitration of α-synuclein and their implications in neurodegenerative diseases. *Archives of biochemistry and biophysics*, 533(1-2):25–32, May 01, 2013.

[380] Stefan Schildknecht, Hanne R. Gerding, Christiaan Karreman, Malte Drescher, Hilal A. Lashuel, Tiago F. Outeiro, Donato A. Di Monte, and Marcel Leist. Oxidative and nitrative

alpha-synuclein modifications and proteostatic stress: implications for disease mechanisms and interventions in synucleinopathies, 2013.

[381] Chengshan Wang, Lin Liu, Lin Zhang, Yong Peng, and Feimeng Zhou. Redox reactions of the α-synucleincu^{2+} complex and their effects on neuronal cell viability. *Biochemistry (Easton)*, 49(37):8134–8142, Sep 21, 2010.

[382] Xiaoyan Wang, Dima Moualla, Josephine A. Wright, and David R. Brown. Copper binding regulates intracellular alpha-synuclein localisation, aggregation and toxicity. *Journal of neurochemistry*, 113(3):704–714, May 2010.

[383] P. De Bie, P. Muller, C. Wijmenga, and L. W. J. Klomp. Molecular pathogenesis of wilson and menkes disease: correlation of mutations with molecular defects and disease phenotypes, -08-23 2007.

[384] Nelson B. Cole, Diane D. Murphy, Jacob Lebowitz, Luca Di Noto, Rodney L. Levine, and Robert L. Nussbaum. Metal-catalyzed oxidation of α-synuclein. *The Journal of biological chemistry*, 280(10):9678, Mar 11, 2005.

[385] Wenbo Zhou, Chunmei Long, Stephen H. Reaney, Donato A. Di Monte, Anthony L. Fink, and Vladimir N. Uversky. Methionine oxidation stabilizes non-toxic oligomers of α-synuclein through strengthening the auto-inhibitory intra-molecular long-range interactions. *Biochimica et Biophysica Acta (BBA) - Molecular Basis of Disease*, 1802(3):322–330, Mar 01, 2010.

[386] Vladimir N. Uversky, Ghiam Yamin, Pierre O. Souillac, John Goers, Charles B. Glaser, and Anthony L. Fink. Methionine oxidation inhibits fibrillation of human α-synuclein *in vitro*, -04-05 2002.

[387] Charles B. Glaser, Ghiam Yamin, Vladimir N. Uversky, and Anthony L. Fink. Methionine oxidation, α-synuclein and parkinson's disease. *Biochimica et biophysica acta*, 1703(2):157–169, Jan 17, 2005.

[388] Marta Martinez-Vicente, Zsolt Talloczy, Susmita Kaushik, Ashish C. Massey, Joseph Maz-

zulli, Eugene V. Mosharov, Roberto Hodara, Ross Fredenburg, Du-Chu Wu, Antonia Follenzi, William Dauer, Serge Przedborski, Harry Ischiropoulos, Peter T. Lansbury, David Sulzer, and Ana Maria Cuervo. Dopamine-modified α-synuclein blocks chaperone-mediated autophagy. *The Journal of clinical investigation*, 118(2):777–788, Feb 01, 2008.

[389] Alexander S. Maltsev, Jue Chen, Rodney L. Levine, and Ad Bax. Site-specific interaction between α-synuclein and membranes probed by nmr-observed methionine oxidation rates. *Journal of the American Chemical Society*, 135(8):2943–2946, Feb 27, 2013.

[390] Omid Tavassoly, Sergiy Nokhrin, Oleg Y. Dmitriev, and Jeremy S. Lee. Cu(ii) and dopamine bind to α-synuclein and cause large conformational changes. *The FEBS journal*, 281(12):2738–2753, Jun 2014.

[391] Yonghwang Ha, Aerin Yang, Seyoung Lee, Kibong Kim, Hyunjeong Liew, Sang Hyung Lee, Ju Eun Lee, Hong-In Lee, Yoo-Hun Suh, Hee-Sung Park, and David G. Churchill. Dopamine and cu+/2+ can induce oligomerization of α-synuclein in the absence of oxygen: Two types of oligomerization mechanisms for α-synuclein and related cell toxicity studies. *Journal of neuroscience research*, 92(3):359–368, Mar 2014.

[392] M. Orlova. Role of zinc in an organism and its influence on processes leading to apoptosis. *British journal of medicine and medical research*, 1(4):239–305, Jan 10, 2011.

[393] Małgorzata Tyszka-Czochara, Agata Grzywacz, Joanna Gdula-Argasińska, Tadeusz Librowski, Bogdan Wiliński, and Włodzimierz Opoka. The role of zinc in the pathogenesis and treatment of central nervous system (cns) diseases. implications of zinc homeostasis for proper cns function. *Acta Poloniae Pharmaceutica*, 71(3):369–377, 2014.

[394] Kai He and Elias Aizenman. Erk signaling leads to mitochondrial dysfunction in extracellular zinc-induced neurotoxicity. *Journal of neurochemistry*, 114(2):452–461, Jul 2010.

[395] Shintaro Hojyo and Toshiyuki Fukada. Roles of zinc signaling in the immune system. *Journal of Immunology Research*, 2016:6762343–21, Jan 01, 2016.

[396] P. Paoletti, A. M. Vergnano, B. Barbour, and M. Casado. Zinc at glutamatergic synapses. *Neuroscience*, 158(1):126–136, Jan 12, 2009.

[397] Angela Maria Vergnano, Nelson Rebola, Leonid P Savtchenko, Paulo S Pinheiro, Mariano Casado, Brigitte L Kieffer, Dmitri A Rusakov, Christophe Mulle, and Pierre Paoletti. Zinc dynamics and action at excitatory synapses. *Neuron*, 82(5):1101–1114, Jun 04, 2014.

[398] Christopher J. Frederickson, Jae-Young Koh, and Ashley I. Bush. The neurobiology of zinc in health and disease. *Nature reviews.Neuroscience*, 6(6):449–462, Jun 2005.

[399] Philippe Pals, Bart Van Everbroeck, Bart Grubben, Maria Kristina Viaene, René Dom, Chris van der Linden, Patrick Santens, Jean Jacques Martin, and Patrick Cras. Case-control study of environmental risk factors for parkinson's disease in belgium. *European journal of epidemiology*, 18(12):1133–1142, 2003.

[400] Huiling Gao, Hehong Sun, Nan Yan, Pu Zhao, He Xu, Wei Zheng, Xiaoyu Zhang, Tao Wang, Chuang Guo, and Manli Zhong. Atp13a2 declines zinc-induced accumulation of α-synuclein in a parkinson's disease model. *International journal of molecular sciences*, 23(14):8035, Jul 21, 2022.

[401] Hiroyasu Sato, Takeo Kato, and Shigeki Arawaka. The role of ser129 phosphorylation of α-synuclein in neurodegeneration of parkinson's disease: a review of *in vivo* models. *Reviews in the neurosciences*, 24(2):115–123, 2013.

[402] Marija Usenovic, Emilie Tresse, Joseph R. Mazzulli, J. Paul Taylor, and Dimitri Krainc. Deficiency of atp13a2 leads to lysosomal dysfunction, α-synuclein accumulation, and neurotoxicity. *The Journal of neuroscience*, 32(12):4240–4246, Mar 21, 2012.

[403] Marija USENOVIC, Adam L. KNIGHT, Arpita RAY, Victoria WONG, Kevin R. BROWN, Guy A. CALDWELL, Kim A. CALDWELL, Igor STAGLJAR, and Dimitri KRAINC. Identification of novel atp13a2 interactors and their role in α-synuclein misfolding and toxicity. *Human molecular genetics*, 21(17):3785–3794, Sep 01, 2012.

[404] Taiji Tsunemi, Kana Hamada, and Dimitri Krainc. Atp13a2/park9 regulates secretion of exosomes and α-synuclein. *The Journal of neuroscience*, 34(46):15281–15287, Nov 12, 2014.

[405] Joo-Yong Lee, Hyo Jin Son, Ji Hyun Choi, Eunsil Cho, Jean Kim, Sun Ju Chung, Onyou Hwang, and Jae-Young Koh. Cytosolic labile zinc accumulation in degenerating dopaminergic neurons of mouse brain after mptp treatment. *Brain research*, 1286:208–214, Aug 25, 2009.

[406] Haruna Tamano, Ryusuke Nishio, Hiroki Morioka, Ryo Furuhata, Yuuma Komata, and Atsushi Takeda. Paraquat as an environmental risk factor in parkinson's disease accelerates age-related degeneration via rapid influx of extracellular zn(2+) into nigral dopaminergic neurons. *Molecular neurobiology*, 56(11):7789–7799, Nov 2019.

[407] Haruna Tamano, Hiroki Morioka, Ryusuke Nishio, Azusa Takeuchi, and Atsushi Takeda. Ampa-induced extracellular zn2+ influx into nigral dopaminergic neurons causes movement disorder in rats. *Neurotoxicology (Park Forest South)*, 69:23–28, Dec 2018.

[408] Ashutosh Kumar, Brajesh Kumar Singh, Israr Ahmad, Smriti Shukla, Devendra Kumar Patel, Garima Srivastava, Vinod Kumar, Haushila Prasad Pandey, and Chetna Singh. Involvement of nadph oxidase and glutathione in zinc-induced dopaminergic neurodegeneration in rats: Similarity with paraquat neurotoxicity. *Brain research*, 1438:48–64, Feb 15, 2012.

[409] Vinod Kumar, Deepali Singh, Brajesh Kumar Singh, Shweta Singh, Namrata Mittra, Rakesh Roshan Jha, Devendra Kumar Patel, and Chetna Singh. Alpha-synuclein aggregation, ubiquitin proteasome system impairment, and l-dopa response in zinc-induced parkinsonism: resemblance to sporadic parkinson's disease. *Molecular and cellular biochemistry*, 444(1-2):149–160, Jul 2018.

[410] M. V. Aguilar, F. J. Jiménez-Jiménez, J. A. Molina, I. Meseguer, C. J. Mateos-Vega, M. J. González-Muñoz, F. de Bustos, C. Gómez-Escalonilla, M. Ort-Pareja, M. Zurdo, and M. C. Martínez-Para. Cerebrospinal fluid selenium and chromium levels in patients with parkinson's disease. *Journal of neural transmission (Vienna, Austria : 1996)*, 105(10-12):1245–1251, 1998.

[411] Muralidhar L. Hegde, Ponnuswamy Shanmugavelu, Bhuma Vengamma, T. S. Sathyanarayana Rao, Rani B. Menon, Ranganath V. Rao, and K. S. Jagannatha Rao. Serum trace element levels and the complexity of inter-element relations in patients with parkinson's disease. *Journal of trace elements in medicine and biology : organ of the Society for Minerals and Trace Elements (GMS)*, 18(2):163–171, 2004.

[412] Alessandro Alimonti, Giovanni Ristori, Franco Giubilei, Maria Antonia Stazi, Anna Pino, Andrea Visconti, Sonia Brescianini, Micaela Sepe Monti, Giovanni Forte, Paolo Stanzione, Beatrice Bocca, Giuseppe Bomboi, Cristina D'Ippolito, Viviana Annibali, Marco Salvetti, and Giuseppe Sancesario. Serum chemical elements and oxidative status in alzheimer's disease, parkinson disease and multiple sclerosis. *Neurotoxicology (Park Forest South)*, 28(3):450–456, May 01, 2007.

[413] George J. Brewer, Steve H. Kanzer, Earl A. Zimmerman, Eric S. Molho, Dzintra F. Celmins, Susan M. Heckman, and Robert Dick. Subclinical zinc deficiency in alzheimer's disease and parkinson's disease. *American Journal of Alzheimer's Disease and Other Dementias*, 25(7):572–575, Nov 2010.

[414] Hai-Wen Zhao, Jie Lin, Xue-Bao Wang, Xing Cheng, Jian-Yong Wang, Bei-Lei Hu, Yan Zhang, Xiong Zhang, and Jian-Hong Zhu. Assessing plasma levels of selenium, copper, iron and zinc in patients of parkinson's disease. *PLoS ONE*, 8(12):e83060, Dec 10, 2013.

[415] Stephanie M. Y. Kong, Brian K. K. Chan, Jin-Sung Park, Kathryn J. Hill, Jade B. Aitken, Louise Cottle, Hovik Farghaian, Adam R. Cole, Peter A. Lay, Carolyn M. Sue, and Antony A. Cooper. Parkinson's disease-linked human park9/atp13a2 maintains zinc homeostasis and promotes α-synuclein externalization via exosomes. *Human molecular genetics*, 23(11):2816–2833, Jun 1 2014.

[416] Ventzislava A. Hristova, Steven A. Beasley, R. Jane Rylett, and Gary S. Shaw. Identification of a novel zn2+-binding domain in the autosomal recessive juvenile parkinson-related e3 ligase parkin. *The Journal of biological chemistry*, 284(22):14978–14986, May 29, 2009.

[417] Dilina do Nascimento Marreiro, Kyria Jayanne Clímaco Cruz, Jennifer Beatriz Silva Morais, Jéssica Batista Beserra, Juliana Soares Severo, and Ana Raquel Soares de Oliveira. Zinc and oxidative stress: Current mechanisms. *Antioxidants*, 6(2):24, Mar 29, 2017.

[418] J. L. Greger. Nutrition versus toxicology of manganese in humans: evaluation of potential biomarkers. *Neurotoxicology*, 20(2-3):205–212, 1999.

[419] Letizia Pontoriero, Marco Schiavina, Maria Grazia Murrali, Roberta Pierattelli, and Isabella C. Felli. Monitoring the interaction of α-synuclein with calcium ions through exclusively heteronuclear nuclear magnetic resonance experiments, -09-15 2020.

[420] Tomás R. Guilarte. Manganese neurotoxicity: new perspectives from behavioral, neuroimaging, and neuropathological studies in humans and non-human primates. *Frontiers in Aging Neuroscience*, 5:23, 2013.

[421] Mahfuzur R. Miah, Omamuyovwi M. Ijomone, Comfort O. A. Okoh, Olayemi K. Ijomone, Grace T. Akingbade, Tao Ke, Bárbara Krum, Airton da Cunha Martins, Ayodele Akinyemi, Nicole Aranoff, Felix Alexandre Antunes Soares, Aaron B. Bowman, and Michael Aschner. The effects of manganese overexposure on brain health. *Neurochemistry international*, 135:104688, May 01, 2020.

[422] Tanja Dučić, Eleonora Carboni, Barry Lai, Si Chen, Bernhard Michalke, Diana F. Lázaro, Tiago F. Outeiro, Mathias Bähr, Elisabeth Barski, and Paul Lingor. Alpha-synuclein regulates neuronal levels of manganese and calcium. *ACS chemical neuroscience*, 6(10):1769–1779, Oct 21, 2015.

[423] Tongjian Cai, Ting Yao, Gang Zheng, Yaoming Chen, Kejun Du, Yunxin Cao, Xuefeng Shen, Jingyuan Chen, and Wenjing Luo. Manganese induces the overexpression of α-synuclein in pc12 cells via erk activation. *Brain research*, 1359:201–207, Nov 04, 2010.

[424] Yan Li, Liguang Sun, Tongjian Cai, Ying Zhang, Shijie Lv, Yu Wang, and Liping Ye. α-synuclein overexpression during manganese-induced apoptosis in sh-sy5y neuroblastoma cells. *Brain research bulletin*, 81(4):428–433, Mar 16, 2010.

[425] Bin Xu, Sheng-Wen Wu, Chun-Wei Lu, Yu Deng, Wei Liu, Yan-Gang Wei, Tian-Yao Yang, and Zhao-Fa Xu. Oxidative stress involvement in manganese-induced alpha-synuclein oligomerization in organotypic brain slice cultures. *Toxicology (Amsterdam)*, 305:71–78, Mar 08, 2013.

[426] Yi Sun, Yonghua He, Lin Yang, Dan Liang, Wenxiang Shi, Xiaonian Zhu, Yueming Jiang, and Chaoyan Ou. Manganese induced nervous injury by α-synuclein accumulation via atp-sensitive k(+) channels and gaba receptors. *Toxicology letters*, 332:164–170, Oct 10, 2020.

[427] Zhi-Qi Liu, Kuan Liu, Zhuo-Fan Liu, Lin Cong, Meng-Yu Lei, Zhuo Ma, Jing Li, Yu Deng, Wei Liu, and Bin Xu. Manganese-induced alpha-synuclein overexpression aggravates mitochondrial damage by repressing pink1/parkin-mediated mitophagy. *Food and chemical toxicology*, 152:112213, Jun 01, 2021.

[428] Tatyana Verina, Jay S. Schneider, and Tomás R. Guilarte. Manganese exposure induces α-synuclein aggregation in the frontal cortex of non-human primates. *Toxicology letters*, 217(3):177–183, Mar 13, 2013.

[429] Dilshan S. Harischandra, Dharmin Rokad, Matthew L. Neal, Shivani Ghaisas, Sireesha Manne, Souvarish Sarkar, Nikhil Panicker, Gary Zenitsky, Huajun Jin, Mechelle Lewis, Xuemei Huang, Vellareddy Anantharam, Arthi Kanthasamy, and Anumantha G. Kanthasamy. Manganese promotes the aggregation and prion-like cell-to-cell exosomal transmission of α-synuclein. *Science signaling*, 12(572):eaau4543. doi: 10.1126/scisignal.aau4543, Mar 12 2019.

[430] Vladimir N. Uversky, Jie Li, and Anthony L. Fink. Evidence for a partially folded intermediate in α-synuclein fibril formation. *J.Biol.Chem.276:10737,2001*, 276(14):10737–10744, Apr 06, 2001.

[431] Bingkuan Xu, Shuai Huang, Yinghui Liu, Chun Wan, Yuanyuan Gu, Dianliang Wang, and Haijia Yu. Manganese promotes α-synuclein amyloid aggregation through the induction of protein phase transition. *The Journal of biological chemistry*, 298(1):101469, Jan 01, 2022.

[432] Sarah H. Shahmoradian, Amanda J. Lewis, Christel Genoud, J. rgen Hench, Tim E. Moors,

Paula P. Navarro, Daniel Castaño-Díez, Gabriel Schweighauser, Alexandra Graff-Meyer, Kenneth N. Goldie, Rosmarie Sütterlin, Evelien Huisman, Angela Ingrassia, Yvonne de Gier, Annemieke J. M. Rozemuller, Jing Wang, Anne De Paepe, Johannes Erny, Andreas Staempfli, Joerg Hoernschemeyer, Frederik Großerüschkamp, Daniel Niedieker, Samir F. el Mashtoly, Marialuisa Quadri, Wilfred F. J. van IJcken, Vincenzo Bonifati, Klaus Gerwert, Bernd Bohrmann, Stephan Frank, Markus Britschgi, Henning Stahlberg, Wilma D. J van de Berg, and Matthias E. Lauer. Lewy pathology in parkinson's disease consists of crowded organelles and lipid membranes. *Nature neuroscience*, 22(7):1099, 2019.

[433] Soumik Ray, Nitu Singh, Rakesh Kumar, Komal Patel, Satyaprakash Pandey, Debalina Datta, Jaladhar Mahato, Rajlaxmi Panigrahi, Ambuja Navalkar, Surabhi Mehra, Laxmikant Gadhe, Debdeep Chatterjee, Ajay Singh Sawner, Siddhartha Maiti, Sandhya Bhatia, Juan Atilio Gerez, Arindam Chowdhury, Ashutosh Kumar, Ranjith Padinhateeri, Roland Riek, G. Krishnamoorthy, and Samir K. Maji. α-synuclein aggregation nucleates through liquid-liquid phase separation. *Nature chemistry*, 12(8):705–716, Aug 2020.

[434] Maarten C. Hardenberg, Tessa Sinnige, Sam Casford, Samuel T. Dada, Chetan Poudel, Elizabeth A. Robinson, Monika Fuxreiter, Clemens F. Kaminksi, Gabriele S. Kaminski Schierle, Ellen A. A. Nollen, Christopher M. Dobson, and Michele Vendruscolo. Observation of an α-synuclein liquid droplet state and its maturation into lewy body-like assemblies. *Journal of molecular cell biology*, 13(4):282–294, Aug 4 2021.

[435] Christian Hoffmann, Roberto Sansevrino, Giuseppe Morabito, Chinyere Logan, R. Martin Vabulas, Ayse Ulusoy, Marcelo Ganzella, and Dragomir Milovanovic. Synapsin condensates recruit alpha-synuclein. *Journal of molecular biology*, 433(12):166961, Jun 11, 2021.

[436] B. A. Racette, L. McGee-Minnich, S. M. Moerlein, J. W. Mink, T. O. Videen, and J. S. Perlmutter. Welding-related parkinsonism: clinical features, treatment, and pathophysiology. *Neurology*, 56(1):8–13, Jan 9 2001.

[437] B. A. Racette, S. D. Tabbal, D. Jennings, L. Good, J. S. Perlmutter, and B. Evanoff. Prevalence of parkinsonism and relationship to exposure in a large sample of alabama welders. *Neurology*,

64(2):230–235, Jan 25 2005.

[438] Murray M. Finkelstein and Michael Jerrett. A study of the relationships between parkinson's disease and markers of traffic-derived and environmental manganese air pollution in two canadian cities. *Environmental research*, 104(3):420–432, Jul 01, 2007.

[439] Jay M. Gorell, Edward L. Peterson, Benjamin A. Rybicki, and Christine Cole Johnson. Multiple risk factors for parkinson's disease. *Journal of the neurological sciences*, 217(2):169–174, Feb 15 2004.

[440] Allison W. Willis, Mario Schootman, Nathan Kung, Bradley A. Evanoff, Joel S. Perlmutter, and Brad A. Racette. Predictors of survival in patients with parkinson disease. *Archives of neurology (Chicago)*, 69(5):601–607, May 01, 2012.

[441] J. M. Gorell, C. C. Johnson, B. A. Rybicki, E. L. Peterson, G. X. Kortsha, G. G. Brown, and R. J. Richardson. Occupational exposures to metals as risk factors for parkinson's disease. *Neurology*, 48(3):650–658, Mar 1997.

[442] Eun-Young Lee, Michael R. Flynn, Guangwei Du, Mechelle M. Lewis, Rebecca Fry, Amy H. Herring, Eric Van Buren, Scott Van Buren, Lisa Smeester, Lan Kong, Qing Yang, Richard B. Mailman, and Xuemei Huang. T1 relaxation rate (r1) indicates nonlinear mn accumulation in brain tissue of welders with low-level exposure. *Toxicological sciences : an official journal of the Society of Toxicology*, 146(2):281–289, Aug 2015.

[443] Eun-Young Lee, Michael R. Flynn, Guangwei Du, Yunqing Li, Mechelle M. Lewis, Amy H. Herring, Eric Van Buren, Scott Van Buren, Lan Kong, Rebecca C. Fry, Amanda M. Snyder, James R. Connor, Qing X. Yang, Richard B. Mailman, and Xuemei Huang. Increased r2* in the caudate nucleus of asymptomatic welders. *Toxicological sciences : an official journal of the Society of Toxicology*, 150(2):369–377, Apr 2016.

[444] Brad A. Racette, Michael Aschner, Tomas R. Guilarte, Ulrike Dydak, Susan R. Criswell, and Wei Zheng. Pathophysiology of manganese-associated neurotoxicity. *Neurotoxicology (Park Forest South)*, 33(4):881–886, Aug 01, 2012.

[445] C. M. Fored, J. P. Fryzek, L. Brandt, G. Nise, B. Sjögren, J. K. Mclaughlin, and W. J. Blot. Parkinson's disease and other basal ganglia or movement disorders in a large nationwide cohort of swedish welders, 2006.

[446] Samuel M. Goldman. Environmental toxins and parkinson's disease. *Annual Review of Pharmacology and Toxicology*, 54:141–164, 2014.

[447] William C. Koller, Kelly E. Lyons, and William Truly. Effect of levodopa treatment for parkinsonism in welders: A double-blind study. *Neurology*, 62(5):730–733, Mar 9 2004.

[448] C. Warren Olanow and Karl Kieburtz. Defining disease-modifying therapies for pd-a road map for moving forward. *Movement disorders*, 25(12):1774–1779, Sep 15, 2010.

[449] Tomás R. Guilarte. Manganese and parkinson's disease: a critical review and new findings. *Environmental health perspectives*, 118(8):1071–1080, Aug 2010.

[450] Tamara Peneder, Petra Scholze, Michael Berger, H. Reither, Georg Heinze, Johanna Bertl, Jan Bauer, Eric Richfield, O. Hornykiewicz, and C. Pifl. Chronic exposure to manganese decreases striatal dopamine turnover in human alpha-synuclein transgenic mice. *Neuroscience*, 180:280–92, 2011.

[451] G. Gianutsos and M. T. Murray. Alterations in brain dopamine and gaba following inorganic or organic manganese administration. *Neurotoxicology*, 3(3):75–81, Nov 1982.

[452] Marco Bisaglia, Alessandra Trolio, Massimo Bellanda, Elisabetta Bergantino, Luigi Bubacco, and Stefano Mammi. Structure and topology of the non-amyloid-beta component fragment of human alpha-synuclein bound to micelles: implications for the aggregation process. *Protein science : a publication of the Protein Society*, 15(6):1408–1416, Jun 2006.

[453] A. Keith Dunker, M. Madan Babu, Elisar Barbar, Martin Blackledge, Sarah E. Bondos, Zsuzsanna Dosztányi, H. Jane Dyson, Julie Forman-Kay, Monika Fuxreiter, Jörg Gsponer, Kyou-Hoon Han, David T. Jones, Sonia Longhi, Steven J. Metallo, Ken Nishikawa, Ruth Nussinov, Zoran Obradovic, Rohit V. Pappu, Burkhard Rost, Philipp Selenko, Vinod Subra-

maniam, Joel L. Sussman, Peter Tompa, and Vladimir N. Uversky. What's in a name? why these proteins are intrinsically disordered: Why these proteins are intrinsically disordered. *Intrinsically disordered proteins*, 1(1):e24157, Apr 1 2013.

[454] Robin van der Lee, Marija Buljan, Benjamin Lang, Robert J. Weatheritt, Gary W. Daughdrill, A. Keith Dunker, Monika Fuxreiter, Julian Gough, Joerg Gsponer, David T. Jones, Philip M. Kim, Richard W. Kriwacki, Christopher J. Oldfield, Rohit V. Pappu, Peter Tompa, Vladimir N. Uversky, Peter E. Wright, and M. Madan Babu. Classification of intrinsically disordered regions and proteins. *Chemical reviews*, 114(13):6589–6631, Jul 09, 2014.

[455] Johnny Habchi, Peter Tompa, Sonia Longhi, and Vladimir N. Uversky. Introducing protein intrinsic disorder. *Chemical reviews*, 114(13):6561–6588, Jul 9 2014.

[456] Miguel Arbesú and Miquel Pons. Integrating disorder in globular multidomain proteins: Fuzzy sensors and the role of sh3 domains. *Archives of Biochemistry and Biophysics*, 677:108161, Nov 30 2019.

[457] Francois-Xavier Theillet, Andres Binolfi, Tamara Frembgen-Kesner, Karan Hingorani, Mohona Sarkar, Ciara Kyne, Conggang Li, Peter B. Crowley, Lila Gierasch, Gary J. Pielak, Adrian H. Elcock, Anne Gershenson, and Philipp Selenko. Physicochemical properties of cells and their effects on intrinsically disordered proteins (idps). *Chemical Reviews*, 114(13):6661–6714, Jul 09, 2014.

[458] Leonhard Geist, Morkos A. Henen, Sandra Haiderer, Thomas C. Schwarz, Dennis Kurzbach, Anna Zawadzka-Kazimierczuk, Saurabh Saxena, Szymon Żerko, Wiktor Koźmiński, Dariush Hinderberger, and Robert Konrat. Protonation-dependent conformational variability of intrinsically disordered proteins. *Protein Science*, 22(9):1196–1205, 2013.

[459] Tsang-Lin Hwang, Susumu Mori, A. J. Shaka, and Peter C. M. van Zijl. Application of phase-modulated clean chemical exchange spectroscopy (cleanex-pm) to detect waterprotein proton exchange and intermolecular noes. *Journal of the American Chemical Society*, 119(26):6203–6204, 1997.

[460] Tsang-Lin Hwang, Peter C. M. Van Zijl, and Susumu Mori. Accurate quantitation of water-amide proton exchange rates using the phase-modulated clean chemical exchange (cleanex-pm) approach with a fast-hsqc (fhsqc) detection scheme, 1998.

[461] Thao T. Le, Pengxiang Chang, Donald J. Benton, John W. McCauley, Munir Iqbal, and Anthony E. G. Cass. Dual recognition element lateral flow assay toward multiplex strain specific influenza virus detection. *Analytical Chemistry*, 89(12):6781–6786, 2017.

[462] J. C. Cox, P. Rudolph, and A. D. Ellington. Automated rna selection. *Biotechnology progress*, 14(6):845–850, 1998.

[463] Michael Zuker. Mfold web server for nucleic acid folding and hybridization prediction. *Nucleic acids research*, 31(13):3406–3415, Jul 1 2003.

[464] Mohamed Mastouri, Sabrine Baachaoui, Amor Mosbah, and Noureddine Raouafi. screening for oligopeptides useful as capture and reporting probes for interleukin-6 biosensing. *RSC advances*, 12(21):133–1313, Apr 28, 2022.

[465] Sondes Ben Aissa, Mohamed Mastouri, Gaëlle Catanante, Noureddine Raouafi, and Jean Louis Marty. Investigation of a truncated aptamer for ofloxacin detection using a rapid fret-based apta-assay, -12-03 2020.

[466] Rajesh Babu Sekar and Ammasi Periasamy. Fluorescence resonance energy transfer (fret) microscopy imaging of live cell protein localizations. *The Journal of Cell Biology*, 160(5):629–633, Mar 03, 2003.

[467] Francesca Mattiroli, Yajie Gu, and Karolin Luger. Fret-based stoichiometry measurements of protein complexes *in vitro*.

[468] M. E. Rice. Ascorbate regulation and its neuroprotective role in the brain. *Trends in neurosciences*, 23(5):209–216, May 2000.

[469] Luc Guilloreau, Sarah Combalbert, Alix Sournia-Saquet, Honoré Mazarguil, and Peter Faller. Redox chemistry of copper-amyloid-β: The generation of hydroxyl radical in the presence

of ascorbate is linked to redox-potentials and aggregation state. *Chembiochem : a European journal of chemical biology*, 8(11):1317–1325, Jul 23, 2007.

[470] Jason Shearer and Veronika A. Szalai. The amyloid-β peptide of alzheimer's disease binds cui in a linear bis-his coordination environment: Insight into a possible neuroprotective mechanism for the amyloid-β peptide. *Journal of the American Chemical Society*, 130(52):17826–17835, Dec 31, 2008.

[471] W. F. Vranken, W. Boucher, T. J. Stevens, R. H. Fogh, A. Pajon, M. Llinas, E. L. Ulrich, J. L. Markley, J. Ionides, and E. D. Laue. The ccpn data model for nmr spectroscopy: development of a software pipeline. *Proteins*, 59(4):687–696, Jun 1 2005.

[472] G. P. Connelly, Y. Bai, M. F. Jeng, and S. W. Englander. Isotope effects in peptide group hydrogen exchange. *Proteins*, 17(1):87–92, Sep 1993.

[473] N. A. Farrow, R. Muhandiram, A. U. Singer, S. M. Pascal, C. M. Kay, G. Gish, S. E. Shoelson, T. Pawson, J. D. Forman-Kay, and L. E. Kay. Backbone dynamics of a free and phosphopeptide-complexed src homology 2 domain studied by 15n nmr relaxation. *Biochemistry*, 33(19):5984–6003, May 17 1994.

[474] M. Piotto, V. Saudek, and V. Sklenár. Gradient-tailored excitation for single-quantum nmr spectroscopy of aqueous solutions. *Journal of Biomolecular NMR*, 2(6):661–665, Nov 1992.

[475] Vincent Breukels, Albert Konijnenberg, Sanne M. Nabuurs, Jurgen F. Doreleijers, Nadezda V. Kovalevskaya, and Geerten W. Vuister. Overview on the use of nmr to examine protein structure. *Current protocols in protein science*, Chapter 17:Unit17.5, Apr 2011.

[476] Ann H. Kwan, Mehdi Mobli, Paul R. Gooley, Glenn F. King, and Joel P. Mackay. Macromolecular nmr spectroscopy for the non-spectroscopist. *The FEBS journal*, 278(5):687–703, Mar 2011.

[477] H. J. Dyson and Peter E. Wright. Coupling of folding and binding for unstructured proteins. *Current opinion in structural biology*, 12(1):54–60, 2002.

[478] H. Jane Dyson and Peter E. Wright. Insights into the structure and dynamics of unfolded proteins from nuclear magnetic resonance. *Advances in Protein Chemistry*, 62:311–340, 2002.

[479] James Keeler. *Understanding NMR spectroscopy*. John Wiley and Sons, Chichester, U.K., 2nd ed. edition, 2010.

[480] Robbins Puthenveetil and Olga Vinogradova. Solution nmr: A powerful tool for structural and functional studies of membrane proteins in reconstituted environments. *The Journal of biological chemistry*, 294(44):15914–15931, Nov 01, 2019.

[481] Sebanti Gupta and Surajit Bhattacharjya. Characterization of the near native conformational states of the sam domain of ste11 protein by nmr spectroscopy. *Proteins, structure, function, and bioinformatics*, 82(11):2957–2969, Nov 2014.

[482] Phineus R. L. Markwick, Thérèse Malliavin, and Michael Nilges. Structural biology by nmr: Structure, dynamics, and interactions. *PLoS Computational Biology*, 4(9):e1000168, Sep 01, 2008.

[483] G. Cornilescu, F. Delaglio, and A. Bax. Protein backbone angle restraints from searching a database for chemical shift and sequence homology. *Journal of Biomolecular NMR*, 13(3):289–302, Mar 1999.

[484] Carlo Camilloni, Paul Robustelli, Alfonso De Simone, Andrea Cavalli, and Michele Vendruscolo. Characterization of the conformational equilibrium between the two major substates of rnase a using nmr chemical shifts. *Journal of the American Chemical Society*, 134(9):3968–3971, Mar 07, 2012.

[485] Alfonso De Simone, Martin Gustavsson, Rinaldo W. Montalvao, Lei Shi, Gianluigi Veglia, and Michele Vendruscolo. Structures of the excited states of phospholamban and shifts in their populations upon phosphorylation. *Biochemistry (Easton)*, 52(38):6684–6694, Sep 24, 2013.

[486] Alfonso De Simone, Barbara Richter, Xavier Salvatella, and Michele Vendruscolo. Toward an accurate determination of free energy landscapes in solution states of proteins. *Journal of the*

American Chemical Society, 131(11):3810–3811, Mar 25, 2009.

[487] Carlo Camilloni, Alfonso De Simone, Wim F. Vranken, and Michele Vendruscolo. Determination of secondary structure populations in disordered states of proteins using nuclear magnetic resonance chemical shifts. *Biochemistry (Easton)*, 51(11):2224–2231, Mar 20, 2012.

[488] Jane R. Allison, Peter Varnai, Christopher M. Dobson, and Michele Vendruscolo. Determination of the free energy landscape of α-synuclein using spin label nuclear magnetic resonance measurements. *Journal of the American Chemical Society*, 131(51):18314–18326, Dec 30, 2009.

[489] Pramodh Vallurupalli, Guillaume Bouvignies, and Lewis E. Kay. Studying "invisible" excited protein states in slow exchange with a major state conformation. *Journal of the American Chemical Society*, 134(19):8148–8161, May 16, 2012.

[490] Vicky A. Higman. Protein nmr: A practical guide, April 10, 2019.

[491] Ian R. Kleckner and Mark P. Foster. An introduction to nmr-based approaches for measuring protein dynamics. *Biochimica et biophysica acta*, 1814(8):942–968, Aug 01, 2011.

[492] Jose Luis Ortega-Roldan, Martin Blackledge, and Malene Ringkjøbing Jensen. Characterizing protein-protein interactions using solution nmr spectroscopy. *Methods in molecular biology (Clifton, N.J.)*, 1764:73–85, 2018.

[493] Allen D. Elster. Chemical exchange - what do you mean by chemical exchange and how does it effect t1 and t2?, 2023. MRIquestions.com.

[494] A. Hvidt and S. O. Nielsen. Hydrogen exchange in proteins. *Advances in Protein Chemistry*, 21:287–386, 1966.

[495] Mallela M. G. Krishna, Linh Hoang, Yan Lin, and S. Walter Englander. Hydrogen exchange methods to study protein folding. *Methods (San Diego, Calif.)*, 34(1):51–64, Sep 2004.

[496] K. Linderstrøm-Lang. Deuterium exchange and protein structure. In *Symposium on protein*

structure, pages 23–34. Methuen London, 1958.

[497] K. Linderstrøm-Lang. Deuterium exchange between peptides and water. *Chem Soc Spec Publ*, 2:1–20, 1955.

[498] A. HVIDT. A discussion of the ph dependence of the hydrogen-deuterium exchange of proteins. *Comptes-rendus des travaux du Laboratoire Carlsberg*, 34:299–317, 1964.

[499] I. Bahar and R. L. Jernigan. Inter-residue potentials in globular proteins and the dominance of highly specific hydrophilic interactions at close separation. *Journal of Molecular Biology*, 266(1):195–214, Feb 14 1997.

[500] N. Bloembergen, E. M. Purcell, and R. V. Pound. Relaxation effects in nuclear magnetic resonance absorption. *Physical Review*, 73(7):679–712, 1948.

[501] Piotr Tekely. Malcolm h. levitt. spin dynamics: basics of nuclear magnetic resonance. john wiley & sons. *Magnetic Resonance in Chemistry*, 40(12):800, 2002.

[502] J. B. Grutzner. *NUCLEAR MAGNETIC RESONANCE SPECTROSCOPY | Principles*, pages 211–237. Encyclopedia of Analytical Science (Second Edition). Elsevier, Oxford, 2005.

[503] Benjamin Dehay, Mathieu Bourdenx, Philippe Gorry, Serge Przedborski, Miquel Vila, Stéphane Hunot, Andrew Singleton, C. W. Olanow, Kalpana M. Merchant, Erwan Bezard, Gregory A. Petsko, and Wassilios G. Meissner. Targeting α-synuclein for treatment of parkinson's disease: mechanistic and therapeutic considerations. *The Lancet Neurology*, 14(8):855–866, 2015.

[504] N. Komarova and A. Kuznetsov. Inside the black box: What makes selex better? *Molecules (Basel, Switzerland)*, 24(19):10.3390/molecules24193598, Oct 7 2019.

[505] H. Hasegawa, N. Savory, K. Abe, and K. Ikebukuro. Methods for improving aptamer binding affinity. *Molecules (Basel, Switzerland)*, 21(4):421, Mar 28 2016.

[506] P. Kalra, A. Dhiman, W. C. Cho, J. G. Bruno, and T. K. Sharma. Simple methods and rational

design for enhancing aptamer sensitivity and specificity. *Frontiers in molecular biosciences*, 5:41, May 14 2018.

[507] Fabian Tolle, Julian Wilke, Jesper Wengel, and Günter Mayer. By-product formation in repetitive pcr amplification of dna libraries during selex. *PLOS ONE*, 9(12):e114693, 2014.

[508] Kelly-Anne Frith, Ronen Fogel, J. P. D. Goldring, Robert G. E. Krause, Makobetsa Khati, Heinrich Hoppe, Mary E. Cromhout, Meesbah Jiwaji, and Janice L. Limson. Towards development of aptamers that specifically bind to lactate dehydrogenase of plasmodium falciparum through epitopic targeting. *Malaria Journal*, 17(1):191, 2018.

[509] M. Y. Zhou and C. E. Gomez-Sanchez. Universal ta cloning. *Current Issues in Molecular Biology*, 2(1):1–7, Jan 2000.

[510] N. Bengoa-Vergniory, R. F. Roberts, R. Wade-Martins, and J. Alegre-Abarrategui. Alpha-synuclein oligomers: a new hope. *Acta Neuropathologica*, 134(6):819–838, Dec 2017.

[511] Thao T. Le, Steven Scott, and Anthony E. G. Cass. Streptavidin binding bifunctional aptamers and their interaction with low molecular weight ligands. *Analytica Chimica Acta*, 761:143–148, 2013.

[512] K. Shao, W. Ding, F. Wang, H. Li, D. Ma, and H. Wang. Emulsion pcr: a high efficient way of pcr amplification of random dna libraries in aptamer selection. *PloS one*, 6(9):e24910, 2011.

[513] R. D. Jenison, S. C. Gill, A. Pardi, and B. Polisky. High-resolution molecular discrimination by rna. *Science (New York, N.Y.)*, 263(5152):1425–1429, Mar 11 1994.

[514] A. Geiger, P. Burgstaller, H. von der Eltz, A. Roeder, and M. Famulok. Rna aptamers that bind l-arginine with sub-micromolar dissociation constants and high enantioselectivity. *Nucleic acids research*, 24(6):1029–1036, Mar 15 1996.

[515] Andrew D. Ellington and Jack W. Szostak. Selection *in vitro* of single-stranded dna molecules that fold into specific ligand-binding structures. *Nature*, 355(6363):850–852, 1992.

[516] G. Aquino-Jarquin and J. D. Toscano-Garibay. Rna aptamer evolution: two decades of selection. *International journal of molecular sciences*, 12(12):9155–9171, 2011.

[517] Andrew M. Waterhouse, James B. Procter, David M. A. Martin, Michèle Clamp, and Geoffrey J. Barton. Jalview version 2–a multiple sequence alignment editor and analysis workbench. *Bioinformatics (Oxford, England)*, 25(9):1189–1191, May 1 2009.

[518] Douglas R. Davies, Amy D. Gelinas, Chi Zhang, John C. Rohloff, Jeffrey D. Carter, Daniel O'Connell, Sheela M. Waugh, Steven K. Wolk, Wesley S. Mayfield, Alex B. Burgin, Thomas E. Edwards, Lance J. Stewart, Larry Gold, Nebojsa Janjic, and Thale C. Jarvis. Unique motifs and hydrophobic interactions shape the binding of modified dna ligands to protein targets. *Proceedings of the National Academy of Sciences*, 109(49):19971–19976, 2012.

[519] Jan P. Elskens, Joke M. Elskens, and Annemieke Madder. Chemical modification of aptamers for increased binding affinity in diagnostic applications: Current status and future prospects. *International journal of molecular sciences*, 21(12):4522. doi: 10.3390/ijms21124522, Jun 25 2020.

[520] Hani A. Alhadrami, Raja Chinnappan, Shimaa Eissa, Anas Abdel Rahamn, and Mohammed Zourob. High affinity truncated dna aptamers for the development of fluorescence based progesterone biosensors. *Analytical Biochemistry*, 525:78–84, May 15 2017.

[521] Abhijeet Dhiman, Anjali Anand, Anita Malhotra, Eshan Khan, Vishal Santra, Amit Kumar, and Tarun Kumar Sharma. Rational truncation of aptamer for cross-species application to detect krait envenomation. *Scientific Reports*, 8(1):17795, 2018.

[522] Carlos Navarro-Paya, Maximo Sanz-Hernandez, and Alfonso De Simone. In silico study of the mechanism of binding of the n-terminal region of α synuclein to synaptic-like membranes. *Life (Basel, Switzerland)*, 10(6):98, Jun 26, 2020.

[523] R. Kruger, W. Kuhn, T. Muller, D. Woitalla, M. Graeber, S. Kosel, H. Przuntek, J. T. Epplen, L. Schols, and O. Riess. Ala30pro mutation in the gene encoding alpha-synuclein in parkinson's disease. *Nature genetics*, 18(2):106–108, Feb 1998.

[524] Erwin Neher and Takeshi Sakaba. Multiple roles of calcium ions in the regulation of neurotransmitter release. *Neuron*, 59(6):861–872, 2008.

[525] S. R. Paik, H. J. Shin, and J. H. Lee. Metal-catalyzed oxidation of alpha-synuclein in the presence of copper(ii) and hydrogen peroxide. *Archives of Biochemistry and Biophysics*, 378(2):269–277, Jun 15 2000.

[526] Jennifer C. Lee, Harry B. Gray, and Jay R. Winkler. Copper(ii) binding to α-synuclein, the parkinson's protein. *Journal of the American Chemical Society*, 130(22):6898–6899, 2008.

[527] S. R. Paik, H. J. Shin, J. H. Lee, C. S. Chang, and J. Kim. Copper(ii)-induced self-oligomerization of alpha-synuclein. *The Biochemical journal*, 340 (Pt 3)(Pt 3):821–828, Jun 15 1999.

[528] Andrés Binolfi, Gonzalo R. Lamberto, Rosario Duran, Liliana Quintanar, Carlos W. Bertoncini, Jose M. Souza, Carlos Cerve nansky, Markus Zweckstetter, Christian Griesinger, and Claudio O. Fernández. Site-specific interactions of cu(ii) with α and β-synuclein: Bridging the molecular gap between metal binding and aggregation. *Journal of the American Chemical Society*, 130(35):11801–11812, Sep 03, 2008.

[529] Vladimir N. Uversky, Jie Li, and Anthony L. Fink. Metal-triggered structural transformations, aggregation, and fibrillation of human α-synuclein: A possible molecular link between parkinson's disease and heavy metal exposure. *Journal of Biological Chemistry*, 276(47):44284–44296, 2001.

[530] Kuen-Phon Wu and Jean Baum. Detection of transient interchain interactions in the intrinsically disordered protein α-synuclein by nmr paramagnetic relaxation enhancement. *Journal of the American Chemical Society*, 132(16):5546–5547, Apr 28, 2010.

[531] Amberley D. Stephens, Nadezhda Nespovitaya, Maria Zacharopoulou, Clemens F. Kaminski, Jonathan J. Phillips, and Gabriele S. Kaminski Schierle. Different structural conformers of monomeric α-synuclein identified after lyophilizing and freezing, -05-11 2018.

[532] Santiago Esteban-Martín, Jordi Silvestre-Ryan, Carlos W Bertoncini, and Xavier Salvatella. Identification of fibril-like tertiary contacts in soluble monomeric α-synuclein. *Biophysical Journal*, 105(5):1192–1198, Sep 03, 2013.

[533] Sebastian McClendon, Carla C. Rospigliosi, and David Eliezer. Charge neutralization and collapse of the c-terminal tail of alpha-synuclein at low ph. *Protein science*, 18(7):1531–1540, Jul 2009.

[534] Priyatosh Ranjan and Ashutosh Kumar. Perturbation in long-range contacts modulates the kinetics of amyloid formation in α-synuclein familial mutants. *ACS chemical neuroscience*, 8(10):2235–2246, Oct 18, 2017.

[535] Yoon hui Sung and David Eliezer. Residual structure, backbone dynamics, and interactions within the synuclein family. *Journal of molecular biology*, 372(3):689–707, Sep 21, 2007.

[536] Christopher G. Dudzik, Eric D. Walter, and Glenn L. Millhauser. Coordination features and affinity of the cu2+ site in the α-synuclein protein of parkinson's disease. *Biochemistry (Easton)*, 50(11):1771–1777, Mar 22, 2011.

[537] Simon C. Drew, Su Ling Leong, Chi L. L. Pham, Deborah J. Tew, Colin L. Masters, Luke A. Miles, Roberto Cappai, and Kevin J. Barnham. Cu2+ binding modes of recombinant α-synuclein - insights from epr spectroscopy. *Journal of the American Chemical Society*, 130(24):7766–7773, Jun 18, 2008.

[538] Yao Tian, Helen F. Stanyon, Joseph D. Barritt, Uroosa Mayet, Pelak Patel, Elena Karamani, Giuliana Fusco, and John H. Viles. Copper 2+ binding to α-synuclein. histidine50 can form a ternary complex with cu2+ at the n-terminus but not a macrochelate, -11-07 2019.

[539] Christos Proukakis, Henry Houlden, and Anthony H. Schapira. Somatic alpha-synuclein mutations in parkinson's disease: Hypothesis and preliminary data. *Movement Disorders*, 28(6):705–712, Jun 2013.

[540] Dhiman Ghosh, Mrityunjoy Mondal, Ganesh M. Mohite, Pradeep K. Singh, Priyatosh Ranjan,

A. Anoop, Saikat Ghosh, Narendra Nath Jha, Ashutosh Kumar, and Samir K. Maji. The parkinson's disease-associated h50q mutation accelerates α-synuclein aggregation *in vitro*. *Biochemistry (Easton)*, 52(40):6925–6927, Oct 08, 2013.

[541] Riccardo Porcari, Christos Proukakis, Christopher A. Waudby, Benedetta Bolognesi, P. Patrizia Mangione, Jack F. S. Paton, Stephen Mullin, Lisa D. Cabrita, Amanda Penco, Annalisa Relini, Guglielmo Verona, Michele Vendruscolo, Monica Stoppini, Gian Gaetano Tartaglia, Carlo Camilloni, John Christodoulou, Anthony H. V. Schapira, and Vittorio Bellotti. The h50q mutation induces a 10-fold decrease in the solubility of α-synuclein. *The Journal of Biological Chemistry*, 290(4):2395–2404, Jan 23, 2015.

[542] Ossama Khalaf, Bruno Fauvet, Abid Oueslati, Igor Dikiy, Anne Laure Mahul-Mellier, Francesco Simone Ruggeri, Martial K. Mbefo, Filip Vercruysse, Giovanni Dietler, Seung Jae Lee, David Eliezer, and Hilal A. Lashuel. The h50q mutation enhances αα-synuclein aggregation, secretion, and toxicity. *The Journal of biological chemistry*, 289(32):21856–21876, Aug 08, 2014.

[543] Rebecca J. Mason, Aimee R. Paskins, Caroline F. Dalton, and David P. Smith. Copper binding and subsequent aggregation of α-synuclein are modulated by n-terminal acetylation and ablated by the h50q missense mutation. *Biochemistry (Easton)*, 55(34):4737–4741, Aug 30, 2016.

[544] Anna Villar-Piqué, Tomás Lopes Da Fonseca, Ricardo Sant'anna, Éva Mónika Szegö, Luis Fonseca-Ornelas, Raquel Pinho, Anita Carija, Ellen Gerhardt, Caterina Masaracchia, Enrique Abad Gonzalez, Giulia Rossetti, Paolo Carloni, Claudio O. Fernández, Debora Foguel, Ira Milosevic, Markus Zweckstetter, Salvador Ventura, and Tiago Fleming Outeiro. Environmental and genetic factors support the dissociation between α-synuclein aggregation and toxicity, -10-05 2016.

[545] Frisco Rose, Miroslav Hodak, and Jerzy Bernholc. Mechanism of copper(ii)-induced misfolding of parkinson's disease protein. *Scientific Reports*, 1(1):11, Jun 14, 2011.

[546] Ying-Chih Chi, Geoffrey S. Armstrong, David N. M. Jones, Elan Z. Eisenmesser, and Chang-Wei Liu. Residue histidine 50 plays a key role in protecting α-synuclein from aggregation at physiological ph. *The Journal of biological chemistry*, 289(22):15474–15481, May 30, 2014.

[547] Antonino Natalello, Federico Benetti, Silvia Maria Doglia, Giuseppe Legname, and Rita Grandori. Compact conformations of α-synuclein induced by alcohols and copper. *Proteins, structure, function, and bioinformatics*, 79(2):611–621, Feb 2011.

[548] Atta Ahmad, Colin S. Burns, Anthony L. Fink, and Vladimir N. Uversky. Peculiarities of copper binding to alpha-synuclein. *Journal of Biomolecular Structure & Dynamics*, 29(4):825–842, 2012.

[549] Honoka Okazaki, Yuka Ohori, Masaya Komoto, Young-Ho Lee, Yuji Goto, Naoya Tochio, and Chiaki Nishimura. Remaining structures at the n- and c-terminal regions of alpha-synuclein accurately elucidated by amide-proton exchange nmr with fitting. *FEBS letters*, 587(22):3709–3714, Nov 15, 2013.

[550] G. Hernandez, F. E. Jr Jenney, M. W. Adams, and D. M. LeMaster. Millisecond time scale conformational flexibility in a hyperthermophile protein at ambient temperature. *Proceedings of the National Academy of Sciences of the United States of America*, 97(7):3166–3170, Mar 28 2000.

[551] Austin E. Smith, Larry Z. Zhou, and Gary J. Pielak. Hydrogen exchange of disordered proteins in escherichia coli. *Protein science : a publication of the Protein Society*, 24(5):706–713, May 2015.

[552] Robyn L. Croke, Christine O. Sallum, Emma Watson, Eric D. Watt, and Andrei T. Alexandrescu. Hydrogen exchange of monomeric α-synuclein shows unfolded structure persists at physiological temperature and is independent of molecular crowding in escherichia coli. *Protein science*, 17(8):1434–1445, Aug 2008.

[553] S. Grzesiek and A. Bax. Amino acid type determination in the sequential assignment procedure of uniformly 13c/15n-enriched proteins. *Journal of biomolecular NMR*, 3(2):185–204, Mar

1993.

[554] S. Mori, C. Abeygunawardana, M. O. Johnson, and P. C. van Zijl. Improved sensitivity of hsqc spectra of exchanging protons at short interscan delays using a new fast hsqc (fhsqc) detection scheme that avoids water saturation. *Journal of magnetic resonance.Series B*, 108(1):94–98, Jul 1995.

[555] Peter S. Kim and Robert L. Baldwin. Specific intermediates in the folding reactions of small proteins and the mechanism of protein folding. *Annual Review of Biochemistry*, 51(1):459–489, 1982.

[556] J. B. Matthew and F. M. Richards. The ph dependence of hydrogen exchange in proteins. *Journal of Biological Chemistry*, 258(5):3039–3044, 1983.

[557] Summer L. Bernstein, Dengfeng Liu, Thomas Wyttenbach, Michael T. Bowers, Jennifer C. Lee, Harry B. Gray, and Jay R. Winkler. α-synuclein: Stable compact and extended monomeric structures and ph dependence of dimer formation. *Journal of the American Society for Mass Spectrometry*, 15(10):1435–1443, Oct 01, 2004.

[558] Agya K. Frimpong, Rinat R. Abzalimov, Vladimir N. Uversky, and Igor A. Kaltashov. Characterization of intrinsically disordered proteins with electrospray ionization mass spectrometry: Conformational heterogeneity of α-synuclein. *Proteins, structure, function, and bioinformatics*, 78(3):714–722, Feb 15, 2010.

[559] Kuen-Phon Wu, Daniel S. Weinstock, Chitra Narayanan, Ronald M. Levy, and Jean Baum. Structural reorganization of α-synuclein at low ph observed by nmr and remd simulations. *Journal of molecular biology*, 391(4):784–796, Aug 28, 2009.

[560] Hamed Shaykhalishahi, Aziz Gauhar, Michael M. Wördehoff, Clara S. R. Grüning, Antonia N. Klein, Oliver Bannach, Matthias Stoldt, Dieter Willbold, Torleif Härd, and Wolfgang Hoyer. Contact between the β1 and β2 segments of α-synuclein that inhibits amyloid formation. *Angewandte Chemie (International ed.)*, 54(30):8837–8840, Jul 20, 2015.

[561] Ewa A. Mirecka, Hamed Shaykhalishahi, Aziz Gauhar, Şerife Akgül, Justin Lecher, Dieter Willbold, Matthias Stoldt, and Wolfgang Hoyer. Sequestration of a β-hairpin for control of α-synuclein aggregation. *Angewandte Chemie (International ed.)*, 53(16):4227–4230, Apr 14, 2014.

[562] Emil Dandanell Agerschou, Patrick Flagmeier, Theodora Saridaki, Céline Galvagnion, Daniel Komnig, Laetitia Heid, Vibha Prasad, Hamed Shaykhalishahi, Dieter Willbold, Christopher M. Dobson, Aaron Voigt, Bjoern Falkenburger, Wolfgang Hoyer, and Alexander K. Buell. An engineered monomer binding-protein for α-synuclein efficiently inhibits the proliferation of amyloid fibrils, -08-21 2019.

[563] Jeffrey C. Kessler, Jean-Christophe Rochet, and Peter T. Lansbury. The n-terminal repeat domain of α-synuclein inhibits β-sheet and amyloid fibril formation. *Biochemistry (Easton)*, 42(3):672–678, Jan 28, 2003.

[564] Volodymyr V. Shvadchak and Vinod Subramaniam. A four-amino acid linker between repeats in the α-synuclein sequence is important for fibril formation. *Biochemistry (Easton)*, 53(2):279–281, Jan 21, 2014.

[565] Björn M. Burmann, Juan A. Gerez, Irena Matečko-Burmann, Silvia Campioni, Pratibha Kumari, Dhiman Ghosh, Adam Mazur, Emelie E. Aspholm, Darius Šulskis, Magdalena Wawrzyniuk, Thomas Bock, Alexander Schmidt, Stefan G. D. Rüdiger, Roland Riek, and Sebastian Hiller. Regulation of α-synuclein by chaperones in mammalian cells, -12-04 2019.

[566] Alexey V. Krasnoslobodtsev, Ivan L. Volkov, Josephat M. Asiago, Jagadish Hindupur, Jean-Christophe Rochet, and Yuri L. Lyubchenko. α-synuclein misfolding assessed with single molecule afm force spectroscopy: Effect of pathogenic mutations. *Biochemistry (Easton)*, 52(42):7377–7386, Oct 22, 2013.

[567] Marco Brucale, Massimo Sandal, Selena Di Maio, Aldo Rampioni, Isabella Tessari, Laura Tosatto, Marco Bisaglia, Luigi Bubacco, and Bruno Samorì. Pathogenic mutations shift the equilibria of α-synuclein single molecules towards structured conformers. *Chembiochem : a*

European journal of chemical biology, 10(1):176–183, Jan 05, 2009.

[568] Olivia Wise-Scira, Aquila Dunn, Ahmet K. Aloglu, Isin T. Sakallioglu, and Orkid Coskuner. Structures of the e46k mutant-type α-synuclein protein and impact of e46k mutation on the structures of the wild-type α-synuclein protein. *ACS chemical neuroscience*, 4(3):498–508, Mar 20, 2013.

[569] Jong Yoon Han, Tae Su Choi, and Hugh I. Kim. Molecular role of ca2+ and hard divalent metal cations on accelerated fibrillation and interfibrillar aggregation of α-synuclein. *Scientific Reports*, 8(1):1–11, Jan 30, 2018.

[570] Sumanta Kar, Samarpita Sen, Saptarshi Maji, Deepashri Saraf, Ruturaj, Rupam Paul, Sohini Dutt, Basudeb Mondal, Enrique Rodriguez-Boulan, Ryan Schreiner, Durba Sengupta, and Arnab Gupta. Copper(ii) import and reduction are dependent on his-met clusters in the extracellular amino terminus of human copper transporter-1. *The Journal of biological chemistry*, 298(3):101631, Mar 2022.

[571] Steven J. Roeters, Aditya Iyer, Galja Pletikapić, Vladimir Kogan, Vinod Subramaniam, and Sander Woutersen. Evidence for intramolecular antiparallel β-sheet structure in alpha-synuclein fibrils from a combination of two-dimensional infrared spectroscopy and atomic force microscopy. *Scientific reports*, 7:41051, Jan 23 2017.

[572] Regina Stoltenburg, Nadia Nikolaus, and Beate Strehlitz. Capture-selex: Selection of dna aptamers for aminoglycoside antibiotics. *Journal of analytical methods in chemistry*, 2012:415697, 2012.

[573] Tanu Bhardwaj, Anurag S. Rathore, and Sandeep Kumar Jha. The selection of highly specific and selective aptamers using modified selex and their use in process analytical techniques for lucentis bioproduction. *RSC advances*, 10(48):28906–28917, Aug 4 2020.

[574] Nelson de Oliveira Manzanza, Lucia Sedlackova, and Raj N. Kalaria. Alpha-synuclein post-translational modifications: Implications for pathogenesis of lewy body disorders. *Frontiers in Aging Neuroscience*, 13, 2021.